

Nu Bich Duyen Do

Novel encapsulation of a medical ultrasound probe

**Dissertation for the
degree of Ph.D**
Applied micro- and nano
systems

**Faculty of Technology, Natural
Sciences and Maritime
Sciences**

Nu Bich Duyen Do

Novel encapsulation of a medical ultrasound probe

A PhD dissertation in
Applied micro- and nano systems

© Nu Bich Duyen Do, 2024

Faculty of Technology, Natural Sciences and Maritime Sciences
University of South-Eastern Norway
Horten

Doctoral dissertations at the University of South-Eastern Norway no. 182

ISSN: 2535-5244 (print)

ISSN: 2535-5252 (online)

ISBN: 978-82-7206-829-4 (print)

ISBN: 978-82-7206-828-7 (online)



This publication is licensed with a Creative Commons license. You may copy and redistribute the material in any medium or format. You must give appropriate credit, provide a link to the license, and indicate if changes were made. Complete license terms at <https://creativecommons.org/licenses/by-nc-sa/4.0/deed.en>

Print: University of South-Eastern Norway

Preface

This doctoral thesis is submitted in partial fulfilment of the requirements for the degree of Doctor of Philosophy at the Faculty of Technology, Natural Sciences and Maritime Sciences, University of South-Eastern Norway (USN), Norway. The project was conducted between January 2018 and September 2021 under the supervision of Associate Professor Kristin Imenes and Adjunct Professor Erik Andreassen. The experimental work of the PhD study was performed at the laboratories of Department of Microsystems (IMS), USN (Horten, Norway); Department of Materials and Nanotechnology, SINTEF Industry (Oslo, Norway); Department of Physics, University of Oslo (Oslo, Norway); and Conpart AS (Skjetten, Norway).

This project has been funded by the Research Council of Norway through the BIA program (grant number: 269618; *Mechanical miniaturization in interventional medical instruments*), and by the Norwegian Micro- and Nano-Fabrication Facility (NorFab, project number: 245963/F50, and 295864 NORFAB III).

Acknowledgements

First of all, I would like to express my sincere gratitude to my supervisors, Adjunct Prof. Erik Andreassen and Assoc. Prof. Kristin Imenes, for the enduring guidance and great support throughout my PhD project. Your advice, patience, and inspiring encouragement helped me in all the difficult time of the project and writing of this thesis. Your great knowledge of materials and material processing as well as medical devices have been the vital inputs for my study.

My appreciation also goes to Prof. Knut E. Aasmundtveit and Assoc. Prof. Hoang-Vu Nguyen for your assistance and constructive feedbacks during my PhD study. Thank you so much for always supporting me since I was your master student.

I am also grateful to the MMIMI team (Dr. Stephen Edwardsen, Mr. Anders Lifjell and Mr. Birger Loype) at GE Vingmed Ultrasound AS (Horten, Norway) for the valuable supports with samples, equipment, and materials during this project.

I also gratefully acknowledge Mr. Paul McMahon and Mr. Marius Johansen at SINTEF Industry; Dr. Jeyanthinath Mayandi at University of Oslo (UiO); Mr. Erik Kalland at Conpart AS; Mrs. Zekija Ramic, Mr. Svein Mindrebøe, Mr. Thomas Martinsen, Dr. Thai Anh Tuan Nguyen, Dr. Tayyib Muhammad and Dr. Chaoqun Cheng at University of South-Eastern Norway (USN); Mr. Thao Ngoc Vo at Ellingsen Systems AS; Dr. Tri Quang Bui at Østfold University College; Dr. Vinh Duy Cao at Norner AS for the enthusiastic assistance with laboratory work.

Special thanks are directed to Prof. Terje Finstad at UiO, Dr. Helge Kristiansen at Conpart AS, Prof. Tao Dong and Dr. Zhongyuan Shi at USN for your help and valuable discussions during my PhD study.

A lot of thanks are sent to my friends at IMS, USN, for the pleasant study and relaxing atmosphere, helpful discussions during the time I was at USN Campus Vestfold.

Last but not least, I would like to express my profound gratitude to my parents, my younger brother, and especially my husband for the love, continuous support, understanding and spiritual encouragement for me during all these challenging years.

Stavanger, May 2023

Nu Bich Duyen Do

Abstract

Ultrasound imaging plays an important role in the diagnosis of cardiovascular diseases. A trans-esophageal echocardiography (TEE) probe uses ultrasound waves to image the heart in real time in three dimensions (3D) from inside the esophagus of the patient.

The current design of the TEE scan head in this study requires manual assembly of several prefabricated parts to provide key functions; heat spreading, electromagnetic interference (EMI) shielding, electrical isolation, and biocompatibility. The aim of this study was to develop new encapsulation concepts (based on materials, designs, or processing methods) to reduce the number of parts. This could be achieved by a two-layer encapsulation (e.g. metallized encapsulation, or encapsulation with two polymer composites). Among the requirements for this device, thermal management is important for the safety, performance, lifetime, and reliability. Therefore, this project focused on the thermal performance of new encapsulation concepts.

The maximum surface temperature of the scan head (in contact with patient) must be below 43 °C to avoid thermal damage to human tissue. A two-layer encapsulation based on a metallized polymer structure was suggested for simplifying the assembly, while accommodating the key functions listed above. Experimental results showed that such an encapsulation could provide adequate heat transfer at low power levels. Thermal simulations were in good agreement with the experiments, when two different thermal contact conductance coefficients were used for the boundary condition in the finite element model, one for the heat source surface and one for the remainder of the scan head surface (the polymer encapsulation). The verified simulation model was used to identify alternative materials for the outer layer of the encapsulation, to improve the heat transfer at higher power levels. The preferred outer material is biocompatible and electrically insulating, and has high thermal conductivity.

Thermally conductive polymer composites were therefore selected as the second main research topic. Composites with hBN particles (thermally conductive and

electrically insulating) were studied. Composite specimens were fabricated by injection moulding, casting and 3D printing (powder bed fusion). The maximum practical hBN loading was 65 wt% for injection moulding with TPU as matrix, 55 wt% for casting with epoxy and 40 wt% for powder bed fusion with TPU. The injection moulded composite with 65 wt% hBN obtained the highest thermal conductivity in this study (2.1 W/mK), which was nearly 10 times higher than that of pure TPU. For a given hBN loading, casting resulted in a higher thermal conductivity than the other two methods. Injection moulding induced a preferred orientation of the platelets, with the platelet normal along the thickness direction of the specimens. The orientation varied through the thickness of the moulded specimens, and it increased with increasing hBN loading. Casting resulted in a low preferred orientation, and powder bed fusion resulted in an almost random orientation. The platelet orientation in injection moulded specimens (characterized by X-ray diffraction) agreed qualitatively with numerical simulations of the injection moulding process. The measured thermal conductivities were compared with four models (the effective medium approximation (EMA) model, the Ordóñez-Miranda model, the Sun model, and the Lewis-Nielsen model) to understand how the conductivity was affected by filler loading and orientation. Selecting the filler loading in the composite is a compromise; increasing the loading increases the thermal conductivity, but reduces the mechanical ductility and increases the melt viscosity.

The heat transfer simulations also demonstrated the applicability of hBN/polymer composites in the two-layer encapsulation of the TEE scan head. These composites could be used in a metallized encapsulation, or in an encapsulation consisting of two layers (an outer layer of hBN/polymer and an inner layer of a thermally and electrically conductive polymer composite).

Keywords: ultrasound imaging medical device, trans-esophageal echocardiography, thermal safety, thermal management, heat transfer simulations, metallized encapsulation, electroplating, thermally conductive polymer composites, thermal conductivity, hexagonal boron nitride, thermoplastic polyurethane, epoxy, injection moulding, casting, powder bed fusion, filler orientation.

List of papers

Peer-reviewed conference contributions included in the thesis:

Conference contributions are not included in online publication

Article 1

Nu Bich Duyen Do, Erik Andreassen, Stephen Edwardsen, Anders Lifjeld, Hoang-Vu Nguyen, Knut E. Aasmundveit, and Kristin Imenes (2019). New encapsulation concepts for medical ultrasound probes – A heat transfer simulation study, Presented at the 22nd European Microelectronics and Packaging Conference and Exhibition (EMPC), Pisa, Italy, 2019, DOI: [10.23919/EMPC44848.2019.8951832](https://doi.org/10.23919/EMPC44848.2019.8951832)

Article 2

Nu Bich Duyen Do, Erik Andreassen, and Kristin Imenes (2020), Thermal management with a new encapsulation approach for a medical device. Presented at the IEEE 8th Electronics System-Integration Technology Conference (ESTC), Tønsberg, Norway, 2020, DOI: [10.1109/ESTC48849.2020.9229798](https://doi.org/10.1109/ESTC48849.2020.9229798)

Article 3

Nu Bich Duyen Do, Kristin Imenes, Knut E. Aasmundveit, Hoang-Vu Nguyen, and Erik Andreassen (2023), Thermally conductive polymer composites with hexagonal boron nitride for medical device thermal management. Presented at the 24th European Microelectronics and Packaging Conference and Exhibition (EMPC), Cambridge, England, 2023.

Peer-reviewed journal papers included in the thesis:

Article 4

Nu Bich Duyen Do, Erik Andreassen, Stephen Edwardsen, Anders Lifjeld, Knut E. Aasmundveit, Hoang-Vu Nguyen and Kristin Imenes (2022), Thermal management of an interventional medical device with double layer encapsulation, *Experimental Heat Transfer*, 35:5, 708-725, DOI: [10.1080/08916152.2021.1946208](https://doi.org/10.1080/08916152.2021.1946208)

Article 5

Nu Bich Duyen Do, Kristin Imenes, Knut E. Aasmundveit, Hoang-Vu Nguyen and Erik Andreassen (2023), Thermal conductivity and mechanical properties of polymer composites with hexagonal boron nitride – A comparison of three processing methods: injection moulding, powder bed fusion and casting, *Polymers* **2023**, *15*, 1552, DOI: [10.3390/polym15061552](https://doi.org/10.3390/polym15061552)

The PhD project was also presented at local conferences and symposiums (NanoNetwork Workshop 2018 (Vestfold, Norway), NanoNetwork Workshop 2019 (Tromsø, Norway), USNexpo in Vestfold in 2018 and 2019).

Table of contents

Preface	I
Acknowledgements	III
Abstract	V
List of papers	VII
Table of contents	IX
Chapter 1. Introduction	1
1.1 Background and motivations	1
1.1.1 Medical ultrasound probe and its encapsulation	1
1.1.2 New encapsulation concepts for medical ultrasound probes	3
1.1.3 Thermal management for medical ultrasound probes.....	6
1.1.4 Electromagnetic interference shielding for medical ultrasound probes	8
1.1.5 Fabrication methods for polymer-based materials	9
1.2 Objectives and thesis outline	11
1.2.1 Objectives.....	11
1.2.2 Thesis outline	11
Chapter 2. Heat transfer of an ultrasound scan head with two-layer encapsulation .	13
2.1 Experimental study of a metallized polymer encapsulation	13
2.1.1 Materials and sample preparation	14
2.1.2 Temperature measurement in tissue-mimicking thermal phantom	15
2.2 Heat transfer simulations for a scan head with two-layer encapsulation...17	
2.2.1 Simulation model for steady state heat transfer	18
2.2.2 Verification of simulation model by experimental results	22
2.2.3 Application of the verified simulation model in selecting materials for the encapsulation of the TEE scan head	24
Chapter 3. Thermally conductive polymer composites	29
3.1 Experimental study of thermally conductive hBN/polymer composites	29
3.1.1 Materials and processing methods.....	29
3.1.2 Preparation of hBN/polymer composite samples	33
3.1.3 Characterization of hBN/polymer composites	36

3.2	Filler orientation in polymer composites.....	37
3.3	Thermal conductivity measurements and models	38
3.3.1	Thermal conductivity of hBN/polymer composites.....	38
3.3.2	Theoretical models for thermal conductivity of polymer composites	43
3.4	Experimental study not presented in the published papers	44
Chapter 4. Summary of the papers		49
4.1	Heat transfer of the TEE scan head with two-layer encapsulation	49
4.1.1	Conference paper 1 (Article 1): New encapsulation concepts for medical ultrasound probes – A heat transfer simulation study.....	49
4.1.2	Conference paper 2 (Article 2): Thermal management with a new encapsulation approach for a medical device	51
4.1.3	Journal paper 1 (Article 4): Thermal management of an interventional medical device with double layer encapsulation	52
4.2	Thermally conductive polymer composites.....	54
4.2.1	Journal paper 2 (Article 5): Thermal conductivity and mechanical properties of polymer composites with hexagonal boron nitride – A comparison of three processing methods: injection moulding, powder bed fusion and casting	54
4.2.2	Conference paper 3 (Article 3): Thermally conductive polymer composites with hexagonal boron nitride for medical device thermal management ...	57
Chapter 5. Conclusions and outlook.....		61
5.1	Conclusions	61
5.2	Outlook.....	63
References		65
Articles		73

Chapter 1. Introduction

1.1 Background and motivations

1.1.1 Medical ultrasound probe and its encapsulation

Ultrasound imaging plays an important role in the diagnosis of cardiovascular diseases. A trans-esophageal echocardiography (TEE) probe uses ultrasound waves to image the heart in real time in three dimensions (3D) from inside the esophagus of patient, see Figure 1.1a. TEE is an essential diagnostic modality for patients with poor trans-thoracic echocardiographic windows (i.e. when using ultrasound to image the heart from outside the patient's body is difficult) or in case detailed imaging of structures distant from the chest wall is necessary. During the TEE test, an ultrasound transducer mounted at the tip of a gastroscopic tube passes through the patient's mouth into the patient's esophagus for cardiac imaging. The proximity of the esophagus to the heart provides a good acoustic window for ultrasound imaging, and hence provides high quality images of the heart [1].

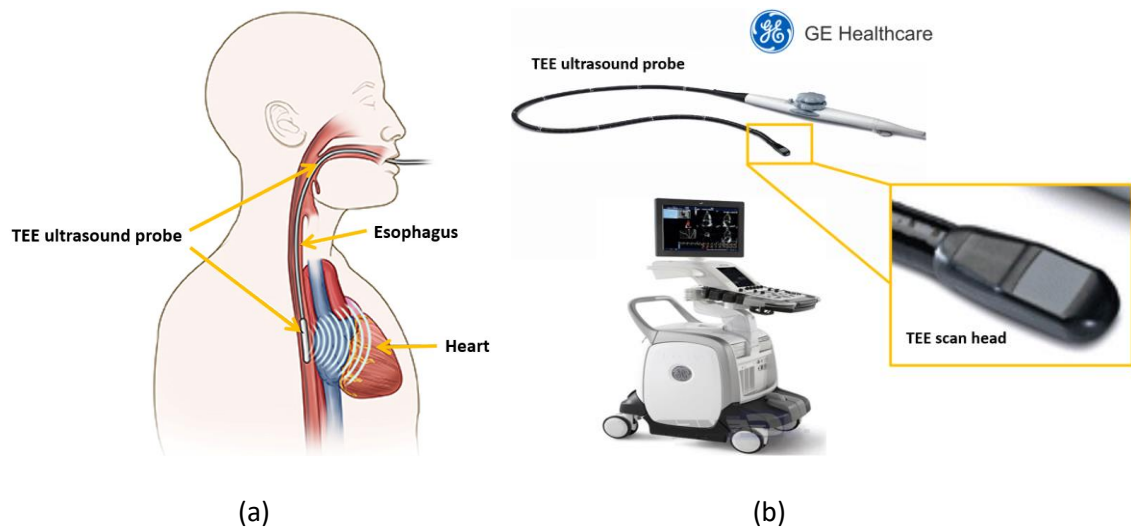


Figure 1.1: (a) Transesophageal echocardiography (TEE) for cardiac imaging from inside the human esophagus [2]; (b) A TEE ultrasound probe (from GE healthcare) for 3D heart imaging. The TEE scan head, i.e. the tip of the TEE probe, shown in the inset is the focus of this study.

This project focuses on the scan head of the TEE probe (i.e. the tip of the TEE probe), referred to as ‘TEE scan head’ or just ‘scan head’. The TEE scan head (as in Figure 1.1b) contains the ultrasound transducer and beamforming electronics. Its current encapsulation requires manual assembly of a substantial number of prefabricated parts, as illustrated in Figure 1.2. These parts provide the TEE scan head with different functions, such as thermal management, electromagnetic interference (EMI) shielding, electrical isolation, biocompatibility, etc.

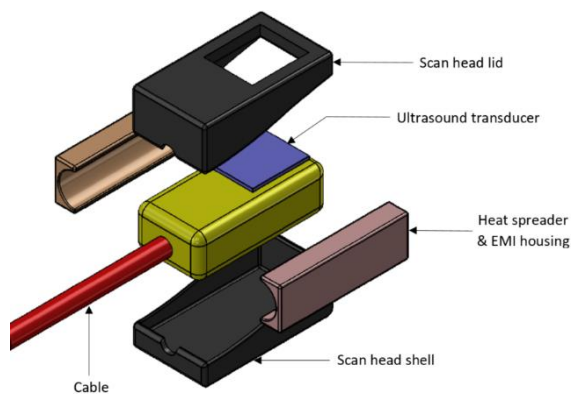


Figure 1.2: Schematic overview of the encapsulation of a simplified TEE scan head. “Heat spreader and EMI housing” parts spread the heat from the ultrasound transducer and give EMI shielding for the scan head. “Scan head lid” and “scan head shell” define the outer shape of the probe head and are in close contact with biological tissues [3].

A particular challenge in the assembly of the TEE scan head is the processing temperature. The ultrasound transducer inside the TEE scan head includes a poled piezoelectric material, which loses the polarization above its Curie temperature. Therefore, manufacturing of the TEE probes should not expose the transducer to temperatures higher than its depolarization temperature (in the range of 80 – 100 °C). Adhesive bonding has been the primary method employed in the assembly steps of the TEE scan head. Since the functional parts of the TEE scan head are relatively small in size, with varying shape, careful alignment and manual application of a small amount of adhesives on their surfaces are challenging and time-consuming. It is therefore desirable to simplify the encapsulation design and the assembly of the TEE scan head to reach a

more efficient manufacturing, while maintaining high image quality and healthcare safety, e.g. protection from heat and electricity, biocompatibility and ease of cleaning.

1.1.2 New encapsulation concepts for medical ultrasound probes

New encapsulations for simplifying the TEE scan head assembly:

The PhD work aimed at developing a simpler encapsulation design and manufacturing process to reduce the assembly complexity of the TEE scan head, without sacrificing the multi-functional performance (i.e. protection from heat, electricity, EMI and biocompatibility). The process temperature should be controlled to avoid the complicated re-polarization step for the TEE ultrasound transducer. The simplification of the probe assembly can be achieved by: (1) selecting materials and corresponding packaging techniques suitable for automated processes (which might be obtained by a single-layer encapsulation, see Figure 1.3a), or (2) reducing the number of process steps by reducing the number of prefabricated parts (which might be obtained by a two-layer encapsulation, see Figure 1.3b).

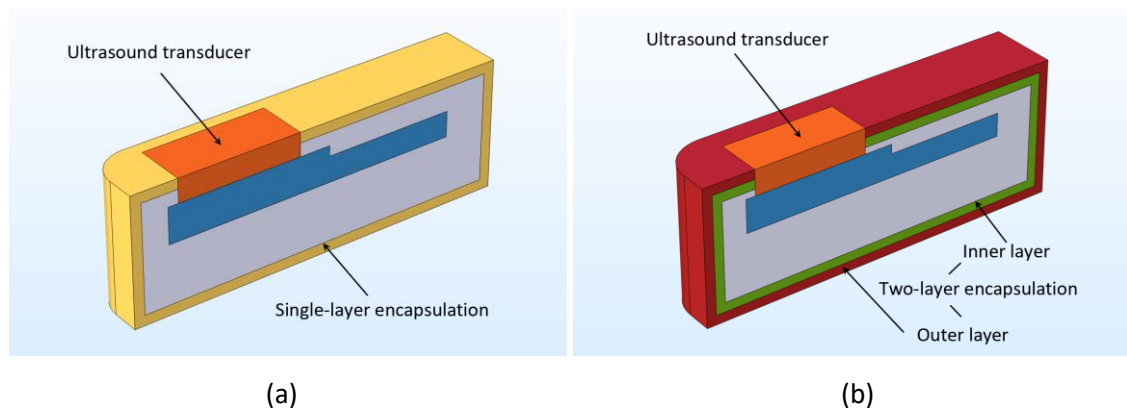


Figure 1.3: Cross-section schematics of the simplified TEE scan head (not drawn to scale), with (a) single-layer encapsulation, or (b) two-layer encapsulation.

Two-layer encapsulation (as illustrated in Figure 1.3b) is a promising solution for simplifying the assembly of the TEE scan head. It could result in the reduction in the number of prefabricated parts. Separate parts in the current encapsulation of the TEE scan head (i.e. heat spreader and EMI housing parts, scan head lid and scan head shell,

as in Figure 1.2) can be incorporated into two encapsulation parts with the two-layer structure. Prefabricated encapsulation parts still exist in the two-layer encapsulation, but their number decreases, leading to the decrease in the number of process steps. The reduction in the number of prefabricated parts, from four parts in the current scan head to two parts with the two-layer encapsulation concept, can therefore simplify the probe assembly.

Encapsulation of TEE scan heads and other interventional medical devices (such as pacemakers, cochlear implants, implantable neuromuscular micro-stimulators, artificial retina implants) is often made of at least two materials [4] to fulfil several functional requirements; not only thermal safety, but also EMI shielding, electrical isolation, and biocompatibility. To the best of our knowledge, there is no single material (e.g. polymers, ceramics, metals, or their composites) for a single-layer encapsulation which can satisfy all the requirements of the TEE scan head, especially the contradictory requirements of electrical isolation and EMI shielding. Hence, a single-layer encapsulation approach was not included in this PhD work. In general, the encapsulation of a medical device usually composes of an electrically conductive material (e.g. metallic based material) which provides EMI shielding [5] and heat transfer ability [6], due to high electrical and thermal conductivity. The second material is commonly an electrically insulating material which is responsible for electrical isolation and biocompatibility, and/or heat spreading, e.g. a polymeric or ceramic based material, or composites of these two materials.

A two-layer encapsulation could be based on: (1) a metal part with a polymer or ceramic coating on the outside, or (2) a polymer-based part metallized on the inside, or (3) two layers consisting of different polymer-based composites. In this thesis, the term "composite" is used for a material with a polymer matrix containing functional fillers/particles.

- In the first case, a thin film of a biocompatible polymer or ceramic covers the outside of a metal part. A metal part provides good heat spreading, EMI shielding and mechanical integrity for the encapsulation. However, an encapsulation with metal

as the main material may be heavier than what is needed for the function. In addition, applying a uniform and smooth coating of a biocompatible polymer (e.g. parylene coating) or ceramic (e.g. Al_2O_3) on a metal part often requires complicated fabrication processes, e.g. chemical vapor deposition, atomic layer deposition [7].

- In the second case, the encapsulation consists of a metal layer deposited on the inner surface of the prefabricated part made of polymer or polymer composite. This encapsulation concept utilizes the advantages of polymeric materials, such as low density, easy and flexible processing, and low cost [8]. Additionally, a metallized encapsulation can be fabricated by combining well-established industrial methods, such as e.g. injection moulding for the polymer-based part, and metallization by vacuum metallization, electroless plating, electroplating, or even spray painting [9], [10]. A thin metal film (in the micro- or nanometer range) can provide enough EMI shielding for a TEE scan head and other non-radiation emitting medical devices [5], [11], [12]. For example, the metallized encapsulation with 10 – 100 μm Cu can provide EMI shielding effectiveness (EMISE) higher than 100 dB in the frequency range of (0.03 – 3) GHz, which is a common frequency range for testing EMISE of medical devices used in professional healthcare facility environment [11]. These values are above the shielding requirements for devices in the classification which applies to TEE scan heads (group 1, class B in the electromagnetic compatibility standards for medical electrical equipment, IEC 60601-1-2 [11] and CISPR 11 [12]). For example, the peak limit for radiated disturbance of these devices, at a measurement distance of 3 m, in the frequency range (1 – 3) GHz is 70 dB [12]. However, for a metallized encapsulation, the trade-off between metal and polymer or polymer composite thickness needs to be considered, so that the encapsulation can provide sufficient heat spreading, to avoid hot spots on the device surface.
- In the third case, two composite layers are responsible for thermal management of the encapsulation. The inner layer of the encapsulation can be made of an electrically conductive polymer-based composite. The composite needs to contain electrically conductive fillers (e.g. metals, carbon-based fillers), to provide the

encapsulation with EMI shielding and good heat spreading. Meanwhile, the outer layer is made of thermally conductive polymer-based composite, responsible for electrical isolation, biocompatibility, and thermal management. The polymer composite of the outer layer should contain thermally conductive but electrically insulating fillers, (such as ceramic fillers, either metal oxides, e.g. alumina (Al_2O_3), quartz (crystalline SiO_2), or non-oxides, e.g. aluminium nitride (AlN), boron nitride (BN), silicon nitride (Si_3N_4), silicon carbide (SiC), etc.). Selecting filler(s) for the two polymer-based composites is important, since the filler types and filler loadings determine the properties (e.g. thermal conductivity, electrical isolation, EMI shielding, etc.) and processability of materials. The two-polymer composite encapsulation parts can be fabricated by common processing methods for polymer-based materials, e.g. two component injection moulding. Thermal transfer and EMI shielding effectiveness measurements of this encapsulation should be conducted at material and product levels, to select the appropriate polymer composites and thickness of each layer suitable for the device to operate properly.

Thermal management of the TEE scan head with metallized encapsulation is presented in Chapter 2 and summarized in Chapter 4 (Article 1 [13], Article 2 [14], Article 4 [3]). The applicability of polymer composites in two-layer encapsulation of the TEE scan head has been evaluated by simulations in Article 3 [15].

1.1.3 Thermal management for medical ultrasound probes

Thermal management of a TEE scan head is crucial for patient safety, as heat is generated by the transducer and the electronics in the scan head during imaging. Therefore, the heat distribution on the surface of the scan head needs to be properly managed to prevent hot spots. According to the standard for the safety and performance of ultrasonic medical diagnostic equipment, IEC 60601-2-37, temperature of medical devices in contact with the patient for 10 minutes or longer must not be higher than $43\text{ }^\circ\text{C}$, to prevent thermal damage to biological tissue [16]. In addition, proper thermal control is vital for the performance, lifetime and reliability of medical devices [4], [9].

Thermal management of medical devices can be based on active solutions (requiring power, e.g. fans for forced convection, pumps for liquid cooling, refrigeration) or passive solutions (e.g. heat sinks, heat spreaders, heat pipes, vapor chambers, phase change materials) [4], [9], [17]. As technological advancements enable medical devices to become more compact, implementing solutions such as heat pipes, vapor chambers, fans, etc. for cooling the device will become more challenging due to space constraints. Instead, the encapsulation of the device can act as an effective heat spreader to dissipate heat generated inside the device. This solution has been applied in the encapsulation of the current TEE scan head. Materials of such encapsulation should hence possess high thermal conductivity to ensure effective heat transfer for the device.

The development of new polymer-based composite materials with enhanced thermal conductivity has been driven by the miniaturization, integration, and functionalization of electronics. Polymer composites have advantages of low density, low cost, and processing flexibility via established methods, such as injection moulding, transfer moulding, compression moulding, casting, 3D printing, etc. The polymer matrix in a composite can be a thermoset (e.g. epoxy, silicone) or a thermoplastic, including elastomers of either type. Most polymers possess low thermal conductivity, typically in the range 0.1 – 0.5 W/m·K [8]. The most commonly used technique to increase the thermal conductivity of a polymer material is to add thermally conductive fillers like metal powders, ceramic powders and carbon-based materials [8]. Some fillers improving thermal conductivity will not contribute to EMI shielding, such as ceramic powder; either metal oxides, e.g. alumina (Al_2O_3), quartz (crystalline SiO_2); or non-oxides, e.g. aluminium nitride (AlN), boron nitride (BN), silicon nitride (Si_3N_4), silicon carbide (SiC), etc. However, fillers such as metal powders (e.g. Cu, Ag, Al, etc.) and carbon-based materials (e.g. carbon black, carbon fibers, carbon nanotubes, graphite, graphene, etc.) will give both electrical conductivity and EMI shielding.

A study of thermally conductive and electrically insulating polymer-based composites (for the TEE scan head encapsulation) is presented in Chapter 3 and Article 5 [18].

1.1.4 Electromagnetic interference shielding for medical ultrasound probes

Undesirable electromagnetic (EM) radiation emitted from electronics under operation can interfere with the signals and cause malfunctions in electronic systems. Emitted EM waves may endanger people's health as well [19]. EMI shielding hence plays an important role in electronics packaging to ensure the proper operation of electronics devices and healthcare safety for humans. The shielding prevents the propagation of both ingress and egress of EM waves and minimizes the unwanted signals passing through a system either by reflection of the wave or by absorption and dissipation of the radiation power inside the materials [5], [20]. The use of metallic sheets is a common method for EMI shielding; and this is the solution utilized in the TEE scan head so far. However, its drawback is poor mechanical flexibility, heavy weight, tendency for corrosion, and limited possibility to tune the shielding effect.

In latter years, research focus in the field of EMI shielding materials has been intensely directed towards the development of polymer-based materials to take advantage of their variable EMI shielding effectiveness. Different strategies have been proposed to achieve EMI shielding with polymer-based composites. Polymer composites containing conductive fillers (e.g. nano metals, carbon-based materials as CNTs, MWCNTs, graphene [20]–[22]; intrinsically conductive polymer [20], [22]; transition metal carbides/carbonitrides (MXenes) [23], [24], etc.) are suitable for EMI shielding due to their capabilities of reflecting incoming waves. Composites formed by loading polymer with fillers having high dielectric constant and/or high magnetic permeability (e.g. metal oxides, ferromagnetic metals and their alloys) can result in effective EMI absorption [20], [25], [26]. Multilayer or porous polymer composites with large surface area and interfacial area are suitable for shielding by multiple reflections [5], [20], [25]. Combining different fillers in the same polymer matrix can enhance the shielding efficiency of the multifunctional composites thanks to synergistic effects [20], [25], [26]. Metallization of plastic surfaces is another common approach for shielding EMI. Metals

can be deposited with different coating techniques, such as vacuum metallization, sputtering, electroplating, and electroless plating, or spray painting [20].

One of the initial targets of this project was to develop a new multi-functional polymer composite for the single-layer encapsulation (suitable for automated packaging process) for simplifying the assembly of the TEE scan head, as well as satisfying all the safety demands (i.e. thermal protection, EMI shielding, electrical isolation and biocompatibility). However, the research target had to be adjusted due to the challenges in selecting one material for the contradictory requirements of EMI shielding and electrical isolation, and the lack of test equipment for evaluating the EMI shielding of materials (at material level).

Instead, an EMI shielding polymer-based composite could be used in the inner layer of the TEE scan head's two-layer encapsulation. Both composites in this encapsulation contribute to the heat transfer. The outer layer should be thermally conductive, but electrically insulating and biocompatible. The EMI shielding inner layer should be thermally and electrically conductive.

A study of the encapsulation consisting of two polymer composite layers for the TEE scan head is presented in Article 3 [15].

1.1.5 Fabrication methods for polymer-based materials

Moulding is a widely utilized packaging technique in the industry today. There are several processes employed for moulding of small parts (as the TEE scan head encapsulation) using polymer-based materials, including injection moulding of thermoplastics, transfer moulding or compression moulding of thermosets [9]. Injection moulding is a well-established method for mass production of polymer-based products. Transfer moulding and compression moulding with thermosets (e.g. epoxy, silicone, etc.) can be conducted at processing temperature lower than the injection moulding temperature. The curing (solidification) of the liquid resin into a solid thermoset (hard or elastomeric) is a chemical reaction (cross-linking); so, the process temperature can be adjusted based on the chemistry of the material. UV-induced curing can be used to

avoid high process temperature, and it may be combined with thermal post-cure. In case that the low processing temperature is required (as in the TEE scan head assembly), the moulding with thermoset is an alternative.

Casting with thermoset-based polymer composites is another processing option for the two-layer composite encapsulation. In a casting process, composites are produced by mixing fillers into resins (such as epoxy, silicone, etc.), followed by pouring or injecting the (filler/polymer) mixture into a mould for curing.

Three-dimensional (3D) printing, also called additive manufacturing (AM), has emerged as a versatile technology platform for product design, rapid prototyping, and manufacturing. This technology enables direct 3D fabrication without the need for moulds or machining, and allows for the production of 3D structures with complex shape across a diverse range of applications, such as aerospace, automotive, energy, medical/dental, architecture and consumer products [27], [28]. 3D printing is a process of building objects layer by layer from a 3D computer-aided design (CAD) model. Customized parts from metals, ceramics, and polymers can be produced by 3D printing. However, polymers are by far the most utilized class of AM materials. The range of polymers compatible for 3D printing encompasses thermoplastics and thermosets including elastomers and composites based on these. 3D printing technologies are classified into different process categories as defined in a common ISO/ASTM standard 52900 [29]. The categories for polymer-based materials include vat photopolymerization, powder bed fusion, material extrusion, material jetting, binder jetting and sheet lamination [27].

In this PhD project, different processing techniques of polymer-based materials were used to prepare samples for testing. Metallized polymer encapsulation was made by material jetting (an AM process also referred to as PolyJet 3D printing) followed by electroplating. Thermally conductive polymer composites were fabricated by injection moulding, casting and powder bed fusion (an AM process).

1.2 Objectives and thesis outline

1.2.1 Objectives

The PhD project was an integrated part of a collaborative research between Department of Microsystems (IMS), University of South-Eastern Norway (USN) and GE Vingmed Ultrasound, a manufacturer of real-time 3D TEE ultrasound probes in Horten, Norway. The project aimed at developing packaging concepts (based on materials, design, and processing methods) for simplifying the assembly of the scan head of the TEE ultrasound probe, while satisfying the multi-functional demands for the device to operate safely inside the patient's body.

Simplification of a TEE scan head assembly could be achieved by a new encapsulation design with fewer prefabricated parts, so that the number of assembly steps could be reduced. Two-layer encapsulation (based on e.g. metallized polymer encapsulation, or encapsulation with two polymer composites) is a potential encapsulation alternative for a more efficient assembly of the TEE scan head.

Among different functions required for the TEE scan head, thermal management is vital to the performance, lifetime, and reliability of the device, and especially the patient safety (e.g. maximum surface temperature of the device not higher than 43 °C to avoid thermal damage to human tissues). Therefore, this project focused on studying new encapsulation concepts and materials for the thermal management of the TEE scan head. The two main research topics presented in this thesis include: (1) thermal management of the TEE scan head with two-layer encapsulation, especially metallized polymer encapsulation, and (2) thermally conductive polymer composites. These topics have been studied in detail through experiments, theories, and simulations.

1.2.2 Thesis outline

This thesis consists of five chapters and attachments (the five published articles).

- Chapter 1 introduces the TEE ultrasound probe (a medical ultrasound imaging device) and the requirements for the encapsulation (thermal management and EMI shielding), and the new encapsulation concepts suggested for a more efficient assembly of the TEE scan head. This chapter also presents the research goals and the thesis outline.
- Chapter 2 presents heat transfer studies of several encapsulation concepts for the TEE scan head, with the focus on a metallized polymer encapsulation (a promising and easily implemented option). Thermal performance of the TEE scan head with the metallized encapsulation was studied by both experiments and simulations. This chapter is also the summary of Articles 1, 2 and 4.
- Chapter 3 summarizes the experimental study of hBN/polymer composites. It also presents the experimental study and simulations of filler orientation in the polymer composites, and the comparison of the experimental thermal conductivity with theoretical models. In addition, this chapter emphasizes the aspect not detailed in article 5 (related to the surface treatment of hBN fillers).
- The major achievements and contributions of the candidate are summarized and highlighted in Chapter 4.
- An outlook and future work are summarized in Chapter 5.

The research results of this PhD project were published in five papers; three papers (Articles 1, 2, 4) focused on the thermal management of a TEE scan head with two-layer encapsulation; and the remaining two papers (Articles 3, 5) focused on studying thermally conductive polymer composites and their relevant processing methods.

Chapter 2. Heat transfer of an ultrasound scan head with two-layer encapsulation

This chapter is adapted from the published Article 1 [13], Article 2 [14] and Article 4 [3].

2.1 Experimental study of a metallized polymer encapsulation

For the TEE scan head, thermal management is important for maintaining the optimal performance, reliability, and lifetime of the devices, and especially the patients' safety. In Article 1 (the preliminary study of new encapsulations for the TEE scan head) [13], thermal performances of several new encapsulation concepts for the TEE scan head were evaluated by heat transfer simulations. Single-layer encapsulation and two-layer encapsulation (e.g. polymer-coated metal encapsulation, metallized polymer encapsulation) were analysed. In addition to the main constraint for the maximum surface temperature (not exceeding 43 °C to avoid thermal damage to biological tissues), the new encapsulation is required to fulfil the demands of EMI shielding, electrical isolation, and biocompatibility, as well as to simplify the assembly of the TEE scan head. The study [13] indicated that a metallized polymer encapsulation is a potential encapsulation concept for the TEE scan head. More details about the study [13] are summarized in Article 1 in Chapter 4.

Thermal management of the TEE scan head with metallized polymer encapsulation was assessed by both experimental work and numerical simulations, and presented in Articles 2, 4. The metallized polymer encapsulation parts were fabricated by 3D printing followed by Cu electroplating. The surface temperature of the test sample with metallized polymer encapsulation was measured in a tissue mimicking thermal phantom, which was stabilized at around 37 °C (human body temperature). The effect of metal layer thickness (0, 10, 80, 150 μm of Cu) for a 0.9 mm thick polymer encapsulation part, for different heat source power levels (0.5 – 2.0 W), was studied by experiments and simulations. The results give insight on the heat transfer of the device and provide a basis for establishing design rules and selecting material alternatives for

the outer layer of the metallized encapsulation, to further improve the thermal performance of such medical devices.

The next sections in Chapter 2 describe the material selection, the fabrication of the metallized polymer encapsulation (including 3D printing of polymer parts followed by Cu electroplating), the preparation of test samples (representing the simplified TEE scan head), and the temperature measurements in a tissue-mimicking phantom. All the experimental work is described in detail in the Experiments section in Article 4 [3].

2.1.1 Materials and sample preparation

A test sample, representing a simplified TEE scan head, included a heat source, a heat sink and a metallized polymer encapsulation, as in Figure 2.1. The heat source represented electronic components generating heat within the scan head, such as the ultrasound transducer and electronics. The geometry of the heat sink was similar to that in a commercial device. The metallized polymer encapsulation consisted of a thin metal layer deposited on the inner surface of the prefabricated polymer parts.

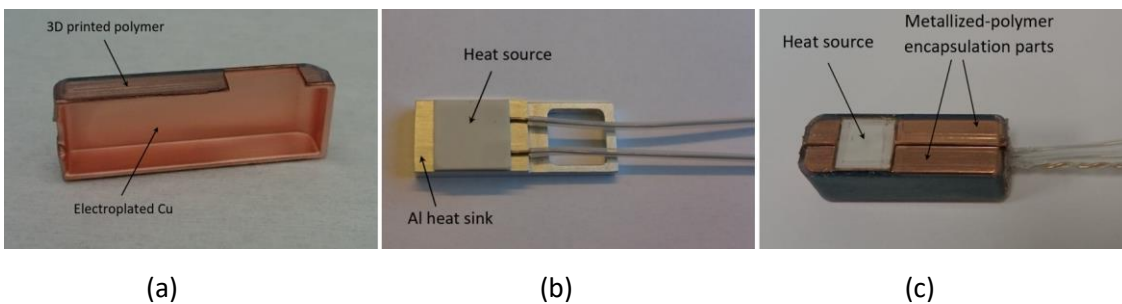


Figure 2.1: (a) Cu electroplated polymer part; (b) Heat source (resistive heating element) bonded to an Al heat sink; (c) Test sample after assembly.

The encapsulation was fabricated by polymer 3D printing followed by electroplating. Two mating parts (one part corresponding to Figure 2.1a) were 3D printed. A UV-cured polymer material was used with the 3D printer Stratasys Objet30 Prime, which is based on PolyJet 3D printing technology [30], belonging to the *material jetting* process category of additive manufacturing [29]. The biocompatible polymer material MED610 (from Stratasys) was selected, because this polymer has the thermal properties similar

to polymer encapsulation materials commonly used for interventional medical devices (e.g. PEI and PEEK), and it also provides electrical isolation and compatibility with biological tissue. A metal layer with desired thickness (10, 80, 150 μm) was deposited on the inner surfaces of the polymer parts (0.9 mm thick) by means of sputtering followed by electroplating. Copper (Cu) was chosen as the electroplating material due to its high thermal conductivity ($400 \text{ Wm}^{-1}\text{K}^{-1}$) [6], its effectiveness in EMI shielding [5], and its low cost. Furthermore, Cu electroplating is a common industrial process [10]. Figure 2.1a shows one encapsulation part after Cu electroplating.

The electroplated parts were subsequently assembled around a heat source and an aluminium (Al) heat sink by adhesives to make the test sample, as illustrated in Figure 2.1. The hole for the electrical wires at the tail of the sample, and the seams between two mating electroplated parts, were sealed with a medical silicone. The remaining volume inside the sample (containing electronic components and cables in a typical scan head) was empty (air) for simplifying the simulations later and representing a worst-case scenario with regards to heat transfer.

2.1.2 Temperature measurement in tissue-mimicking thermal phantom

The surface temperature of the test samples with attached thermocouples (as in Figure 2.2) was measured for 80 minutes (about twice the duration of a common TEE exam [16], [31]), when placed in a tissue-mimicking thermal phantom (National Physical Laboratory, England), stabilized at around 37 $^{\circ}\text{C}$ (see Figure 2.3). Test samples with 0, 10, 80 and 150 μm thick Cu layers were tested. The effect of the heat source power was also considered.

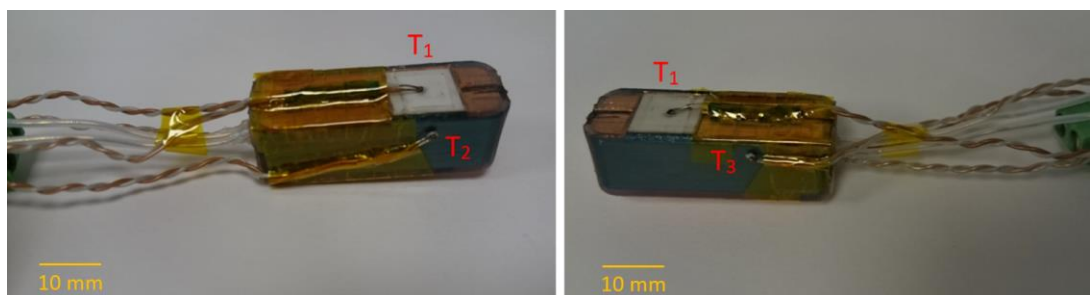


Figure 2.2: Thermocouples (T_1 , T_2 , T_3) on the surface of the test sample.

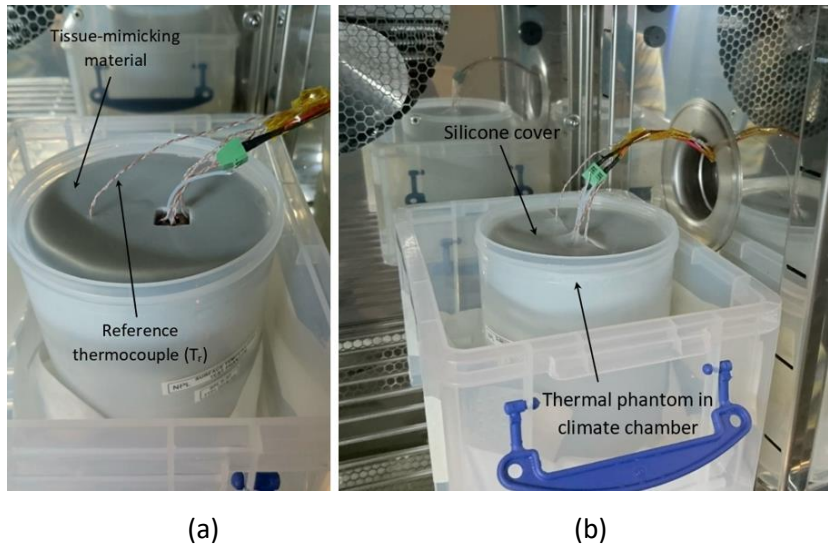


Figure 2.3: A test sample in a tissue-mimicking thermal phantom in a climate chamber.

Type T thermocouples were positioned at three different locations on the test sample (as in Figure 2.2), to determine the maximum surface temperature during the test. Thermocouple T_1 was placed on the surface of the exposed heat source; thermocouple T_2 was placed on the vertical surface, near the heat source; thermocouple T_3 was placed on the other vertical surface, a bit further away from the heat source. The temperature of the thermal phantom was also measured with a thermocouple (T_r in Figure 2.3a). The thermocouple T_r was inserted into the thermal phantom ca. 46 mm away from thermocouple T_1 , and at nearly the same depth as T_1 (ca. 50 mm from the top surface of the phantom). The thermocouples were logged (TC08 and PicoLog 6, PicoTech) every 10 s for 80 minutes. The heat source was connected to a power supply (R&S NGE100, Rohde & Schwartz), and four different power levels (0.5, 1.0, 1.5, 2.0 W) were applied in the measurements.

Figure 2.4 shows an example of the results of the temperature measurement in the tissue-mimicking thermal phantom. The maximum surface temperature of the test sample (T_1) appears on the surface of the heat source (not encapsulated). Thermocouple T_2 shows a higher temperature than thermocouple T_3 , due to T_2 being closer to the heat source of the test sample.

ΔT is defined as the difference between the maximum scan head surface temperature (T_1) and the temperature of thermal phantom (T_r), at steady state. Results showed that the steady state ΔT (obtained by both experiments and simulations) increases linearly with increasing power. In addition, ΔT decreases with increasing Cu thickness (better heat spreading), following an exponential function. The experimental results also show which combinations of Cu layer thickness and power that satisfy the temperature criterion ($T_1 < 43$ °C, i.e. $\Delta T < 6$ °C). For a power level of 0.5 W, a Cu layer thickness around 100 μm (on a 0.9 mm thick polymer encapsulation) is a good trade-off between thermal performance and cost/time for the metallization process. More details can be found in Article 4 [3].

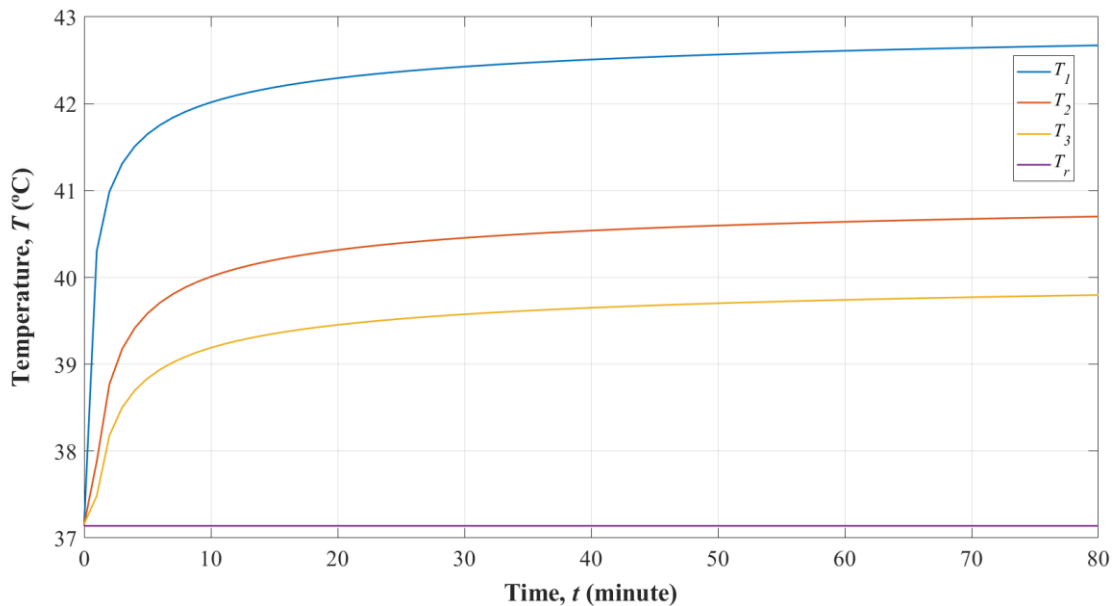


Figure 2.4: Measured temperatures for a test sample with polymer thickness 0.9 mm, Cu thickness 150 μm , and heat source power 0.5 W.

2.2 Heat transfer simulations for a scan head with two-layer encapsulation

This section summarizes the heat transfer simulations for the TEE scan head with two-layer encapsulation (e.g. metallized encapsulation, two-polymer composite encapsulation).

2.2.1 Simulation model for steady state heat transfer

A simulation model, representing the experimental test sample (Figure 2.1c) in the thermal phantom, was defined in COMSOL Multiphysics 5.3a. The model (Figure 2.5) includes a heat source, a heat sink and a two-layer encapsulation. The heat source represented electronic components generating heat within the scan head, such as the ultrasound transducer and electronics. The geometry of the heat sink was similar to that in a commercial device. The encapsulation covered the entire scan head, except the heat source's surface, which is the ultrasound lens, as shown in Figure 2.1c.

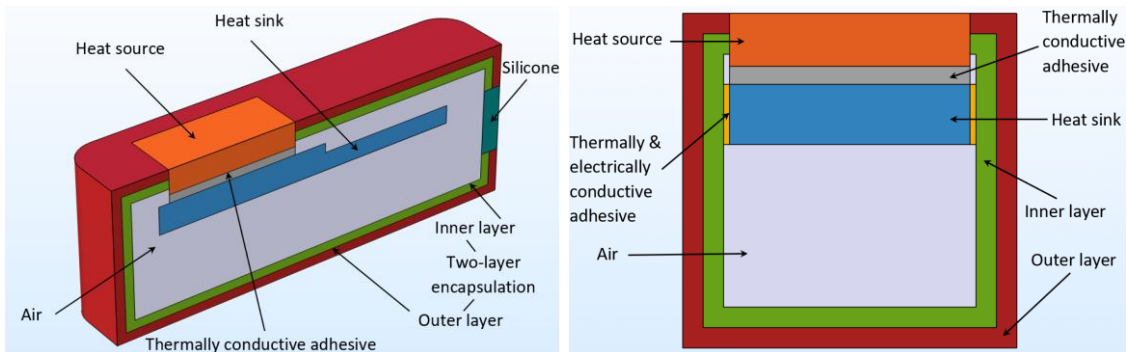


Figure 2.5: Cross-section schematics of the test sample (not drawn to scale), consisting of a heat source, a heat sink and a two-layer encapsulation. The heat source was bonded to the heat sink using a thermally conductive adhesive. The heat sink was coupled to the inner layer via a thermally and electrically conductive adhesive. The hole for the electrical wires of the heat source was sealed with silicone. The remaining volume inside the sample (containing electronic components and cables in a typical scan head) was empty (air) for simplifying the simulations and representing a worst-case scenario with regards to heat transfer.

The heat source was modelled with uniform volumetric heat generation. In this study, steady-state thermal conduction is considered the main mechanism of heat transport. The thermal contacts between the components in the scan head were assumed to be perfect. The heat transfer can be described by the thermal diffusion equation, which is derived from the principles of conservation of energy and Fourier's law [6]. The steady-state heat equation is:

$$k\nabla^2 T + q = 0 \quad (2.1)$$

where k is the thermal conductivity (W/(m·K)) of the solid material; ∇^2 is the Laplace operator; T is the scalar temperature field (K); q is the rate at which energy is generated per unit volume of the medium (W/m³).

For the outer surfaces of the scan head (in contact with the thermal phantom), a heat flux boundary condition with a thermal contact conductance (TCC) coefficient was applied:

$$q_0 = h_c(T_{ext} - T) \quad (2.2)$$

where h_c is the TCC coefficient (Wm⁻² K⁻¹); T_{ext} is the temperature of the phantom (K), (assumed to be constant, 37 °C in this case); T is the temperature of the scan head surface (K); q_0 is the heat flux (Wm⁻²). The TCC coefficient is the inverse of the thermal contact resistance [32], [33]. The TCC coefficients were used for the exterior of the scan head, as in Figure 2.6.

- In Article 1 (the preliminary study on heat transfer simulations of different encapsulation concepts for the TEE scan head) [13], the heat transfer coefficient (or TCC coefficient), h_c , was set to be 400 (W/(m²·K)). This value was based on the calculation from esophageal heat transfer measurements on a pig.
- In the studies on heat transfer of the TEE scan head with two-layer encapsulation (Article 3 [15] and Article 4 [3]), the h_c values were determined by comparing the simulated and measured steady-state surface temperatures. To obtain a good agreement between the simulation and experiments, the steady-state heat transfer model was calibrated with two h_c values for the boundary conditions of the scan head exterior surface (towards the thermal phantom); one for the un-encapsulated heat source (250 Wm⁻²K⁻¹) and one for the outer encapsulation layer (46 Wm⁻²K⁻¹).

The main constraint of the heat transfer simulations is to keep the maximum surface temperature of the scan head below 43 °C to ensure thermal safety for patients. Another

constraint is the outer dimensions of the scan head, which should be similar to, or smaller than, those of the existing scan head (1 mm). This sets limits for the thickness of the encapsulation.

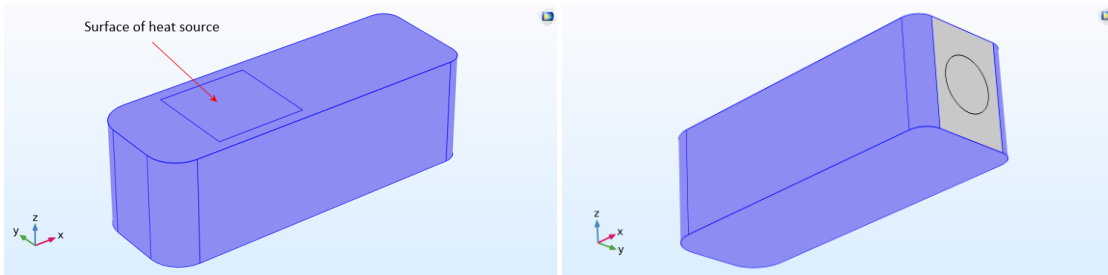


Figure 2.6: Illustration of thermal contact surfaces (in blue) for which Equation (2.2) was applied.

The thermal conductivities of the materials in the model are listed in Table 2.1. In Articles 1 and 4, only isotropic thermal conductivity has been considered for the metallized polymer encapsulation. In addition to the metallized polymer encapsulation, the two-layer encapsulation for the TEE scan head can be based on a metallized polymer composite (cases 1b, 1c in Table 2.1), or it can consist of two polymer composites (case 2 in Table 2.1).

Similar to the metallized polymer encapsulation, the metallized polymer composite (cases 1b, 1c) also consists of a metal layer (0.15 mm) deposited on the inner surface of prefabricated polymer composite part (0.9 mm). The metal layer provides heat transfer and EMI shielding, while the outer layer provides electrical insulation, biocompatibility, and some heat transfer. In an encapsulation consisting of two composite layers (case 2), both layers will contribute to the heat transfer. The outer layer should be thermally conductive, but electrically insulating and biocompatible. The inner layer should be thermally and electrically conductive, to take care of both heat transfer and EMI shielding. The total encapsulation thickness in the simulations was 1 mm, due to the thickness limit of the current encapsulation of the TEE scan head. Two cases of thickness combination (0.5/0.5 mm and 0.9/0.1 mm, corresponding to case 2a and 2b, respectively) for the two-layer encapsulation with two composites were simulated.

Table 2.1: Material data used in the thermal simulations.

Component	Material	Thermal conductivity k ($\text{Wm}^{-1}\text{K}^{-1}$)
Heat source	Metal ceramic heater [34]	20
Heat sink	Al alloy 6082 [35]	180
Adhesive between heat source and heat sink	Thermally conductive adhesive [36]	1.3
Adhesive between heat sink and encapsulation	Thermally and electrically conductive adhesive [37]	2.5
Coverage of the hole for the electrical wires	Medical silicone	0.2*
Remaining volume inside the sample	Air [38]	$k(T)$ via COMSOL's material library
<i>Case 1: Metallized encapsulation (metallized polymer, or metallized polymer composite)</i>		
Inner layer (0.15 mm)	Electroplated Cu [39]	380
Outer layer (0.9 mm)	Typical polymer (case 1a)	0.2* (isotropic)
	hBN/TPU, assumed isotropic (case 1b)	2.1 (isotropic)
	hBN/TPU, anisotropic (case 1c)	2.1 (through-plane) ** (this work) 12 (in-plane) ** [40]
<i>Case 2: Encapsulation consisting of two composite layers (total thickness 1.0 mm)</i>		
Inner layer: 0.5 mm (case 2a) or 0.9 mm (case 2b)	Thermally and electrically conductive polymer composite from Celanese	4.5 (through-plane) *** 34 (in-plane) *** [41]
Outer layer: 0.5 mm (case 2a) or 0.1 mm (case 2b)	hBN/TPU (thermally conductive and electrically insulating)	2.1 (through-plane) ** (this work) 12 (in-plane) ** [40]

* Values from references [42], [43].

** The through-plane value (2.1 W/mK) is the highest obtained in our experimental study. The in-plane value (12 W/mK) is estimated based on ref. [40] which studied the anisotropic thermal conductivity of injection moulded hBN/PEEK composites. The highest in-plane and through-plane values in that study were 2 W/mK and 12 W/mK, respectively, for 60 wt% hBN (with size of 25 – 30 μm).

*** Values based on a commercial material (Celanese CoolPoly E5521) [41]. These values seem to be among the highest reported for commercial materials. Other materials were also simulated; one from Avient (with 5.5 W/mK through-plane and 19 W/mK in-plane) and one from Sabic (with 1.5 W/mK through-plane and 18 W/mK in-plane).

Thermally conductive and electrically insulating polymer composites (e.g. hBN/polymer composites) have been studied in Article 5 [18] and also presented in Chapter 3. Examples of commercially available, thermally, and electrically conductive polymer composites are shortly mentioned in Table 2.1. The thermally conductive polymer composites often have anisotropic thermal conductivity, due to the filler shapes (e.g. hBN platelets, carbon-based material, etc.) and effects of processing methods. Hence, anisotropic thermal conductivity is included in the simulation study on the thermal performance of the two-layer encapsulation consisting of two polymer composites in Article 3 [15].

The 3D model was meshed using tetrahedral elements (see Figure 2.7), with quadratic shape functions. The mesh sizes were selected so that they adequately described the heat flow in the thinnest layer of the model (e.g. 10 μm thick Cu layer). The mesh had one element across the thin layers in the model (e.g. adhesive layers, Cu layer in the metallized encapsulation). An initial check with finer meshes (two elements across the thin layers, as well as an overall finer mesh with five times the number of elements) gave the same value for the maximum surface temperature, within 0.1 K. Hence, the mesh was optimized for simulation accuracy and calculation time.

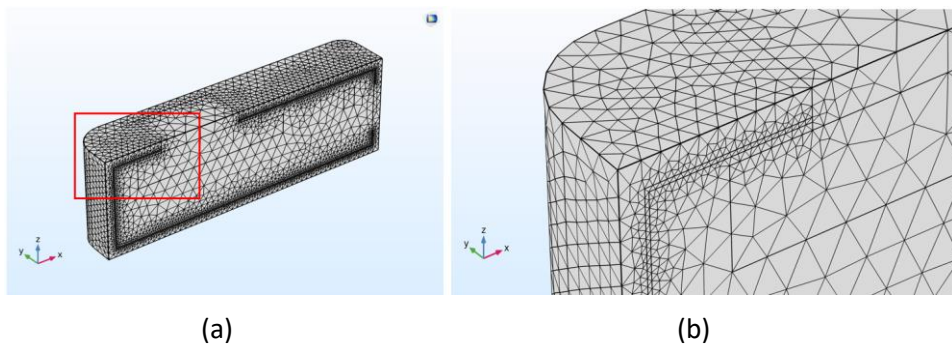


Figure 2.7: (a) Mesh on one half of the model, with a 0.9 mm thick polymer layer and a 150 μm thick Cu layer; (b) a zoom-in corresponding to the red rectangle in (a).

2.2.2 Verification of simulation model by experimental results

With the thermal conductivities in Table 2.1, the simulation model (with the metallized polymer encapsulation) was first calibrated with the experimental data (ΔT

vs. Cu thickness (0, 10, 80, 150 μm) and heat source power (0.5, 1.0, 1.5, 2.0 W), i.e. 16 data points) by adjusting a single TCC coefficient (h_c). With a h_c value of $75 \text{ Wm}^{-2} \text{ K}^{-1}$, the simulated ΔT values agreed well with the experimental data of samples having a non-zero Cu layer thickness. However, the ΔT values of the samples without Cu were grossly overestimated, as shown in Figure 9 in Article 4 [3]. Alternatively, a h_c value could be found so that ΔT values for zero Cu samples agreed with experiments, but then the ΔT values for non-zero Cu samples were underestimated. Hence, the balance between the two main thermal flow paths, "directly" through the heat source and via the encapsulation, was obviously poorly modelled with one h_c value.

To improve the prediction of the simulation model, two different TCC coefficients were used; h_{c1} for the heat source surface (modelled as Al_2O_3) and h_{c2} for the remainder of the scan head surface (the polymer encapsulation). A TCC coefficient accounts for effects of e.g. surface roughness at the interface, but it is evidently also related to bulk properties of the contacting materials, such as the thermal conductivity [33], [44]. Hence, it is argued that the heat source and the polymer encapsulation, with thermal conductivities differing by a factor 100 and different surface roughnesses, can have different TCC coefficients. These coefficients also effectively account for differences in contact area/pressure towards the thermal phantom. A good overall fit to all experimental data points (with and without a Cu inner layer, at different power levels) was achieved with h_{c1} and h_{c2} set to $250 \text{ Wm}^{-2} \text{ K}^{-1}$ and $46 \text{ Wm}^{-2} \text{ K}^{-1}$, respectively. More details about the calibration of the simulation model are presented in Article 4 [3].

Article 4 [3] also presents simulation results related to: temperature distributions for different encapsulations (with and without Cu); relationship between the polymer layer thickness (t_{po}) and the maximum surface temperature increase (ΔT) for different Cu thickness at a specific power level (0.5 W); the simulated effect of thermal conductivity of the outer layer material on the maximum surface temperature increase for different power levels.

2.2.3 Application of the verified simulation model in selecting materials for the encapsulation of the TEE scan head

2.2.3.1 Selection of promising materials for encapsulation of the TEE scan head

According to the FEM results in section 2.2.2, the polymer of the metallized encapsulation (made of Cu and polymer) must be replaced by a material with higher thermal conductivity if the power level is above 0.5 W. This material could be a polymer-filler composite with high thermal conductivity. Such a composite should also fulfil other safety requirements, such as electrical isolation and biocompatibility. An advantage of using a polymer-based composite is the compatibility of this material type with well-developed packaging techniques, such as moulding processes (e.g. injection moulding, transfer moulding, or compression moulding) [9]. Composites based on a biocompatible polymer matrix and thermally conductive and electrically insulating fillers are promising candidates. The polymer could be a thermoset (e.g. biocompatible epoxy or silicone) or a thermoplastic (e.g. PEI or PEEK) [43]. Common thermally conductive and electrically insulating fillers are ceramic fillers; for example, metal oxides (e.g. alumina (Al_2O_3) or quartz (crystalline SiO_2)), or non-oxide fillers (e.g. aluminum nitride (AlN), boron nitride (BN), silicon nitride (Si_3N_4)) [8]. Ohashi et al. [45] successfully prepared a polymer composite with thermal conductivity of $8.2 \text{ Wm}^{-1}\text{K}^{-1}$ from epoxy with 74 vol% AlN. The composite was applied in fabricating encapsulants for dissipating the heat generated in electronic devices. Thermal conductivity of $21.3 \text{ Wm}^{-1}\text{K}^{-1}$ was achieved for an epoxy/BN composite in a study by Zhu et al. [46]. Kusunose et al. [47] measured a thermal conductivity of $9.2 \text{ Wm}^{-1}\text{K}^{-1}$ for an epoxy composite with 60 vol% Si_3N_4 nanowires. Biocompatible ceramics can also be considered as outer layer materials for the metallized encapsulation. The outer encapsulation can e.g. be fabricated by powder injection moulding using AlN ($100 - 300 \text{ Wm}^{-1}\text{K}^{-1}$) [8], [48], [49].

Such suggestions for materials of the metallized encapsulation, based on the heat transfer simulations in Chapter 2, motivated the experimental study of thermally conductive polymer composites in Chapter 3.

2.2.3.2 Application of thermally conductive polymer composites for two-polymer composite encapsulation of the TEE scan head

The heat transfer simulation was also used in studying the application of thermally conductive polymer composites for the two-layer encapsulation of the TEE scan head in Article 3 [15]. The thermally conductive polymer composites could be applied in a metallized polymer composite encapsulation (cases 1b, 1c in Table 2.1), or in the encapsulation consisting of two polymer composites (cases 2a, 2b in Table 2.1).

The thermally conductive polymer composite of the encapsulation's outer layer (in all cases 1 and 2) is required to be electrically insulating, to fulfil the safety demand of the device (electrical isolation). This could be achieved by the hBN/polymer composites studied in Chapter 3. For the encapsulation's inner layer (cases 2a, 2b), the thermally conductive polymer composites should be electrically conductive to provide both heat transfer and EMI shielding for the device.

The thermally conductive polymer composites often have anisotropic thermal conductivity, due to effects of filler shapes (e.g. hBN platelets, carbon-based material as CNT, carbon fibers, etc.) and processing methods (e.g. injection moulding, casting, etc.). Hence, anisotropic thermal conductivity is included when simulating heat transfer of the device with encapsulation containing polymer composite(s).

Several combinations of materials and layer thicknesses were simulated for the encapsulation consisting of two polymer composite layers. Such encapsulations include an inner layer of commercial, thermally and electrically conductive materials and an outer layer of the best thermally conductive and electrically insulating hBN/TPU composite obtained in Article 5 [18]. The highest through-plane thermal conductivity of the composites was 2.1 W/mK, for the injection moulded hBN/TPU composite containing 65 wt% hBN. In the heat transfer simulations, the scan head encapsulation must satisfy the safety requirement that the maximum surface temperature (T_{max}) of the scan head (in contact with human tissue) must be below 43 °C.

The simulation results (in Figure 2.9 and Figure 2.10) have demonstrated the applicability of the hBN/polymer composites in the two-layer encapsulation of the TEE scan head, particularly a metallized encapsulation (with 0.15 mm of Cu and 0.9 mm of hBN/TPU), or in a 1.0 mm thick encapsulation consisting of two layers (an outer layer of hBN/TPU and an inner layer of a commercial, thermally and electrically conductive polymer composite). Such encapsulations provide the TEE scan head with adequate heat transfer for power levels up to about 0.6 W. The results also show that for all cases 1 and 2 in Table 2.1, the simulated T_{max} occurs at the surface of the heat source, which is not encapsulated.

Since commercial polymer composites have different conductivities and degrees of thermal anisotropy, thermal simulations were also employed to investigate the overall effect of anisotropic thermal conductivities on the surface temperature of the device with the two-polymer composite encapsulation. The simulations were performed with a range of different in-plane and through-plane thermal conductivities for the inner layer, of both cases 2a and 2b (0.5/0.5mm and 0.9/0.1mm). Results of using thermal simulations (with anisotropic material data) for evaluating and comparing anisotropic materials are presented in detail in Figure 9 of Article 3 [15].

Simulation of metallized encapsulation (case 1a-1c)

Simulation of an isotropic metallized polymer encapsulation (case 1a in Table 2.1) shows that for a power of ca 0.5 W, T_{max} reached the limit of 43 °C, as in Figure 2.8. In this case, the surface temperature varies from 39.9 °C to 42.9 °C. The maximum surface temperature T_{max} occurs at the surface of the heat source, which is not encapsulated. The T_{max} satisfies the safety demand, i.e. no spots on the surface are hotter than 43 °C.

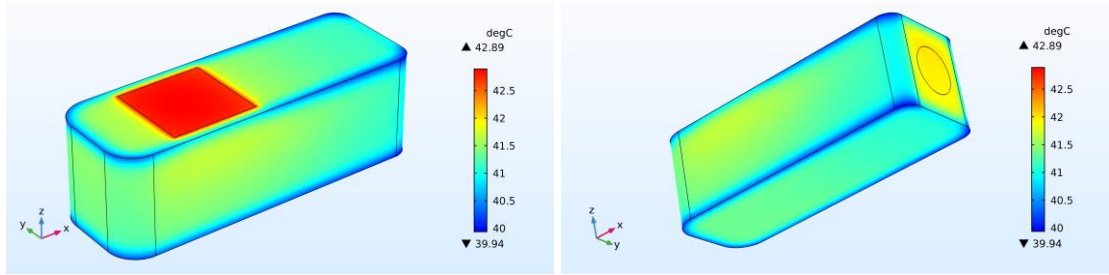


Figure 2.8: Simulated surface temperature for case 1a in Table 2.1. The outer polymer thickness is 0.9 mm, the inner Cu layer is 150 μm thick, the heat source power is 0.5 W.

If the polymer is replaced by the hBN/polymer composite with the highest thermal conductivity in Article 5 [18], and isotropy is assumed (case 1b, Figure 2.9a), T_{max} is reduced to 42.2 $^{\circ}\text{C}$ for the same power (0.5 W). $T_{max} = 43^{\circ}\text{C}$ is reached for a power of 0.59 W. With the anisotropic material model (case 1c, Figure 2.9b), T_{max} is reduced to 42.1 $^{\circ}\text{C}$ for the same power (0.5 W). The anisotropic material provides better heat transfer, due to its higher in-plane conductivity. The term ‘in-plane’ here relates to any direction along a plane (of the moulded encapsulation part) which has a normal vector in the thickness direction.

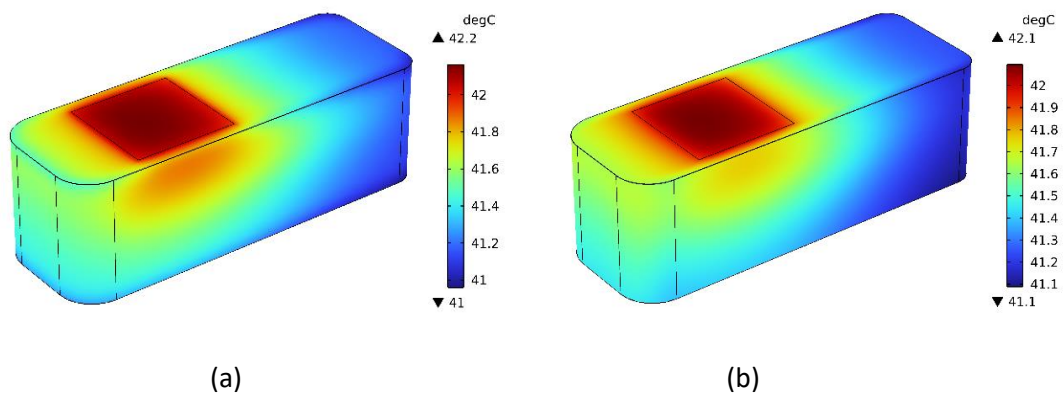


Figure 2.9: Simulated surface temperature of the TEE scan head with power 0.5 W. (a) Case 1b in Table 2.1. (b) Case 1c in Table 2.1.

Simulation of encapsulation consisting of two polymer composites (case 2a, b)

Two cases of two-layer polymer composite encapsulations were simulated (case 2a and 2b in Table 2.1). Both layers have fillers that increase the thermal conductivity. The

inner layer is electrically conductive, while the outer layer is electrically insulating. Thermal performance of such encapsulations was similar to that of the metallized encapsulations (Figure 2.10 vs. Figure 2.9). With our hBN/TPU composite in the outer layer and the Celanese composite (the commercial material with the highest thermal conductivity reported) in the inner layer, the limit $T_{max} = 43\text{ }^{\circ}\text{C}$ is reached for a power in the range 0.55 – 0.60 W.

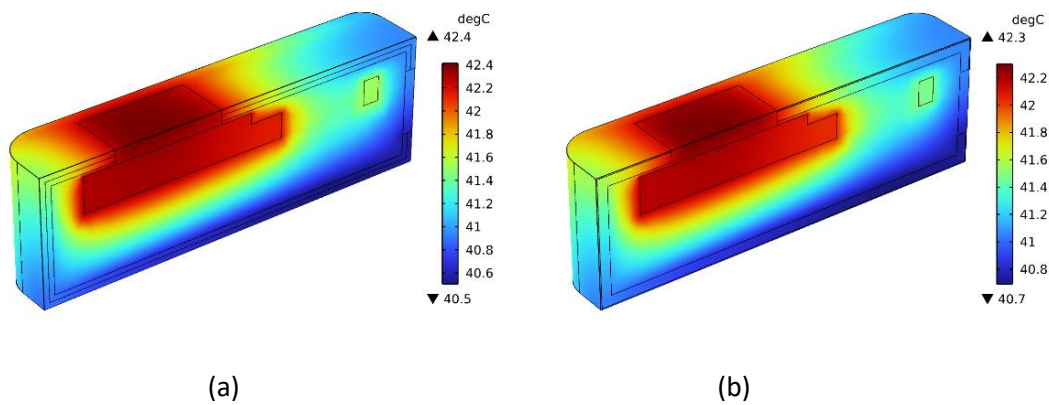


Figure 2.10: Heat transfer simulation of the TEE scan head (half model) with power 0.5 W. (a) Case 2a (0.5/0.5 mm thickness combination). (b) Case 2b (0.9/0.1 mm thickness combination).

Chapter 3. Thermally conductive polymer composites

This chapter is adapted from the published Article 3 [15] and Article 5 [18].

3.1 Experimental study of thermally conductive hBN/polymer composites

3.1.1 Materials and processing methods

The miniaturisation and higher processing capacity of electronics components often result in excessive thermal loading [9], [50]. Thermal management is therefore critical to the performance and reliability of electronic devices. In addition to effective heat dissipation, electrical insulation is necessary for many applications, including mobile devices and medical devices [4], [9]. Hence, polymer-based composite materials that are thermally conducting but electrically insulating are frequently employed in electronic packaging [9].

Materials for thermally conductive hBN/polymer composites:

Polymer-based materials allow for mass production using well-established techniques like injection moulding, transfer moulding, etc. [8], [9]. The polymer matrix in a composite can be a thermoset (e.g. epoxy, silicone) or a thermoplastic, including elastomers of either type. The thermal conductivity of most polymers is low, often ranging from 0.1 to 0.5 W/m·K [8]. Incorporating thermally conductive but electrically insulating inorganic fillers into the polymer matrix is an efficient method for improving the thermal conductivity while retaining its electrical insulation [8], [51]. Common fillers are crystalline ceramic materials, either metal oxides (e.g., alumina (Al₂O₃), quartz (crystalline SiO₂)), or non-oxides (e.g., aluminium nitride (AlN), boron nitride (BN), silicon nitride (Si₃N₄), silicon carbide (SiC)) [8]. Thanks to the high intrinsic thermal conductivity and good electrical insulating properties, hexagonal boron nitride (hBN) has got attention. The filler hBN has been used for improving the thermal conductivity of polymer-based composites, see examples in Table 3.1.

Table 3.1: Some studies of hBN/polymer composites (wt% = weight percentage, vol% = volume percentage)

Materials	Filler Loading	Processing Method	Thermal Conductivity
hBN/epoxy [46]	95 wt%	Compression moulding	21.3 W/m·K (in-plane) 7 W/m·K (through-plane)
hBN/PU [52]	80 vol%	Freeze drying & hot pressing	39 W/m·K (in-plane) 11.5 W/m·K (through-plane)
hBN/polyimide [53]	60 vol%	Spin-cast (film)	17.5 W/m·K (in-plane) 5.4 W/m·K (through-plane)
hBN/epoxy [54]	57 vol%	Casting	5.27 W/m·K (through-plane)
hBN/PE [55]	50 vol%	Injection moulding	3.66 W/m·K (through-plane)
hBN/PEEK [40]	60 wt%	Injection moulding	12.45 W/m·K (in-plane) 2.34 W/m·K (through-plane)
hBN/epoxy [56]	60 wt%	Casting	1.052 W/mK (through-plane, 421 % higher than pure epoxy)
hBN/TPU [57]	50 wt%	Solution mixing & hot pressing	3.06 W/mK (through-plane)
hBN/PA12 [58]	40 wt%	Powder bed fusion	0.55 W/m·K (through-plane, 77% higher than pure PA12)
hBN/Al ₂ O ₃ /PA12 [59]	15 wt% hBN and 35 wt% Al ₂ O ₃	Powder bed fusion	1.05 W/m·K (through-plane, 275% higher than pure PA12)
hBN/AlN/TPU [60]	15 wt% hBN and 20 wt% AlN	Powder bed fusion	0.9 W/m·K (through-plane, 391% higher than pure TPU)
hBN/TPU [61]	30 wt%	Fused deposition modelling (material extrusion)	1.51 W/m·K (in-plane) 1.26 W/m·K (through-plane)
hBN/TPU [this study]	65 wt%	Injection moulding	2.1 W/mK (through-plane, 990 % higher than pure TPU)
hBN/epoxy [this study]	55 wt%	Casting	2.02 W/mK (through-plane, 1315 % higher than pure epoxy)
hBN/TPU [this study]	40 wt%	Powder bed fusion	0.56 W/mK (through-plane, 460 % higher than pure TPU)

Hexagonal BN consists of B and N atoms arranged in a honeycomb configuration with a layer structure similar to graphite. The covalent bonds between B and N atoms within the layers are strong, while the bonds between layers are weak van der Waals forces [62], [63]. The platelet-shaped particle of hBN results from its crystal structure. The platelets have high in-plane thermal conductivity of about 300–600 W/m·K, whereas the through-plane thermal conductivity is in the range 2–30 W/m·K [53], [62]–[64]. Furthermore, hBN is electrically insulating and has a wide band gap (about 5.97 eV). It also has high thermal stability and good mechanical properties [62], [63], [65]. Because of the strong B–N bonds, hBN is chemically stable, e.g., towards oxidation. However, this makes the functionalisation of hBN challenging [63]. hBN also has good biocompatibility [63], [66], [67], which is essential in medical applications.

The thermal conductivity of the composites containing hBN is affected by the orientation of the hBN platelets in the polymer matrix, because of the shape and anisotropic thermal conductivity of the filler hBN [8], [62]. The hBN platelets can be oriented via processing or by using electric or magnetic fields [8], [46], [62], [68], [69]. Different processing methods for polymer-based composites have different effects on the distribution and orientation of the platelets, as well as dispersing agglomerates and stacks of single platelets.

Processing methods for thermally conductive hBN/polymer composites:

Processing methods of thermally conductive polymer composites include melt compounding (e.g., followed by injection moulding) and mixing with a resin followed by casting and polymerisation (curing) [8], [9], [62]. Injection moulding (IM) is one of the most common manufacturing processes for the mass production of polymer or polymer composite parts [9], [70]. The hBN platelets are reported to be preferentially oriented with the platelet normal in the through-plane (thickness) direction of injection moulded parts, because of the shear stress in the IM process [8], [62].

In a casting process, composites are produced by mixing fillers into a resin (e.g. epoxy, silicone), followed by pouring or injecting the mixture into a mould for curing.

The casting of hBN/polymer composites may lead to almost randomly oriented platelets [54], [62], [63].

Powder bed fusion (PBF) is one of the most common 3D printing (additive manufacturing) processes for polymer materials. The feedstock is powder, and thermal energy (e.g., from a laser) selectively fuses regions of a powder bed, layer-by-layer, to fabricate 3D objects [27]. Compared to moulding processes, PBF and other 3D printing techniques have the principal advantages of the fast prototyping and production of personalised parts with complex geometry. Few polymer types are commercially available for PBF. Polyamide 12 (PA12) and thermoplastic polyurethane (TPU) are among the most common polymers. Polyamide-based composites are also used in PBF, with glass-based fillers (e.g., glass fibres, glass beads) or carbon-based fillers (e.g., carbon black, carbon fibres, carbon nanotubes, graphite) [27], [71], [72]. There is a growing interest in developing new materials and composites for PBF, as well as the optimisation of PBF processing parameters.

There are several articles about PBF of polymer composites with thermally and electrically conductive fillers (e.g., carbon-based fillers such as carbon fibres [73], graphite [74], CNT [75] and graphene [76], or metal fillers such as Cu [77], and Ag [78]). On the contrary, the literature on PBF with thermally conductive and electrically insulating polymer-based composites is sparse, and most studies use PA12 as the polymer matrix. Yang et al. [58] studied PBF of hBN/PA12 composites, for which co-powders were prepared by combining solid-state shear milling and cryogenic pulverisation. Yuan et al. [59] investigated the effect of incorporating Al₂O₃ and hBN on thermal and mechanical properties of PA12 composites processed by PBF. Hon et al. [79] examined the effects of processing parameters on the mechanical properties of the PBF composites containing PA12 and SiC. Zhang et al. [60] combined AlN and hBN for enhancing the thermal conductivity of TPU composites processed by PBF.

The thermally conductive hBN/polymer composites were aimed to apply for the encapsulation of the TEE scan head. Encapsulation materials used in the human body must meet several safety requirements, such as good heat transfer, electrical insulation,

mechanical integrity, biocompatibility, and in some cases, a 'soft touch' [3], [4]. A high loading of inorganic fillers (e.g., hBN) is generally required to achieve a significant increase in thermal conductivity of polymer-based composites. However, this normally increases the material hardness and reduces ductility [8], [62]. A soft polymer can be used as the matrix material to compensate for this.

Thermoplastic polyurethane elastomers (TPU) are soft materials based on a block copolymer containing hard and soft segments. In the TPU, the hard segments act as physical crosslinks for the soft segments. TPU has high elasticity over a wide temperature range and high wear resistance [27], [72], [80]. It is frequently used for PBF and IM, and its appropriateness for biomedical applications has been recently emphasized [71]. Therefore, the TPU "Ultrasint TPU 88A" (in the form of powder for PBF) was chosen as the matrix for composites processed by PBF and IM in this study.

Results of the study on thermally conductive hBN/polymer composites are summarised in Article 5 in Chapter 4. The study on thermally conductive hBN/polymer composites focused on: (1) orientation of hBN in composites processed by different methods (IM, casting, PBF); (2) thermal conductivity of composites with different filler loadings and filler types; (3) comparison of the obtained hBN/polymer composites with published values; (4) fitting of experimental data to several thermal conductivity models, as well as (5) hardness and tensile properties of hBN/polymer composites.

3.1.2 Preparation of hBN/polymer composite samples

3.1.2.1 Materials

The materials used in this study are summarised in Table 3.2. The polymer matrix was thermoplastic polyurethane (TPU) for injection moulding and powder bed fusion (3D printing) and epoxy for casting. Three hBN powder types (BN1, BN2, BN3) with different platelet sizes and degrees of agglomeration were used. BN1 (with average size of 1 μm) and BN2 (with average size of 12 μm) mainly contained hBN platelets, while BN3 (with average size of 20 μm) contained both platelets and agglomerates of platelets.

Table 3.2: Materials used for preparation of hBN/polymer composites.

Name	Materials	Product name, Supplier
hBN particles		
BN1	hBN powder with average particle size of $\sim 1 \mu\text{m}$	Boron nitride powder, $1 \mu\text{m}$, 98% (product no. 255475), Sigma Aldrich, Merck
BN2 ^a	hBN powder. Single platelets with median particle size (D_{50}) of $12 \mu\text{m}$ and size distribution in the range (0.8–40) μm , specific surface area (BET) $\sim 6 \text{ m}^2/\text{g}$	HeBoFill LL-SP 120, Henze Boron Nitride Products AG, Germany
BN3 ^a	hBN powder. Platelet agglomerates with D_{50} of $20 \mu\text{m}$ and size distribution in the range (0.5–31) μm , BET $\sim 4 \text{ m}^2/\text{g}$	HeBoFill CL-ADH 020, Henze Boron Nitride Products AG, Germany
Polymer matrix		
TPU	Ultrasint TPU 88A (in the form of powder)	BASF, Germany
Epoxy ^b	An epoxy system (for casting) containing: <ul style="list-style-type: none"> - 35 wt% unmodified bisphenol-F epoxy resin (Araldite GY 285-1) - 35 wt% reactive diluent (Araldite DY 026) - 30 wt% amine-based curing agent (Jeffamine D-230 Polyetheramine) 	Huntsman

^a Information about BN2 and BN3 as provided by the supplier [81], [82]. Size distributions of BN2 (single platelets) and BN3 (partly agglomerated) can be found in Figure S1 in Article 5 [18]. The BN3 powder had a partly agglomerated particle structure, claimed to provide good lubricating properties and low viscosity increase [82]. Platelets and spherical agglomerates of BN3 are shown in Figure 3.1 (showing a cast specimen with 55 wt% BN3).

^b The epoxy system was formulated to have a low viscosity, suitable for preparing composites with high filler content.

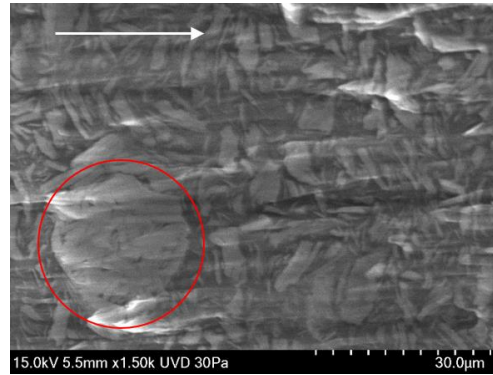


Figure 3.1: SEM micrographs of ion milled cross-sections of a cast specimen with 55 wt% BN3 (C_55BN3). The white arrows show the direction of the disc normal. An agglomerate of hBN platelets is inside the red circle.

3.1.2.2 Fabrication of hBN/polymer composites

The hBN/polymer composites were fabricated by injection moulding (IM), powder bed fusion (PBF) and casting, as examples in Figure 3.2. Details about the equipment and processing parameters used for IM, PBF or casting of the hBN/polymer composites can be found in Article 5 [18].

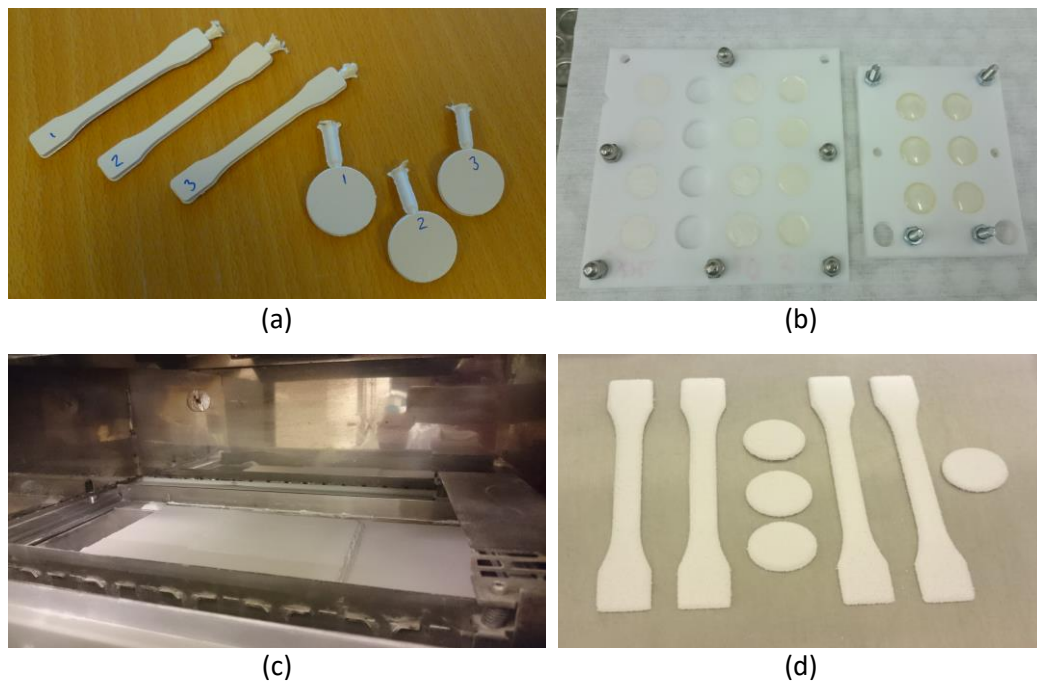


Figure 3.2: (a) Injection moulded specimens containing 65 wt% BN3 (IM_65BN3); (b) cast specimens in Teflon moulds; (c) PBF 3D printer; and (d) PBF specimens.

3.1.3 Characterization of hBN/polymer composites

The hBN/polymer composite specimens were characterised by measuring *thermal conductivity, tensile properties, hardness, SEM* and *DSC*. These characterization methods for the hBN/polymer composites are presented in detail in Article 5 [18].

The orientation of hBN platelets in the composite specimens was characterised by *X-ray diffraction (XRD)*. The degree of orientation of hBN platelets in the polymer matrix is described by $\langle \cos^2\theta \rangle$, where $\langle \cos^2\theta \rangle$ denotes the average of all platelets, and θ is the angle between a platelet surface normal and the specimen surface normal (i.e., the vector along the thickness direction of the specimen). Hence, perfect out-of-plane, in-plane and random orientation of hBN platelets in the specimen corresponds to $\langle \cos^2\theta \rangle = 0, 1$ and $1/3$, respectively, as shown in Figure 3.3. The XRD measurements were conducted for the injection moulded hBN/TPU disc specimens in their original thickness (2 mm) and their half-thickness (1 mm), to evaluate the orientation of hBN platelets in the ‘skin’ and core regions of the injection moulded specimens.

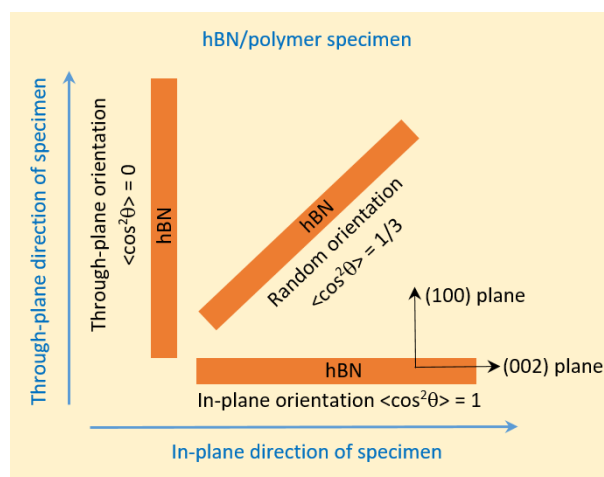


Figure 3.3 : Orientation of hBN platelets; through-plane, random and in-plane.

Results of hardness test for IM, cast and PBF composites, and tensile properties of IM and cast composites are presented in detail in Section 4.5 in Article 5 [18]. The SEM and DSC results can be found in Section S8 in the Supplementary Materials of Article 5 [18].

3.2 Filler orientation in polymer composites

Due to the shape and anisotropic thermal conductivity of hBN, thermal conductivity of hBN/polymer composites is affected by the filler orientation in the polymer matrix, induced by the processing methods. Hence, the orientation of hBN platelets in the specimens was characterized by XRD measurements and compared with numerical simulations.

The XRD measurement results show that injection moulding induces a preferred orientation of the platelets, with the platelet normal along the thickness direction of the moulded part. A $\langle \cos^2\theta \rangle$ value close to 1 means that hBN platelets are highly in-plane oriented, which is referred to as in-plane orientation. Casting results in a low preferred orientation, and powder bed fusion results in an almost random orientation. The experimental results also show that the in-plane orientation of hBN platelets near the surface of a moulded disc (IM_BN3) increases with increasing hBN loading, while the opposite trend is observed in the center region of the disc (IM_BN3_center), as shown in Figure 11 in Article 5 [18]. Furthermore, the center region of the moulded part (IM_BN3_center) has lower in-plane orientation than the region near the surface (IM_BN3).

Numerical simulations of the injection moulding process (in Moldex3D) were performed to illustrate how the platelets achieve their preferred orientation through the thickness of the injection moulded discs. The simulation results agreed with the $\langle \cos^2\theta \rangle$ values from the XRD measurements. In the simulations, the platelets showed in-plane alignment (with high $\langle \cos^2\theta \rangle$) in the 'shell' near the surface of the injection moulded disc, and less preferred alignment (with lower $\langle \cos^2\theta \rangle$) in the core of the disc. *More details about the simulation of filler orientation in injection moulding (using Moldex3D) are presented in Section S7 in the Supplementary Materials of Article 5 [18].*

Filler orientation by injection moulding was also reported by Grundler et al. [83] for their polymer composites with graphite flakes. The injection moulding process induced a structure of anisotropic layers within the injection moulded (composite) plates. Their

injection moulded plates (with 2 mm thickness) had three separate regions with different orientations of the graphite flakes within the polymer matrix (PA6). An alignment of the graphite flakes transverse to the injection direction was observed in the middle region (core) of the plate, while both surface areas of the plate had a distribution of the graphite flakes in injection direction. This anisotropic layer structure has a significant influence on thermal conductivity of composites in different directions. The through-plane thermal conductivity of the middle of the injection moulded composite plate (1 mm) was significantly higher than that of the complete plate (in 2 mm). It was also much higher than the in-plane thermal conductivity of the same region.

In a study of injection moulded polyamide 6 with Cu platelets, Heinle et al. [84] observed similar platelet orientations, and orientation variations through the specimen thickness, as in our study. Heinle et al. moulded specimens with different thicknesses (2, 3 and 4 mm). The three layers through the thickness of the injection moulded specimens represented the two symmetric shell layers (with high in-plane orientation of Cu platelets) and the core layer (with lower orientation). The core/shell ratio increased with increasing specimen thickness (2, 3 and 4 mm). Due to a thicker core, 4 mm thick specimens had almost three times higher through-plane conductivity than 2 mm thick specimens (for 40 vol% platelets). Heinle et al. also measured the conductivity in different directions; through-plane, in-plane along the flow direction and in-plane transverse to the flow. For 40 vol% platelets, the conductivities were almost the same in the two first directions, while it was almost two times higher in the third direction.

3.3 Thermal conductivity measurements and models

3.3.1 Thermal conductivity of hBN/polymer composites

3.3.1.1 Experimental thermal conductivity of hBN/polymer composites

The experimental study on thermal conductivity of hBN/polymer composites in Article 5 [18] reports the effects of filler loading, filler type, processing method and temperature on the thermal conductivity of hBN/polymer composites, as well as how

the processing parameter changes affect the thermal conductivity of the (hBN/TPU) composites produced by PBF.

Figure 3.4 shows the thermal conductivity of hBN/polymer composites fabricated by injection moulding (IM), casting (C) and powder bed fusion (PBF) as a function of hBN loading. The highest conductivity (2.1 W/mK) was measured for an injection moulded specimen with the highest hBN loading in this study (65 wt% BN3). This conductivity is almost 10 times higher than that of the pure TPU (injection moulded reference). For the cast composites, a 14-time higher conductivity was obtained with 55 wt% BN3. For a given hBN loading, the cast composites had the highest conductivity and the highest increase relative to the unfilled material. Among the PBF composites, the specimen with 40 wt% BN3, processed with the highest laser energy density, had the highest conductivity, which was 6 times higher than that of the pure TPU fabricated by PBF.

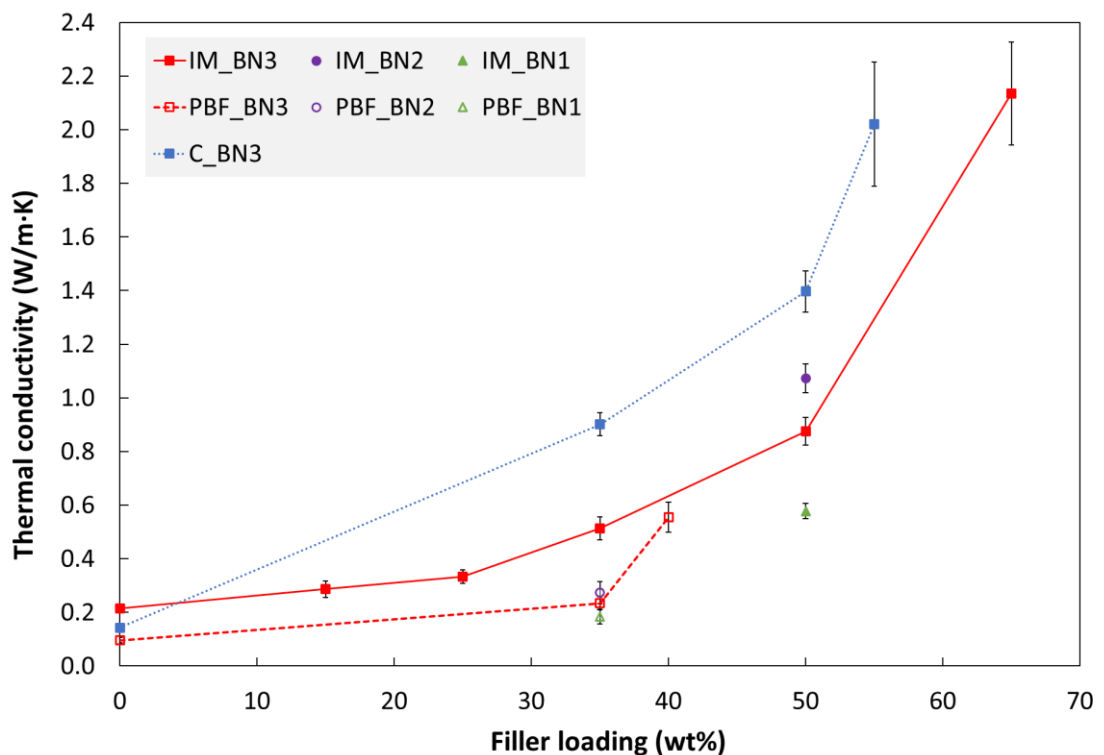


Figure 3.4. Thermal conductivity (at 30 °C) of composites fabricated by injection moulding ("IM"), powder bed fusion ("PBF") and casting ("C") as a function of hBN loading. The PBF specimen with 40 wt% BN3 was processed with a higher laser energy density than the other PBF specimens in this figure.

The thermal conductivity increases with increasing hBN loading for all three processing methods in this study. The slope of the thermal conductivity vs. filler loading appears to increase at around 30 wt% filler (about 18 vol% for IM hBN/TPU), and with a further increase at loadings from about 50 wt% (about 34 vol% for IM hBN/TPU). According to experimental literature on composites with hBN, the percolation threshold for thermal conductivity is about 20–25 vol% for randomly oriented platelets (studies with hBN size in the range of 3–8 μm [85], average particle size of 5 μm [69] and no size given [86]). For highly through-plane-orientated platelets, the threshold is reported to be about 10–15 vol% (studies with average particle sizes of 25 μm [87], 8 μm [88] and 5 μm [69]). Hence, the thermal percolation threshold depends on the orientation of the hBN platelets in the polymer matrix. Above the percolation threshold, the platelets form thermally conductive pathways in the polymer matrix.

Injection moulded composites have lower conductivity than cast composites. This is due to the preferred in-plane orientation of the hBN platelets in the former case, as demonstrated by the XRD data in Article 5. Yuan et al. [64] also showed that a high in-plane orientation of the platelets leads to a low conductivity enhancement in the through-plane direction.

Figure 3.4 also shows that for IM composites with 50 wt% hBN, BN2 and BN1 gave the highest and lowest thermal conductivity, respectively. The same trend was observed for the PBF composites, although the effect was weaker. With the same hBN loading, BN2 results in higher conductivity than BN3. Although some agglomerates in BN3 are broken up during processing, the lower conductivity with BN3 is probably due to platelets being less dispersed. Powders with hBN agglomerates, such as BN3, are claimed to have more isotropic properties and easier processing due to a lower viscosity from spherical fillers [46]. BN1 gives lower thermal conductivity than the two other powders at the same filler loading. This effect is observed for both IM and PBF specimen. The smaller platelets in BN1 gives a larger total surface area. This will reduce the conductivity of the composite if the matrix-filler interfacial thermal resistance is high

[89]. The weak bonding between the polymer matrix and the hBN surface probably lead to high interfacial thermal resistance [90].

The surface of the hBN particles can be modified chemically in order to improve the dispersion of hBN particles and achieve a stronger hBN/polymer interface, thereby improving the thermal conductivity and the mechanical properties [63], [67], [91]–[93]. However, the chemical inertness and oxidation resistance of hBN make the functionalisation of hBN challenging (see more details in Section 3.4 about ‘Surface treatment of hBN’).

The effect of temperature on the thermal conductivity of hBN/polymer composites; as well as how the processing parameter changes affect the thermal conductivity of the PBF composites are reported in detail in Article 5 [18].

3.3.1.2 Comparison with published thermal conductivity values

Although the main objective of the study of thermally conductive polymer composites is to contribute to the understanding of the effects on thermal conductivity of hBN loading, hBN type, hBN platelet orientation and processing methods, it is interesting to compare the thermal conductivity of the composites (hBN/TPU and hBN/epoxy) with some commercially available polymer composites (Table 3.3) and published values for similar composites (Table 3.1 and Figure 3.5). However, such comparisons are challenging, due to differences in mixing/processing method, hBN loading, hBN particle size and matrix material.

The highest through-plane thermal conductivity of our hBN/TPU composites is 2.1 W/mK, obtained by injection moulding of TPU with 65 wt% hBN. This thermal conductivity is higher than that of most commercial thermally conductive and electrically insulating materials, e.g. from Sabic, Covestro, Celanese and Kraiburg (Table 3.3). However, the commercial materials seem to have better mechanical properties.

Comparison with published values for similar composites of other research, as in Table 3.1 and Figure 3.5, shows that important factors affecting thermal conductivity of hBN/polymer composites include hBN filler type, mixing method and surface treatment

of the fillers. The matrix material, in particular its viscosity, should be carefully selected to obtain processable composites with higher filler loadings. Furthermore, using two filler types (with different sizes and/or shapes) could improve thermal conductivity, thanks to synergetic effects (formation of large thermally conductive network by building bridges between fillers and increasing the filler packing density, reduction in the system viscosity) [8].

Table 3.3: Through-plane thermal conductivity of some commercially available polymers, that are thermally conductive and electrically insulating and suitable for injection moulding.

Supplier – Materials	Through-plane thermal conductivity (W/mK)
Sabic – LNP Konduit Compounds (with PA6, PPS or PC matrix) [94]	0.6 – 1.5
Covestro - Makrolon TC (with PC matrix) [95]	0.2 – 0.3
Celanese – Coolpoly D Series (with PP, PA6, PPS, LCP, or TPE matrix) [41]	0.6 – 1.9
Kraiburg – Thermoplast K (HTC1500/117, with TPE matrix) [96]	1.5
TCPoly - Ice9 Flex (TPE with two filler types) [97]	2
Our hBN/TPU composites (65 wt% hBN)	2.1

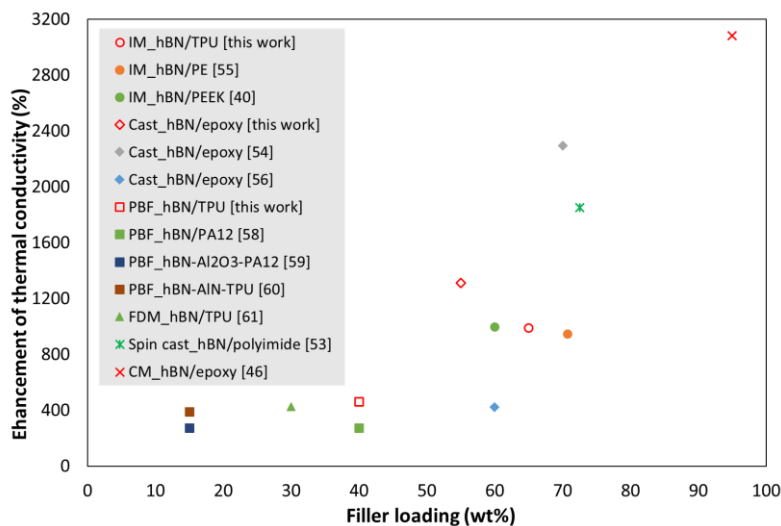


Figure 3.5: Comparison of the thermal conductivity enhancement (%) for the hBN/polymer composites prepared with different hBN loading (wt%) and processing methods [40], [46], [53]–[56], [58]–[61]. Abbreviations of processing methods in the legend: injection moulding (IM), powder bed fusion (PBF), fused deposition modeling (FDM), compression moulding (CM).

3.3.2 Theoretical models for thermal conductivity of polymer composites

The measured thermal conductivities of hBN/polymer composites are compared with four theoretical models, particularly, the effective medium approximation (EMA) model developed by Nan et al. [98], the models of Ordóñez-Miranda et al. [99], Sun et al. [100], and Lewis-Nielsen et al. [84]. These models were included as tools to help in understanding the experimental data, especially how the thermal conductivities of the composites are affected by the fraction and orientation of the hBN platelets and the nature of the interphase between the platelets and the polymer matrix. The reason to include four models, but not simply one, is that they are based on different assumptions and provide different predictions. Many published articles only use one of these models without arguing for their choice of model. Analysing our experimental data using these models also provides a deeper understanding of the models and their limitations. Furthermore, the Sun model [100] is quite new, and, to the best of our knowledge, we are the first to use and evaluate it (apart from the articles cited by Sun et al.). The comparisons of the experimental thermal conductivity with these four models showed that:

- At the low hBN loadings, the EMA model of Nan et al. [98] resulted in a fair prediction of the conductivity. Underprediction at higher loading is interpreted to be because this model does not take into account the formation of platelet-platelet contact, resulting in local conducting paths (pre-percolation).
- The Sun model [100] (based on a finite element analysis) considers the anisotropic thermal conductivity of the hBN platelets, in addition to the effects included in the EMA model. However, it predicts lower conductivities than the EMA model.
- For the Lewis-Nielsen model [84], in addition to the conductivities of the two phases (like other models), this model has two empirical constants, one representing the maximum filler volume fraction and the other for geometry factor representing the effective particle shape in the direction of conductivity measurement. However, the drawback of this model is that the geometry factor is mainly an empirical fitting

parameter; hence, the model might fit to the experimental data by some sets of these two constants, but no physical basis.

- The Ordóñez-Miranda model [99] is limited to a random platelet orientation, but it predicts the experimental data for cast specimens better than the EMA model. Hence, the Ordóñez-Miranda model should be generalised to account for particle orientation.

Details about these models and their equations used for calculating the thermal conductivity of polymer composites are presented in Sections S11 – S14 in The Supplementary Materials of Article 5 [18].

3.4 Experimental study not presented in the published papers

In this PhD project, the surface treatment of hBN was studied by experiments. This section presents the experimental process, the results and the challenges of the chemical functionalization of hBN.

Surface treatment of hBN:

The surface of the hBN particles can be modified chemically, in order to improve the dispersion of hBN particles, and achieve a stronger hBN/polymer interface, thereby improving the mechanical properties and the thermal conductivity [63], [67]. There are wet and dry routes, including covalent methods (e.g. oxidation of hBN with a strong acid or base at high temperature and/or high pressure), non-covalent methods (e.g. coatings of organic compounds on inorganic particles), and solid-state methods (e.g. thermal treatment, high-energy radiation, or strong mechanical forces) [63]. However, the chemical inertness and oxidation resistance of hBN make the functionalization of hBN challenging.

In our study, chemical functionalization was tried for the BN₃ powder. The hBN particles were treated with a strong oxidation agent (nitric acid) followed by silanization (using the aminosilane coupling agent APTES) [67]. However, the coupling agent could

not be attached to the hBN particles, based on analyses using IR spectroscopy (FTIR) and energy dispersive X-ray spectroscopy (EDS). More details about the chemical treatment of hBN are presented as follows.

Experimental process of the chemical functionalization of hBN:

Raw BN powders were dispersed in a HNO₃ solution (65 wt%), achieving a final content of 1 mg/ml. They were sonicated for 12 hours in an ultrasonic bath (FinnSonic M12). The mixture was stabilized overnight, so that the total acid treatment time was 24 hours.

The acid treated BN powders were washed by deionized (DI) water until neutralization (checking by pH-indicator paper, Sigma Aldrich, Merck) and filtered (using PTFE filter paper, Sartorius). Some of them were used for the next chemical treatment steps; some were dried in an oven (at 120 °C for 24 hours) and then stored in nitrogen cabinet for further characterization.

The wet acid-treated powders were then sonicated for 12 hours, in a solution of 10 wt% of 3-aminopropyl-triethoxysilane (APTES, product no. 741442, Sigma Aldrich, Merck) in ethanol (95%), with the final content of 1 mg acid treated BN/1 ml APTES solution. The mixture was stabilized overnight, so that the total APTES treatment time was 24 hours.

The final functionalized products (APTES-modified BN) were washed three times by DI water, filtered (using PTFE paper) and totally dried in an oven at 120 °C for 24 hours. The dry powders were (grinded) and then stored (in a nitrogen cabinet) for further usage or characterization. Some pictures of the experimental process are shown in Figure 3.6.

For comparison, BN powders were also directly modified with APTES (10 wt% in ethanol), without treating with HNO₃. This sample is called APTES-modified raw BN.

The EDS analysis was performed using SEM, for the raw hBN and the chemically treated hBN deposited on Cu tape. The hBN powders were also analyzed by FTIR.

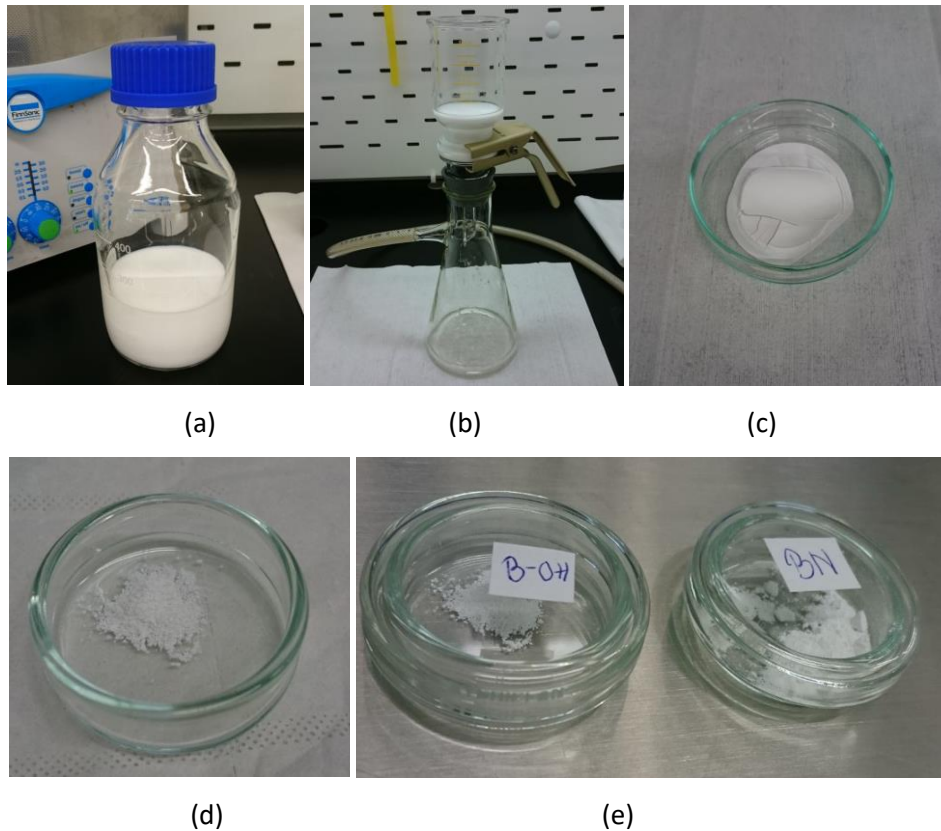


Figure 3.6: Some steps in the chemical treatment process of hBN: (a) the mixture of hBN and APTES solution after sonication, (b) filtering of the hBN mixture, (c) the chemically treated hBN on the PTFE filter paper, (d) the APTES-modified acid-treated hBN powders after drying and grinding, (e) the acid-treated hBN powders (B-OH) and the raw hBN powders (BN).

Experimental results:

The analyses using EDS and FTIR, as in Table 3.4 and Figure 3.7, showed no significant difference between the raw BN, the acid-treated BN, and the APTES-modified BN powders. The used acid treatment process (with HNO_3) was not effective in introducing $-\text{OH}$ groups on the surface of BN, through an oxidation process. This resulted in unsuccessful attachment of the coupling agent APTES to the acid-treated BN particles. In addition, the used method at lab-scale was not suitable for mass production, so that the produced amount of the chemically modified hBN was not enough for preparing hBN/polymer composites by injection moulding, casting or PBF later.

Table 3.4: Atomic composition (from EDS) of the raw BN, acid-treated BN, APTES-modified acid-treated BN, APTES-modified raw BN

Atomic percent (%)	B	C	N	O	Si
Raw BN	45.71	1.66	49.74	2.89	0
Acid-treated BN	46.01	1.68	49.58	2.73	0
APTES-modified acid-treated BN	45.82	2.04	48.86	3.07	0.21
APTES-modified raw BN	45.82	1.83	49.19	3.00	0.16

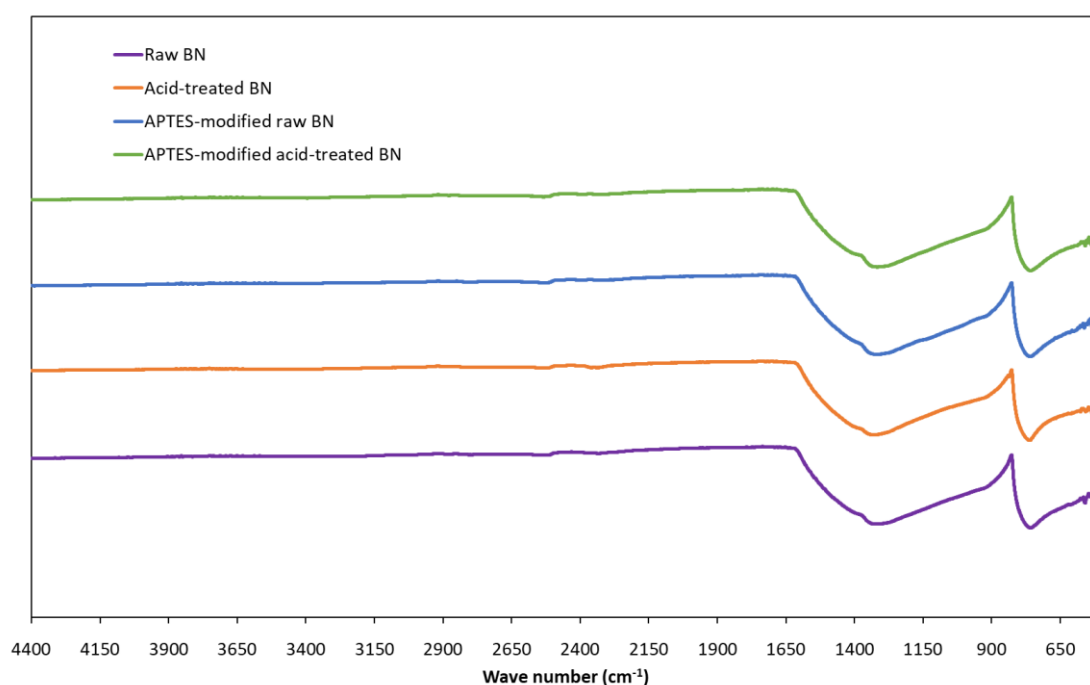


Figure 3.7: FTIR spectra of raw BN, acid-treated BN, APTES-modified acid-treated BN, APTES-modified raw BN

Chapter 4. Summary of the papers

This PhD thesis is based on five published papers (two journal papers and three conference papers). These papers focus on two main research topics: (1) heat transfer of the TEE scan head with two-layer encapsulation, presented in three papers (articles 1, 2, 4); and (2) thermally conductive polymer composites, presented in two papers (articles 3, 5). The below order of the papers is arranged following the workflow of the Phd project.

4.1 Heat transfer of the TEE scan head with two-layer encapsulation

4.1.1 Conference paper 1 (Article 1): New encapsulation concepts for medical ultrasound probes – A heat transfer simulation study

This paper presents heat transfer simulations of the TEE scan head. The objective of this study is to screen encapsulation designs and materials which can simplify the encapsulation of the scan head. The main output to consider for the simulations is the maximum surface temperature of the TEE scan head (T_{max}), which must be below 43 °C to ensure thermal safety for patients.

In this heat transfer simulation study, thermal performance of several TEE scan head encapsulation concepts was compared. The simplification of the TEE scan head assembly could be related to: (1) selecting materials and corresponding packaging techniques suitable for automated processes (which might be achieved by a single-layer encapsulation, see Figure 1.3a), or (2) reducing the number of prefabricated parts to reduce the number of process steps (which might be obtained by a two-layer encapsulation, see Figure 1.3b). Hence, the two encapsulation concepts are analyzed: single-layer encapsulation and two-layer encapsulation. The single-layer encapsulation could be made of one multi-functional material (e.g. composites) for one encapsulation layer. While the two-layer encapsulation could be based on metallized-polymer, or

polymer-coated metal structure. The metallized polymer encapsulation contains a thin metal layer deposited on the inner surface of prefabricated polymer parts. While the polymer-coated metal encapsulation contains a thin coating of a polymer covering the outer surface of prefabricated metal parts.

The simulations are based on steady-state thermal conduction, perfect thermal contact between domains in the scan head, and a convective heat flux boundary condition applied to the outer surface of the scan head in contact with the human esophagus. The boundary condition has the heat transfer coefficient h_c of $400 \text{ W}/(\text{m}^2\cdot\text{K})$, based on the esophageal heat transfer measurements on a pig. More details about this simulation model can be found in Figure 2.5 and Section 2.2.1.

The simulation results show that a single-layer encapsulation, with appropriate thermal conductivity and thickness, can provide sufficient heat transfer for the TEE scan head. However, the selected material(s) should also comply with other functional requirements. The materials need thermal conductivity higher than $20 \text{ W}/(\text{m}\cdot\text{K})$ for the encapsulation thickness of 0.5 mm or $10 \text{ W}/\text{mK}$ for the 1 mm encapsulation thickness, while satisfying EMI shielding, electrical isolation, and biocompatibility.

On the other hand, the two-layer encapsulation can provide the multi-functional performance required for the TEE scan head. For the polymer-coated metal encapsulation, any combination of inner metal layer thickness in the range of (0.5 – 0.9) mm and outer polymer layer thickness in the range of (10 – 100) μm will satisfy the thermal requirement. For the metallized polymer encapsulation, the inner metal layer made of e.g. Cu must be thicker than 50 μm when the thickness of a typical polymer material is 0.5 mm, to satisfy the thermal requirement ($T_{\text{max}} \leq 43 \text{ }^\circ\text{C}$).

This heat transfer simulation study is the basis for the following experimental studies of new encapsulations for thermal management of the TEE scan head (Articles 2 and 4).

Candidate's contribution: original idea, designs, simulations, and writing.

4.1.2 Conference paper 2 (Article 2): Thermal management with a new encapsulation approach for a medical device

This paper presents an experimental study on thermal performance of the metallized polymer encapsulation for the TEE scan head. This two-layer encapsulation is a potential encapsulation approach for simplifying the device assembly. The metallized polymer encapsulation was fabricated by 3D printing (material jetting or PolyJet technology) with a biocompatible polymer, followed by Cu electroplating. The surface temperature of a simplified model of the TEE scan head, with this two-layer encapsulation, was measured in a tissue mimicking thermal phantom, stabilized at around 37 °C (human body temperature). The encapsulations based on a 0.9 mm thick polymer part, electroplated with a 10, 80 or 150 μm thick Cu layer were tested at different power levels (0.5, 1.0, 1.5, 2 W). The effect of the power supplied to the model was also considered.

The experimental results show that the metallized polymer encapsulation can provide adequate thermal dissipation for the device (i.e. maximum surface temperature of the device below the thermal safety limit of 43 °C), when the Cu layer thickness of the encapsulation is at least 80 μm, for the heat source power not higher than 0.5 W. In addition, for a given Cu thickness, the maximum surface temperature of the device is a linear function of the supplied power.

Candidate's contribution: original idea, protocol design, design of experimental setup, all experimental work, and writing paper.

4.1.3 Journal paper 1 (Article 4): Thermal management of an interventional medical device with double layer encapsulation

In this paper, the heat transfer of a simplified TEE scan head with a metallized polymer encapsulation was studied by experimental work and numerical simulations. The test samples consisted of a heat source, a heat sink and a metallized polymer encapsulation made of a 3D printed biocompatible polymer part with a Cu layer electroplated on the inside. The focus of the study was to investigate encapsulation parameters, with regards to the thermal safety requirement that the maximum surface temperature of the scan head (in contact with human tissue) must be below 43 °C. Samples with encapsulations having a 0.9 mm thick polymer outer layer, and an electroplated Cu inner layer (0, 10, 80 or 150 μm thick), were tested with different power levels (0.5 - 2.0 W) supplied to the heat source in the sample. The heat source was connected to some sections of the encapsulation via an aluminium heat sink (see Figure 2.5). The surface temperature of the test sample was measured in a tissue mimicking thermal phantom, which was stabilized at around 37 °C (human body temperature) in a climate chamber.

To the best of our knowledge, this study is the first to investigate the role of a metallized polymer encapsulation for the thermal management of a TEE scan head. In addition, the thermal simulation study gives insight on the heat transfer of the device and provides a basis for establishing design rules and selecting material alternatives for the outer layer of the metallized encapsulation, to further improve the thermal performance of such devices.

Experimental results showed that the maximum steady-state surface temperature could be reduced significantly by a 10 μm thick Cu layer, compared to no Cu layer. Increasing the Cu layer thickness further had a rather small effect, at least for low power levels. The maximum steady-state surface temperature was an exponential function of the Cu layer thickness. In addition, this steady-state temperature increased linearly with increasing power supplied to the sample. Test samples with a Cu electroplated polymer

encapsulation and a heat source power of 0.5 W satisfied the maximum temperature requirement ($< 43\text{ }^{\circ}\text{C}$) when the Cu layer was not thinner than about $80\text{ }\mu\text{m}$.

A finite element model of the TEE scan head with the two-layer encapsulation, for steady-state thermal simulations, was calibrated with the temperature measurements. To obtain a good prediction of all experiments, with and without a Cu inner layer, two thermal contact conductance coefficients were needed for the boundary conditions of the scan head exterior surface (towards the thermal phantom); one coefficient for the un-encapsulated heat source ($250\text{ Wm}^{-2}\text{K}^{-1}$) and one for the polymer encapsulation ($46\text{ Wm}^{-2}\text{K}^{-1}$). With this calibration, simulated steady-state temperatures were in good agreement with the experiments for all Cu layer thicknesses and power levels. The verified simulation model was used to suggest material properties for the outer layer that can allow for higher power levels. The preferred outer material is a biocompatible and electrically insulating material with high thermal conductivity, e.g. a biocompatible ceramic or a thermally conductive and electrically insulating polymer composite.

The simulation model verified by temperature measurement data in this paper enables quick computations and trustable evaluation of the thermal management of TEE scan head with two-layer encapsulation. This verified heat transfer model (in Comsol) is then employed for studying the applicability of different polymer composites for the TEE scan head encapsulation (in Article 3).

Candidate's contribution: original idea, protocol design, design of experimental setup, all experimental work, simulations, writing and editing paper.

4.2 Thermally conductive polymer composites

4.2.1 Journal paper 2 (Article 5): Thermal conductivity and mechanical properties of polymer composites with hexagonal boron nitride – A comparison of three processing methods: injection moulding, powder bed fusion and casting

This study was motivated by the previous research on the thermal management of the TEE scan head with the metallized polymer encapsulation (Article 4). The verified heat transfer simulation model of the TEE scan head with this two-layer encapsulation suggested the outer layer's material of the encapsulation have high thermal conductivity and electrical insulation (e.g. ceramics, polymer composites), so that the device could operate safely at higher power levels. Polymer composites with hexagonal boron nitride (hBN) may fulfil such requirements.

The focus of this study is to compare hBN/polymer composites, fabricated by injection moulding (IM), powder bed fusion (PBF) and casting. A thermoplastic polyurethane (TPU) was selected as the matrix for IM and PBF, and an epoxy was the matrix for casting. To the best of our knowledge, this is the first study that has processed TPU with hBN using PBF, with only a mixture of the two powders. The specimens were characterised by measuring thermal conductivity, tensile properties, and hardness. The orientation of hBN platelets in the specimens was characterised by X-ray diffraction (XRD) and compared with numerical simulations (in Moldex3D). The measured thermal conductivities were also interpreted using platelet orientation measurements (XRD), and by comparing with four models from the literature: the effective medium approximation (EMA) model of Nan et al., the Ordóñez-Miranda model, the Sun model, and the Lewis-Nielsen model.

This study has provided new insights on the effects of the fabrication method and hBN loading on the thermal conductivity and mechanical properties of hBN/polymer composites. With the process equipment used, the maximum practical hBN loading was

65 wt% for injection moulding with TPU as matrix, 55 wt% for casting with epoxy and 40 wt% for powder bed fusion with TPU. The thermal conductivity of the composites increased with increasing hBN loading. The highest thermal conductivity in this study (2.1 W/mK) was measured for an IM specimen with 65 wt% hBN. However, for a given hBN loading, casting resulted in a higher thermal conductivity than the other two methods. This was partly due to the platelet orientation in cast specimens (being more favourable than the orientation induced by injection moulding) and partly due to the matrix material (the epoxy probably resulting in a relatively lower interfacial thermal resistance, and less porosity).

Injection moulding induced a preferred orientation of the platelets, with the platelet normal along the thickness direction of the specimens. The orientation also varied through the thickness of the moulded specimens, and it increased with increasing hBN fraction. The platelet orientation in injection moulded specimens agreed qualitatively with numerical simulations. The simulations of the injection moulding process (in Moldex3D) illustrated how the platelets achieve their preferred orientation through the thickness of the injection moulded discs. The simulation results were in good agreement with the $\langle \cos^2\theta \rangle$ values from the XRD measurements. The platelets have in-plane alignment (with high $\langle \cos^2\theta \rangle$) in the 'shell' near the surface of the injection moulded disc, and less preferred alignment (with lower $\langle \cos^2\theta \rangle$) in the core of the disc. The same filler orientation by injection moulding was also reported by Grundler et al. [83] for the polymer composites with graphite flakes, and by Heinle et al. [84] for the polymer composites with Cu platelets.

The thermal conductivity data were discussed by a comprehensive comparison with four models for the thermal conductivity of composites. These models were included as tools to help in understanding the experimental data, especially how the thermal conductivities of the composites are affected by the loading and orientation of the hBN platelets and the nature of the interphase between the platelets and the polymer matrix. These models are based on different assumptions and provide different predictions about thermal conductivities vs. filler loading. Analysing our experimental

data using these models provides a deeper understanding of the models and their limitations. Furthermore, the Sun model is quite new, and, to the best of our knowledge, we are the first to use and evaluate it (apart from the cited articles by Sun et al.).

At low hBN loadings, the EMA model resulted in a fair prediction of the conductivity. Underprediction at higher loading is interpreted to be because this model does not consider the formation of platelet-platelet contact, resulting in local conducting paths (pre-percolation). The Sun model (based on a finite element analysis) considers the anisotropic thermal conductivity of the hBN platelets, in addition to the effects included in the EMA model. However, it generally predicts lower conductivities than the EMA model. For the Lewis-Nielsen model, in addition to the conductivities of the two phases (like other models), this model has two empirical constants, one representing the maximum filler volume fraction and the other for geometry factor representing the effective particle shape in the direction of conductivity measurement. However, the drawback of this model is that the geometry factor is mainly an empirical fitting parameter; hence, the model might fit to the experimental data by some sets of these two constants, but no physical basis. The Ordóñez-Miranda model is limited to a random platelet orientation, but it predicts the experimental data for cast specimens better than the EMA model. Hence, the Ordóñez-Miranda model should be generalised to account for particle orientation.

For mechanical properties of the hBN/polymer composites, adding hBN increased the hardness and tensile modulus of the materials and the tensile strength at high hBN loadings. The tensile strength of the IM specimens had a minimum as a function of filler loading, while the strain at break decreased with a sharp reduction between 15 and 35 wt% hBN. These trends can be explained by two mechanisms which occur when adding hBN: reinforcement and embrittlement. Powder bed fusion resulted in even more brittle composites, and some type of hBN-polymer compatibilization is probably needed to achieve adequate mechanical properties, in addition to the PBF process enhancements. For a specific application, selecting the hBN loading in the polymer composites should be a compromise, because increasing the filler loading increases the thermal

conductivity, but also reduces the ductility of the material, and has a negative effect on the processability via higher viscosity.

Candidate's contribution: original idea, design of experimental setup, all experimental work, simulations, data analysis, writing and editing paper.

4.2.2 Conference paper 3 (Article 3): Thermally conductive polymer composites with hexagonal boron nitride for medical device thermal management

This study is a continuation of the previous research on the encapsulation of the TEE scan head (Articles 1, 2, 4) and thermally conductive polymer composites (Article 5). This paper adds results for: (1) Polymer composites with different hBN powder types, (2) Comparison with published thermal conductivity values, (3) Thermal simulations of the TEE scan head with various polymer composites, and with anisotropic thermal conductivity.

In this study, hBN/polymer composites were fabricated with thermoplastic polyurethane (TPU) or epoxy as matrix materials, by injection moulding, powder bed fusion or casting. The specimens were experimentally characterized by thermal conductivity measurement. Three hBN powder types (BN1, BN2, BN3) with different platelet sizes and degrees of agglomeration were used. BN1 (with average size of 1 μm) and BN2 (with average size of 12 μm) mainly contained hBN platelets, while BN3 (with average size of 20 μm) contained both platelets and agglomerates of platelets. Thermal simulations (in Comsol) were performed for the TEE scan head with a limit for the maximum surface temperature (43 °C). For the encapsulation of this device, several material combinations were simulated, using anisotropic thermal conductivity data. This included encapsulations with inner layers of commercial, thermally and electrically conductive materials and an outer layer of the best thermally conductive (and electrically insulating) hBN/TPU composite fabricated in the experimental work.

The results have provided new insights on the effect of hBN powder type on the thermal conductivity of hBN/polymer composites. With the three powder types used in this study, both the average particle size and the degree of agglomeration affect the conductivity. The conductivity of the composite is lowest for the smallest platelets (BN1). This is probably due to these giving the largest platelet-polymer interface area in combination with high interfacial thermal resistance. Powders with some platelet agglomerates (BN3) facilitate processing but give lower conductivity than powders with only "free" platelets (BN2). The latter result in better dispersed platelets, which are more effective in transferring heat.

The highest through-plane thermal conductivity of the hBN/polymer composites obtained in this study was 2.1 W/mK for the injection moulded hBN/TPU composite containing 65 wt% BN3. The thermal conductivity of our composites (hBN/TPU and hBN/epoxy) were also compared with some commercially available polymer composites and published values for similar composites. Such comparisons are challenging, due to differences in mixing/processing method, hBN loading, hBN particle size and matrix material. In general, the highest through-plane thermal conductivity of our hBN/TPU composites is higher than that of most commercial, thermally conductive, and electrically insulating materials. However, the commercial materials seem to have better mechanical properties.

The applicability of hBN/polymer composites in a two-layer encapsulation of the TEE scan head was evaluated by steady-state thermal simulations. The simulation constraint is to keep the maximum surface temperature of the scan head below 43 °C to ensure the patients' safety. The hBN/polymer composite can be used safely in a metallized encapsulation (with 0.15 mm of Cu and 0.9 mm of hBN/TPU), or in a 1.0 mm thick encapsulation consisting of two layers (an outer layer of hBN/TPU and an inner layer of a thermally and electrically conductive polymer composite, with 0.5 mm outer/0.5 mm inner or 0.1 mm outer/ 0.9 mm inner thickness combination). Such encapsulations provide the TEE scan head with adequate heat transfer for power levels up to 0.6 W.

Finally, thermal simulations were also performed with a range of different in-plane and through-plane thermal conductivities, to compare and evaluate the overall effect of anisotropic materials on the surface temperature of the TEE scan head. More detailed results are presented in Figure 9 in Article 3 [15].

Candidate's contribution: original idea, design of experimental setup, all experimental work, simulations, data analysis, and writing.

Chapter 5. Conclusions and outlook

5.1 Conclusions

The PhD project aimed at developing packaging concepts (based on materials, design, and processing methods) for a more efficient assembly of the scan head of the TEE ultrasound probe, while maintaining its multi-functional performance to operate safely inside a patient's body, such as adequate heat transfer, EMI shielding, electrical isolation and biocompatibility. The complexity of the TEE scan head assembly can be reduced by reducing the number of process steps via reducing the number of prefabricated parts. This could be achieved by applying two-layer encapsulation (e.g. metallized encapsulation, or encapsulation with two polymer composites) for the TEE scan head.

The initial simulation study showed that a two-layer encapsulation based on a metallized polymer component is promising, both in terms of simplifying the assembly and in terms of accommodating multi-functional requirements. The experiments show that a metallized polymer encapsulation can provide adequate thermal dissipation for the TEE scan head. The steady-state heat transfer simulations were in good agreement with the experiments, for a finite element model using two thermal contact conductance coefficients for the boundary condition. The verified model was used to suggest alternative materials for the outer layer of the metallized encapsulation, to improve the thermal performance of the scan head. The preferred outer material is a biocompatible and electrical insulating material with high thermal conductivity, e.g. a biocompatible ceramic or a thermally conductive and electrically insulating polymer composite.

Thermally conductive polymer composite was therefore selected as the second main research topic for this project. The polymer composites (based on TPU or epoxy) filled with the highly thermally conductive and electrically insulating ceramic filler hBN were evaluated at material level by experimental and theoretical studies. The hBN/polymer composite samples were fabricated by injection moulding, casting, or 3D printing

powder bed fusion. The experiments showed that the maximum practical hBN loading was 65 wt% for injection moulding with TPU as matrix, 55 wt% for casting with epoxy and 40 wt% for powder bed fusion with TPU. The injection moulded composite with 65 wt% hBN obtained the highest thermal conductivity in this study (2.1 W/mK), which was nearly 10 times higher than the thermal conductivity of the pure TPU. For a given hBN loading, casting resulted in a higher thermal conductivity than the other two methods. The filler orientation in the hBN/polymer specimens fabricated by three methods were characterized by XRD. The hBN orientation in injection moulded specimens also agreed qualitatively with numerical simulations. The measured thermal conductivities were compared with four models (EMA, O-M, Sun, L-N models) to understand how the composite thermal conductivities were affected by filler loading and orientation (affected by processing methods). Selecting the filler loading in the polymer composites should be a compromise between the required properties and the processing convenience, since increasing the filler loading increases the thermal conductivity, but reduces the ductility of the composites, and has a negative effect on the processability due to higher viscosity.

The steady-state heat transfer simulation study has also demonstrated the applicability of hBN/polymer composites in the two-layer encapsulation of the TEE scan head. The hBN/polymer composite could be used in a metallized encapsulation (with 0.15 mm of Cu and 0.9 mm of hBN/TPU), or in a 1.0 mm thick encapsulation consisting of two layers (an outer layer of hBN/TPU and an inner layer of a commercial, thermally and electrically conductive polymer composite).

There are limitations of this PhD work. For example, the EMI shielding effectiveness should be quantified for both the metallized polymer encapsulation and the hBN/polymer composite materials. Other properties (e.g. impact, flammability rating, biocompatibility, etc.) should be evaluated, especially for the hBN/polymer composites.

5.2 Outlook

The research results of this PhD project have brought several interesting topics for potential future studies.

Thermal management of TEE scan head with two-layer encapsulation:

In this thesis, the steady-state heat transfer simulation model (verified by the surface temperature measurements) enables quick computations to evaluate the thermal performance of the TEE scan head with two-layer encapsulation. Further work should extend the model to establish physical description of the heat transfer from the TEE scan head to the thermal phantom or to the tissue of the human esophagus. A more comprehensive model should include the thermal phantom (or the human tissue) in the computational domain, and the simulation should be transient.

Thermally conductive polymer composites:

The heat transfer simulations have confirmed the applicability of the hBN/polymer composites for the two-layer encapsulation of the TEE scan head at power levels below 0.6 W. Future work should include fabricating prototypes with the two-layer encapsulation containing the hBN/polymer composite, and performing experimental measurements (e.g. the temperature measurement in the thermal phantom), in order to verify the suitability of using the hBN/polymer composites as the outer layer of the metallized encapsulation, or the encapsulation with two polymer composites.

For the encapsulation with two polymer composites, thermally and electrically conductive polymer composite for the inner layer should be carefully selected, so that the inner layer can provide not only the heat transfer but also the EMI shielding for the device. Some commercial, thermally, and electrically conductive plastics can be considered for the inner layer of the two-composite encapsulation. The prefabricated parts of such encapsulation could be produced by well-established industrial techniques for mass production, e.g. two-component injection moulding. Additionally, the appropriate selection of fillers (types, loadings) for the two polymer composites is also

important to obtain the trade-off between the properties required for the device (e.g. thermal conductivity, electrical isolation, EMI shielding, etc.) and processability of materials (affected by material viscosity).

EMI shielding should also be evaluated by experiments at product level, to confirm the suitability of using the metallized encapsulation (with polymer or hBN/polymer composite as the outer layer) or the encapsulation containing two polymer composites, for protecting the medical device from the electromagnetic interference.

In addition, future work should consider healthcare safety (e.g. biocompatibility, ease of cleaning, etc.) of the TEE scan head with the two-layer encapsulation containing the new polymer composite materials.

For the theoretical study of thermal conductivity of hBN/polymer composites, the Ordóñez-Miranda model agreed well with the experimental data for the cast specimens, but this model is limited to a random platelet orientation. Hence, it should be generalised to account for particle orientation in specimens prepared by other processing methods, e.g. injection moulding.

The results of XRD measurements and simulations of the injection moulding process in Chapter 3 have explained how the filler orientation in the hBN/polymer composite changes through the thickness of the injection moulded specimens. This results in anisotropic thermal conductivity in injection moulded specimens. In future studies, more simulations of the injection moulding process could be conducted to obtain the local platelet orientation in the two-layer encapsulation. From this, the local anisotropic thermal conductivity, in each element of the Comsol model, can be calculated with an appropriate thermal conductivity model (e.g. the EMA model or the O-M model). Hence, a thermal simulation of the TEE scan head with a two-layer encapsulation can be performed, using the local anisotropic thermal conductivities as material input. Such a comprehensive simulation study will provide a thorough understanding of the effect of processing on the thermal performance of the TEE scan head with the two-layer encapsulation containing thermally conductive polymer composites.

References

- [1] E. C. Pua, S. F. Idriss, P. D. Wolf, and S. W. Smith, "Real-time 3D transesophageal echocardiography," *Ultrason. Imaging*, vol. 26, no. 4, pp. 217–232, 2004, doi: 10.1177/016173460402600402.
- [2] Saint Luke's, "Transesophageal Echocardiography (TEE)." <https://www.saintlukeskc.org/health-library/transesophageal-echocardiography-tee>
- [3] N. B. D. Do, E. Andreassen, S. Edwardsen, A. Lifjeld, K. E. Aasmundtveit, H.-V. Nguyen, and K. Imenes, "Thermal management of an interventional medical device with double layer encapsulation," *Exp. Heat Transf.*, pp. 1–18, Jul. 2021, doi: 10.1080/08916152.2021.1946208.
- [4] R. Bahru, A. A. Hamzah, and M. A. Mohamed, "Thermal management of wearable and implantable electronic healthcare devices: Perspective and measurement approach," *International Journal of Energy Research*. 2020. doi: 10.1002/er.6031.
- [5] C. R. Paul, *Introduction to Electromagnetic Compatibility: Second Edition (Chapters 10, 5, Appendix B)*. 2006. doi: 10.1002/0471758159.
- [6] F. P. Incropera, D. P. DeWitt, T. L. Bergman, and A. S. Lavine, *Fundamentals of Heat and Mass Transfer 6th Edition*. 2007. doi: 10.1016/j.applthermaleng.2011.03.022.
- [7] J. M. H. Morales, "Evaluating biocompatible barrier films as encapsulants of medical micro devices," Université Grenoble Alpes, 2016.
- [8] H. Chen, V. V. Ginzburg, J. Yang, Y. Yang, W. Liu, Y. Huang, L. Du, and B. Chen, "Thermal conductivity of polymer-based composites: Fundamentals and applications," *Progress in Polymer Science*, vol. 59. pp. 41–85, 2016. doi: 10.1016/j.progpolymsci.2016.03.001.
- [9] R. Tummala, *Fundamentals of Microsystems Packaging*. McGraw-Hill Education, 2001.
- [10] M. Schlesinger and M. Paunovic, *Modern Electroplating: Fifth Edition*. 2011. doi: 10.1002/9780470602638.
- [11] IEC, *IEC 60601-1-2 - Medical electrical equipment - Part 1-2: General requirements for basic safety and essential performance - Collateral Standard: Electromagnetic disturbances - Requirements and tests*. 2014.
- [12] CISPR, *CISPR 11:2009 - Industrial, scientific and medical equipment - Radio-frequency disturbance characteristics - Limits and methods of measurements*. 2010.
- [13] N. B. D. Do, E. Andreassen, S. Edwardsen, A. Lifjeld, H. V. Nguyen, K. E. Aasmundtveit, and K. I. Imenes, "New encapsulation concepts for medical ultrasound probes- A heat transfer simulation study," presented at the 2019 22nd European Microelectronics and Packaging Conference and Exhibition, EMPC 2019, Pisa, Italy, 2019. doi: 10.23919/EMPC44848.2019.8951832.
- [14] D. Nu Bich Duyen, A. Erik, and I. Kristin, "Thermal management with a new encapsulation approach for a medical device," presented at the 2020 IEEE 8th Electronics System-Integration Technology Conference, ESTC 2020, Tønsberg, Norway, 2020. doi: 10.1109/ESTC48849.2020.9229798.
- [15] D. Nu Bich Duyen, I. Kristin, A. Knut E., N. Hoang-Vu, and A. Erik, "Thermally conductive polymer composites with hexagonal boron nitride for medical device

- thermal management,” presented at the 2023 24th European Microelectronics and Packaging Conference and Exhibition, EMPC 2023, Cambridge, England, 2023.
- [16] IEC, *IEC 60601-2-37 - Particular requirements for the safety of ultrasonic medical diagnostic and monitoring equipment*. 2004.
- [17] C. Yadav and R. R. Sahoo, “Effect of nano-enhanced PCM on the thermal performance of a designed cylindrical thermal energy storage system,” *Exp. Heat Transf.*, vol. 34, no. 4, pp. 356–375, Jun. 2021, doi: 10.1080/08916152.2020.1751744.
- [18] N. B. D. Do, K. Imenes, K. E. Aasmundtveit, H.-V. Nguyen, and E. Andreassen, “Thermal Conductivity and Mechanical Properties of Polymer Composites with Hexagonal Boron Nitride—A Comparison of Three Processing Methods: Injection Moulding, Powder Bed Fusion and Casting,” *Polymers*, vol. 15, no. 6, p. 1552, Mar. 2023, doi: 10.3390/polym15061552.
- [19] F. Ozdemir and A. Kargi, “Electromagnetic Waves and Human Health,” in *Electromagnetic Waves*, 2011. doi: 10.5772/16343.
- [20] S. Geetha, K. K. Satheesh Kumar, C. R. K. Rao, M. Vijayan, and D. C. Trivedi, “EMI shielding: Methods and materials-A review,” *J. Appl. Polym. Sci.*, vol. 112, no. 4, pp. 2073–2086, 2009, doi: 10.1002/app.29812.
- [21] K. Chizari, M. Arjmand, Z. Liu, U. Sundararaj, and D. Therriault, “Three-dimensional printing of highly conductive polymer nanocomposites for EMI shielding applications,” *Mater. Today Commun.*, vol. 11, pp. 112–118, 2017, doi: 10.1016/j.mtcomm.2017.02.006.
- [22] J. M. Thomassin, C. Jérôme, T. Pardoën, C. Bailly, I. Huynen, and C. Detrembleur, “Polymer/carbon based composites as electromagnetic interference (EMI) shielding materials,” *Mater. Sci. Eng. R Rep.*, vol. 74, no. 7, pp. 211–232, 2013, doi: 10.1016/j.mser.2013.06.001.
- [23] V. M. Hong Ng, H. Huang, K. Zhou, P. S. Lee, W. Que, J. Z. Xu, and L. B. Kong, “Recent progress in layered transition metal carbides and/or nitrides (MXenes) and their composites: synthesis and applications,” *J. Mater. Chem. A*, 2017, doi: 10.1039/c6ta06772g.
- [24] R. Sun, H. B. Zhang, J. Liu, X. Xie, R. Yang, Y. Li, S. Hong, and Z. Z. Yu, “Highly Conductive Transition Metal Carbide/Carbonitride(MXene)@polystyrene Nanocomposites Fabricated by Electrostatic Assembly for Highly Efficient Electromagnetic Interference Shielding,” *Adv. Funct. Mater.*, 2017, doi: 10.1002/adfm.201702807.
- [25] D. D. L. Chung, “Materials for electromagnetic interference shielding,” *J. Mater. Eng. Perform.*, 2000, doi: 10.1016/j.actaastro.2011.06.004.
- [26] Z. Guo, Y. Chen, and N. L. Lu, *Multifunctional Nanocomposites for Energy and Environmental Applications*. Weinheim, Germany: Wiley-VCH Verlag GmbH & Co. KGaA, 2018. doi: 10.1002/9783527342501.
- [27] S. C. Ligon, R. Liska, J. Stampfl, M. Gurr, and R. Mülhaupt, “Polymers for 3D Printing and Customized Additive Manufacturing,” *Chemical Reviews*, vol. 117, no. 15. pp. 10212–10290, 2017. doi: 10.1021/acs.chemrev.7b00074.

- [28] R. D. Farahani, M. Dubé, and D. Therriault, "Three-Dimensional Printing of Multifunctional Nanocomposites: Manufacturing Techniques and Applications," *Advanced Materials*. pp. 5794–5821, 2016. doi: 10.1002/adma.201506215.
- [29] ISO/ASTM, *ISO/ASTM 52900-2015: Additive manufacturing -- General principles -- Terminology*. 2015.
- [30] Stratasys, "Objet30 Prime," *Tech. Datasheet*, 2016.
- [31] Humber River Hospital, "Preparing for your Transesophageal Echocardiogram (TEE)," no. 2012_05 REV 2016_02, 2016.
- [32] S. Babu, K. Manisekar, A. P. S. Kumar, and D. Rajenthirakumar, "Experimental Study of Thermal Contact Resistance in Hardened Bearing Surfaces," *Exp. Heat Transf.*, vol. 28, no. 2, pp. 189–203, Mar. 2015, doi: 10.1080/08916152.2013.860503.
- [33] M. Asif and A. Tariq, "Correlations of Thermal Contact Conductance for Nominally Flat Metallic Contact in Vacuum," *Exp. Heat Transf.*, 2016, doi: 10.1080/08916152.2015.1024352.
- [34] Heat Scientific, "Heat Scientific MCH Metal Ceramic Heater," *HS-PS101012Y Datasheet*, 2018.
- [35] Aalco, "Aluminium alloy 6082," *Tech. Datasheet*, 2019.
- [36] Epoxy Technology, "EPO-TEK T7109-19," *Tech. Datasheet*, 2019.
- [37] Epoxy Technology, "EPO-TEK EJ2189-LV," *Tech. Datasheet*, 2017.
- [38] COMSOL Multiphysics v. 5.3a, "COMSOL Material Library," *COMSOL AB Swden*, 2018.
- [39] K. Jagannadham, "Thermal conductivity of copper-graphene composite films synthesized by electrochemical deposition with exfoliated graphene platelets," *Metall. Mater. Trans. B Process Metall. Mater. Process. Sci.*, 2012, doi: 10.1007/s11663-011-9597-z.
- [40] S. Gul, S. Arican, M. Cansever, B. Beylergil, M. Yildiz, and B. Saner Okan, "Design of Highly Thermally Conductive Hexagonal Boron Nitride-Reinforced PEEK Composites with Tailored Heat Conduction Through-Plane and Rheological Behaviors by a Scalable Extrusion," *ACS Appl. Polym. Mater.*, vol. 5, no. 1, pp. 329–341, Jan. 2023, doi: 10.1021/acspapm.2c01534.
- [41] Celanese, "Celanese Thermally conductive plastics CoolPoly TCP." Celanese corporation, 2023. [Online]. Available: <https://www.celanese.com/products/coolpoly-thermal-conductivity-plastics/>
- [42] G. Wypych, *Handbook of Polymers: Second Edition*. 2016. doi: 10.1016/C2015-0-01462-9.
- [43] A. J. T. Teo, A. Mishra, I. Park, Y. J. Kim, W. T. Park, and Y. J. Yoon, "Polymeric Biomaterials for Medical Implants and Devices," *ACS Biomaterials Science and Engineering*. 2016. doi: 10.1021/acsbiomaterials.5b00429.
- [44] Y. Duan and H. Yang, "Influence of thermal contact resistance of cementing interface on radial heat transfer in wellbore," *Exp. Heat Transf.*, vol. 34, no. 1, pp. 68–84, Jan. 2021, doi: 10.1080/08916152.2020.1715511.
- [45] M. Ohashi, S. Kawakami, Y. Yokogawa, and G. C. Lai, "Spherical aluminum nitride fillers for heat-conducting plastic packages," *J. Am. Ceram. Soc.*, 2005, doi: 10.1111/j.1551-2916.2005.00456.x.

- [46] Z. Zhu, P. Wang, P. Lv, T. Xu, J. Zheng, C. Ma, K. Yu, W. Feng, W. Wei, and L. Chen, "Densely packed polymer/boron nitride composite for superior anisotropic thermal conductivity," *Polym. Compos.*, 2018, doi: 10.1002/pc.24615.
- [47] T. Kusunose, T. Yagi, S. H. Firoz, and T. Sekino, "Fabrication of epoxy/silicon nitride nanowire composites and evaluation of their thermal conductivity," *J. Mater. Chem. A*, 2013, doi: 10.1039/c3ta00686g.
- [48] N. G. Berg, T. Paskova, and A. Ivanisevic, "Tuning the biocompatibility of aluminum nitride," *Mater. Lett.*, 2017, doi: 10.1016/j.matlet.2016.11.041.
- [49] M. Qin, H. Lu, H. Wu, Q. He, C. Liu, X. Mu, Y. Wang, B. Jia, and X. Qu, "Powder injection molding of complex-shaped aluminium nitride ceramic with high thermal conductivity," *J. Eur. Ceram. Soc.*, 2019, doi: 10.1016/j.jeurceramsoc.2018.11.037.
- [50] S. Bhanushali, P. C. Ghosh, G. P. Simon, and W. Cheng, "Copper Nanowire-Filled Soft Elastomer Composites for Applications as Thermal Interface Materials," *Adv. Mater. Interfaces*, vol. 4, no. 17, pp. 1700387–1700387, Sep. 2017, doi: 10.1002/admi.201700387.
- [51] D. Li, D. Zeng, Q. Chen, M. Wei, L. Song, C. Xiao, and D. Pan, "Effect of different size complex fillers on thermal conductivity of PA6 thermal composites," *Plast. Rubber Compos.*, vol. 48, no. 8, pp. 347–355, Sep. 2019, doi: 10.1080/14658011.2019.1626596.
- [52] N. Zhao, J. Li, W. Wang, W. Gao, and H. Bai, "Isotropically Ultrahigh Thermal Conductive Polymer Composites by Assembling Anisotropic Boron Nitride Nanosheets into a Biaxially Oriented Network," *ACS Nano*, vol. 16, no. 11, pp. 18959–18967, Nov. 2022, doi: 10.1021/acsnano.2c07862.
- [53] M. Tanimoto, T. Yamagata, K. Miyata, and S. Ando, "Anisotropic thermal diffusivity of hexagonal boron nitride-filled polyimide films: Effects of filler particle size, aggregation, orientation, and polymer chain rigidity," *ACS Appl. Mater. Interfaces*, vol. 5, no. 10, pp. 4374–4382, 2013, doi: 10.1021/am400615z.
- [54] Y. Xu and D. D. L. Chung, "Increasing the thermal conductivity of boron nitride and aluminum nitride particle epoxy-matrix composites by particle surface treatments," *Compos. Interfaces*, vol. 7, no. 4, pp. 243–256, Jan. 2000, doi: 10.1163/156855400750244969.
- [55] G.-W. Lee, M. Park, J. Kim, J. I. Lee, and H. G. Yoon, "Enhanced thermal conductivity of polymer composites filled with hybrid filler," *Compos. Part Appl. Sci. Manuf.*, vol. 37, no. 5, pp. 727–734, May 2006, doi: 10.1016/j.compositesa.2005.07.006.
- [56] J. Gu, Q. Zhang, J. Dang, and C. Xie, "Thermal conductivity epoxy resin composites filled with boron nitride: THERMAL CONDUCTIVITY EPOXY RESIN COMPOSITES," *Polym. Adv. Technol.*, vol. 23, no. 6, pp. 1025–1028, Jun. 2012, doi: 10.1002/pat.2063.
- [57] T. Fei, Y. Li, B. Liu, and C. Xia, "Flexible polyurethane/boron nitride composites with enhanced thermal conductivity," *High Perform. Polym.*, vol. 32, no. 3, pp. 324–333, Apr. 2020, doi: 10.1177/0954008319862044.
- [58] L. Yang, L. Wang, and Y. Chen, "Solid-state shear milling method to prepare PA12/boron nitride thermal conductive composite powders and their selective laser sintering 3D-printing," *J. Appl. Polym. Sci.*, vol. 137, no. 23, pp. 1–13, 2020, doi: 10.1002/app.48766.

- [59] Y. Yuan, W. Wu, H. Hu, D. Liu, H. Shen, and Z. Wang, "The combination of Al₂O₃ and BN for enhancing the thermal conductivity of PA12 composites prepared by selective laser sintering," *RSC Adv.*, vol. 11, no. 4, pp. 1984–1991, 2021, doi: 10.1039/D0RA09775F.
- [60] X. Zhang, W. Wu, T. Zhao, and J. Li, "The combination of AlN and h-BN for enhancing the thermal conductivity of thermoplastic polyurethane composites prepared by selective laser sintering," *J. Appl. Polym. Sci.*, Aug. 2022, doi: 10.1002/app.53051.
- [61] J. Gao, M. Hao, Y. Wang, X. Kong, B. Yang, R. Wang, Y. Lu, L. Zhang, M. Gong, L. Zhang, D. Wang, and X. Lin, "3D printing boron nitride nanosheets filled thermoplastic polyurethane composites with enhanced mechanical and thermal conductive properties," *Addit. Manuf.*, vol. 56, pp. 102897–102897, Aug. 2022, doi: 10.1016/j.addma.2022.102897.
- [62] C. Yu, J. Zhang, W. Tian, X. Fan, and Y. Yao, "Polymer composites based on hexagonal boron nitride and their application in thermally conductive composites," *RSC Adv.*, vol. 8, no. 39, pp. 21948–21967, 2018, doi: 10.1039/C8RA02685H.
- [63] Z. Zheng, M. Cox, and B. Li, "Surface modification of hexagonal boron nitride nanomaterials: a review," *J. Mater. Sci.*, vol. 53, no. 1, pp. 66–99, Jan. 2018, doi: 10.1007/s10853-017-1472-0.
- [64] C. Yuan, B. Duan, L. Li, B. Xie, M. Huang, and X. Luo, "Thermal Conductivity of Polymer-Based Composites with Magnetic Aligned Hexagonal Boron Nitride Platelets," *ACS Appl. Mater. Interfaces*, vol. 7, no. 23, pp. 13000–13006, 2015, doi: 10.1021/acsami.5b03007.
- [65] Y. Zhang, W. Gao, Y. Li, D. Zhao, and H. Yin, "Hybrid fillers of hexagonal and cubic boron nitride in epoxy composites for thermal management applications," *RSC Adv.*, 2019, doi: 10.1039/c9ra00282k.
- [66] A. Merlo, V. R. S. S. Mokkalapati, S. Pandit, and I. Mijakovic, "Boron nitride nanomaterials: Biocompatibility and bio-applications," *Biomater. Sci.*, 2018, doi: 10.1039/c8bm00516h.
- [67] G. Ciofani, G. G. Genchi, I. Liakos, A. Athanassiou, D. Dinucci, F. Chiellini, and V. Mattoli, "A simple approach to covalent functionalization of boron nitride nanotubes," *J. Colloid Interface Sci.*, vol. 374, no. 1, pp. 308–314, May 2012, doi: 10.1016/j.jcis.2012.01.049.
- [68] Y. Xue, X. Li, H. Wang, F. Zhao, D. Zhang, and Y. Chen, "Improvement in thermal conductivity of through-plane aligned boron nitride/silicone rubber composites," *Mater. Des.*, vol. 165, pp. 107580–107580, 2019, doi: 10.1016/j.matdes.2018.107580.
- [69] Z. Lin, Y. Liu, S. Raghavan, K. S. Moon, S. K. Sitaraman, and C. P. Wong, "Magnetic alignment of hexagonal boron nitride platelets in polymer matrix: Toward high performance anisotropic polymer composites for electronic encapsulation," *ACS Appl. Mater. Interfaces*, vol. 5, no. 15, pp. 7633–7640, 2013, doi: 10.1021/am401939z.
- [70] R. J. Crawford, "Plastics engineering," in *The Queen's University of Belfast*, 1998, pp. 530–530.

- [71] Shangqin Yuan, "Development and optimization of selective laser sintered-composites and structures for functional applications," 2018. doi: 10.32657/10356/73195.
- [72] S. Yuan, F. Shen, C. K. Chua, and K. Zhou, "Polymeric composites for powder-based additive manufacturing: Materials and applications," *Prog. Polym. Sci.*, vol. 91, pp. 141–168, Apr. 2019, doi: 10.1016/j.progpolymsci.2018.11.001.
- [73] F. Sillani, F. de Gasparo, M. Schmid, and K. Wegener, "Influence of packing density and fillers on thermal conductivity of polymer powders for additive manufacturing," *Int. J. Adv. Manuf. Technol.*, vol. 117, no. 7–8, pp. 2049–2058, Dec. 2021, doi: 10.1007/s00170-021-07117-z.
- [74] F. Lupone, E. Padovano, O. Ostrovskaya, A. Russo, and C. Badini, "Innovative approach to the development of conductive hybrid composites for Selective Laser Sintering," *Compos. Part Appl. Sci. Manuf.*, vol. 147, pp. 106429–106429, Aug. 2021, doi: 10.1016/j.compositesa.2021.106429.
- [75] S. Yuan, Y. Zheng, C. K. Chua, Q. Yan, and K. Zhou, "Electrical and thermal conductivities of MWCNT/polymer composites fabricated by selective laser sintering," *Compos. Part Appl. Sci. Manuf.*, vol. 105, pp. 203–213, Feb. 2018, doi: 10.1016/j.compositesa.2017.11.007.
- [76] A. Ronca, G. Rollo, P. Cerruti, G. Fei, X. Gan, G. Buonocore, M. Lavorgna, H. Xia, C. Silvestre, and L. Ambrosio, "Selective Laser Sintering Fabricated Thermoplastic Polyurethane/Graphene Cellular Structures with Tailorable Properties and High Strain Sensitivity," *Appl. Sci.*, vol. 9, no. 5, pp. 864–864, Feb. 2019, doi: 10.3390/app9050864.
- [77] L. Lanzl, K. Wudy, S. Greiner, and D. Drummer, "Selective laser sintering of copper filled polyamide 12: Characterization of powder properties and process behavior," *Polym. Compos.*, vol. 40, no. 5, pp. 1801–1809, May 2019, doi: 10.1002/pc.24940.
- [78] P. Gruber, G. Ziólkowski, M. Olejarczyk, E. Grochowska, V. Hoppe, P. Szymczyk-Ziółkowska, and T. Kurzynowski, "Influence of bioactive metal fillers on microstructural homogeneity of PA12 composites produced by polymer Laser Sintering," *Arch. Civ. Mech. Eng.*, vol. 22, no. 3, pp. 117–117, Jul. 2022, doi: 10.1007/s43452-022-00442-4.
- [79] K. K. B. Hon and T. J. Gill, "Selective Laser Sintering of SiC/Polyamide Composites," *CIRP Ann.*, vol. 52, no. 1, pp. 173–176, 2003, doi: 10.1016/S0007-8506(07)60558-7.
- [80] A. Frick and A. Rochman, "Characterization of TPU-elastomers by thermal analysis (DSC)," *Polym. Test.*, vol. 23, no. 4, pp. 413–417, Jun. 2004, doi: 10.1016/j.polymertesting.2003.09.013.
- [81] Henze Boron Nitride Products AG, "HeBoFill® LL-SP 120," *Tech. Datasheet*, pp. 8374–8374, 2020.
- [82] Henze Boron Nitride Products AG, "HeBoFill® CL-ADH 020," *Tech. Datasheet*, pp. 49–50, 2020.
- [83] M. Grundler, T. Derieth, and A. Heinzl, "Polymer compounds with high thermal conductivity," presented at the PROCEEDINGS OF THE REGIONAL CONFERENCE GRAZ 2015 – POLYMER PROCESSING SOCIETY PPS: Conference Papers, Graz, Austria, 2016, p. 030015. doi: 10.1063/1.4965485.

- [84] C. Heinle, Z. Brocka, G. Hülder, G. Ehrenstein, and T. Osswald, "Thermal conductivity of polymers filled with non-isometric fillers: A process dependent, anisotropic property," presented at the Proceedings of the 67th Annual Technical Conference of the Society of Plastics Engineers (ANTEC 2009, Chicago), Chicago, Jun. 2009, pp. 883–889.
- [85] F. Kargar, Z. Barani, R. Salgado, B. Debnath, J. S. Lewis, E. Aytan, R. K. Lake, and A. A. Balandin, "Thermal Percolation Threshold and Thermal Properties of Composites with High Loading of Graphene and Boron Nitride Fillers," *ACS Appl. Mater. Interfaces*, vol. 10, no. 43, pp. 37555–37565, 2018, doi: 10.1021/acsami.8b16616.
- [86] C. Pan, J. Zhang, K. Kou, Y. Zhang, and G. Wu, "Investigation of the through-plane thermal conductivity of polymer composites with in-plane oriented hexagonal boron nitride," *Int. J. Heat Mass Transf.*, vol. 120, no. December, pp. 1–8, 2018, doi: 10.1016/j.ijheatmasstransfer.2017.12.015.
- [87] D. Ding, M. Zou, X. Wang, G. Qin, S. Zhang, S. Y. Chan, Q. Meng, Z. Liu, Q. Zhang, and Y. Chen, "Thermal conductivity of polydisperse hexagonal BN/polyimide composites: Iterative EMT model and machine learning based on first principles investigation," *Chem. Eng. J.*, vol. 437, pp. 135438–135438, Jun. 2022, doi: 10.1016/j.cej.2022.135438.
- [88] J. Liu, W. Li, Y. Guo, H. Zhang, and Z. Zhang, "Improved thermal conductivity of thermoplastic polyurethane via aligned boron nitride platelets assisted by 3D printing," *Compos. Part Appl. Sci. Manuf.*, vol. 120, no. February, pp. 140–146, 2019, doi: 10.1016/j.compositesa.2019.02.026.
- [89] J. Ordonez-Miranda and J. J. Alvarado-Gil, "Thermal conductivity of nanocomposites with high volume fractions of particles," *Compos. Sci. Technol.*, vol. 72, no. 7, pp. 853–857, Apr. 2012, doi: 10.1016/j.compscitech.2012.02.016.
- [90] K. Pietrak and T. Wiśniewski, "A review of models for effective thermal conductivity of composite materials," *J. Power Technol.*, vol. [Online] 95:1, 2014.
- [91] S. Daneshmehr, F. Román, and J. M. Hutchinson, "The surface modification of boron nitride particles," *J. Therm. Anal. Calorim.*, 2019, doi: 10.1007/s10973-019-09160-1.
- [92] Z. Cui, A. J. Oyer, A. J. Glover, H. C. Schniepp, and D. H. Adamson, "Large scale thermal exfoliation and functionalization of boron nitride," *Small*, 2014, doi: 10.1002/sml.201303236.
- [93] S. Ryu, K. Kim, and J. Kim, "Silane surface treatment of boron nitride to improve the thermal conductivity of polyethylene naphthalate requiring high temperature molding," *Polym. Compos.*, vol. 39, no. S3, pp. E1692–E1700, Jun. 2018, doi: 10.1002/pc.24680.
- [94] Sabic, "Rethinking your heat sink materials." Sabic, 2020. [Online]. Available: <https://www.sabic.com/en/industries/electrical-and-electronics/lighting/thermal-conductive>
- [95] Covestro Deutschland AG - Engineering Plastics, "Whitepaper 'Power-Tools mit maximaler Leistung und Lebensdauer.'" Covestro, 2022. [Online]. Available: <https://solutions.covestro.com/en/highlights/articles/theme/product->

technology/makrolon-tc-thermal-conductive-plastics-next-generation-heat-management

- [96] Kraiburg, “Technical datasheet - Kraiburg THERMOLAST K (HTC1500/117).” Kraiburg TPE, 2023. [Online]. Available: <https://www.kraiburg-tpe.com/en/thermolast-k>
- [97] TCPoly, “Technical datasheet - Ice9 Flex (Thermally conductive, electrically non-conducting plastic TC-TPE1-145-000).” TCPoly, 2019. [Online]. Available: <https://tcpoly.com/purchase-ice9-materials/>
- [98] C.-W. Nan, R. Birringer, D. R. Clarke, and H. Gleiter, “Effective thermal conductivity of particulate composites with interfacial thermal resistance,” *J. Appl. Phys.*, vol. 81, no. 10, pp. 6692–6699, May 1997, doi: 10.1063/1.365209.
- [99] J. Ordóñez-Miranda, J. J. Alvarado-Gil, and R. Medina-Ezquivel, “Generalized Bruggeman Formula for the Effective Thermal Conductivity of Particulate Composites with an Interface Layer,” *Int. J. Thermophys.*, vol. 31, no. 4–5, pp. 975–986, May 2010, doi: 10.1007/s10765-010-0756-2.
- [100] Y. Sun, L. Zhou, Y. Han, L. Cui, and L. Chen, “A new anisotropic thermal conductivity equation for h-BN/polymer composites using finite element analysis,” *Int. J. Heat Mass Transf.*, vol. 160, pp. 120157–120157, 2020, doi: 10.1016/j.ijheatmasstransfer.2020.120157.

Articles

Five published papers (including two journal papers and three conference papers) are attached to this PhD thesis.

Article 1

N. B. D. Do, E. Andreassen, S. Edwardsen, A. Lifjeld, H.-V. Nguyen, K. E. Aasmundveit, and K. Imenes, "New Encapsulation Concepts for Medical Ultrasound Probes-A Heat Transfer Simulation Study," *2019 22nd European Microelectronics and Packaging Conference & Exhibition (EMPC)*, Pisa, Italy, 2019, pp. 1-7, DOI: [10.23919/EMPC44848.2019.8951832](https://doi.org/10.23919/EMPC44848.2019.8951832)

Not included in online dissertation

Article 2

N. B. D. Do, E. Andreassen and K. Imenes, "Thermal management with a new encapsulation approach for a medical device," *2020 IEEE 8th Electronics System-Integration Technology Conference (ESTC)*, Tønsberg, Norway, 2020, pp. 1-5, DOI: [10.1109/ESTC48849.2020.9229798](https://doi.org/10.1109/ESTC48849.2020.9229798)

Not included in online dissertation

Article 3

N. B. D. Do, K. Imenes, K. E. Aasmundveit, H.-V. Nguyen and E. Andreassen, "Thermally conductive polymer composites with hexagonal boron nitride for medical device thermal management," *2023 24th European Microelectronics and Packaging Conference & Exhibition (EMPC)*, Cambridge, England, 2023.

Not included in online dissertation

Article 4

Nu Bich Duyen Do, Erik Andreassen, Stephen Edwardsen, Anders Lifjeld, Knut E. Aasmundveit, Hoang-Vu Nguyen & Kristin Imenes (2022), Thermal management of an interventional medical device with double layer encapsulation, *Experimental Heat Transfer*, 35:5, 708-725, DOI: [10.1080/08916152.2021.1946208](https://doi.org/10.1080/08916152.2021.1946208)



Experimental Heat Transfer

A Journal of Thermal Energy Generation, Transport, Storage, and Conversion

ISSN: (Print) (Online) Journal homepage: <https://www.tandfonline.com/loi/ueht20>

Thermal management of an interventional medical device with double layer encapsulation

Nu Bich Duyen Do, Erik Andreassen, Stephen Edwardsen, Anders Lifjeld, Knut E. Aasmundtveit, Hoang-Vu Nguyen & Kristin Imenes

To cite this article: Nu Bich Duyen Do, Erik Andreassen, Stephen Edwardsen, Anders Lifjeld, Knut E. Aasmundtveit, Hoang-Vu Nguyen & Kristin Imenes (2022) Thermal management of an interventional medical device with double layer encapsulation, Experimental Heat Transfer, 35:5, 708-725, DOI: [10.1080/08916152.2021.1946208](https://doi.org/10.1080/08916152.2021.1946208)

To link to this article: <https://doi.org/10.1080/08916152.2021.1946208>



© 2021 The Author(s). Published with license by Taylor & Francis Group, LLC.



[View supplementary material](#)



Published online: 05 Jul 2021.



[Submit your article to this journal](#)



Article views: 885



[View related articles](#)



[View Crossmark data](#)



Citing articles: 1 [View citing articles](#)

Thermal management of an interventional medical device with double layer encapsulation

Nu Bich Duyen Do^a, Erik Andreassen^{a,b}, Stephen Edwardsen^c, Anders Lifjeld^c, Knut E. Aasmundtveit^a, Hoang-Vu Nguyen^a, and Kristin Imenes^a

^aDepartment of Microsystems, University of South-Eastern Norway, Borre, Norway; ^bDepartment of Materials and Nanotechnology, SINTEF Industry, Oslo, Norway; ^cGE Vingmed Ultrasound AS, Horten, Norway

ABSTRACT

This paper presents a thermal study of a double-layer encapsulation for an interventional medical device, which operates temporarily inside the human esophagus for cardiac imaging. The surface temperature of test samples, representing the device, was assessed by experiments and numerical simulations. The test samples consisted of a heat source, a heat sink and a double-layer encapsulation consisting of a 3D printed biocompatible polymer (thickness 0.9 mm), with an electroplated Cu inner layer (0, 10, 80 or 150 μm thick). The surface temperature of test samples was measured in a tissue-mimicking thermal phantom at 37°C, with different heat source power levels. Experimental results showed that the maximum steady-state surface temperature could be reduced significantly by a 10 μm thick Cu layer (compared to no Cu layer). Increasing the Cu layer thickness further had a rather small effect, at least for low power levels. The maximum steady-state surface temperature was an exponential function of the Cu layer thickness. Test samples with a Cu electroplated polymer encapsulation and a heat source power of 0.5 W satisfied the maximum temperature limit for thermal safety (43°C) when the Cu layer was thicker than about 80 μm . Simulated surface temperatures were in good agreement with experimental values, for a model using two different thermal contact conductance coefficients (for different materials) for the sample-phantom boundary condition. The simulation model was also used to suggest alternative materials for the outer layer of an encapsulation with a metal inner layer, for reducing the surface temperature.

ARTICLE HISTORY

Received 4 March 2021
Accepted 16 June 2021

KEYWORDS


Interventional medical device; thermal safety; thermal management; heat transfer; metallized polymer encapsulation

Introduction

Ultrasound imaging plays an important role in the diagnosis of cardiovascular diseases. Imaging the heart with a probe inside the esophagus, known as trans-esophageal echocardiography (TEE), has the capability of providing high quality images of the heart. The TEE probe passes through the mouth of the patient into the esophagus, and provides 3D images of the heart in real time [1]. The tip of a TEE probe, referred to as ‘scan head’ in this paper, contains the ultrasound transducer and electronics. The thermal management of a TEE scan head is important with respect to patient safety, since the transducer and the electronics in the scan head generate heat during imaging. Therefore, the temperature distribution on the surface of the scan head must be well controlled to avoid hot spots. According to the standard for the safety and performance of ultrasonic medical diagnostic equipment, IEC 60601-2-37, the temperature of medical devices in contact with the patient for 10 minutes or more

CONTACT Kristin Imenes  Kristin.Imenes@usn.no  University of South-Eastern Norway, Department of Microsystems, Borre, Norway

This article has been republished with minor changes. These changes do not impact the academic content of the article.

 Supplemental data for this article can be accessed on the [publisher's website](#)

© 2021 The Author(s). Published with license by Taylor & Francis Group, LLC.

This is an Open Access article distributed under the terms of the Creative Commons Attribution-NonCommercial-NoDerivatives License (<http://creativecommons.org/licenses/by-nc-nd/4.0/>), which permits non-commercial re-use, distribution, and reproduction in any medium, provided the original work is properly cited, and is not altered, transformed, or built upon in any way.

must not exceed 43°C, to avoid thermal damage to biological tissue [2]. Thermal management is also critical for the performance, lifetime and reliability of the device [3, 4].

Thermal management of medical devices can be based on active solutions (requiring power, e.g. fans for forced convection, pumps for liquid cooling, refrigeration) or passive solutions (e.g. heat sinks, heat spreaders, heat pipes, vapor chambers, phase change materials) [3–5]. Technological advancements enable medical devices to become more compact. Hence, implementing solutions such as heat pipes, vapor chambers, fans, etc. for cooling the device will become more challenging due to the need of space. If the encapsulation of a device can act as an effective heat spreader to dissipate heat generated inside the device, this will be a compact solution.

Encapsulation of medical devices (e.g. TEE scan heads, and other implantable devices such as pacemakers, cochlear implants, implantable neuromuscular micro-stimulators, artificial retina implants) is often composed of two materials [3] to fulfill several functional requirements, not only related to thermal safety, but also electromagnetic interference (EMI) shielding, electrical isolation, and biocompatibility. Firstly, an electrically conductive material (e.g. a metallic material) provides EMI shielding [6] and heat transfer ability [7], due to high electrical and thermal conductivity. Secondly, an electrically insulating material (e.g. a polymeric or ceramic material) is responsible for electrical isolation and biocompatibility. The encapsulation can be built from several separate parts as in Figure 1 (with inner parts made of metals, and outer parts made of polymers or ceramics), or it can be a double-layer structure.

A double-layer encapsulation may be based on a metal part with a polymer or ceramic coating on the outside, or a polymer part metallized on the inside [8, 9]. In the first case, a thin film of a biocompatible polymer or ceramic covers the outside of a metal part. A metal part provides good heat spreading, EMI shielding and mechanical integrity for the encapsulation. However, an encapsulation with metal as the main material may be heavier than what is needed for the function. In addition, applying a uniform and smooth coating of a biocompatible polymer (e.g. parylene coating) or ceramic (e.g. Al_2O_3) on a metal part often requires complicated fabrication processes, such as chemical vapor deposition, or atomic layer deposition [9]. In the second case, the inner surface of a biocompatible polymer part is coated with a thin metal layer. This encapsulation concept utilizes the advantages of polymers, such as low density, easy and flexible processing, high electrical resistivity, and

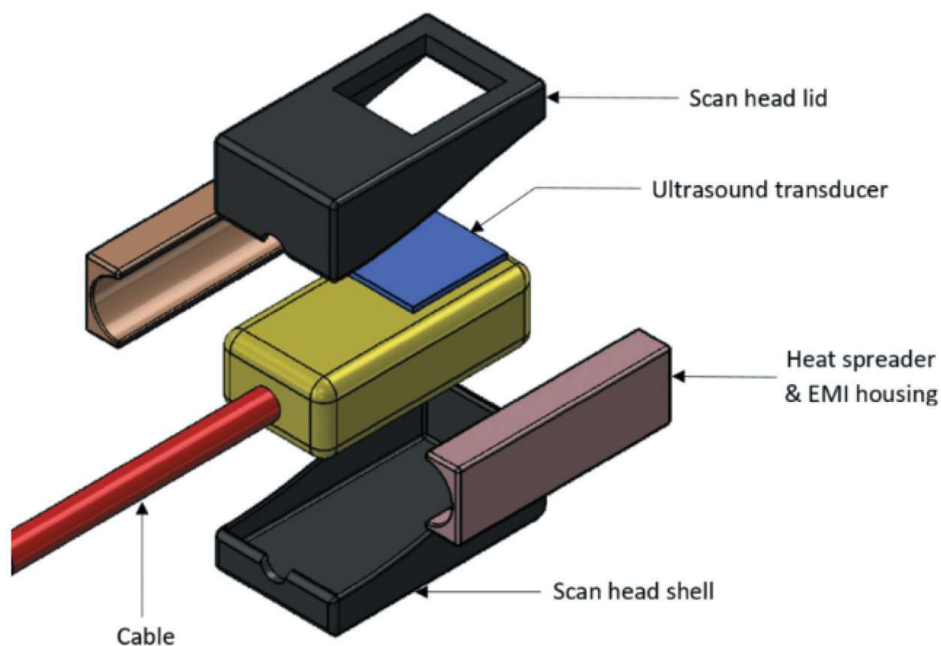


Figure 1. Schematic overview of the encapsulation of a TEE scan head, with metal parts for heat spreading and EMI shielding, and a biocompatible shell for sealing the device.

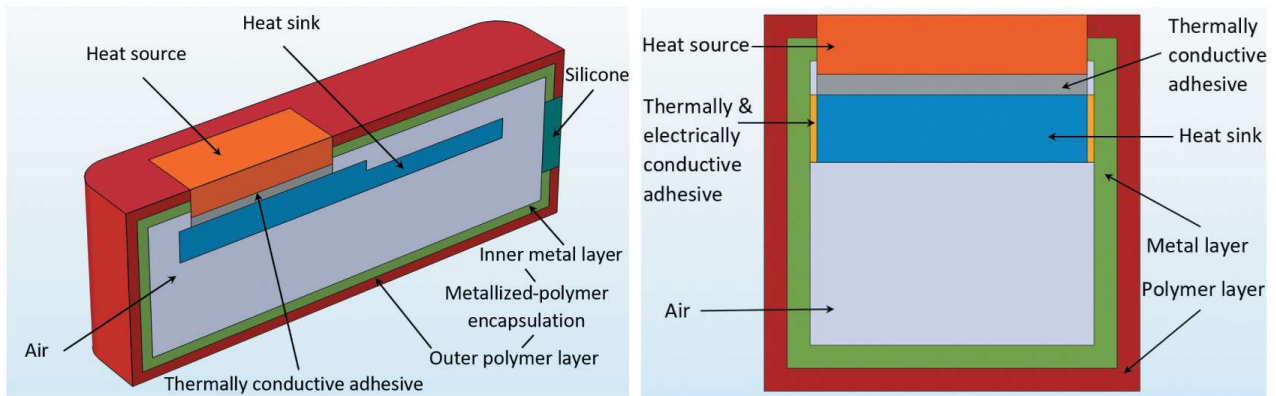


Figure 2. Schematic of cross-sections of the test sample (not drawn to scale), consisting of a heat source, a heat sink and a metallized polymer encapsulation.

low cost [10]. Additionally, a metallized polymer encapsulation can be fabricated by combining well-established industrial methods, such as e.g. injection molding for the polymer part, and metallization by vacuum metallization, electroless plating, electroplating, or even spray painting [4, 11]. A thin metal film (in the micro- or nanometer range) can provide enough EMI shielding for a TEE scan head and other non-radiation emitting medical devices [6, 12, 13]. However, for a metallized polymer encapsulation, the trade-off between metal and polymer thickness needs to be considered, so that the encapsulation can provide sufficient heat spreading, to avoid hot spots on the surface.

In a recent heat transfer simulation study [14], we compared the thermal performances of several TEE scan head encapsulation concepts. Ref [14]. indicated that a metallized polymer encapsulation (as illustrated in Figure 2) can provide good heat spreading, and acceptable maximum surface temperature for low power levels. Hence, this article presents a detailed study of the thermal management of a scan head with a metallized polymer encapsulation. The main thermal requirement for a TEE scan head is that the maximum surface temperature must be below 43°C. In this article we study the effect of metal layer thickness (0, 10, 80, 150 μm of Cu) for a 0.9 mm thick polymer encapsulation, for different heat source power levels (0.5–2.0 W). To the best of our knowledge, this study is the first to investigate the role of a metallized polymer encapsulation for the thermal management of a TEE scan head. In addition, we present simulations that give insight on the heat transfer of the device, and provide a basis for establishing design rules and selecting material alternatives for the outer layer of the metallized encapsulation, in order to further improve the thermal performance of such devices.

Methodology

The sub-section “Experiments” describes the fabrication of the metallized polymer encapsulation, the preparation of test samples, and the temperature measurements in a tissue-mimicking phantom. The sub-section “Simulation of steady-state heat transfer” summarizes the model and approach for simulating the heat transfer of our device with metallized encapsulation. The third sub-section summarizes uncertainties in the experimental measurements and their effects on the parameters obtained by fitting simulations to experiments.

Experiments

Sample preparation

A simplified structure, representing the TEE scan head, was used for the thermal characterization. This test sample (with dimensions of about 37 mm \times 13 mm \times 12 mm) included a heat source, a heat sink and a metallized polymer encapsulation, as illustrated in Figure 2. The heat source represented electronic components generating heat within the scan head, such as the ultrasound transducer and

electronics. The geometry of the heat sink was similar to that in a commercial device. The metallized polymer encapsulation consisted of a thin metal layer deposited on the inner surface of the prefabricated polymer parts.

The encapsulation was fabricated by polymer 3D printing followed by electroplating. Two mating parts (one part corresponding to the half shown to the left in Figure 2) were 3D printed. A UV-cured polymer material was used with the 3D printer Stratasys Objet30 Prime, which is based on PolyJet 3D printing technology [15], belonging to the *material jetting* process category of additive manufacturing [16]. The biocompatible polymer material MED610 (from Stratasys) was selected, because the thermal properties of this material are similar to polymer encapsulation materials commonly used for interventional medical devices (e.g. the thermoplastic materials PEI and PEEK). MED610 also provides adequate electrical isolation and compatibility with biological tissue. A metal layer with desired thickness (10, 80, 150 μm) was deposited on the inner surfaces of the polymer parts (0.9 mm thick) by means of sputtering followed by electroplating. Copper (Cu) was chosen as the electroplating material due to its high thermal conductivity ($400 \text{ W m}^{-1} \text{ K}^{-1}$) [7], its effectiveness in EMI shielding [6], and its low cost. Furthermore, Cu electroplating is a common industrial process [11]. Figure 3a shows one encapsulation part after Cu electroplating. Details about the fabrication of the electroplated encapsulation are presented in the Supplementary Materials.

Based on preliminary electroplating trials, a polymer thickness of 0.9 mm was selected to ensure that the polymer part would not deform as a result of the electroplating. The thinnest Cu layer used in this study was 10 μm . This thickness will provide adequate EMI shielding effectiveness for the TEE scan head [6, 12, 13]. The thickest Cu layer in this study, 150 μm , was chosen in order to have a reasonable time for the electroplating process [11]. The standard deviation of the measured Cu thickness of the electroplated polymer part was about 10% (see Table S2 in the Supplementary Materials). Therefore, three Cu layer thicknesses (10, 80 and 150 μm) were used in this study, to evaluate the effect of metal thickness on the heat transfer.

The electroplated parts were subsequently assembled around a heat source and an aluminum (Al) heat sink to make a test sample representing a TEE scan head, as illustrated in Figure 2 and Figure 3. The heat source, a commercial resistive heating element (metal ceramic heater from Heat Scientific), was bonded to the heat sink using a thermally conductive adhesive (Epotek T7109-19), which was cured at 80°C for 2 hours. Two sides of the Al heat sink were attached to the Cu surfaces of the two encapsulation parts by thin layers of a thermally and electrically conductive adhesive (Epotek EJ2189-LV), which was cured at 40°C for 9 hours. This curing condition differed from the recommendation of the manufacturer (150°C , 1 hour) [17], in order to avoid thermally induced distortion of the polymer parts [18]. The hole for the electrical wires at the tail of the sample, and the seams between two mating electroplated parts, were sealed with a medical silicone, cured at 40°C for 6 hours. The remaining volume inside the sample (containing electronic components and cables in a typical scan head) was empty (air) for simplifying the simulations and representing a worst-case scenario with regards to heat transfer.

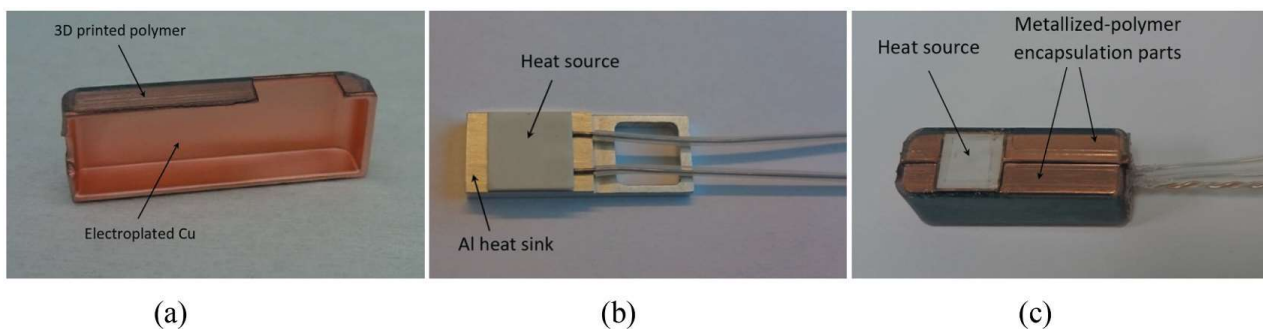


Figure 3. (a) Cu electroplated polymer part; (b) Heat source (resistive heating element) bonded to an Al heat sink; (c) Test sample after assembly.

Temperature measurements

The surface temperature of the test samples was measured for 80 minutes (about twice the duration of a common TEE exam [2, 19]), when placed in a tissue-mimicking thermal phantom (National Physical Laboratory, England), stabilized at around 37°C, see Figure 4. Test samples with 0, 10, 80 and 150 μm thick Cu layers were tested. The effect of the heat source power was also considered.

The thermal phantom is cylindrical with diameter 11 cm and height 11.5 cm. It is made of a tissue-mimicking material (TMM), prepared according to the standard IEC 60601-2-37. The TMM contains agar, glycerol, water and inorganic particles (e.g. SiC, Al₂O₃). Such thermal phantoms are commonly used for measuring ultrasound transducer surface temperature [2, 20, 21]. The acoustic and thermal properties are comparable to those of soft tissues [21]. Details about components and properties of the thermal phantom are given in ref [22]. When performing the temperature measurements in this study, the glycerol solution (which the phantom is stored in to prevent it from drying out) was removed to imitate the human esophagus environment. The test sample with attached thermocouples was carefully inserted into a cavity in the phantom (Figure 4), to avoid damaging the fragile phantom material. Note that some areas of the test sample surface were not in contact with the phantom, due to the thermocouples, the wires and the Kapton tape fixing the thermocouples (see Figure 5). The effect of

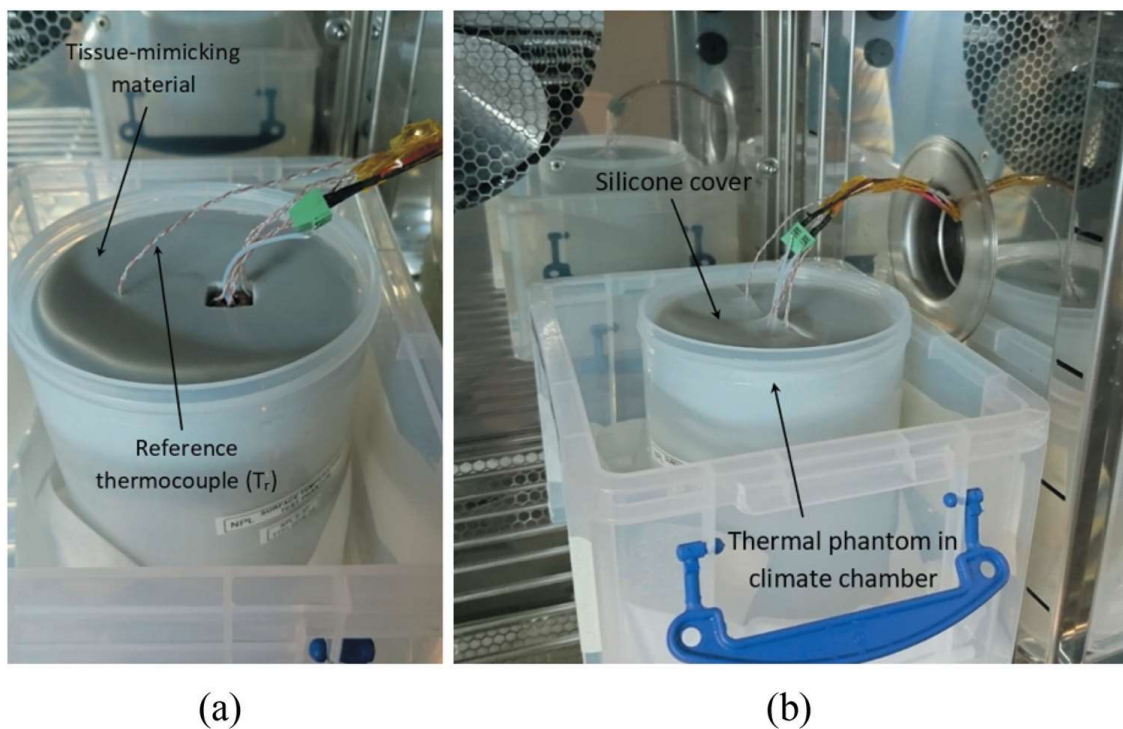


Figure 4. Test sample placed in a tissue-mimicking thermal phantom in a climate chamber.

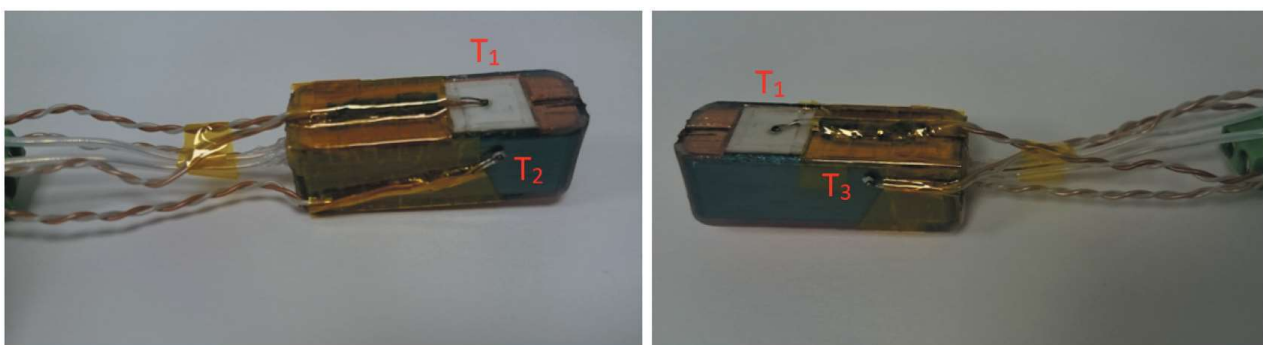


Figure 5. Thermocouples (T₁, T₂, T₃) on the surface of the test sample.

this is that the measured temperatures will be on the conservative side, due to the lower heat transfer to the phantom. However, also for a real scan head some surface areas may not be in contact with the tissue.

Before the test, the sample was kept in the phantom cavity for about 3 hours to stabilize at 37°C in the climate chamber. The end of the sample with the wires is facing up in the phantom (see [Figure 4a](#)), and this surface is not in contact with the phantom. The top surface of the phantom was covered by a sheet of silicone material (0.5 mm thick) during testing, as shown in [Figure 4b](#). This was for preventing the phantom material from drying out, and reducing the effect of air flow due to the fan in the climate chamber.

Type T thermocouples were positioned at three different locations on the test sample ([Figure 5](#)), in order to determine the maximum surface temperature during the test. Thermocouple T_1 is placed on the surface of the exposed heat source; thermocouple T_2 is placed on the vertical surface, near the heat source; thermocouple T_3 is placed on the other vertical surface, a bit further away from the heat source. The thermocouples were in contact with the sample surface via a thin layer of a thermal paste (Arctic MX-2), and they were fixed by Kapton tape. Note that these thermocouples measure a mixture of the sample surface temperature and the phantom temperature. However, the temperature measured at the heat source surface is dominated by the heat source, not the phantom, due to the heat source having the highest thermal effusivity. The temperature of the thermal phantom was also measured with a thermocouple (T_r in [Figure 4a](#)). The distance between the thermocouple T_r and the wall of the cavity in the thermal phantom was about 3.8 cm.

The thermocouples were logged (TC08 and PicoLog 6, PicoTech) every 10 s for 80 minutes. The heat source was connected to a power supply (R&S NGE100, Rohde & Schwartz), and four different power levels (0.5, 1.0, 1.5, 2.0 W) were used in the measurements. Five samples were fabricated and tested; two with Cu thickness 10 μm , one with 80 μm , one with 150 μm and one without Cu. For each sample, the temperature measurements were repeated twice (at all power levels), with 1 hour in between to let the sample return to 37°C.

Simulation of steady-state heat transfer

A simulation model, representing the experimental test sample ([Figure 2](#)) in the thermal phantom, was defined in COMSOL Multiphysics 5.3a. The heat source was modeled with uniform volumetric heat generation. The thermal conductivities of the materials in the model are listed in [Table 1](#). The thermal contacts between the components in the scan head were assumed to be perfect. The basis for this assumption is that metal-polymer thermal contact conductance (TCC) coefficients are on the order of $10^8 \text{ Wm}^{-2} \text{ K}^{-1}$ [30] and metal-metal TCC coefficients are even higher [30], and these conductances are

Table 1. Material properties of all components in the simulation model.

Component	Material	Thermal conductivity k ($\text{Wm}^{-1} \text{ K}^{-1}$)
Heat source	Metal ceramic heater [23] (Al_2O_3 and W)	20
Heat sink	Al alloy 6082 [24]	180
Adhesive between heat source and heat sink	Thermally conductive adhesive (Epotek T7109-19) [25]	1.3
Adhesive between heat sink and encapsulation	Thermally and electrically conductive adhesive (Epotek EJ2189-LV) [17]	2.5
Inner layer of encapsulation	Electroplated Cu [26]	380
Outer layer of encapsulation	Polymer material (Stratasys MED610)	0.2 ^a
Coverage of the hole for the electrical wires	Medical silicone	0.2 ^a
Remaining volume inside the sample	Air [27]	$k(T)$ via COMSOL's material library

^aThermal conductivity selected based on common values from references [28, 29].

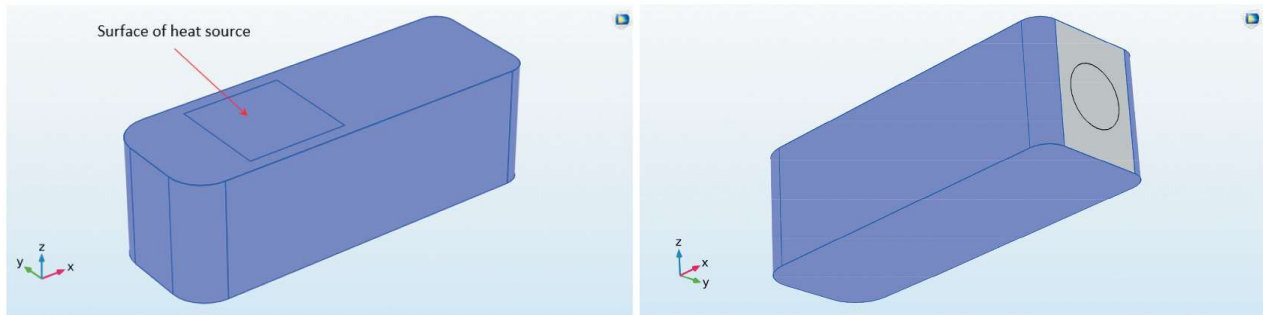


Figure 6. Illustration of thermal contact surfaces (in blue) for which Equation 1 was applied.

much larger than the conductance of the polymer layer in our model ($0.2 \text{ Wm}^{-1} \text{ K}^{-1} / 0.9 \text{ mm} \sim 10^2 \text{ Wm}^{-2} \text{ K}^{-1}$). For the outer surfaces of the scan head (in contact with the thermal phantom), a heat flux boundary condition with a TCC coefficient was applied:

$$q_0 = h_c(T_{ext} - T) \quad (1)$$

where h_c is the TCC coefficient; T_{ext} is the temperature of the phantom, (assumed to be constant, 37°C in our case); T is the temperature of the scan head surface; q_0 is the heat flux. The TCC coefficient is the inverse of the thermal contact resistance [31, 32]. Values for TCC coefficients were determined by comparing the simulated and measured steady-state surface temperatures, as detailed in the [section 3.2 Calibration of the simulation model](#).

The TCC coefficients mentioned above were used for the exterior of the scan head except the “tail” of the scan head (gray surface in [Figure 6](#)). In the experiment, this tail sees a small volume of air, i.e. the space between the encapsulation and the silicone lid covering the phantom’s cavity, see [Figure 4](#). The heat transfer coefficient for still air is often in the range $(2\text{--}25) \text{ Wm}^{-2} \text{ K}^{-1}$ [7]. A value of $15 \text{ Wm}^{-2} \text{ K}^{-1}$ was used in some simulations. However, including such a heat transfer coefficient for the tail of the scan head had no significant effect on the simulated maximum surface temperature (occurring at the un-encapsulated heat source). Hence, this extra heat transfer coefficient was not used in the results presented below.

The 3D model was meshed using free tetrahedral elements, see [Figure 7](#). The mesh had one element across the thin layers in the model (Cu and adhesive layers). An initial check with finer meshes (two elements across the thin layers, as well as an overall finer mesh with five times the number of elements) gave the same value for the maximum surface temperature, within 0.1 K. Hence, the mesh was

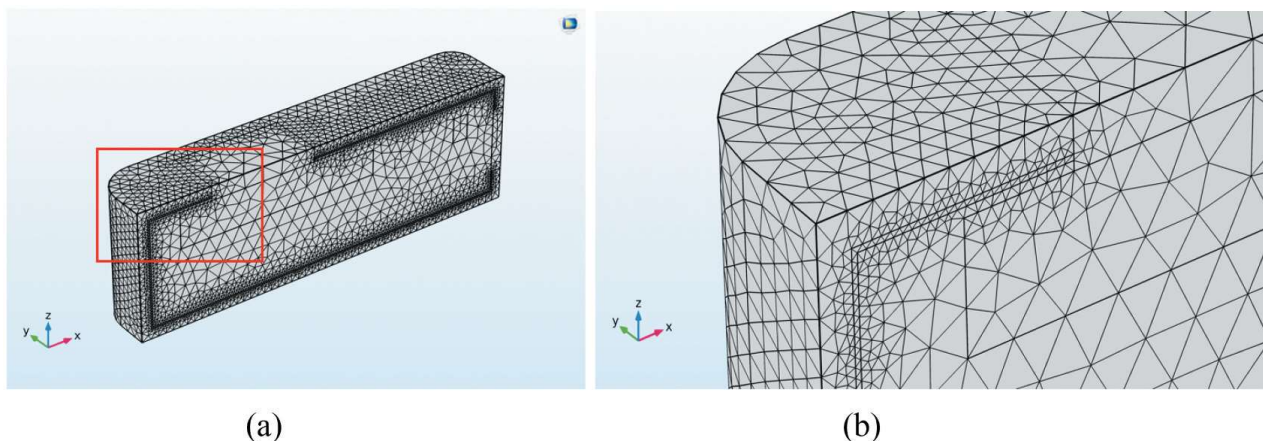


Figure 7. (a) Mesh on one half of the model, with a 0.9 mm thick polymer layer and a $150 \mu\text{m}$ thick Cu layer; (b) a zoom-in corresponding to the red rectangle in (a).

optimized with regard to simulation accuracy and calculation time. Details about the mesh are given in Table S3 in the Supplementary Materials.

Uncertainties and error calculations

What are the dominating uncertainties in the experimental measurements and how do these affect the parameters obtained by fitting simulations to experiments? Regarding the Cu thickness, the main source of uncertainty is the variation in Cu thickness over the sample, due to the deposition method. The Cu thickness was measured at 10–15 points on three cross-sections of the sample (altogether 40 points per sample, see Figure S1 in Supplementary materials). The average values were close to the nominal values ($\pm 1 \mu\text{m}$). The relative standard deviations were about 10%, i.e. for the $10 \mu\text{m}$ the standard deviation was $\pm 1 \mu\text{m}$. Details are given in Table S2 in Supplementary materials. The relative uncertainty in the polymer thickness is much smaller than that of the Cu thickness.

The power supplied to the test sample has an estimated uncertainty of about 1–2%, when the power is in the range of (0.5–2) W. This uncertainty estimate was determined using the uncertainty propagation law [33], based on the known uncertainties of voltage and current for the power supply used.

The variation in ΔT between repeated tests (with the same sample, not removed from the phantom, and with the same thermocouples mounted), was within the accuracy of the thermocouple used ($\pm 0.5^\circ\text{C}$); and that between two samples fabricated with the same nominal Cu thickness was within 1°C . Therefore, only measurements for one sample for each Cu thickness are presented in the Results section, as the example in Figure 8.

For comparison with simulations, steady-state temperatures of T_1 were estimated by fitting functions to the measured temperature transients of the 80 minute tests (as shown in Figure 8). Several functions, e.g. a power function, gave good fits to the experimental data. The difference between extrapolated values of the fitted function ($t \rightarrow \infty$) and experimental values at 80 minutes were small (lower than 0.3°C). Hence, the experimental values of T_1 at 80 minutes were used for calculating ΔT , and calibrating the simulation model.

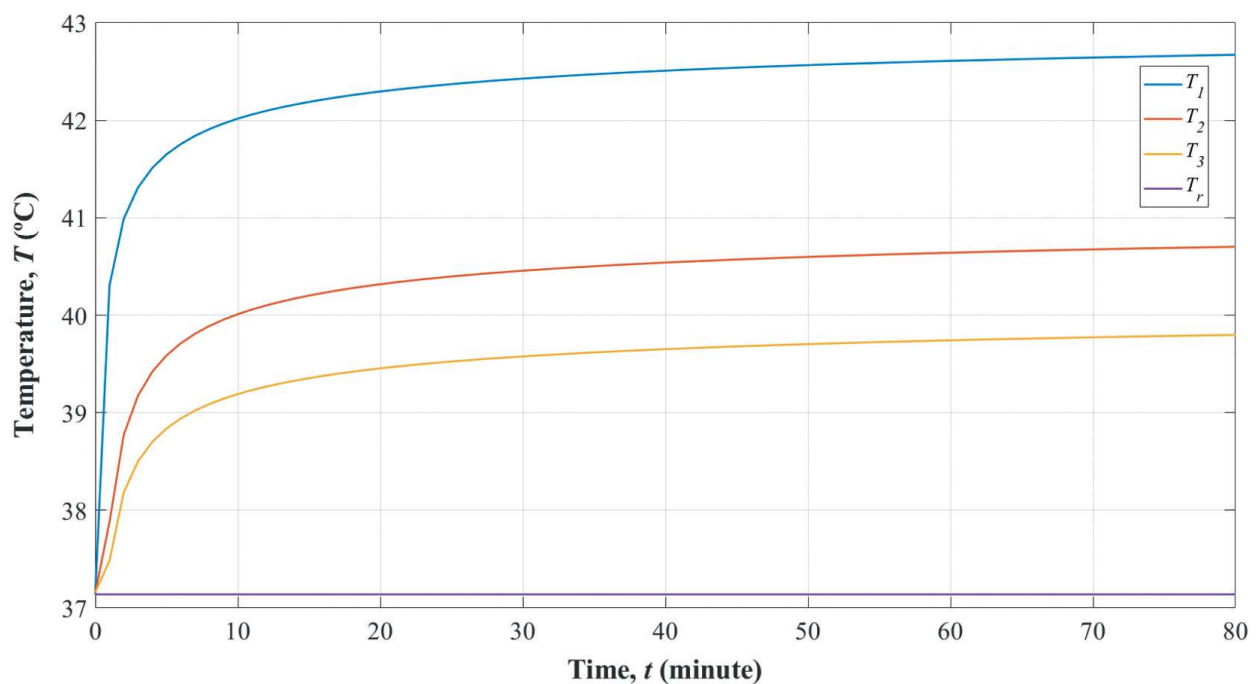


Figure 8. Measured temperatures for a test sample with polymer thickness 0.9 mm, Cu thickness $150 \mu\text{m}$, and heat source power 0.5 W. T_1 , T_2 , T_3 are surface temperatures measured at different positions (shown in Figure 5), and T_r is the temperature measured in the thermal phantom (shown in Figure 4).

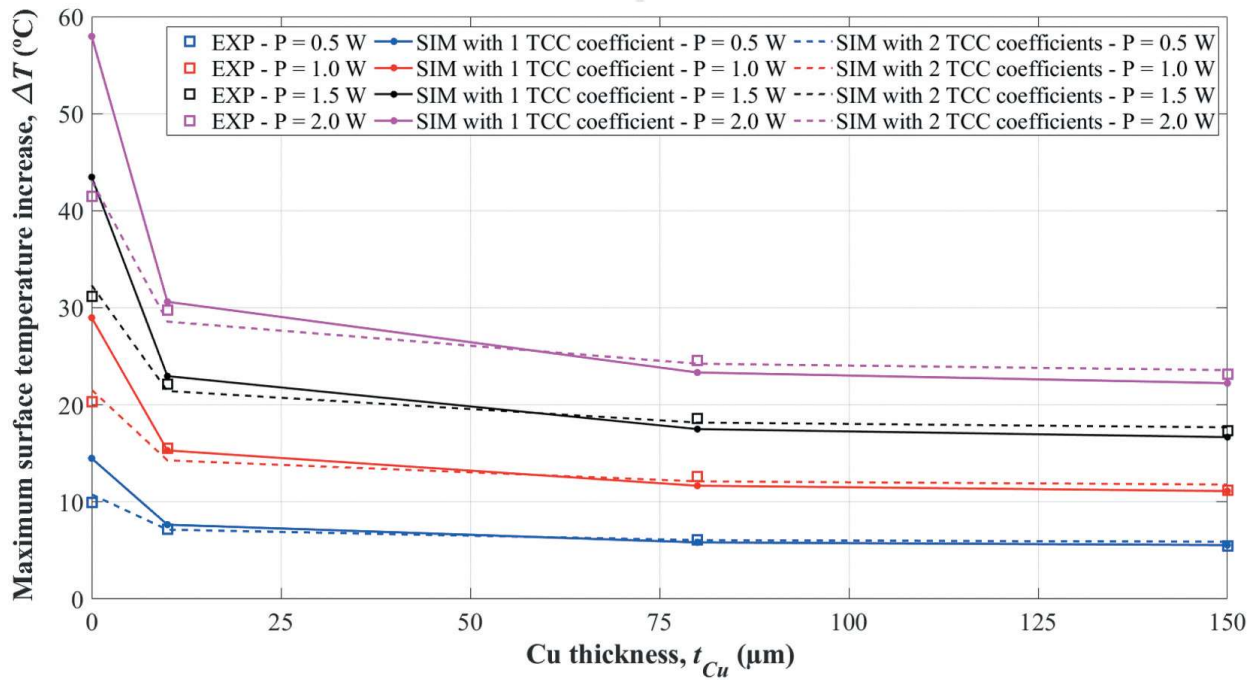


Figure 9. Simulated (SIM) and experimental (EXP) results for polymer encapsulations (0.9 mm) with 0, 10, 80 and 150 μm thick Cu layers, at different power levels. Experimental data are shown as squares, simulated data based on one TCC coefficient ($h_c = 75 \text{ Wm}^{-2}\text{K}^{-1}$) are shown as solid lines, and simulated data based on two TCC coefficients ($h_{c1} = 250 \text{ Wm}^{-2}\text{K}^{-1}$ and $h_{c2} = 46 \text{ Wm}^{-2}\text{K}^{-1}$) are shown as dashed lines.

When calibrating the simulation model by adjusting the two TCC coefficients (as in Figure 9), the uncertainties of the TCC coefficients h_{c1} and h_{c2} are $12 \text{ Wm}^{-2}\text{K}^{-1}$ and $4 \text{ Wm}^{-2}\text{K}^{-1}$, respectively. This is an estimate based on the dominating experimental uncertainties given above, as well as a requirement that systematic errors (differences between experimental and simulated ΔT) vs. Cu thickness should be minimized.

Results and discussion

Experimental results

As described in the introduction, the surface temperature limit for medical devices in contact with the human body for 10 minutes or more is 43°C . Hence, our study focuses on the maximum surface temperature, and how it varies with Cu layer thickness (0, 10, 80, 150 μm) and heat source power (0.5, 1.0, 1.5, 2.0 W).

Figure 8 shows temperature measurements for a case with 0.5 W power, and an encapsulation with polymer thickness 0.9 mm and Cu thickness 150 μm . After about one hour, the system is close to steady state. As expected, the maximum surface temperature of the test sample appears on the surface of the heat source (which is exposed, not encapsulated), shown as T_1 in Figure 5 and Figure 8. On the vertical exterior surfaces of the encapsulation, thermocouple T_2 shows a higher temperature than thermocouple T_3 . This is due to T_2 being closer to the heat source of the test sample, as shown in Figure 5.

We define ΔT as the difference between the maximum scan head surface temperature (T_1) and the temperature of thermal phantom (T_r), at steady state. Relationships between the measured ΔT and the Cu layer thickness (t_{Cu}), for different power levels (P), are shown in Figure 9 and Figure 10. ΔT increases linearly with increasing power because we consider steady state temperatures. Furthermore, ΔT decreases with increasing Cu thickness (better heat spreading), following an exponential function, as shown in Figure 10. The experimental results for this simplified test sample (Figure 9 and Figure 10)

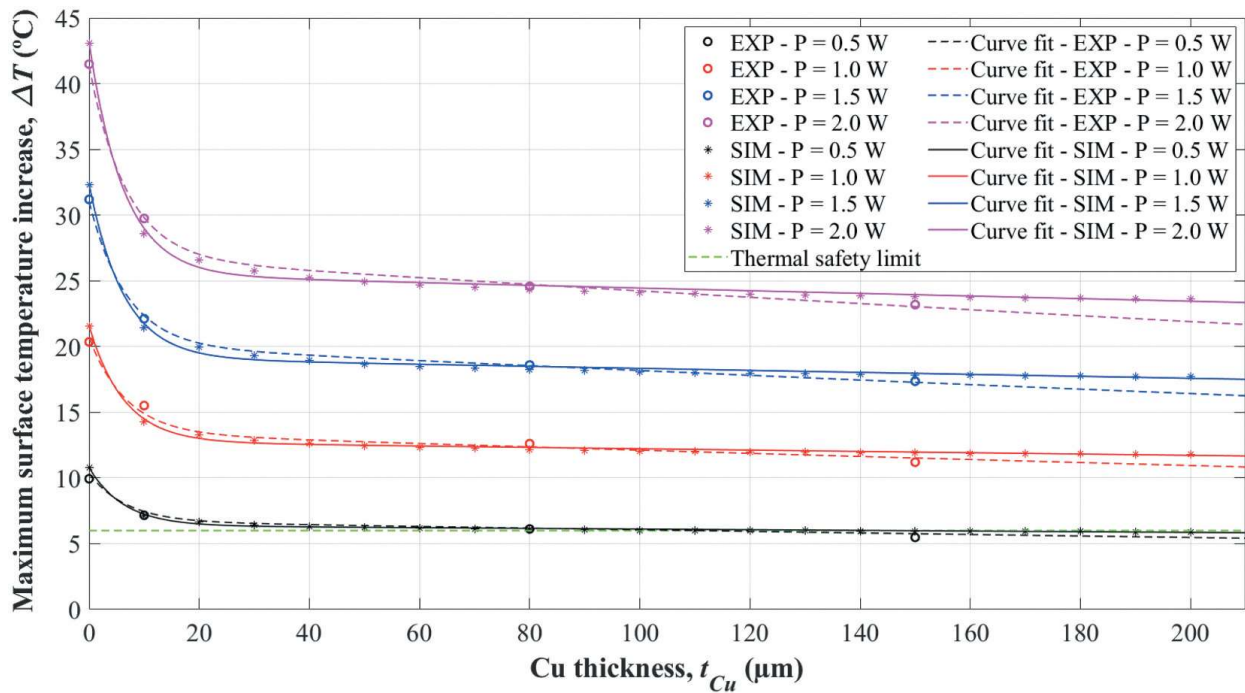


Figure 10. The relationship between the Cu layer thickness (t_{Cu}) and the increase in surface temperature above the phantom temperature at steady state (ΔT), for four different power levels (P). Dashed lines are fits (based on Equation 2) to experimental data (EXP, open circles), while solid lines are corresponding fits to simulations (SIM, asterisks). The thermal safety limit corresponds to $\Delta T = 6^\circ\text{C}$ (green dashed line).

show which combinations of Cu layer thickness and power that satisfy the temperature criterion ($T_1 < 43^\circ\text{C}$, i.e. $\Delta T < 6^\circ\text{C}$). For the examined combinations and a power level of 0.5 W, it is satisfied when the Cu layer is thicker than about 80 μm . Figure 10 also shows that increasing the Cu thickness from 80 to 150 μm has a small effect on ΔT . For a power level of 0.5 W, a Cu layer thickness around 100 μm (on a 0.9 mm thick polymer encapsulation) may be a good trade-off between thermal performance and cost/time for the metallization process.

Calibration of the simulation model

With the thermal conductivities in Table 1, the simulation model was first calibrated with the experimental data (ΔT vs. Cu thickness and heat source power, i.e. 16 data points) by adjusting a single TCC coefficient (h_c). With a h_c value of $75 \text{ W m}^{-2} \text{ K}^{-1}$, the simulated ΔT values agreed well with the experimental data of samples having a non-zero Cu layer thickness. However, the ΔT values of the samples without Cu were grossly overestimated, as shown in Figure 9 (solid lines). Alternatively, a h_c value could be found so that ΔT values for zero Cu samples agreed with experiments, but then the ΔT values for non-zero Cu samples were underestimated. Hence, the balance between the two main thermal flow paths, “directly” through the heat source and via the encapsulation, was obviously poorly modeled. To try to obtain a good agreement for the entire dataset, the values for the thermal conductivities of the parts in the scan head were varied (within reasonable limits), while also varying the TCC coefficient. However, the overprediction mentioned above remained gross. A situation with only random errors (due to unavoidable uncertainties in the experimental values), and no systematic errors related to the presence of a Cu layer or not, could not be obtained. Furthermore, the areas for thermal contact with the phantom, on different surfaces of the scan head, were also varied, in an attempt to be closer to the experimental situation (some areas shielded from contact by wires, etc.). However, the overall prediction remained poor, with a systematic error related to the presence of a Cu layer, and not only random errors.

As a next step in trying to improve the prediction, we allowed for having two different TCC coefficients; h_{c1} for the heat source (modeled as Al_2O_3) surface and h_{c2} for the remainder of the scan head surface (the polymer encapsulation). A TCC coefficient accounts for effects of e.g. surface roughness at the interface, but it is evidently also related to bulk properties of the contacting materials, such as the thermal conductivity [32, 34]. Hence, we argue that the heat source and the polymer encapsulation, with thermal conductivities differing by a factor 100 and also different surface roughnesses, can have different TCC coefficients. However, these coefficients also effectively account for differences in contact area/pressure toward the thermal phantom.

A good overall fit was achieved with h_{c1} and h_{c2} set to $250 \text{ Wm}^{-2} \text{ K}^{-1}$ and $46 \text{ Wm}^{-2} \text{ K}^{-1}$, respectively, see Figure 9 and Figure 10, and these coefficients were used in all simulations reported in Figure 10 and later. However, note that the simulations underpredict the (small) reduction in ΔT when increasing the Cu thickness from 80 to 150 μm , see Figure 10. The remaining, rather small, difference between simulated and experimental data can be explained by various factors. One factor could be in the experimental data themselves. As mentioned in the experimental section, the thermocouple on the heat source measures a mix of the sample surface temperature and the phantom temperature. The mixing ratio may depend on the temperature, hence, e.g. the Cu layer thickness. Another factor could be that the idealized simulation model did not take into consideration the variation in the Cu layer thickness (about 10%, as presented in Table S2 in the Supplementary Materials). In addition, the thickness of the adhesive layers in the test samples may vary somewhat from sample to sample due to the manual assembly, but a constant thickness is assumed in the simulation model.

It is relevant to compare the TCC coefficients found above with the convective heat transfer coefficients for the human esophagus determined experimentally by Liao et al. [35]. Liao et al. investigated the heat transfer properties of the esophagus wall, as an indication of segmental blood flow changes during mechanical distension. The device used in their set-up was an ultrasound probe with a polyurethane bag attached to its tip. They found the heat transfer coefficient to be in the range $100\text{--}220 \text{ Wm}^{-2} \text{ K}^{-1}$, depending on the blood flow rate as affected by distension temperature. We interpret their results to indicate that the heat transfer coefficient of the esophagus wall was around $150 \text{ Wm}^{-2} \text{ K}^{-1}$ at body temperature.

Simulation results

The simulated ΔT values (using the two TCC coefficients given in the preceding Section 3.2 Calibration of the simulation model), as well as the experimental data, were well represented by an exponential function:

$$\Delta T = (ae^{bt_{Cu}} + ce^{dt_{Cu}})P \quad (2)$$

where a , b , c , d are fitting parameters, t_{Cu} is the Cu thickness and P is the heat source power. Details about the fitting parameters for the simulated ΔT and the experimental ΔT are presented in the Supplementary Materials. Figure 10 shows the maximum surface temperature increase as a function of Cu thickness at different power levels.

The simulation model can be used to visualize the temperature distributions. An example is shown in Figure 11. In this case the encapsulation has a Cu layer thickness of 150 μm , and the heat source power is 0.5 W. The surface temperature varies from 39.9°C to 42.9°C. The maximum surface temperature occurs at the surface of the heat source, which is not encapsulated. The maximum surface temperature here satisfies the safety requirement; i.e. no spots on the surface are hotter than 43°C.

Figure 12 shows simulated temperature distributions for different encapsulations, with Cu (a) and without Cu (b and c). There is a clear difference between encapsulations with and without Cu, regarding the balance between the two main heat flow paths to the phantom; the main path through

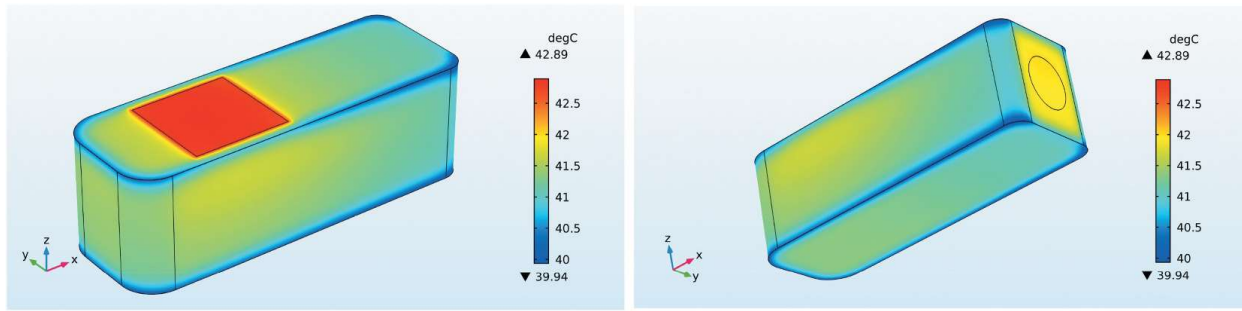
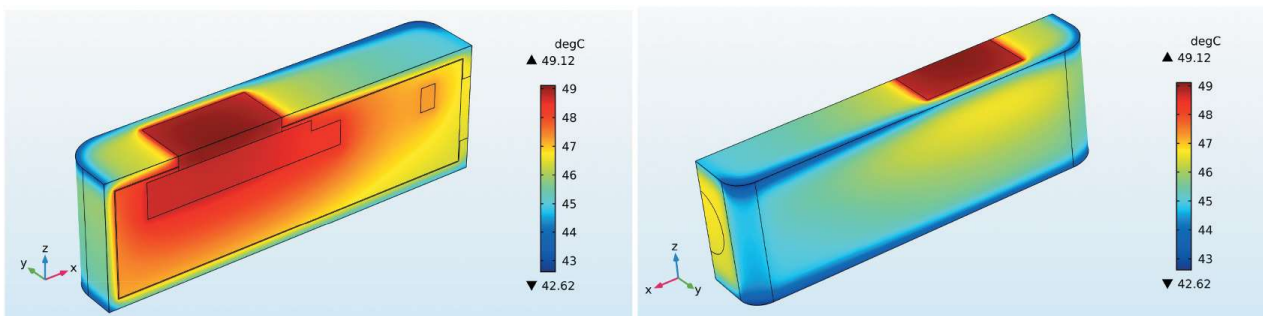
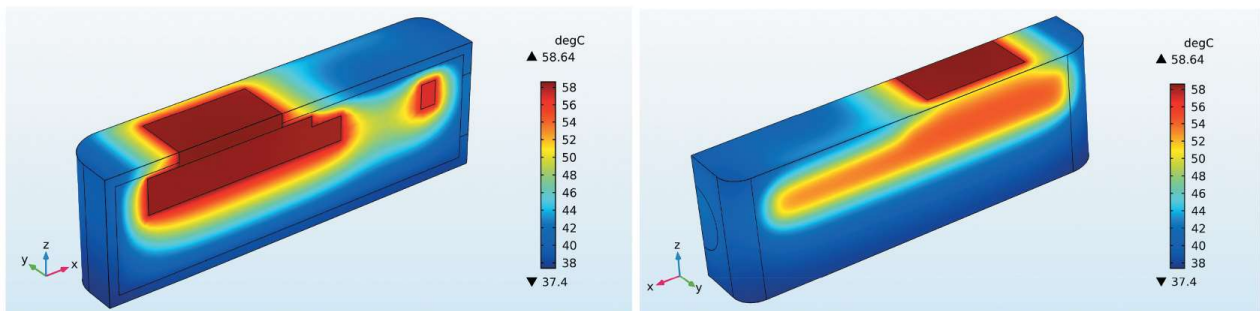


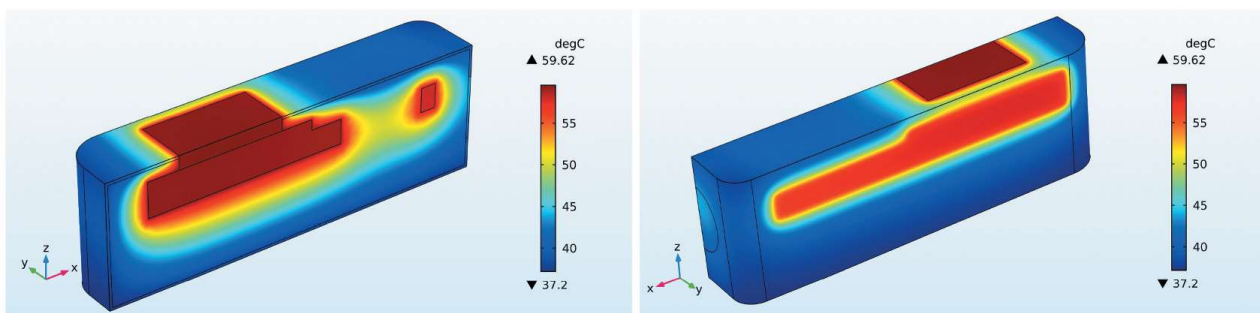
Figure 11. Simulated surface temperature. The outer polymer thickness is 0.9 mm, the inner Cu layer is 150 μm thick, and the heat source power is 0.5 W.



(a)



(b)



(c)

Figure 12. Simulated temperature distributions for three different encapsulations (1 W in all cases) (a) 0.9 mm thick polymer layer and 80 μm thick Cu layer (temperature range: 42.6–49.1°C); (b) 0.9 mm thick polymer layer and no Cu layer (temperature range: 37.4–58.6°C); (c) 0.25 mm thick polymer layer and no Cu layer (temperature range: 37.2–59.6°C).

the heat source “window” (with area 1 cm^2) and the secondary path through the polymer encapsulation. The secondary flow path is more pronounced when the encapsulation has a Cu layer, due to better heat spreading. The balance between these two paths can also be assessed by the relative heat flow through the heat source window. This relative heat flow is 30% in Figure 12a, and 54% in

Figure 12b. The heat flux is almost constant over this window. Hence, a plot of relative heat flow vs. Cu thickness is similar to a plot of ΔT vs. Cu thickness. (However, the relative heat flow is independent of power level, since we consider the steady state.)

Figure 13 shows the simulated relationship between the polymer layer thickness (t_{po}) and the maximum surface temperature increase (ΔT), for different Cu thickness, at a power level of 0.5 W. Note that the simulation model was parameterized with the outer dimensions fixed, and a reduction in polymer thickness had to be compensated for by an increase in the thickness of the adhesive layer (between the Al heat sink and the encapsulation). However, this had no effect on the trends in this figure. As a check of this, some simulations were performed in which the thermal conductivity of the adhesive was increased from its nominal value ($2.5 \text{ Wm}^{-1}\text{K}^{-1}$) to the value of the Al heat sink ($180 \text{ Wm}^{-1}\text{K}^{-1}$). Results from these simulations are shown as a dashed green line. For a given Cu thickness, ΔT increases with increasing polymer thickness, due to the increasing thermal insulation of the thermal flow path through the encapsulation. However, the effect of the polymer thickness is small in this interval (0.25–1 mm), and it decreases with decreasing Cu thickness. For a very thin Cu layer (e.g. $2 \mu\text{m}$ Cu in **Figure 13**), the effect of polymer thickness on ΔT is negligible. When there is no Cu layer, ΔT decreases slightly with increasing polymer thickness (also seen in **Figure 12c** vs. **Figure 12b**), due to the increased heat spreading in the (thicker) polymer layer, dominating over the increased thermal insulation. When the polymer thickness is increased, the increased in-plane heat spreading in the polymer layer (typically occurring near the heat source and the heat sink) prevails over the reduced heat flow perpendicular to the polymer wall.

The simulations show that this scan head design and encapsulation concept satisfies the thermal criterion ($\Delta T < 6^\circ\text{C}$) for power levels up to about 0.5 W. In order to use a Cu plated encapsulation at higher power levels, the polymer must be replaced by a material with higher thermal conductivity. Our simulation model can be used to evaluate the effect of increased thermal conductivity of the outer layer. However, the model is probably not valid for materials

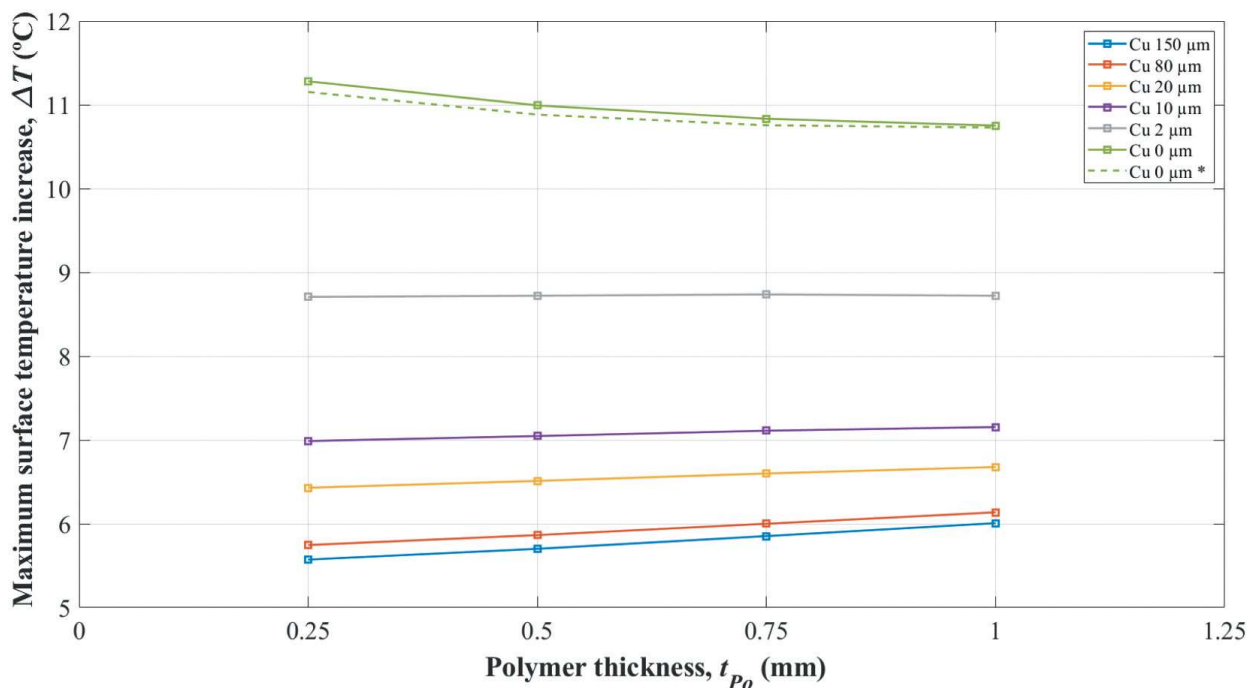


Figure 13. Simulated effect of polymer layer thickness (t_{po}) on the surface temperature increase (ΔT) for different Cu layer thicknesses. The heat source power was 0.5 W in these simulations. The dashed green line represents a case in which the thermal conductivity of the adhesive (between the Al heat sink and the encapsulation) was increased from its nominal value ($2.5 \text{ Wm}^{-1}\text{K}^{-1}$) to the value of the Al heat sink ($180 \text{ Wm}^{-1}\text{K}^{-1}$).

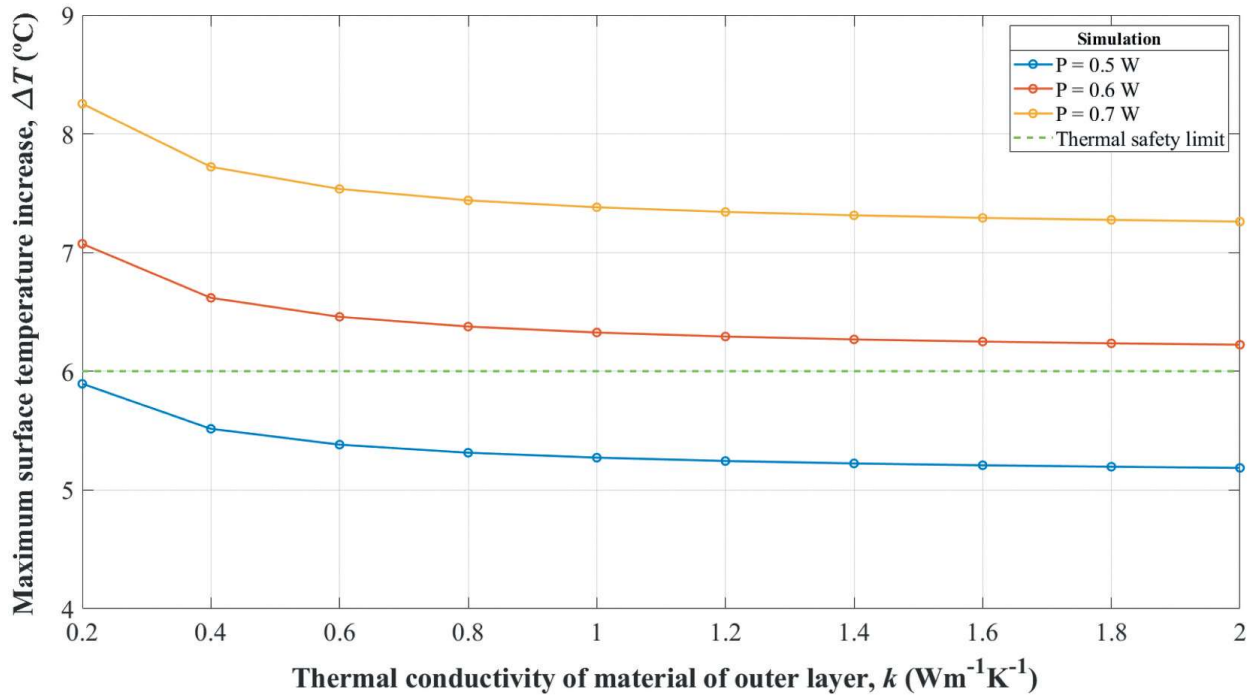


Figure 14. Simulated effect of the thermal conductivity (k) of the outer layer material on the maximum surface temperature increase (ΔT), for different power levels. The polymer outer layer is 0.9 mm thick, and the Cu inner layer is 150 μm thick.

with much higher thermal conductivity than the one used in the calibration. Figure 14 shows the simulated effect of the thermal conductivity (k) of the outer layer material on the maximum surface temperature increase (ΔT), for different power levels (P). Increasing the thermal conductivity from 0.2 to 2 $\text{Wm}^{-1}\text{K}^{-1}$ reduces ΔT by about 1°C.

Simulations with extreme values for the polymer thermal conductivity can be used to assess the thermal limits of a scan head design. If the polymer has zero thermal conductivity, all the heat transfer to the phantom will be through the 1 cm^2 “window” of the heat source, with or without a Cu layer on the polymer part. As an example (see Figure S2 in the Supplementary Materials), for a power of 1 W this would give a ΔT value of 40.0°C. In the other limit, for very high polymer thermal conductivities, ΔT approaches about 9.8°C (for 1 W power), with or without Cu. This corresponds to a heat flow fraction through the heat source window of about 0.25. This is then a value characterizing this particular design. Hence, with 1 W power, the temperature criterion, $\Delta T \leq 6^\circ\text{C}$, can not be reached with this design.

Material selection for the outer layer

This metallized encapsulation can only be used at power levels above 0.5 W if the polymer of the Cu electroplated encapsulation is replaced by a material with higher thermal conductivity. Polymer-based composites with fillers with high thermal conductivity can be taken into consideration for the outer layer of a metallized encapsulation. Such a composite should also fulfill other safety requirements, such as electrical isolation and biocompatibility. An advantage of using a polymer-based composite is the compatibility of this material type with well-developed packaging techniques, such as molding processes (e.g. injection molding, transfer molding, or compression molding) [4]. Composites based on a biocompatible polymer matrix and thermally conductive and electrically insulating fillers are promising candidates. The polymer could be a thermoset (e.g. biocompatible epoxy or silicone) or a thermoplastic (e.g. PEI or PEEK) [29]. Common thermally conductive and electrically insulating fillers are ceramic fillers; for example, metal oxides (e.g. alumina (Al_2O_3) or quartz (crystalline SiO_2)), or non-oxide fillers (e.g. aluminum nitride (AlN), boron nitride (BN), silicon nitride (Si_3N_4)) [10].

Ohashi et al. [36] successfully prepared a polymer composite with thermal conductivity of $8.2 \text{ Wm}^{-1}\text{K}^{-1}$ from epoxy with 74 vol% AlN. The composite was applied in fabricating encapsulants for dissipating the heat generated in electronic devices. Thermal conductivity of $21.3 \text{ Wm}^{-1}\text{K}^{-1}$ was achieved for an epoxy/BN composite in a study by Zhu et al. [37]. Kusunose et al. [38] measured a thermal conductivity of $9.2 \text{ Wm}^{-1}\text{K}^{-1}$ for an epoxy composite with 60 vol% Si_3N_4 nanowires. Biocompatible ceramics can also be considered as outer layer materials for the metallized encapsulation. The outer encapsulation can e.g. be fabricated by powder injection molding using AlN ($100\text{--}300 \text{ Wm}^{-1}\text{K}^{-1}$) [10, 39, 40].

Conclusions

In this paper, the thermal management of a simplified trans-esophageal echocardiography (TEE) scan head was studied by experimental work and numerical simulations. Scan head test samples with a metallized polymer encapsulation were fabricated. The encapsulation consisted of a 3D printed polymer part with a Cu layer electroplated on the inside. The focus of the study was to investigate encapsulation parameters, with regards to the requirement that the maximum surface temperature of the scan head (in contact with human tissue) must be below 43°C .

Samples with encapsulations having a 0.9 mm thick polymer outer layer, and an electroplated Cu inner layer (0, 10, 80 or 150 μm thick), were tested with different power levels (0.5–2.0 W) supplied to the heat source in the sample. The heat source was connected to some sections of the encapsulation via an aluminum heat sink. The surface temperature of the test sample was measured in a tissue mimicking thermal phantom, which was stabilized at around 37°C (human body temperature) in a climate chamber.

Experimental results showed that the maximum steady-state surface temperature could be reduced significantly by a 10 μm thick Cu layer (compared to no Cu layer). Increasing the Cu layer thickness further had a rather small effect, at least for low power levels. The maximum steady-state surface temperature was an exponential function of the Cu layer thickness. As expected for this steady-state temperature, it increased linearly with increasing power supplied to the sample. Test samples with a Cu electroplated polymer encapsulation and a heat source power of 0.5 W satisfied the maximum temperature requirement ($< 43^\circ\text{C}$) when the Cu layer was thicker than about 80 μm .

A finite element model, for steady-state thermal simulations, was calibrated with the temperature measurements. In order to obtain a good prediction of all experiments, with and without a Cu inner layer, two thermal contact conductance coefficients were needed for the boundary conditions of the scan head exterior surface (toward the thermal phantom); one coefficient for the un-encapsulated heat source ($250 \text{ Wm}^{-2}\text{K}^{-1}$) and one for the polymer encapsulation ($46 \text{ Wm}^{-2}\text{K}^{-1}$). With this calibration, simulated steady-state temperatures were in good agreement with the experiments, i.e. for all Cu layer thicknesses and power levels. The simulation model was used to suggest material properties for the outer layer that can allow for higher power levels. The preferred outer material is a biocompatible and electrically insulating material with high thermal conductivity, e.g. a biocompatible ceramic or a thermally conductive and electrically insulating polymer composite.

The simulation model in this paper enables quick computations to evaluate the thermal management of TEE scan head designs with (double layer) metallized encapsulation. Further work is needed to extend the validity of the model to a wider range of encapsulation materials, and to establish a more fundamental physical description of the heat transfer from the TEE scan head to the thermal phantom, and to the tissue of the human esophagus. A more comprehensive model should include the thermal phantom (or the human tissue) in the computational domain, and the simulation should be transient.

Nomenclature

h_c	thermal contact conductance coefficient ($\text{Wm}^{-2} \text{K}^{-1}$)
h_{c1}	thermal contact conductance coefficient for the heat source ($\text{Wm}^{-2} \text{K}^{-1}$)
h_{c2}	thermal contact conductance coefficient for the external surfaces of the encapsulation of the test sample in contact with the phantom surface ($\text{Wm}^{-2} \text{K}^{-1}$)
k	thermal conductivity of a material ($\text{Wm}^{-1} \text{K}^{-1}$)
P	power supplied to the heat source of the test sample (W)
q_0	heat flux (Wm^{-2})
T	simulated temperature of the surface of the TEE scan head ($^{\circ}\text{C}$)
T_{ext}	simulated temperature of the thermal phantom ($^{\circ}\text{C}$)
T_1	measured temperature of the thermocouple placed on the heat source surface in the test sample ($^{\circ}\text{C}$)
T_2	measured temperature of the thermocouple placed on the vertical surface of the encapsulation, near the heat source ($^{\circ}\text{C}$)
T_3	measured temperature of the thermocouple placed on the vertical surface of the encapsulation, far from the heat source ($^{\circ}\text{C}$)
T_r	measured temperature of the thermocouple placed in the thermal phantom ($^{\circ}\text{C}$)
ΔT	difference between T_1 and T_r ($^{\circ}\text{C}$); i.e. $\Delta T = T_1 - T_r$
t	measurement time (s)
t_{Cu}	thickness of the Cu layer in the metallized encapsulation (m)
t_{po}	thickness of the polymer layer in the metallized encapsulation (m)
a, b, c, d	fitting parameters

Acknowledgments

This work was funded by the Research Council of Norway through the BIA program (grant number: 269618; *Mechanical miniaturization in interventional medical instruments*), and by the Norwegian Micro- and Nano-Fabrication Facility (NorFab, project number: 245963/F50). The authors gratefully acknowledge Mrs. Zekija Ramic, Mr. Svein Mindrebøe, Dr. Thai Anh Tuan Nguyen and Mr. Thao Ngoc Vo at the University of South-Eastern Norway (USN) for their assistance with laboratory work. We sincerely thank Dr. Helge Kristiansen at Conpart AS, Prof. Tao Dong and Dr. Zhongyuan Shi at USN for valuable discussions.

Disclosure statement

No potential competing interest was reported by the authors.

Funding

This work was funded by the Research Council of Norway through the BIA program (grant number: 269618; *Mechanical miniaturization in interventional medical instruments project*), and by the Norwegian Micro- and Nano-Fabrication Facility (NorFab, project number: 245963/F50).

Data availability statement

The raw/processed data required to reproduce these findings cannot be shared at this time due to legal restrictions.

References

- [1] E. C. Pua, S. F. Idriss, P. D. Wolf, and S. W. Smith, "Real-time 3D transesophageal echocardiography," *Ultrason. Imaging.*, vol. 26, no. 4, pp. 217–232, 2004. DOI: [10.1177/016173460402600402](https://doi.org/10.1177/016173460402600402).
- [2] IEC, IEC 60601-2-37 - Particular requirements for the safety of ultrasonic medical diagnostic and monitoring equipment, 2004.
- [3] R. Bahru, A. A. Hamzah, and M. A. Mohamed. "Thermal management of wearable and implantable electronic healthcare devices: perspective and measurement approach," *Int. J. Energy Res.*, 2020. DOI: [10.1002/er.6031](https://doi.org/10.1002/er.6031).
- [4] R. Tummala. *Fundamentals of Microsystems Packaging*, USA: McGraw-Hill Education, 2001. <https://www.mhprofessional.com/9780071418072-usa-fundamentals-of-microsystems-packaging>

- [5] C. Yadav and R. R. Sahoo, "Effect of nano-enhanced PCM on the thermal performance of a designed cylindrical thermal energy storage system," *Exp. Heat Transf.*, vol. 34, no. 4, pp. 356–375, 2021. DOI: [10.1080/08916152.2020.1751744](https://doi.org/10.1080/08916152.2020.1751744).
- [6] C. R. Paul. *Introduction to Electromagnetic Compatibility*. Second. (Chapters 10, 5, Appendix B), USA: John Wiley & Sons, Inc., 2006. DOI: [10.1002/0471758159](https://doi.org/10.1002/0471758159). <https://onlinelibrary.wiley.com/doi/book/10.1002/0471758159>
- [7] F. P. Incropera, D. P. DeWitt, T. L. Bergman, and A. S. Lavine. *Fundamentals of Heat and Mass Transfer*. 6th Ed. USA: John Wiley & Sons, Inc., 2007. DOI: [10.1016/j.applthermaleng.2011.03.022](https://doi.org/10.1016/j.applthermaleng.2011.03.022).
- [8] G. Jiang and D. D. Zhou, Technology advances and challenges in hermetic packaging for implantable medical devices, 2009. DOI: [10.1007/978-0-387-98120-8_2](https://doi.org/10.1007/978-0-387-98120-8_2).
- [9] J. M. H. Morales. *Evaluating Biocompatible Barrier Films as Encapsulants of Medical Micro Devices*. France: Université Grenoble Alpes, 2016.
- [10] H. Chen, *et al.*, "Thermal conductivity of polymer-based composites: fundamentals and applications," *Prog. Polym. Sci.*, vol. 59, pp. 41–85, 2016. DOI: [10.1016/j.progpolymsci.2016.03.001](https://doi.org/10.1016/j.progpolymsci.2016.03.001).
- [11] M. Schlesinger and M. Paunovic. *Modern Electroplating*. Fifth Ed. USA; 2011. DOI: [10.1002/9780470602638](https://doi.org/10.1002/9780470602638).
- [12] IEC, IEC 60601-1-2 - Medical electrical equipment - Part 1-2: general requirements for basic safety and essential performance - Collateral Standard: electromagnetic disturbances - Requirements and tests, 2014.
- [13] CISPR, EN 55011:2007 - Industrial, scientific and medical equipment - radio-frequency disturbance characteristics - Limits and methods of measurements, 2007.
- [14] N. B. D. Do, *et al.*, New encapsulation concepts for medical ultrasound probes- A heat transfer simulation study, in: 2019 22nd Eur. Microelectron. Packag. Conf. Exhib. EMPC 2019, Pisa, Italy, 2019. DOI: [10.23919/EMPC44848.2019.8951832](https://doi.org/10.23919/EMPC44848.2019.8951832).
- [15] Stratatsys. "Objet30 Prime," *Tech. Datasheet*, p. 3-2 to 3-9, 2016.
- [16] ISO/ASTM, ISO/ASTM 52900-2015: additive manufacturing – General principles – Terminology, 2015.
- [17] Epoxy Technology. "EPO-TEK EJ2189-LV," *Tech. Datasheet*, p. 2, 2017.
- [18] Stratatsys. "Biocompatible Clear MED610," *Tech. Datasheet*, p. 2, 2018.
- [19] Humber River Hospital, Preparing for your Transesophageal Echocardiogram (TEE), (2016).
- [20] J. Calvert, F. Duck, S. Clift, and H. Azaim. "Surface heating by transvaginal transducers, Ultrasound Obstet," *Gynecol.*, 2007. DOI: [10.1002/uog.3973](https://doi.org/10.1002/uog.3973).
- [21] P. Miloro, E. Martin, and A. Shaw, "Temperature elevation measured in a tissue-mimicking phantom for transvaginal ultrasound at clinical settings," *Ultrasound*, vol. 25, no. 1, pp. 6–15, 2017. DOI: [10.1177/1742271X16684529](https://doi.org/10.1177/1742271X16684529).
- [22] National Physical Laboratory, Tissue phantom for assessment of surface temperature of an ultrasonic transducer, Datasheet. (2017).
- [23] Heat Scientific, Heat scientific MCH Metal Ceramic Heater, HS-PS101012Y Datasheet. (2018).
- [24] Aalco. "Aluminium alloy 6082," *Tech. Datasheet*, p. 2, 2019.
- [25] Epoxy Technology. "EPO-TEK T7109-19," *Tech. Datasheet*, p. 2, 2019.
- [26] K. Jagannadham, "Thermal conductivity of copper-graphene composite films synthesized by electrochemical deposition with exfoliated graphene platelets," *Metall. Mater. Trans. B Process Metall. Mater. Process. Sci.*, vol. 43, no. 2, pp. 316–324, 2012. DOI: [10.1007/s11663-011-9597-z](https://doi.org/10.1007/s11663-011-9597-z).
- [27] COMSOL Multiphysics v. 5.3a, *COMSOL Material Library*, Sweden: COMSOL AB, 2018.
- [28] G. Wypych. *Handbook of Polymers*. Second Ed. Toronto, Canada: ChemTec Publishing, 2016. DOI: [10.1016/C2015-0-01462-9](https://doi.org/10.1016/C2015-0-01462-9). <https://www.elsevier.com/books/handbook-of-polymers/wypych/978-1-895198-92-8>
- [29] A. J. T. Teo, *et al.*, "Polymeric biomaterials for medical implants and devices," *ACS Biomater. Sci. Eng.*, vol. 2, no. 4, pp. 454–472, 2016. DOI: [10.1021/acsbiomaterials.5b00429](https://doi.org/10.1021/acsbiomaterials.5b00429).
- [30] S. Sandell, *et al.*, "Enhancement of thermal boundary conductance of metal–polymer system," *Nanomaterials*, vol. 10, no. 4, pp. 670, 2020. DOI: [10.3390/nano10040670](https://doi.org/10.3390/nano10040670).
- [31] S. Babu, K. Manisekar, A. P. S. Kumar, and D. Rajenthirakumar, "experimental study of thermal contact resistance in hardened bearing surfaces," *Exp. Heat Transf.*, vol. 28, no. 2, pp. 189–203, 2015. DOI: [10.1080/08916152.2013.860503](https://doi.org/10.1080/08916152.2013.860503).
- [32] M. Asif and A. Tariq, "Correlations of thermal contact conductance for nominally flat metallic contact in vacuum," *Exp. Heat Transf.*, vol. 29, no. 4, pp. 456–484, 2016. DOI: [10.1080/08916152.2015.1024352](https://doi.org/10.1080/08916152.2015.1024352).
- [33] J. R. Taylor and W. Thompson, An introduction to error analysis: the study of uncertainties in physical measurements, 1997.
- [34] Y. Duan and H. Yang, "Influence of thermal contact resistance of cementing interface on radial heat transfer in wellbore," *Exp. Heat Transf.*, vol. 34, no. 1, pp. 68–84, 2021. DOI: [10.1080/08916152.2020.1715511](https://doi.org/10.1080/08916152.2020.1715511).
- [35] D. Liao, *et al.*, "Oesophageal heat transfer properties indication of segmental blood flow changes during distension," *Neurogastroenterol. Motil.*, vol. 20, no. 4, pp. 298–303, 2008. DOI: [10.1111/j.1365-2982.2007.01031.x](https://doi.org/10.1111/j.1365-2982.2007.01031.x).
- [36] M. Ohashi, S. Kawakami, Y. Yokogawa, and G. C. Lai, "Spherical aluminum nitride fillers for heat-conducting plastic packages," *J. Am. Ceram. Soc.*, vol. 88, no. 9, pp. 2615–2618, 2005. DOI: [10.1111/j.1551-2916.2005.00456.x](https://doi.org/10.1111/j.1551-2916.2005.00456.x).

- [37] Z. Zhu, *et al.*, “Densely packed polymer/boron nitride composite for superior anisotropic thermal conductivity,” *Polym. Compos.*, vol. 39, no. S3, pp. E1653–E1658, 2018. DOI: [10.1002/pc.24615](https://doi.org/10.1002/pc.24615).
- [38] T. Kusunose, T. Yagi, S. H. Firoz, and T. Sekino, “Fabrication of epoxy/silicon nitride nanowire composites and evaluation of their thermal conductivity,” *J. Mater. Chem. A*, vol. 1, no. 10, pp. 3440, 2013. DOI: [10.1039/c3ta00686g](https://doi.org/10.1039/c3ta00686g).
- [39] N. G. Berg, T. Paskova, and A. Ivanisevic, “Tuning the biocompatibility of aluminum nitride,” *Mater. Lett.*, vol. 189, pp. 1–4, 2017. DOI: [10.1016/j.matlet.2016.11.041](https://doi.org/10.1016/j.matlet.2016.11.041).
- [40] M. Qin, *et al.*, “Powder injection molding of complex-shaped aluminium nitride ceramic with high thermal conductivity,” *J. Eur. Ceram. Soc.*, vol. 39, no. 4, pp. 952–956, 2019. DOI: [10.1016/j.jeurceramsoc.2018.11.037](https://doi.org/10.1016/j.jeurceramsoc.2018.11.037).

SUPPLEMENTARY MATERIALS

Thermal management of an interventional medical device with double layer encapsulation

Nu Bich Duyen Do^a, Erik Andreassen^{a,b}, Stephen Edwardsen^c, Anders Lifjeld^c, Knut E. Aasmundtveit^a, Hoang-Vu Nguyen^a, and Kristin Imenes^{a*}

^a*University of South-Eastern Norway, Department of Microsystems, Borre, Norway;*

^b*SINTEF Industry, Oslo, Norway*

^c*GE Vingmed Ultrasound AS, Horten, Norway*

* Corresponding author: Kristin.Imenes@usn.no

1. Fabrication of Cu electroplated polymer encapsulation part

The polymer part was fabricated by polymer 3D printing. The biocompatible polymer material MED610 (from Stratasys) was used with the 3D printer Stratasys Objet30 Prime. A metal layer with desired thickness was then deposited on the inner surfaces of the polymer parts by means of sputtering followed by electroplating.

To increase the adhesion between the Cu layer and the polymer part, the latter was first treated with plasma [1,2]. A very thin layer of Cr (about 15 nm) was then coated on the plasma treated polymer surfaces using e-beam evaporation, in the physical vapor deposition (PVD) system from AJA International [2,3]. After this, a Cu layer of about 200 nm was sputtered on the Cr layer immediately, in the same PVD unit to provide an electrical conductive base for the subsequent electroplating [3]. Cu electroplating was carried out in acid copper sulfate solution (Sigma-Aldrich) (i.e. an electrolyte with primary constituents of Cu²⁺ sulfate (CuSO₄·5H₂O) and sulfuric acid), at room temperature. A reverse pulse deposition technique was employed to get high quality electroplated Cu and ensure uniform coverage of Cu on the inner surfaces of the polymer parts [4,5]. Process parameters for the fabrication of the metallized polymer encapsulation parts are summarized in Table S1.

Table S1: Process parameters for the fabrication of the metallized polymer encapsulation.

Process	Equipment	Process parameters
Plasma treatment	α Alpha Plasma – AL 18 Tabletop Unit	Power: 200 W O ₂ flow: 40 sccm (standard cm ³ /min) Ar flow: 60 sccm Time: 3 minutes
E-beam of Cr	Sputtering system of AJA International Inc.	Current: 8 mA Pressure: 4·10 ⁻⁶ Torr Current rate: 0.08 A/s
Sputtering of Cu	Sputtering system of AJA International Inc.)	Power: 50 W Ar gas: 10 sccm Pressure: 4·10 ⁻³ Torr Current rate: 0.6 A/s
Electroplating of Cu	Pulse Reverse Power Supply PE86CB of Plating Electronic GmbH	Reverse pulse deposition: Pulsed current density (<i>i</i>): 10 mA/cm ² Pulse length (<i>t_{on}</i>): 400 ms The off period (<i>t_{off}</i>): 20 ms

2. Characterization of Cu electroplated polymer encapsulation part

Cross-sections of electroplated parts were characterized by optical microscopy (Neophot 32, Carl Zeiss). The Cu layer thickness was measured (Table S2) and the electroplating process was evaluated. In preliminary electroplating trials, Cu was deposited on 3D printed parts with different polymer thicknesses (0.5 mm and 0.9 mm). The 0.5 mm thick part was deformed after plating, due to stresses induced by the electroplating [5]. Hence, a polymer part thickness of 0.9 mm was selected, to ensure that it would withstand the electroplating with regard to dimensional tolerances. Table S2 presents the measured average Cu thickness (10, 80, 150 μm) of encapsulation parts with polymer thickness 0.9 mm. The variation in thickness can be explained by the geometry of the polymer parts and the electroplating layout.

Table S2: Measured Cu thickness, t_{Cu} , of encapsulation parts (E10, E80, E150) with polymer thickness 0.9 mm. The average Cu thickness (t_{Cu}) is based on three cross-sections along the length of one encapsulation part (three red lines in Figure S1), with 15 measurements around the cross-sections L1, L2, and 10 measurements around the cross-section L3.

Part	Nominal Cu thickness (μm)	t_{Cu} (μm)
E10	10	10 ± 1
E80	80	80 ± 7
E150	150	149 ± 15

The thinnest Cu layer in this study was 10 μm . This value was selected in order to provide adequate EMI shielding effectiveness (EMI SE) for the TEE scan head. A Cu layer thicker than 10 μm gives an EMI SE above 100 dB in the frequency range of 30 MHz – 3 GHz [6], which is a common frequency range for testing EMI shielding of medical devices [7,8]. These EMI SE values are above the requirements for medical devices classified in the same group as the TEE scan head (group 1, class B) [7]. The thickest Cu layer in this study, 150 μm , was chosen in order to have a reasonable time for the electroplating process [5]. Therefore, three Cu layer thicknesses were used in this study (10, 80 and 150 μm), to evaluate the effect of metal thickness on the heat transfer. The standard deviation of the measured Cu thicknesses was about 10% (see Table S2).

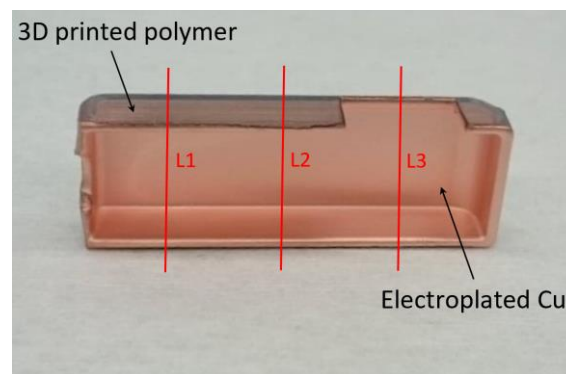


Figure S1: Cu electroplated polymer part; L1, L2, L3 are positions of cross-sections for measuring the Cu thickness.

3. Meshing of the simulation model

The model in COMSOL was meshed using free tetrahedral elements. The mesh sizes were selected so that they adequately described the heat flow in the thinnest layer of the model (e.g. 10 μm thick Cu layer). Details are presented in Table S3. The mesh in the paper (based on settings in Table S3) had 754637 elements. Our initial check using a finer mesh (for all domains, leading to 3146082 elements) gave the same result for the maximum surface temperature, within 0.1 K. We also used the mesh statistics tool in COMSOL to evaluate the mesh quality. With the mesh in this paper, the COMSOL mesh quality parameter has an average value of 0.634 and a minimum value of 0.154. These values fulfill COMSOL's recommendation for good meshes, for which the minimum value should be greater than 0.1.

Table S3: Mesh sizes for different domains in the simulation model

Domain	Element size parameters
Cu layer	Meshed with "fine mesh" setting with these parameters: <ul style="list-style-type: none"> - Maximum element size: 2.94 mm - Minimum element size: 0.009 mm - Maximum element growth rate: 1.45 - Curvature factor: 0.5 - Resolution of narrow regions: 0.6
Adhesives	Meshed with "fine mesh" setting with these parameters: <ul style="list-style-type: none"> - Maximum element size: 2.94 mm - Minimum element size: 0.045 mm - Maximum element growth rate: 1.45 - Curvature factor: 0.5 - Resolution of narrow regions: 0.6
Remaining parts	Meshed with "normal mesh" setting with these parameters: <ul style="list-style-type: none"> - Maximum element size: 3.68 mm - Minimum element size: 0.5 mm - Maximum element growth rate: 1.5 - Curvature factor: 0.6 - Resolution of narrow regions: 0.5

4. Simulation results – Fitting parameters for simulations and experimental data

The simulated ΔT values (using the two TCC coefficients), as well as the experimental data, were well represented by an exponential function:

$$\Delta T = (ae^{bt_{Cu}} + ce^{dt_{Cu}})P$$

where a , b , c , d are fitting parameters, t_{Cu} is the Cu thickness and P is the heat source power. The fitting parameters for the simulated ΔT are $a = 8.82$; $b = -0.16$; $c = 12.75$; $d = -0.0004$. The fitting parameters for the experimental ΔT are $a = 7.27$; $b = -0.15$; $c = 13.41$; $d = -0.001$. These fittings are shown in Figure 10 in the manuscript.

5. Simulation results – Assessing the thermal limits of the scan head design

Simulations with extreme values for the polymer thermal conductivity can be used to assess the thermal limits of the scan head design. Examples of the effect of polymer thermal conductivity on the maximum surface temperature increase is shown in Figure S2.

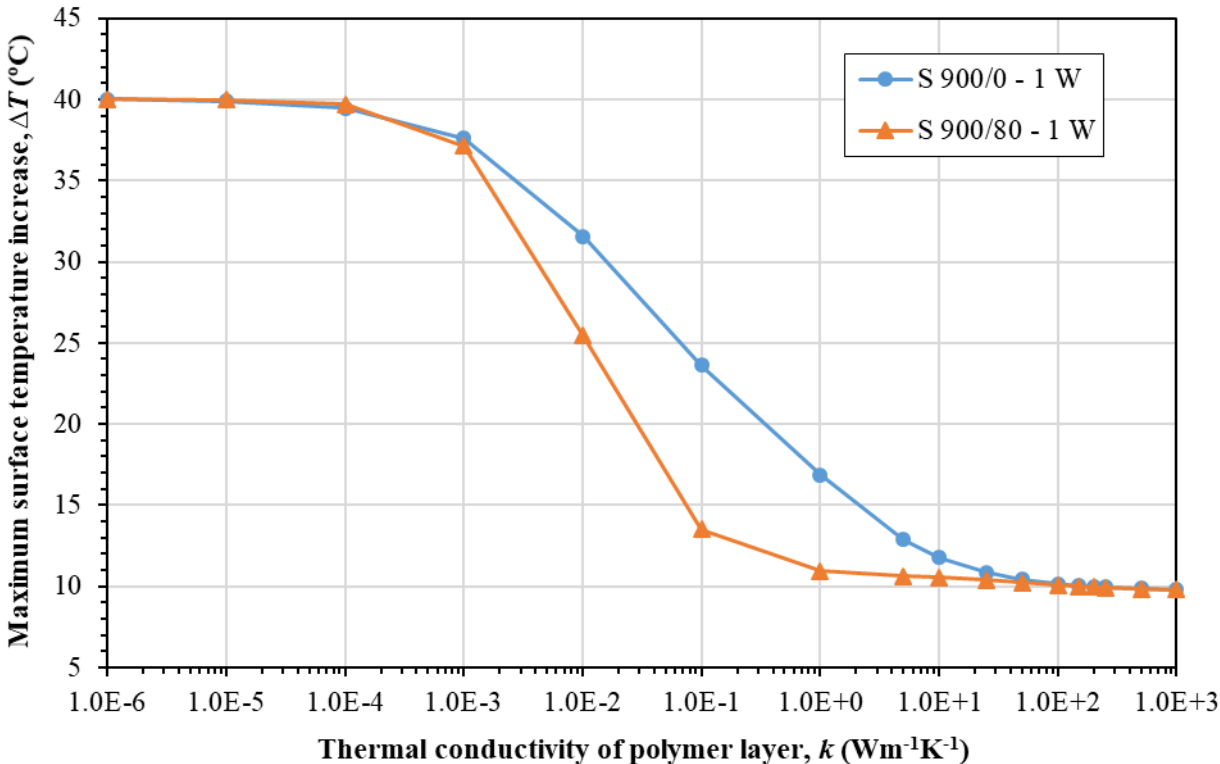


Figure S2: Simulated effect of the polymer thermal conductivity on the maximum surface temperature increase, for a power of 1 W. "S 900/0" is the sample with an encapsulation consisting of a 0.9 mm thick polymer layer and no Cu layer; "S 900/80" is the sample with an

encapsulation consisting of a 0.9 mm thick polymer layer and a 80 μm thick Cu layer. Two thermal contact conductance coefficients ($250 \text{ Wm}^{-2}\text{K}^{-1}$ and $46 \text{ Wm}^{-2}\text{K}^{-1}$) were used in the simulations (see Section 3.2 in the manuscript regarding the calibration of the simulation model for details).

References

- [1] Y.S. Lin, H.M. Liu, Enhanced adhesion of plasma-sputtered copper films on polyimide substrates by oxygen glow discharge for microelectronics, *Thin Solid Films*. (2008). <https://doi.org/10.1016/j.tsf.2007.07.162>.
- [2] L.J. Martin, C.P. Wong, Chemical and mechanical adhesion mechanisms of sputter-deposited metal on epoxy dielectric for high density interconnect printed circuit boards, *IEEE Trans. Components Packag. Technol.* (2001). <https://doi.org/10.1109/6144.946488>.
- [3] B.I. Noh, J.W. Yoon, J.H. Choi, S.B. Jung, Effect of Cr thickness on adhesion strength of Cu/Cr/polyimide flexible copper clad laminate fabricated by roll-to-roll process, *Mater. Trans.* (2010). <https://doi.org/10.2320/matertrans.M2009276>.
- [4] X. Zhang, K.N. Tu, Z. Chen, Y.K. Tan, C.C. Wong, S.G. Mhaisalkar, X.M. Li, C.H. Tung, C.K. Cheng, Pulse electroplating of copper film: A study of process and microstructure, in: *J. Nanosci. Nanotechnol.*, 2008. <https://doi.org/10.1166/jnn.2008.452>.
- [5] M. Schlesinger, M. Paunovic, *Modern Electroplating: Fifth Edition*, 2011. <https://doi.org/10.1002/9780470602638>.
- [6] C.R. Paul, *Introduction to Electromagnetic Compatibility: Second Edition (Chapters 10, 5, Appendix B)*, 2006. <https://doi.org/10.1002/0471758159>.
- [7] IEC, IEC 60601-1-2 - Medical electrical equipment - Part 1-2: General requirements for basic safety and essential performance - Collateral Standard: Electromagnetic disturbances - Requirements and tests, 2014.
- [8] CISPR, EN 55011:2007 - Industrial, scientific and medical equipment - radio-frequency disturbance characteristics - Limits and methods of measurements, 2007.

Article 5

Do, N.B.D.; Imenes, K.; Aasmundtveit, K.E.; Nguyen, H.-V.; Andreassen, E. Thermal Conductivity and Mechanical Properties of Polymer Composites with Hexagonal Boron Nitride — A Comparison of Three Processing Methods: Injection Moulding, Powder Bed Fusion and Casting. *Polymers* **2023**, *15*, 1552, DOI: [10.3390/polym15061552](https://doi.org/10.3390/polym15061552)

Article

Thermal Conductivity and Mechanical Properties of Polymer Composites with Hexagonal Boron Nitride—A Comparison of Three Processing Methods: Injection Moulding, Powder Bed Fusion and Casting

Nu Bich Duyen Do ¹, Kristin Imenes ¹, Knut E. Aasmundtveit ¹, Hoang-Vu Nguyen ¹ and Erik Andreassen ^{1,2,*} ¹ Department of Microsystems, University of South-Eastern Norway, 3184 Borre, Norway² SINTEF Industry, 0373 Oslo, Norway

* Correspondence: erik.andreassen@sintef.no; Tel.: +47-98-28-24-92

Abstract: Materials providing heat dissipation and electrical insulation are required for many electronic and medical devices. Polymer composites with hexagonal boron nitride (hBN) may fulfil such requirements. The focus of this study is to compare composites with hBN fabricated by injection moulding (IM), powder bed fusion (PBF) and casting. The specimens were characterised by measuring thermal conductivity, tensile properties, hardness and hBN particle orientation. A thermoplastic polyurethane (TPU) was selected as the matrix for IM and PBF, and an epoxy was the matrix for casting. The maximum filler weight fractions were 65%, 55% and 40% for IM, casting and PBF, respectively. The highest thermal conductivity (2.1 W/m·K) was measured for an IM specimen with 65 wt% hBN. However, cast specimens had the highest thermal conductivity for a given hBN fraction. The orientation of hBN platelets in the specimens was characterised by X-ray diffraction and compared with numerical simulations. The measured thermal conductivities were discussed by comparing them with four models from the literature (the effective medium approximation model, the Ordóñez-Miranda model, the Sun model, and the Lewis-Nielsen model). These models predicted quite different thermal conductivities vs. filler fraction. Adding hBN increased the hardness and tensile modulus, and the tensile strength at high hBN fractions. The strength had a minimum as the function of filler fraction, while the strain at break decreased. These trends can be explained by two mechanisms which occur when adding hBN: reinforcement and embrittlement.

Keywords: hexagonal boron nitride; thermoplastic polyurethane; injection moulding; powder bed fusion; casting; thermal conductivity



Citation: Do, N.B.D.; Imenes, K.; Aasmundtveit, K.E.; Nguyen, H.-V.; Andreassen, E. Thermal Conductivity and Mechanical Properties of Polymer Composites with Hexagonal Boron Nitride—A Comparison of Three Processing Methods: Injection Moulding, Powder Bed Fusion and Casting. *Polymers* **2023**, *15*, 1552. <https://doi.org/10.3390/polym15061552>

Academic Editors: Byungohk Rhee, Lih-Sheng Turng, Christian Hopmann, Jinsu Gim and Swee Leong Sing

Received: 18 December 2022

Revised: 16 March 2023

Accepted: 17 March 2023

Published: 21 March 2023



Copyright: © 2023 by the authors. Licensee MDPI, Basel, Switzerland. This article is an open access article distributed under the terms and conditions of the Creative Commons Attribution (CC BY) license (<https://creativecommons.org/licenses/by/4.0/>).

1. Introduction

The miniaturisation and increased processing capacity of electronics components often result in high thermal loading [1,2]. Thermal management therefore plays an important role for the performance and reliability of electronic devices. In addition to efficient heat dissipation, electrical insulation is required for many applications, such as mobile devices and medical devices [1,3]. Hence, thermally conducting but electrically insulating polymer-based composite materials are often used in electronic packaging [1,4].

Polymer-based materials have low density and low cost, and allows for mass production with well-established techniques, such as injection moulding and transfer moulding [1,5]. The polymer matrix in a composite can be a thermoset (e.g., epoxy) or a thermoplastic, including elastomers of either type. Most polymers have low thermal conductivity, typically in the range 0.1–0.5 W/m·K [5]. Incorporating thermally conductive but electrically insulating inorganic fillers into the polymer matrix is an effective solution for improving the thermal conductivity while maintaining its electrical insulation properties [5,6]. Common fillers are crystalline ceramic materials, either metal oxides (e.g.,

alumina (Al_2O_3), quartz (crystalline SiO_2), or non-oxides (e.g., aluminium nitride (AlN), boron nitride (BN), silicon nitride (Si_3N_4), silicon carbide (SiC)) [5]. Hexagonal boron nitride (hBN) has received attention due to its high intrinsic thermal conductivity and good electrical insulating properties. The filler hBN has been used for enhancing the thermal conductivity of polymer-based composites, see examples in Table 1.

Table 1. Some studies of hBN/polymer composites. (wt% = weight percentage, vol% = volume percentage).

Materials	Filler Loading	Processing Method	Thermal Conductivity
hBN/epoxy [7]	95 wt%	Compression moulding	21.3 W/m·K (in-plane) 7 W/m·K (through-plane)
hBN/epoxy [8]	57 vol%	Casting	5.27 W/m·K (through-plane)
hBN/polyimide [9]	60 vol%	Spin-cast (film)	17.5 W/m·K (in-plane) 5.4 W/m·K (through-plane)
hBN/PE [10]	50 vol%	Injection moulding	3.66 W/m·K
hBN/PA12 [11]	40 wt%	Powder bed fusion	0.55 W/m·K (77% higher than pure PA12)
hBN/ Al_2O_3 /PA12 [12]	15 wt% hBN and 35 wt% Al_2O_3	Powder bed fusion	1.05 W/m·K (275% higher than pure PA12)
hBN/AlN/TPU [13]	15 wt% hBN and 20 wt% AlN	Powder bed fusion	0.9 W/m·K (391% higher than pure TPU)
hBN/TPU [14]	30 wt%	Fused deposition modelling (material extrusion)	1.51 W/m·K (in-plane) 1.26 W/m·K (through-plane)

Hexagonal BN consists of B and N atoms arranged in a honeycomb configuration with a layer structure similar to graphite. Within the layers, there are strong covalent bonds between B and N atoms, while the bonds between layers are weak van der Waals forces [15,16]. The crystal structure of hBN results in platelet-shaped particles. The platelets have high in-plane thermal conductivity of about 300–600 W/m·K, whereas the through-plane thermal conductivity is in the range 2–30 W/m·K [4,9,15,16]. Furthermore, hBN is electrically insulating and has a wide band gap (about 5.97 eV). It also has high thermal stability and good mechanical properties [15–17]. Due to the strong B–N bonds, hBN is chemically stable, e.g., towards oxidation. However, this makes the functionalisation of hBN challenging [16]. hBN also has good biocompatibility [16,18,19], which is essential in medical applications.

Due to the hBN particles' shape and anisotropic thermal conductivity, the orientation of the hBN platelets in the polymer matrix affects the thermal conductivity of the composite [5,15]. Particles can be oriented via processing or by using electric or magnetic fields [5,7,15,20,21]. Different processing methods for polymer-based composites have different impacts with regard to distributing and orienting the platelets, as well as dispersing agglomerates and stacks of platelets into single platelets. Hence, in general, the properties of polymer composites are affected by the choice of processing method [22].

Approaches for preparing thermally conductive polymer composites include melt compounding (e.g., followed by injection moulding) and mixing with a resin followed by casting and polymerisation (curing) [1,5,15]. Injection moulding (IM) is one of the most common manufacturing processes for the mass production of polymer or polymer composite parts [1,23]. The hBN platelets are reported to be preferentially oriented with the platelet normal in the through-plane (thickness) direction of injection moulded parts, owing to the shear stress in the IM process [5,15]. In a casting process, composites are produced by mixing fillers into a resin such as epoxy, followed by pouring or injecting the mixture into a mould for curing. The casting of hBN/polymer composites can result in almost randomly oriented platelets [5,8,15].

Powder bed fusion (PBF) is one of the most common 3D printing (additive manufacturing) processes for polymer materials. The feedstock is powder, and thermal energy (e.g., from a laser) selectively fuses regions of a powder bed, layer-by-layer, to fabricate 3D objects [24]. Compared to moulding processes, the principal advantages of PBF and other 3D printing techniques include the fast prototyping and production of personalised parts with complex geometry. Few polymer types are commercially available for PBF. Among the most common are polyamide 12 (PA12) and thermoplastic polyurethane (TPU). Polyamide-based composites are also used in PBF, with glass-based fillers (e.g., glass fibres, glass beads) or carbon-based fillers (e.g., carbon black, carbon fibres, carbon nanotubes, graphite) [24–26]. There is a growing interest in developing new materials and composites for PBF, as well as the optimisation of PBF processing parameters.

There are several articles about PBF of polymer composites with thermally and electrically conductive fillers (e.g., carbon-based fillers such as carbon fibres [27], graphite [28], CNT [29] and graphene [30], or metal fillers such as Cu [31] and Ag [32]). On the contrary, the literature on PBF with thermally conductive and electrically insulating polymer-based composites is sparse, and most studies use PA12 as the polymer matrix. Yang et al. [11] studied PBF of hBN/PA12 composites, for which co-powders were prepared by combining solid-state shear milling and cryogenic pulverisation [11]. Yuan et al. [12] investigated the effect of incorporating Al₂O₃ and hBN on thermal and mechanical properties of PA12 composites processed by PBF. Hon et al. [33] examined the effects of processing parameters on the mechanical properties of the PBF composites containing PA12 and SiC. Zhang et al. [13] combined AlN and hBN for enhancing the thermal conductivity of TPU composites processed by PBF.

This research was motivated by our previous study on the encapsulation of interventional medical devices [34]. Encapsulation materials used in the human body must meet several requirements, such as good heat transfer, electrical insulation, mechanical integrity, biocompatibility, and in some cases, a ‘soft touch’ [3,34]. To achieve a significant increase in thermal conductivity in polymer-based composites, a high loading of inorganic fillers (e.g., hBN) is generally required. However, this normally results in increased hardness [5,15] and reduced ductility. To compensate for this, a soft polymer can be used as the matrix material.

Thermoplastic polyurethane elastomers (TPU) are soft materials based on a block copolymer containing hard and soft segments, and where the former act as physical crosslinks for the soft segments. TPU offers high elasticity over a broad temperature range and high wear resistance [24,26,35]. It is commonly used for PBF and IM, and its suitability for biomedical applications has recently been highlighted [25]. Therefore, the TPU “Ultrasint TPU 88A” (in the form of powder for PBF) was selected as the matrix for composites processed by PBF and IM in this study.

This article focuses on comparing the thermal conductivities of hBN/polymer composites processed by three methods, IM and PBF (with TPU as matrix) and casting (with epoxy as matrix). To the best of our knowledge, this is the first study that has processed TPU with hBN using PBF, with only a mixture of the two powders. The measured thermal conductivities are interpreted using platelet orientation measurements (X-ray diffraction), and by comparing with models by Nan et al. [36], Ordóñez-Miranda et al. [37], Sun et al. [38], and Lewis-Nielsen et al. [39]. These models were included as tools to help in understanding the experimental data, especially how the thermal conductivities of the composites are affected by the fraction and orientation of the hBN platelets and the nature of the interphase between the platelets and the polymer matrix. The reason as to why we have included four models and not simply one is that they are based on different assumptions and provide different predictions. Hence, a comparison of the models has a value in itself. Analysing our experimental data using these models provides a deeper understanding of the models and their limitations.

Thermally conductive composites for demanding applications (e.g., the encapsulation of a medical device in our case) also need good mechanical properties. Hence, the study also includes an assessment of the mechanical properties (hardness, tensile modulus, tensile

strength, and strain at break) of the composites. Typically, the hBN fraction in the composite must be a compromise, because increasing the fraction increases the thermal conductivity, but also reduces the ductility of the material, and has a negative effect on the processability via higher viscosity.

2. Materials and Methods

2.1. Materials

The materials used in this study are summarised in Table 2. The polymer matrix was thermoplastic polyurethane (TPU) for injection moulding and powder bed fusion (3D printing) and epoxy for casting.

Table 2. Materials used for preparation of hBN/polymer composites.

Short Name	Description	Product Name, Supplier
BN3 ^a	hBN powder. Platelet agglomerates with D ₅₀ of 20 µm and size distribution in the range (0.5–31) µm, BET ~4 m ² /g	HeBoFill CL-ADH 020, Henze Boron Nitride Products AG, Lauben, Germany
TPU	Thermoplastic polyurethane (in the form of powder). An elastomer with Shore A hardness 88.	Ultrasint TPU 88A, BASF, Ludwigshafen am Rhein, Germany
Epoxy ^b	An epoxy system (for casting) containing: - 35 wt% unmodified bisphenol-F epoxy resin (Araldite GY 285-1) - 35 wt% reactive diluent (Araldite DY 026) - 30 wt% amine-based curing agent (Jeffamine D-230 Polyetheramine)	Huntsman, The Woodlands, TX, USA

^a Information regarding BN3 as provided by the supplier [40]. Size distributions of BN3 are shown in Figure S1 in the Supplementary Materials. The BN3 powder had a partly agglomerated particle structure, claimed to provide good lubricating properties and low viscosity increase [40]. Platelets and spherical agglomerates are shown in Figure S2a in the Supplementary Materials. ^b The epoxy system was formulated to have a low viscosity, suitable for preparing composites with high filler content.

2.2. Specimen Preparation

Injection moulded specimens were prepared using a 15 cm³ micro batch compounder (DSM Midi 2000) followed by injection moulding with a table-top machine (DSM). TPU and hBN powders were mixed in the compounder for 3 min in nitrogen atmosphere, and then injection moulded with melt temperature 220 °C and mould temperature 40 °C. Moulded specimens for thermal conductivity measurement were 2 mm thick discs with diameters of 25 mm, while specimens for tensile testing were 2 mm thick and 75 mm long (ISO 527-2, type 1BA), see Figure 1. The maximum practical filler content for this processing route was about 65 wt%. Details about the injection moulded specimens are presented in Table S2 in the Supplementary Materials.

Cast epoxy-hBN specimens were prepared by vacuum mixing, followed by casting into a Teflon mould (Figure 1) and then curing at 150 °C for 18 h. The epoxy system contains 35 wt% bisphenol-F epoxy resin, 35 wt% diluent and 30 wt% curing agent. This system has a low viscosity, which is suitable for high filler concentrations. At the highest filler content (55 wt%), there was no formation of voids or air bubbles during mixing and casting. To have clean and planar surfaces, the cast specimens (2 mm thick discs with diameters of 13 mm) were grinded and polished on both sides. Details about cast specimens are presented in Table S2 in the Supplementary Materials.

For powder bed fusion (PBF), a tabletop PBF 3D printer (Sharebot SnowWhite) with a CO₂ laser was used to fabricate specimens of a (TPU and hBN) powder mixture. The density and mechanical properties of PBF parts are related to the laser energy density per volume, E_V , which is defined as:

$$E_V = \frac{P}{v d L} \quad (1)$$

where P (W) is the laser power; v (m/s) is the laser scanning speed; d (m) is the hatching distance (the distance between two adjacent laser scan lines); and L (m) is the layer thickness. E_V (J/m^3) represents the amount of energy supplied to a volume element of the powder bed. In order to identify appropriate processing parameters for the hBN/TPU composites, the starting point was the parameters suggested for the pure TPU by the material supplier. However, a higher energy was needed with the printer used, and similarly for the pure TPU. Regarding the chamber temperature, the same settings were used for TPU with and without hBN, because the hBN did not have a large effect on the melting and crystallisation temperatures, see the DSC results in Section S8 in the Supplementary Materials. Details about the printing parameters are provided in Section S2 of the Supplementary Materials.

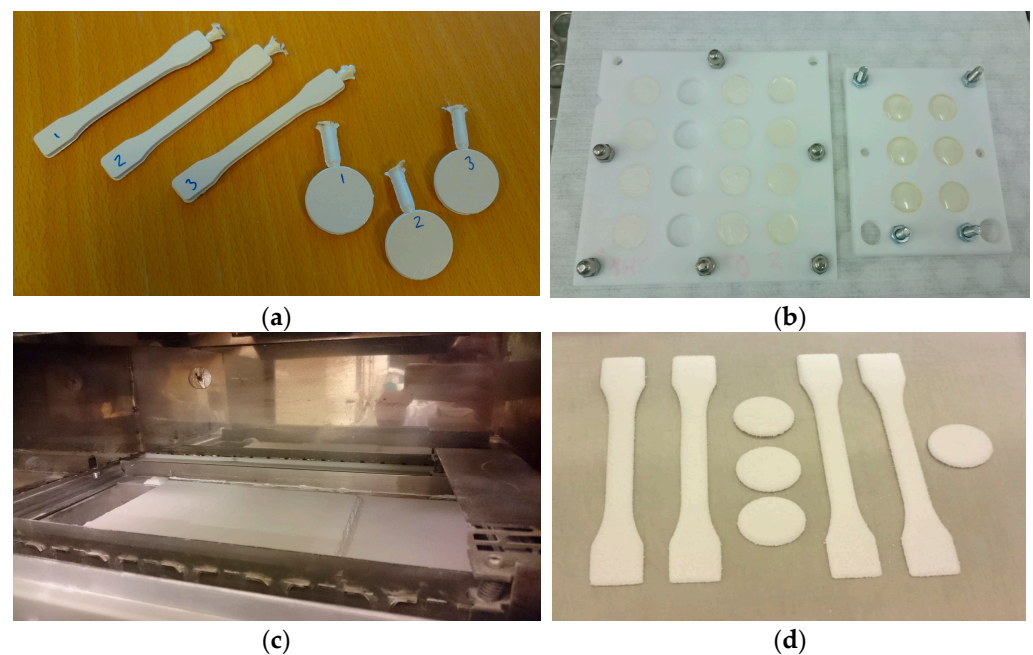


Figure 1. (a) Injection moulded specimens (IM_65BN3); (b) cast specimens in Teflon moulds; (c) PBF 3D printer; and (d) PBF specimens.

Most of the PBF specimens in this study were built “flat” (Figure 1), i.e., with the largest surfaces parallel to the plane of the powder bed (the XY plane; the powder recoater moves along the X-axis, and the powder bed moves along the Z-axis). Some specimens were also built “standing”, i.e., with the surface normal in the XY plane. Before printing, the powder was dried in a vacuum oven at 50 °C for 3 h to remove moisture. The maximum filler content used in the PBF process was 40 wt%. At higher hBN loading, the printed parts did not have sufficient cohesion to be used for tensile testing or thermal conductivity measurements. Details regarding the specimens are presented in Tables S2 and S3 in the Supplementary Materials.

2.3. Characterisation of hBN/Polymer Composites

2.3.1. Thermal Conductivity Measurement

The thermal conductivity of 2 mm thick specimens was indirectly determined by the non-contact, transient laser flash analysis (LFA) method [41], using the equation:

$$k = \alpha \cdot C_p \cdot \rho \quad (2)$$

where k is the thermal conductivity ($\text{W}/\text{m}\cdot\text{K}$); α is the thermal diffusivity (mm^2/s); C_p is the specific heat capacity at constant pressure ($\text{J}/\text{g}\cdot\text{K}$); and ρ is the mass density (g/cm^3).

The thermal diffusivity was determined at 30, 50, 80 and 110 °C with an LFA instrument (LFA 457 MicroFlash, Netzsch GmbH, Selb, Germany). All specimens, including

a reference (Pyroceram 9606), were spray coated with a thin layer of graphite (Graphit 33, Kontakt Chemie, Zele, Belgium) on both sides to reduce reflection, maximise heat absorption and ensure similar surface properties. The thermal diffusivity was determined by the analysis software of the LFA instrument (Netzsch Proteus Software 6.3) using the radiation model without pulse correction.

A Pyroceram reference (diameter 13 mm, thickness 2.5 mm) with known C_p [42] was measured simultaneously, under the same conditions as the composite specimens. Each measurement of a composite specimen was compared to the reference using the analysis software to estimate the unknown C_p value of the composite. Average α and average C_p at each temperature were then used for calculating k at that temperature.

The specimen dimensions were measured at room temperature using a digital calliper. The thickness and diameter were averaged over five measurements and used for calculating the volume. Each specimen was weighed using a balance with 0.1 mg resolution to calculate the mass density ρ . The density of some specimens was also measured gravimetrically (XS204 with density kit, Mettler Toledo, Greifensee, Switzerland). The difference between this density and the density calculated from mass and volume was negligible.

LFA measurements were repeated three times for each specimen at each temperature. Furthermore, for injection moulded specimens, two specimens were measured for each filler concentration, while for PBF and casting, only one specimen was measured for each filler concentration. The variance was dominated by the measurement error (which was about 5–10% at 30 °C, and lower at higher temperatures), not the variation from specimen to specimen.

2.3.2. Tensile Testing

Tensile testing of injection moulded specimens was performed at room temperature, following the standard ISO 527, with a universal test machine (Zwick Z250, Ulm, Germany), using a 2.5 kN load cell. The crosshead speed was 0.5 mm/min up to a strain of 0.25%, and then changed to 25 mm/min (as suggested in ISO 527-1:2012). The tests were run with a slow crosshead speed initially for the accurate determination of the tensile modulus. These speeds were chosen in order to obtain nominal strain rates similar to those typically used in the tensile testing of plastics, with the most common (larger) test specimen 1A of ISO 527-2. PBF specimens were tested with a smaller machine (Lloyd Instruments LR50K, Bognor Regis, UK) without an extensometer. Average values for three to five tests are reported, and standard deviations are included in figures. The stress reported in this paper is the engineering stress, i.e., force divided by the initial cross section. An example of the repeatability of the tensile test is shown in Figure S3 in the Supplementary Materials.

2.3.3. Hardness Measurement

The hardness (Shore A and Shore D) of the specimens were measured with a durometer (Bareiss digi test II, Oberdischingen, Germany) at room temperature, following the standard ASTM D2240. Three specimens were stacked to have the thickness required for the measurements. At least three measurements were performed for each filler content. Hardness measurements were not applicable to the PBF specimens due to high surface roughness.

2.3.4. X-ray Diffraction (XRD)

The orientation of the hBN particles was characterised by X-ray diffraction (XRD), using a Thermo Fisher Equinox 1000 diffractometer (monochromatic Cu $K\alpha$ radiation; wavelength 1.5418 Å). The operating condition was 40 kV voltage and 30 mA current.

The angle between the specimen surface and the incoming X-ray beam was kept constant at 13.3° (the tilt angle: chosen as half the 2θ value of one of the peaks used.) Hence, the length of the X-ray beam path from the front surface to the back surface of a 2 mm thick specimen is:

$$(2 \text{ mm})/\sin(13.3^\circ) = 8.7 \text{ mm}$$

The linear X-ray absorption coefficients of the TPU/hBN composites are typically in the range $8\text{--}10\text{ cm}^{-1}$ (increasing with increasing hBN loading). Note that these are only estimates, as we do not know the element composition of the TPU. If the incoming beam intensity is set to unity, and we consider the peak with 2θ equal to two times the tilt angle, the detected diffracted intensity originating from the centre of a 2 mm thick specimen is simply:

$$\exp(-9 \cdot 0.87) = 4 \cdot 10^{-4}$$

For comparison, the diffracted intensity from depths of 0.1 mm and 0.3 mm would be about 0.50 and 0.10, respectively, or about 1150 and 240 higher than that from the centre. Furthermore, depending on the beam diameter and the detector slits, the diffraction from deep layers may not be detected at all.

In the diffractograms, the peaks at about 26.6° and 41.5° are the (002) and (100) reflections of hBN. If we assume perfect hBN platelets, the ratio of these two peaks can be used to determine the orientation of the platelets, using Equations (3) and (4) [9,43]:

$$\langle \cos^2\theta \rangle = \frac{1}{1 + 2K} \quad (3)$$

$$K = n \frac{I_{(100)}}{I_{(002)}} \quad (4)$$

In these equations $I_{(100)}$ and $I_{(002)}$ are the integrated intensities of the (100) and (002) peaks, respectively [44], and n is a normalisation coefficient, determined to be 6.25 by Tanimoto et al. [9]. Note that we have not corrected n for the constant tilt angle of our experiment. In this paper, the degree of orientation of hBN platelets in the polymer matrix is described by $\langle \cos^2\theta \rangle$, where $\langle \cos^2\theta \rangle$ denotes the average of all platelets, and θ is the angle between a platelet surface normal and the specimen surface normal (i.e., the vector along the thickness direction of the specimen). Hence, perfect out-of-plane, in-plane and random orientation of hBN platelets in the specimen corresponds to $\langle \cos^2\theta \rangle = 0, 1$ and $1/3$, respectively.

3. Results

3.1. Thermal Conductivity of hBN/TPU and hBN/Epoxy Composites

Figure 2 shows the thermal conductivity of hBN/polymer composites fabricated by injection moulding (IM), casting (C) and powder bed fusion (PBF) as a function of hBN content. The highest conductivity ($2.14\text{ W/m}\cdot\text{K}$) was measured for an injection moulded specimen with the highest hBN fraction in this study (65 wt%). This conductivity was 9.7 times higher than that of the pure TPU (injection moulded reference). For the cast composites, a conductivity, which was 14 times higher than that of the pure epoxy, was obtained with 55 wt% hBN. For a given hBN content, the cast composites had the highest conductivity and the highest increase relative to the unfilled material. Among the PBF composites, the specimen with 40 wt% hBN, processed with the highest laser energy density (see Table S3 in the Supplementary Materials for more details), had the highest thermal conductivity, which was 5.8 times higher than that of the pure TPU (fabricated by PBF).

Figure 3 shows the thermal conductivity of PBF composites with 40 wt% hBN as a function of PBF laser energy density (E_V , see Equation (1)). For the main data series in this figure (PBF_40BN3; red open squares), E_V was increased by increasing the laser power or decreasing the scanning speed. There is a clear increase in conductivity with increasing laser energy density for this data series. In addition to the main data series, four single points are also included in the figure, representing other process variations: increasing the nominal E_V by reducing the layer thickness from 0.1 to 0.08 mm resulted in a reduction in conductivity (specimen PBF_40BN3_d_08). Specimens that were built along the z direction of the 3D printer (specimen codes ending in “_z”) had higher conductivity than those that were printed “flat” in the XY plane (all the other data points in the figure). Increasing the chamber temperature from $88\text{ }^\circ\text{C}$ to $92\text{ }^\circ\text{C}$ had no significant effect (PBF_40BN3_b_92).

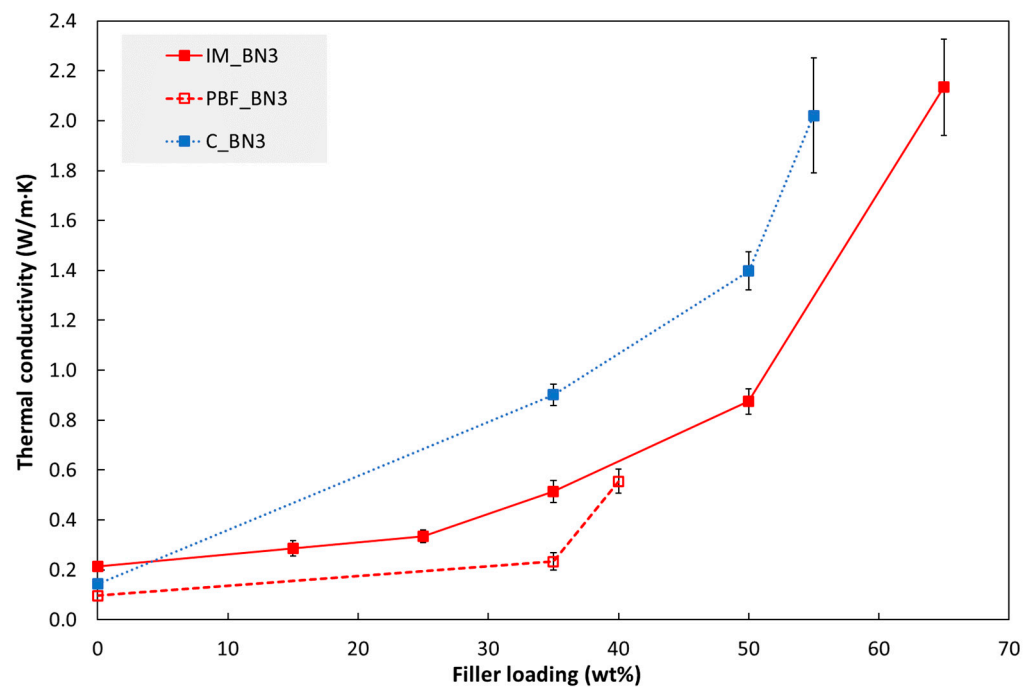


Figure 2. Thermal conductivity (at 30 °C) of composites fabricated by injection moulding (“IM”), powder bed fusion (“PBF”) and casting (“C”) as a function of hBN (BN3) loading. The PBF specimen with 40 wt% hBN was processed with a higher laser energy density than the other PBF specimens in this figure, see Figure 3 and Table S3 in the Supplementary Materials.

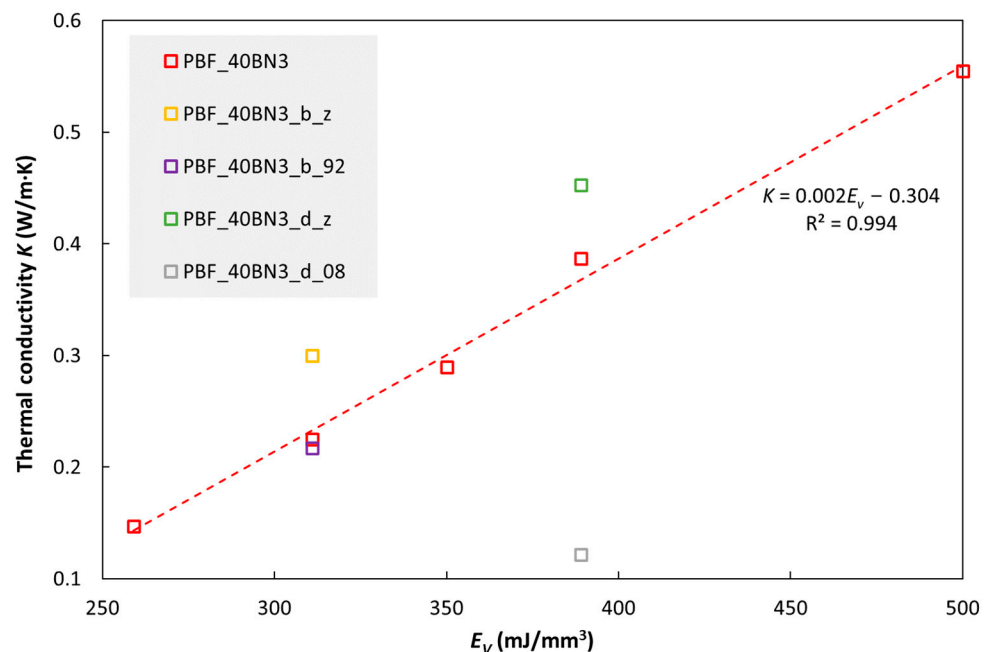


Figure 3. Thermal conductivity (at 30 °C) of TPU with 40 wt% hBN (BN3) as a function of E_V (laser energy density, see Equation (1)). For details about the specimens, see the main text and Table S3 in the Supplementary Materials.

Figure 4 shows the thermal conductivity of cast hBN/epoxy composites as a function of the temperature. For all hBN fractions in the figure (0 to 55 wt%), the thermal conductivity decreases approximately linearly with increasing temperature. For pure epoxy, the conductivity drops by about 9% when increasing the temperature from 30 °C to 110 °C. For composites with 35–55 wt% hBN, the corresponding drop is about 25% (the differences

between the three hBN fractions were not statistically significant). Similar temperature effects were observed for IM and PBF composites.

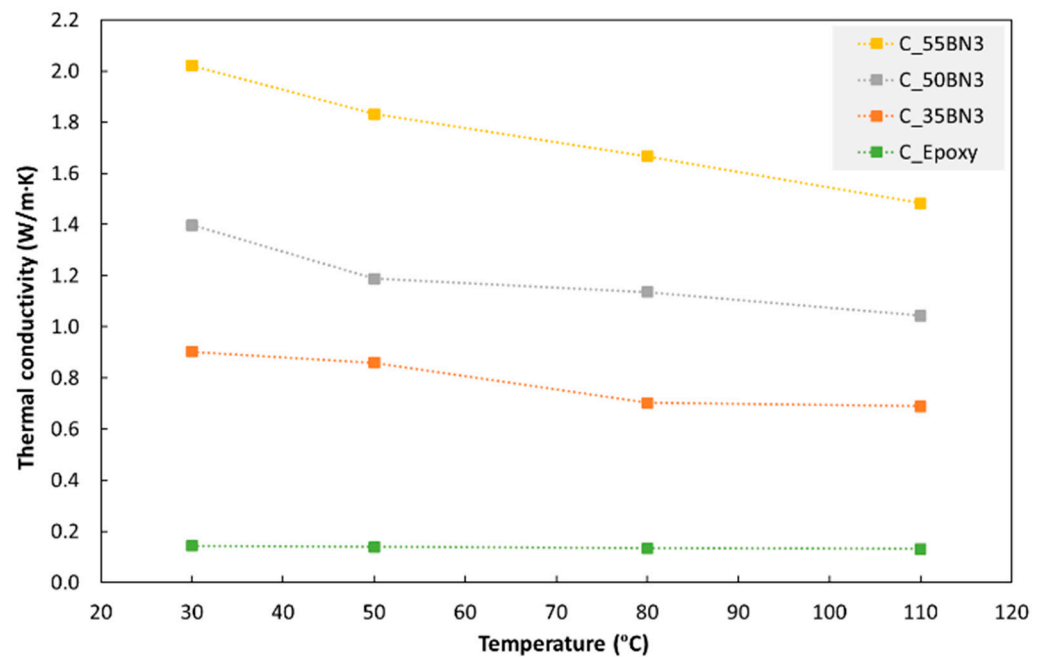


Figure 4. Thermal conductivity of cast composites with different hBN (BN3) fractions (0, 35, 50 and 55 wt%) as a function of temperature.

3.2. Hardness and Tensile Properties

The hardness values of injection moulded and cast specimens are presented in Figure 5. In both cases, the hardness increases with increasing hBN content (note that two different Shore scales are used in the figure).

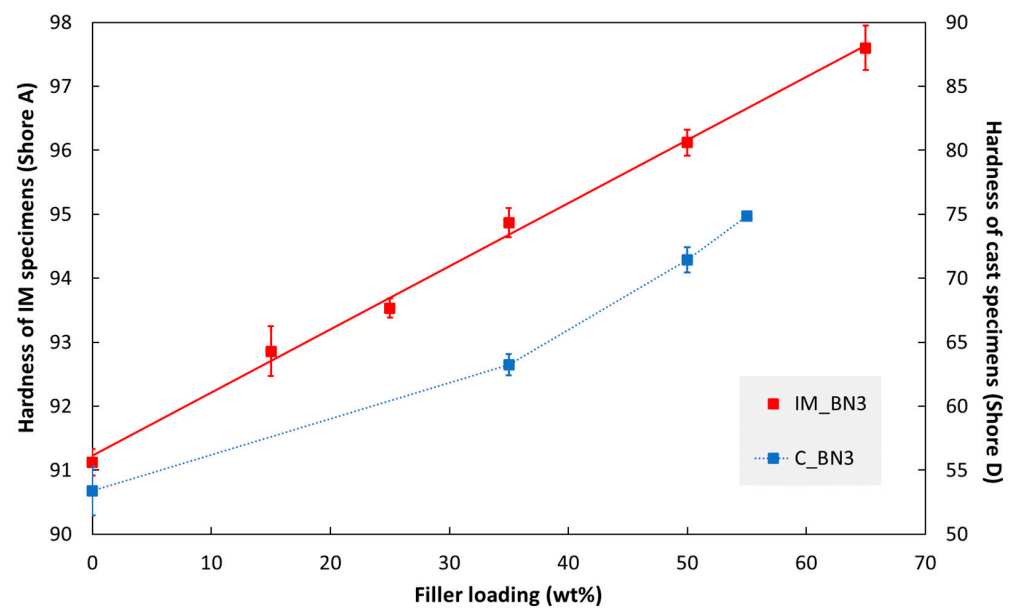


Figure 5. Hardness of injection moulded (IM) and cast (C) specimens as a function of hBN loading.

The tensile properties of injection moulded specimens are shown in Figures 6–8. The tensile modulus increases monotonously with increasing filler loading in this range. The strength and strain at break values are almost unaffected by adding 15% hBN. With 35% hBN, both these values are reduced. With 50% hBN, the strength values are higher

than that for 100% TPU, while the strain at break values are similar to those for 35% hBN. With 65% hBN, the highest strength and the lowest strain at break are observed.

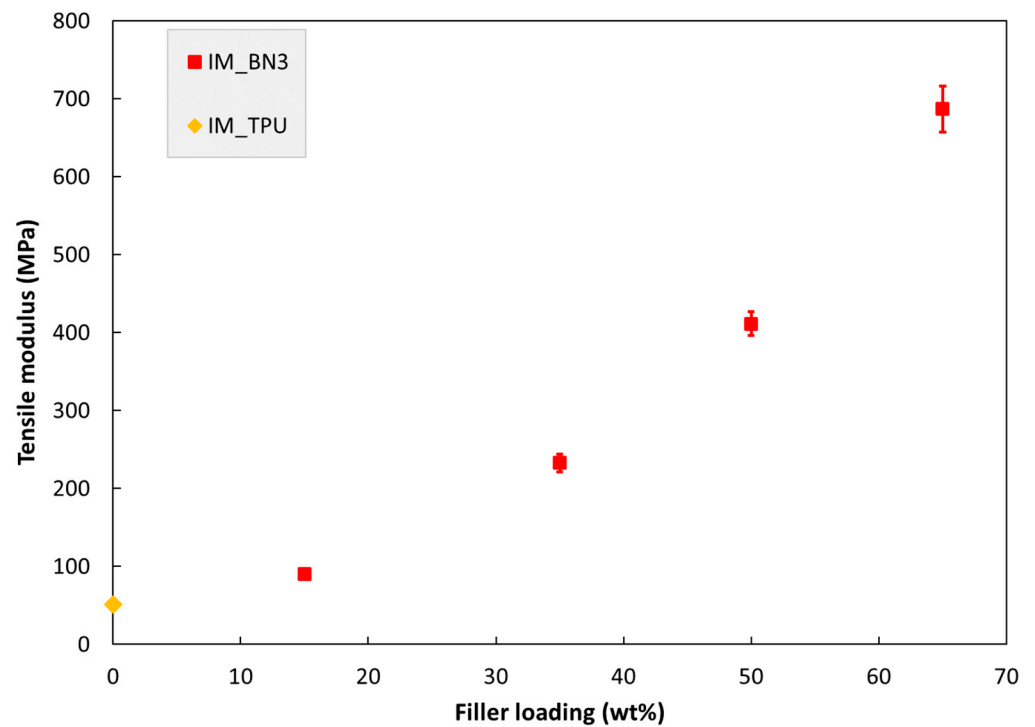


Figure 6. Tensile modulus of injection moulded specimens as a function of hBN loading. The specimen IM_TPU is 100% TPU.

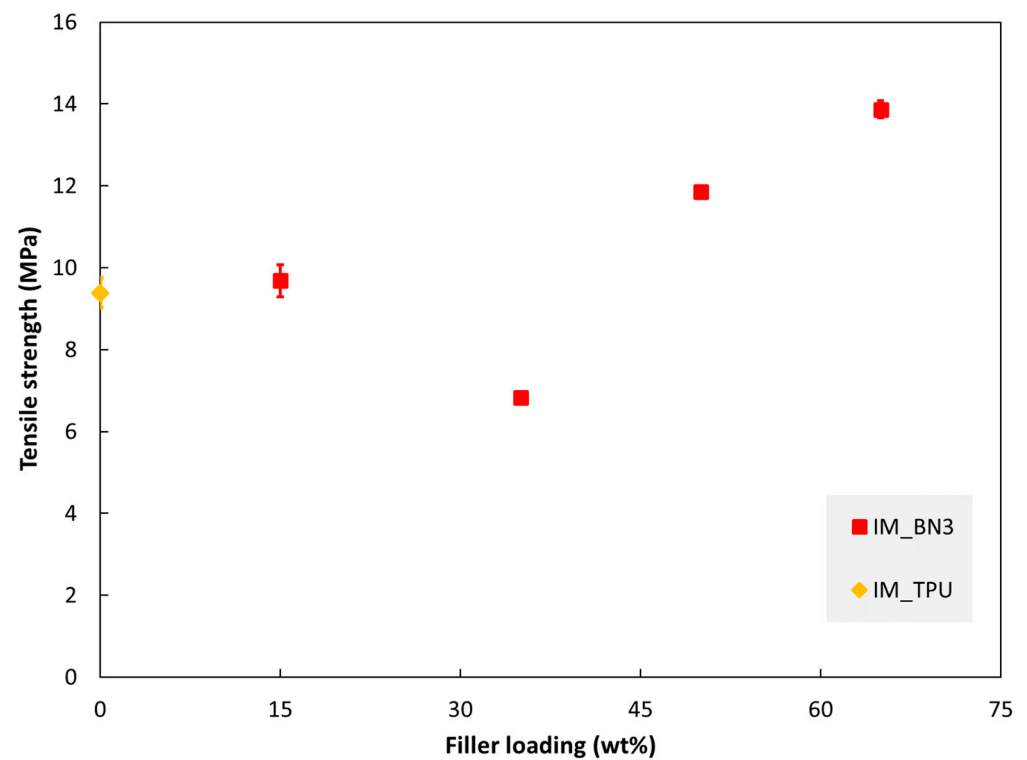


Figure 7. Tensile strength of injection moulded specimens as a function of hBN loading.

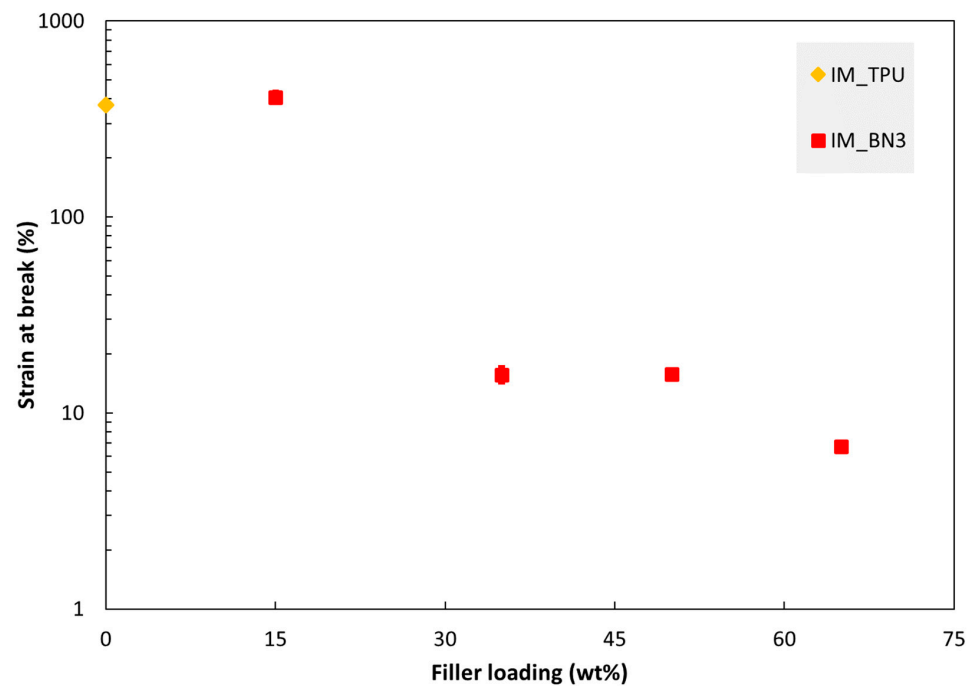


Figure 8. Strain at break of injection moulded specimens as a function of hBN loading.

The PBF composites are more brittle than the IM composites, although pure TPU is also more brittle when processed by PBF. Figure 9 shows the strain at break of some PBF specimens as the function of printing parameters. Note the similarity with the trends for the thermal conductivity in Figure 3. For the main data series in this figure (PBF_40BN3; red open squares), the laser energy density, E_V , was increased by increasing the laser power or decreasing the scanning speed. In these cases, the strain at break increases with increasing E_V . However, increasing E_V by reducing the layer thickness (L) from 0.1 to 0.08 mm reduces the strain at break, as seen for specimen PBF_40BN3_d_08. The two specimens built along the z direction (specimen names ending with “_z”) have higher strain at break than those printed in the XY plane (all the other data points in the figure).

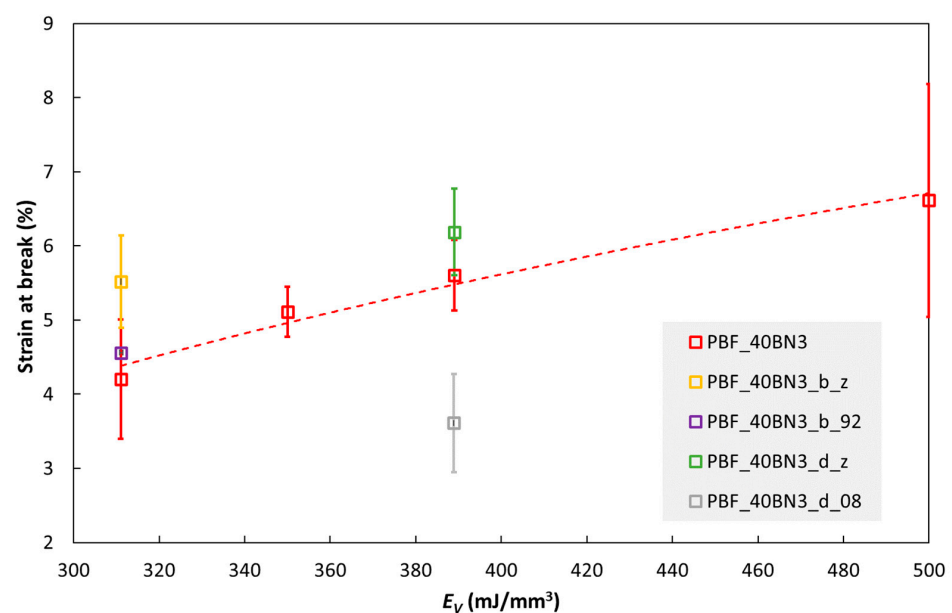


Figure 9. Strain at break of PBF specimens with 40 wt% hBN (BN3) as a function of volumetric energy density E_V . The specimen codes are explained in Table S3 in the Supplementary Materials.

3.3. hBN Platelet Orientation

Characterisation of hBN Platelet Orientation by XRD

XRD was used to characterise the orientation of hBN platelets in the polymer matrices. Figure 10 shows an example of XRD data for specimens with 35 wt% BN3, fabricated by injection moulding and casting. The diffraction patterns of the two specimens have very different 100/002 peak ratios. Figure 11 shows the effect of hBN loading on the orientation.

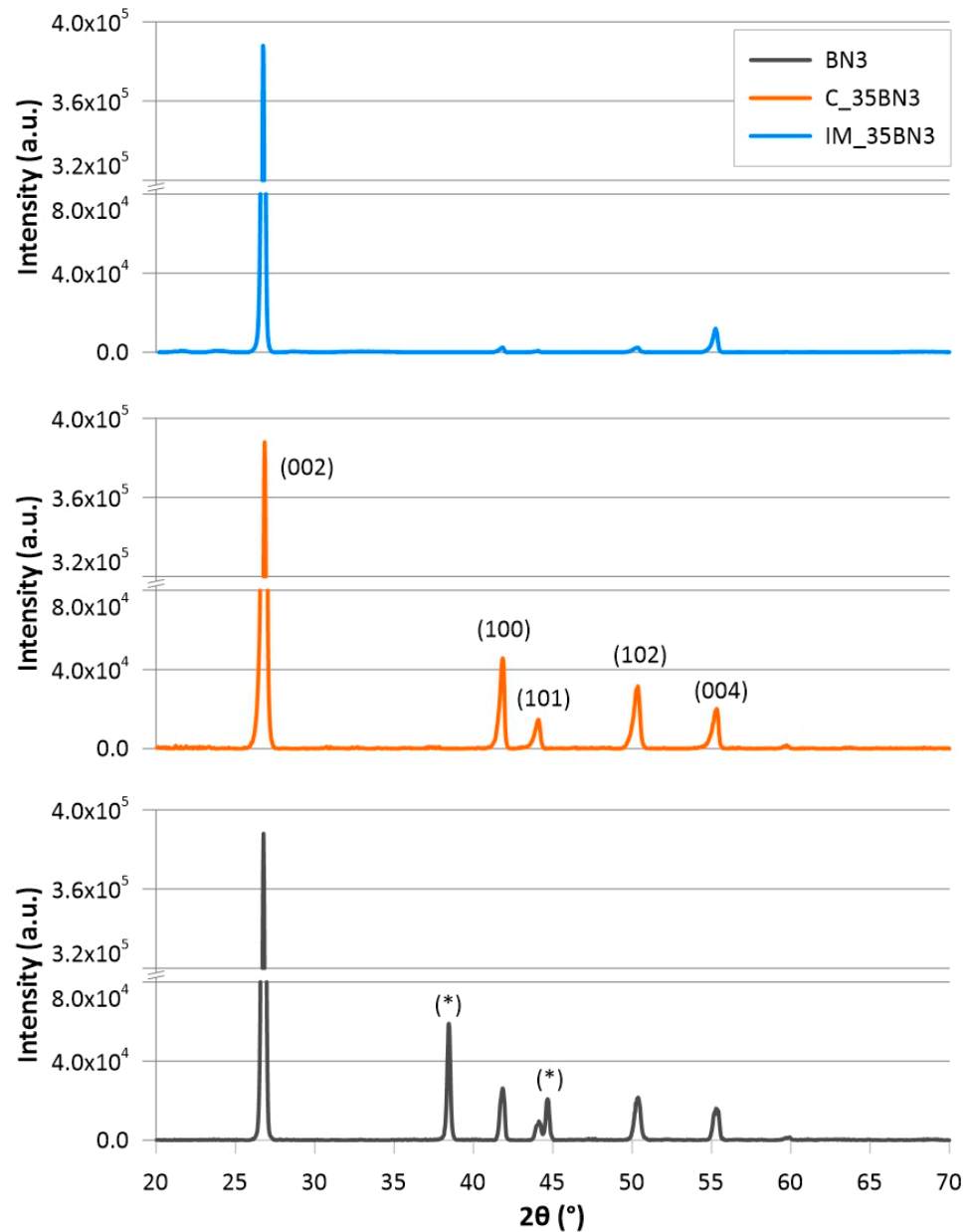


Figure 10. XRD patterns of pure BN (BN3) and specimens with 35 wt% BN3 fabricated by injection moulding (IM_35BN3) and casting (C_35BN3). The diffractogram of the pure hBN has peaks originating from the sample holder (marked with *) due to the small hBN sample size.

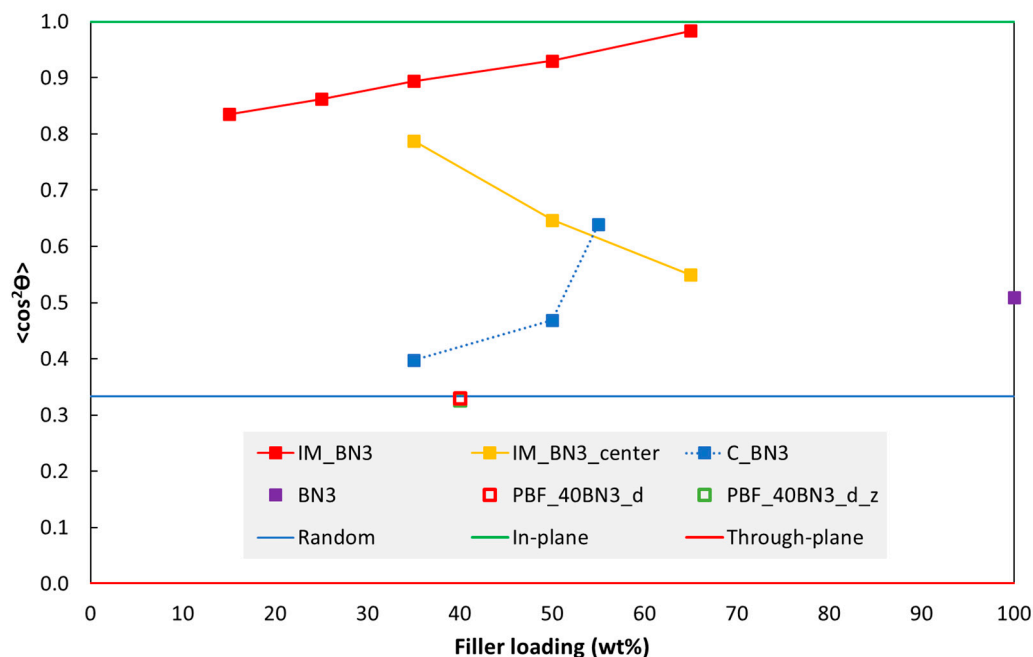


Figure 11. Orientation of hBN platelets ($\langle \cos^2\theta \rangle$ from Equation (3)) as a function of hBN loading in discs fabricated by injection moulding (IM_BN3), casting (C_BN3) and PBF (PBF_40BN3_d; PBF_40BN3_d_z). Data from the centre of an IM specimen (after grinding and polishing away half the thickness) are also included (IM_BN3_centre). The solid lines correspond to through-plane, random and in-plane orientations. The data points of the two PBF specimens overlap (open square symbols).

4. Discussion

Section 4.1 starts with a discussion of the platelet orientation in injection moulded discs, focusing on the variation through the thickness and the effect of hBN loading. Then, the orientation in discs fabricated with the two other methods are discussed briefly. Section 4.2 discusses effects of hBN loading, hBN powder type and the processing method on the measured thermal conductivity, as well as the effect of test temperature. Section 4.3 compares our experimental conductivity data with the literature data. Section 4.4 compares our experimental conductivity data with model predictions. The mechanical properties are discussed in Section 4.5.

4.1. Orientation of hBN Platelets

Data for the orientation of hBN platelets in IM discs are shown in Figure 11. This $\langle \cos^2\theta \rangle$ value is dominated by diffraction from regions near the surface, typically the outer 0.3–0.4 mm, with gradually less intensity from deeper layers. This is based on the estimated X-ray penetration depths (see Experimental Section), and the XRD measurements with half-thickness discs (specimen IM_BN3_centre in Figure 11).

The $\langle \cos^2\theta \rangle$ values of hBN platelets near the surface of a “full” disc increases with increasing hBN loading, while the opposite trend is observed for “half-thickness” discs.

It can be questioned if the observed effect of hBN loading can be an artefact due to the X-ray absorption coefficient varying with the hBN loading. If we assume that the orientation is highest near the surface of the 2 mm disc and the linear X-ray absorption coefficient increases with BN loading (see Experimental Section), this could contribute to the observed trends; a higher BN loading would result in less diffracted intensity from deeper layers with lower orientation (or higher orientation for “half-thickness” discs), and, hence, a higher observed $\langle \cos^2\theta \rangle$ value as an artefact. It is difficult to quantify this effect because we do not know the orientation distribution through the cross section a priori. However, with the estimated low effect of hBN loading on the absorption coefficient, we

believe that the effects of hBN loading on the $\langle \cos^2\theta \rangle$ values in Figure 11 reflect real effects in the IM specimens.

A $\langle \cos^2\theta \rangle$ value close to 1 means that hBN platelets are highly in-plane oriented. Our results, as shown in Figure 11, indicate that the centre region of the IM specimen (IM_BN3_centre) has lower $\langle \cos^2\theta \rangle$ values than the region near the surface. For the IM disc with 35 wt% hBN, the $\langle \cos^2\theta \rangle$ value of the half-specimen IM_BN3_centre is quite close to that of the full specimen IM_BN3, implying a more uniform orientation through the cross-section of the specimen.

A variation in platelet orientation through the disc thickness agrees with numerical simulations of platelet orientation induced by the injection moulding process (Figure S4 in the Supplementary Materials). A variation from the surface to the central region (core) is well known for IM parts, in particular for fibres [45], but also for plate-like particles [46]. The typical orientation resulting from the flow between two parallel mould cavity walls is a core-shell-skin structure with a shell layer of plates aligned along the walls (due to the high shear strain rate in this position) and a core layer with lower in-plane orientation, or even transverse orientation. Between the core and shell layers, there is a transition layer. The outer-most skin of a moulded part is deposited directly from the fountain flow at the flow front, and this skin layer typically has lower in-plane orientation than the shell layer.

As mentioned in Section S7 in the Supplementary Materials, the simulated maximum and minimum orientation through the thickness can be tuned by model parameter. The effect of hBN loading on increasing the maximum orientation through the thickness while reducing the minimum orientation value, as in Figure 11, can also be modelled qualitatively by decreasing the value of the particle–particle interaction parameter C_I (Supplementary Materials). A similar experimental trend of the orientation in the shell layer increasing with particle loading was observed for glass fibres [45]. However, according to [47], there is no clear dependency of C_I on the filler loading, and different experiments have showed contradictory results.

For cast discs of epoxy with hBN, the $\langle \cos^2\theta \rangle$ value also increases with increasing hBN loading (Figure 11), although the values are lower than for the IM discs. For an hBN loading of 35 wt%, $\langle \cos^2\theta \rangle$ is close to 1/3, implying random orientation. A random orientation would be expected due to the mixing prior to casting, and was also observed by Yuan et al. [4] and Lin et al. [21] in their reference specimens. The higher $\langle \cos^2\theta \rangle$ values (preferred in-plane orientation) for higher hBN loadings could be related to the high viscosity and the specimen preparation. Due to the high viscosity, the material had to be pressed into the open mould with a tool in order to make a specimen without voids. This could have induced an in-plane orientation of platelets, especially near the surfaces. A tendency for platelet stacking due to a high concentration [4,14] (less space for the platelets to arrange freely) could contribute to the orientation at a certain distance from the surface as well.

The two PBF discs with 40 wt% hBN in Figure 11, printed in the XY plane and “standing”, respectively, have a $\langle \cos^2\theta \rangle$ value close to 1/3, i.e., a random orientation. There are several studies of polymer PBF with added glass or carbon fibres, and these report a preferred fibre orientation in the powder spreading direction, i.e., the direction the powder recoater unit is travelling [48–50]. The degree of orientation depends on the type of recoater (roller, blade), the recoater speed and the layer thickness. The orientation mechanism is the shear flow induced by the recoater. Numerical models have been used to understand the flow dynamics in the recoating/packing process, and also the formation of voids [51]. In many cases, the fibre orientation is low. Hence, the nearly random orientation of the hBN platelets in our study is in line with the literature. The flow dynamics of the hBN platelets may also differ from that of the fibres in the literature. At the surface of the recoated layer, there may be some platelets being “combed down” to an in-plane (XY) orientation by the recoater. These oriented platelets, in combination with possible small voids/gaps between the fused layers, may have a negative effect on the thermal conductivity perpendicular to the layers, as well as on the mechanical properties.

4.2. Thermal Conductivity

The thermal conductivity increases with increasing hBN loading for all three processing methods in this study. The slope of the thermal conductivity vs. filler loading appears to increase at around 30 wt% filler (about 18 vol% for IM hBN/TPU), and with a further increase at loadings from about 50 wt% (about 34 vol% for IM hBN/TPU).

According to experimental literature on composites with hBN, the percolation threshold for thermal conductivity is about 20–25 vol% for randomly oriented platelets (studies with hBN size in the range of 3–8 μm [52], average particle size of 5 μm [21] and no size given [53]). For highly through-plane-orientated platelets, the threshold is reported to be about 10–15 vol% (studies with average particle sizes of 25 μm [54], 8 μm [55] and 5 μm [21]). Hence, the thermal percolation threshold depends on the orientation of the hBN platelets in the polymer matrix. Above the percolation threshold, the platelets form thermally conductive pathways in the polymer matrix. We will return to a discussion of conductivity vs. hBN fraction in the next section, when comparing experimental data with model predictions.

Injection moulded composites have lower conductivity than cast composites. This is due to the preferred in-plane orientation of the hBN platelets in the former case, as shown by the XRD data discussed in Section 4.1. Yuan et al. [4] also showed that a high in-plane orientation of the platelets leads to a low conductivity enhancement in the through-plane direction.

In a study of injection moulded polyamide 6 with Cu platelets, Heinle et al. [39] observed similar platelet orientations, and orientation variations through the specimen thickness, as in our study. Heinle et al. moulded specimens with different thicknesses (2, 3 and 4 mm), and the core/shell ratio increased with increasing specimen thickness (2, 3 and 4 mm). Due to a thicker core, 4 mm thick specimens had almost a three times higher through-plane conductivity than 2 mm thick specimens (for 40 vol% platelets). Heinle et al. also measured the conductivity in different directions; through-plane, in-plane along the flow direction and in-plane transverse to the flow. For 40 vol% platelets, the conductivities were almost the same in the two first directions, while it was almost two times higher in the third direction.

In addition to BN3, two other hBN types (BN1 and BN2) were used in some experiments (see Supplementary Materials, Sections S1 and S9). BN1 has smaller platelets than BN2 and BN3. BN2 mainly contains hBN platelets, while BN3 contains both platelets and spherical agglomerates of platelets (Figure S2a).

BN2 results in higher conductivity than BN3. Although some agglomerates are broken up during processing, the lower conductivity with BN3 is probably due to platelets being less dispersed. Powders with hBN agglomerates (as BN3) are claimed to have more isotropic properties and easier processing due to a lower viscosity from spherical fillers [5].

With the same hBN weight fraction in the composite, BN1 results in lower thermal conductivity than the two other powders. This effect is observed for both IM and PBF specimens, at all temperatures. The smaller platelets in BN1 probably results in a larger total surface area and smaller average distance between platelets in the composite (if randomly distributed). A larger surface area will reduce the conductivity of the composite if the matrix-filler interfacial thermal resistance is high [56]. On the other hand, above a certain platelet fraction, a reduction in the average distance between platelets can increase the conductivity due to a higher possibility of platelets coming into contact, thus leading to conducting “chains” of platelets and, consequently, percolation [57]. In our case, the negative effect of increased surface area seems to dominate. Different powders may also have varying tendencies for agglomeration and deagglomeration during processing, and this affects the conductivity. Li et al. [58] reported a similar size effect on thermal conductivity in polyimide films with micro- and nano-sized BN.

Note that the interfacial thermal resistance refers to the combined effect of two thermal resistances [59]: (1) the thermal contact resistance caused by poor mechanical and chemical bonding between the two phases and (2) the thermal boundary resistance due to differences

in the physical properties of the two phases. In our case, the former resistance is probably dominating due to poor adhesion between the polymer matrix and the hBN surface.

The surface of the hBN particles can be modified chemically in order to improve the dispersion of hBN particles and achieve a stronger hBN/polymer interface, thereby improving the thermal conductivity and the mechanical properties [16,19,60–62]. There are wet and dry routes, including covalent methods (e.g., oxidation of hBN with a strong acid or base at high temperature and/or high pressure), non-covalent methods (e.g., coatings of organic compounds or inorganic particles) and solid-state methods (e.g., thermal treatment, high-energy radiation or strong mechanical forces) [16]. However, the chemical inertness and oxidation resistance of hBN make the functionalisation of hBN challenging.

In our study, chemical functionalisation was tried for the BN₃ powder. The hBN particles were treated with a strong oxidation agent (nitric acid) followed by silanization (using the aminosilane coupling agent APTES) [19]. However, the coupling agent could not be attached to the hBN particles based on analyses using IR spectroscopy and energy dispersive X-ray spectroscopy.

The thermal conductivity of the polymer matrices and the hBN/polymer composites decreases as a function of the temperature (Figure 4). The relative decrease is more pronounced for the composites. This can be due to the mismatch in thermal expansion coefficients between the platelets (low expansion coefficient) and the polymer matrix (high expansion coefficient). When increasing the temperature, the mismatch will result in an increase in the distance between adjacent filler platelets in thermal pathways, and may also induce gaps between platelets and matrix. Both effects will reduce the conductivity of the composite [51,54].

4.3. Comparison with Published Thermal Conductivity Values for Composites with hBN

Although the main objective of this paper is to contribute to the understanding of thermal conductivity vs. hBN loading, hBN platelet orientation, etc., via processing method, it is also interesting to compare with published values for similar composites, as in Table 1. However, such comparisons are challenging, due to differences in mixing/processing methods, hBN loading, hBN particle size and matrix material.

- Compression moulded hBN/epoxy in ref. [7] achieved a thermal conductivity of 7 W/m·K with 95 wt% hBN. Cast hBN/epoxy in ref. [8] reached a thermal conductivity of 5.3 W/m·K with 57 vol% hBN (with size of 5–11 µm), but values for lower hBN loadings were not presented. Our highest thermal conductivity for cast hBN/epoxy composites was 2.0 W/m·K for 55 wt% (about 28 vol%) hBN (with size of ca. 20 µm). Our casting resin could not be processed with a filler loading higher than this.
- For injection moulding, ref. [10] achieved 3.7 W/m·K for PE with 50 vol% hBN with particle diameter 4–5 µm. Our injection moulded composite based on TPU with 65 wt% hBN (about 48 vol%) reached a thermal conductivity of 2.1 W/m·K. The higher value in ref. [10] could be due to a better dispersion and more homogeneous distribution of hBN particles.
- For PBF composites, refs. [12,13] achieved relatively higher thermal conductivities than in our study. This could be due to synergetic effects of using two filler types (hBN and Al₂O₃ in ref. [12], hBN and AlN in ref. [13]).
- For PBF composites with only one filler type, our results are similar to those in ref. [11] with regard to (hBN/PA12). Ref. [11] reported a thermal conductivity of 0.55 W/m·K with 40 wt% hBN (275% higher than the pure PA12 processed with PBF). Our best PBF composite with 40 wt% hBN had a thermal conductivity of 0.56 W/m·K (ca. 460% higher than the pure TPU processed with PBF).

Hence, hBN particle type and mixing method are important factors, as well as surface treatment of the particles. The matrix material, in particular its viscosity, must be carefully selected in order to obtain processable composites with higher particle loadings. Furthermore, synergetic effects can be achieved when using two particle types.

4.4. Experimental Thermal Conductivity vs. Model Predictions

Comparing the experimental thermal conductivity data with models can aid the discussion. Many models have been developed for the thermal conductivity of composites. This section presents data obtained with four models (see Supplementary Materials for details and also some comparisons). One reason for including these four models is that they provide quite different predictions. Many articles only use one of these models without arguing for their choice of model. Furthermore, one of the models (the Sun model) is quite new, and, to the best of our knowledge, we are the first to use and evaluate it (apart from the cited article by Sun et al.).

4.4.1. The Thermal Conductivity Model of Nan et al.

Nan et al. [36] introduced a Maxwell–Garnett-type effective medium approximation (EMA) model (see Section S11 in the Supplementary Materials) which has been used in many studies of hBN/polymer composites [4,20,53]. The Nan model includes effects of particle shape (ellipsoids, which can represent platelets), particle orientation and interfacial thermal resistance. However, it is limited to particles with isotropic thermal conductivity, while hBN platelets are anisotropic. Furthermore, this model does not take into account filler-filler contact or nonuniform particle distributions (nor do any of the models in this section). Hence, it is restricted to low filler fractions, and it cannot predict the percolation threshold, or effects of non-homogeneous platelet distributions or poor platelet dispersion (stacks and agglomerates).

Some insight can be gained by comparing our experimental data with the Nan model, with different values for the filler-matrix interfacial thermal resistance (R_{BD}) and platelet orientation ($\langle \cos^2\theta \rangle$) in the model. Section S11 in the Supplementary Materials provides details about the Nan model and a background for the model parameters used in our study, including a simple sensitivity analysis.

For the injection moulded discs, a simplified picture is that the average platelet orientation through the disc thickness is almost independent of hBN loading, with $\langle \cos^2\theta \rangle$ of around 0.8, referring to the average of red and yellow solid square symbols in Figure 11. Figure 12 compares experimental data with the Nan model with relevant model parameters. For hBN loadings of up to about 15 vol%, the experimental data are merely below the model predictions (almost on the green solid line corresponding to $\langle \cos^2\theta \rangle = 0.85$ and $R_{BD} = 10^{-6} \text{ m}^2\text{W/K}$). This is reasonable; even though the experimental $\langle \cos^2\theta \rangle$ (average over the thickness) may be comparatively lower than 0.85, the R_{BD} value may be lower than $10^{-6} \text{ m}^2\text{W/K}$, and the platelets are probably not homogeneously distributed and not perfectly dispersed (from agglomerates).

The steeper slope for the experimental data in the range 15–35 vol% is probably due to the formation of some platelet-platelet contact, resulting in local conductive paths and a boost in conductivity. This could be represented as a reduction in the effective R_{BD} value for the Nan model (here, “effective” means that there is some filler-filler contact in the specimens which is not accounted for in the model, in which R_{BD} is strictly defined to represent filler-matrix contact). Other causes, however less likely, could be that there is a substantial core in the disc with a lower $\langle \cos^2\theta \rangle$ than which was captured by our measurements, or that the filler-matrix resistance decreases with increasing hBN loading.

The last experimental data point at that 48 vol% is above the Nan model predictions with reasonable input parameters. The Nan model predicts this datapoint if $\langle \cos^2\theta \rangle$ is set to 0.67 and R_{BD} is set to 0. However, the $\langle \cos^2\theta \rangle$ value is probably higher than 0.67, and the mismatch between the model and the experimental data is probably due to even more platelet-platelet contact in the specimen (than at lower loadings). Finally, note that BN3 data were used in Figure 12 while hBN-type BN2 resulted in even higher conductivity (Figure S7 in the Supplementary Materials), while having roughly the same platelet aspect ratio.

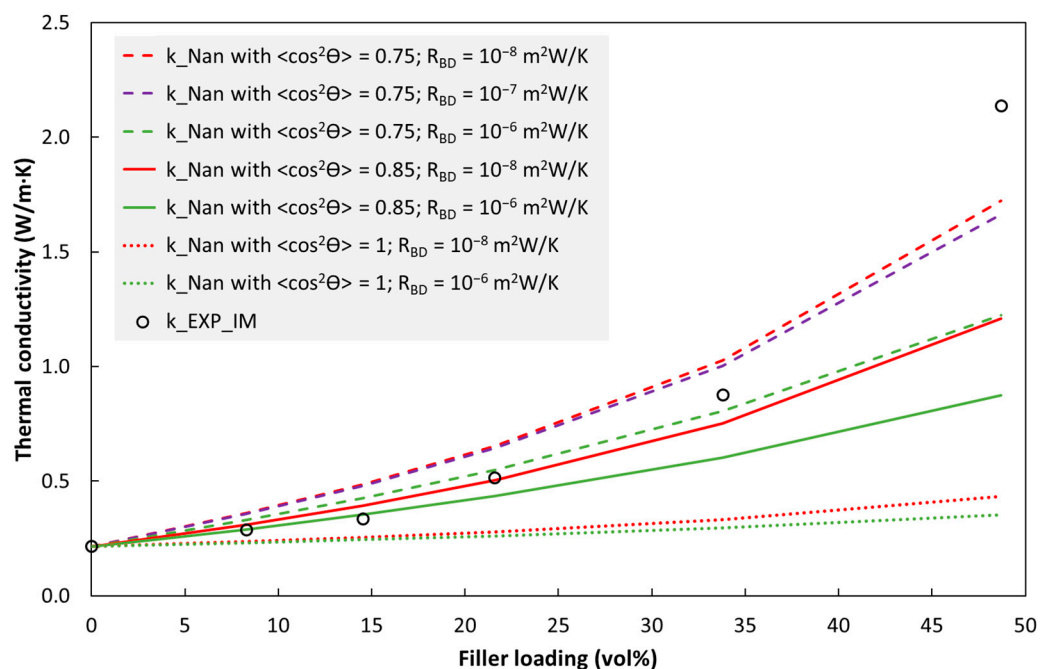


Figure 12. Nan model compared with the measured values for injection moulded BN3/TPU (k_{EXP_IM}). Model parameters are given in the legend and in the Supplementary Materials. For all $\langle \cos^2\theta \rangle$ values in this figure, the curves for $R_{BD} = 0$ and $10^{-8} \text{ m}^2\text{W/K}$ almost overlap.

A similar trend is observed for the experimental data of cast specimens vs. the Nan model, see Figure S13 in Section S12 in the Supplementary Materials. Hence, also in the cast specimens, platelet-platelet contact seems to form at high hBN loadings.

4.4.2. The Thermal Conductivity Model of Ordóñez-Miranda et al.

Ordóñez-Miranda et al. [37] combined the Nan model above with the Bruggeman integration principle. The resulting model is claimed to be better at high particle volume fractions than the Nan model. However, Ordóñez-Miranda et al. only considered the case with a random orientation of particles.

As shown in Figure S14 in the Supplementary, the Ordóñez-Miranda model predictions are quite different from those of the Nan model (Figure S13). When comparing with the experimental data for cast specimens, and assuming a random orientation of platelets, the Ordóñez-Miranda model is closer to the experimental values than the Nan model when using relevant values for the interfacial thermal resistance. Furthermore, with the Ordóñez-Miranda model, only a very small reduction in interfacial thermal resistance (corresponding to the formation of some chains of platelets effective in the through-plane direction) is needed to capture the last data point (with an hBN volume fraction of 38.5%). The Nan model with random orientation cannot capture this data point, even with zero interfacial thermal resistance.

4.4.3. The Thermal Conductivity Model of Sun et al.

Based on a finite element model, Sun et al. [38] derived an analytical model for the thermal conductivity of hBN/polymer composites. In addition to the effects included in the Nan model above, the Sun model also takes into account the anisotropic thermal conductivity of the hBN platelets. Hence, in principle, it should be more accurate than the Nan model. However, the Sun model has the same limitations as the models above regarding an absence of filler-filler contact and a homogeneous platelet distribution. The Sun model and our implementation are presented in Section S13 of the Supplementary Materials.

The Sun model generally predicts lower conductivities than the Nan model. For the cast specimens, the Sun model underestimates the conductivity for all three data points in

the interval 20–40 vol% hBN, see Figure S15 in the Supplementary Materials. As for the Nan model, the experimental data has a larger curvature vs. filler loading (vol% hBN) than the model predictions.

4.4.4. The Lewis-Nielsen Thermal Conductivity Model

This simple model has been used in studies of composites with platelets [39,63]. In addition to the conductivities of the two phases, the model has two semi-empirical constants (see Section S14 in the Supplementary Materials for details). The first constant represents the maximum volume fraction (often 0.8–0.85 for platelets [39,63]), and the second is a geometry factor for the particles. This geometry factor represents the effective particle shape in the direction in which the conductivity is measured. Hence, the average particle orientation is embedded in this geometry factor. The drawback of this model is that the geometry factor is mainly an empirical fitting parameter. Some comparisons between model predictions and experimental data are shown in Section S14 in the Supplementary Materials.

Heinle et al. [39] used a three-layer Lewis-Nielsen model for the through-plane thermal conductivity of injection moulded specimens. The three layers through the thickness of the specimens represented the two symmetric shell layers (with high in-plane orientation of Cu platelets) and the core layer (with lower orientation). This model resulted in good predictions of thermal conductivity vs. the Cu platelet volume fraction for different specimen thicknesses (2, 3 and 4 mm), which had different shell/core ratios. The model also predicted the conductivity in different directions (through-plane, in-plane along the flow direction and in-plane transverse to the flow).

4.5. Hardness and Tensile Properties

The high stiffness and strength of hBN platelets can, in principle, enhance the hardness, stiffness and strength of thermoplastics. However, the interphase between the two is weak [5], thus reducing the effectiveness of the platelets and rather inducing defects which reduce mechanical properties, in particular those involving strains above the elastic limit, i.e., most properties except the modulus of the composite. Prindl [64] injection moulded three thermoplastic materials (a polypropylene, a polyamide 6 and a thermoplastic elastomer) with hBN and found that properties such as strain at break, tensile strength and impact strength generally decreased when adding hBN. The least negative effect was observed for the polyamide 6.

The hardness enhancement effect of hBN platelets is about the same in injection moulded and cast specimens (Figure 5). The slightly larger relative enhancement in the former case could be related to the platelet concentration either in the outer layer or the platelet orientation.

The relative modulus enhancement (Figure 6) is larger than the relative hardness enhancement. This was expected due to the lower strain level for the modulus determination. Nevertheless, the modulus enhancement is rather low, given the high modulus of the hBN platelets relative to that of the TPU.

Regarding tensile strength and strain at break vs. hBN fraction (Figures 7 and 8), the trends above 15% hBN could be explained by two mechanisms which occur when adding fillers. Increasing the hBN content reduces the ductility, i.e., reduces the strain at break. However, increasing the hBN content also reinforces the material, i.e., shifts the stress–strain curve upwards (to a higher stress for a given strain). From 15 to 35% hBN, the first mechanism dominates both the strength and strain at break, while from 35 to 50%, the second mechanism dominates.

In addition to BN3, another hBN type (BN2) was also used in some tests (material data and results are shown in Sections S1, S5 and S10 in the Supplementary Materials). BN2 mainly contains hBN platelets, while BN3 contains both hBN platelets and spherical agglomerates of hBN platelets (Figure S2a). There was no clear effect of hBN type on the tensile modulus. This could be due to the low strain, for which effects of particle size may be small. For the strength and strain at break, there are some effects of hBN type

that are statistically significant. Especially at 35% hBN, but also at 50% hBN, BN2 results in a higher strength than BN3. This could be due to the agglomerates in BN3. At 50% hBN, the higher strength with BN2 could partly be due to better particle dispersion (and no agglomerates) and less micro-voids and imperfections. This agrees with the fact that BN2 also resulted in the highest thermal conductivity at this loading (see Figure S7 in the Supplementary Materials).

The PBF composites are more brittle than the IM composites due to voids caused by the thermal history and absence of melt flow in the PBF process (the flow in the IM process may relatively improve the wetting of hBN particles with TPU melt). In addition, the type of recoater used may not be optimal for such composites, see also Section 4.1. A decrease in tensile properties when adding hBN was also observed in the PBF study by Yang et al. [11], although they used hBN/PA12 co-powders, prepared by solid-state shear milling and cryogenic pulverisation.

Increasing the energy density in the PBF process improves the tensile strength and strain at break to a certain degree (Figure 9) due to better melting and fusion. However, the energies are high and there is a risk for the chemical degradation of the TPU. It may be that the hBN platelets reflect some of the laser energy, and they will also spread the heat away from the area hit by the laser beam.

The PBF specimens built along the z direction have higher strength and higher strain at break (and also higher thermal conductivity) than those printed in the XY plane. Usually, the opposite is observed for PBF, whereby specimens printed in the z direction have lower strength and strain at break. In our case, it could be that the bulk temperatures in the part during printing are higher for parts printed in the z direction. A difference in temperature history could mean a difference in achieving some TPU-hBN adhesion and reducing voids, and this could dominate over the usual “weakest chain” interlayer failure of PBF parts.

5. Conclusions

This study has provided new insights on the effects of the fabrication method and hBN loading on the thermal conductivity and mechanical properties of hBN/polymer composites. Injection moulding, casting and powder bed fusion were utilised for fabricating composite specimens. The hBN platelet orientation in the specimens was characterised by XRD measurements.

Injection moulding induced a preferred orientation of the platelets, with the platelet normal along the thickness direction of the specimens. Furthermore, the orientation varied through the thickness of the moulded specimens, and it increased with increasing hBN fraction. The platelet orientation in injection moulded specimens agreed qualitatively with numerical simulations. Casting only resulted in a low preferred orientation, and powder bed fusion resulted in an almost random orientation.

With the process equipment used, the maximum practical hBN loading was 65 wt% for injection moulding with TPU as matrix, 55 wt% for casting with epoxy and 40 wt% for powder bed fusion with TPU. The thermal conductivity of the composites increased with increasing hBN loading. The highest thermal conductivity in this study (2.1 W/mK) was obtained with injection moulding with 65 wt% hBN. However, for a given hBN loading, casting resulted in a higher thermal conductivity than the other two methods. This was partly due to the platelet orientation in cast specimens (in particular being more favourable than the orientation induced by injection moulding) and partly due to the matrix material (the epoxy probably resulting in a relatively lower interfacial thermal resistance, and also less porosity).

The conductivity and orientation data were discussed by a comprehensive comparison with four models for the thermal conductivity of composites. At low hBN loadings, the Nan model resulted in a fair prediction of the conductivity. Underprediction at higher loading is interpreted to be due to the fact that this model does not take into account the formation of platelet-platelet contact, resulting in local conducting paths (pre-percolation). The Ordóñez-Miranda model is limited to a random platelet orientation, but it predicts the experimental

data for cast specimens better than the Nan model. Hence, the Ordóñez-Miranda model should be generalised to account for particle orientation.

Adding hBN increased the hardness and tensile modulus of the materials. For injection moulded specimens, the tensile strength had a minimum vs. hBN loading, while the strain at break decreased monotonously, with a sharp reduction between 15 and 35% hBN. These trends can be explained by two mechanisms which occur when adding hBN: reinforcement and embrittlement. Powder bed fusion resulted in even more brittle composites, and some type of hBN-polymer compatibilization is probably needed to achieve adequate mechanical properties, in addition to process enhancements.

Supplementary Materials: The following supporting information can be downloaded at: <https://www.mdpi.com/article/10.3390/polym15061552/s1>. The Supplementary Materials contain additional details about materials (Sections S1 and S3) and experiments (Sections S2, S4–S6), as well as additional results on numerical simulation of platelet orientation in injection moulded discs (Section S7); DSC measurement (Section S8); additional data for thermal conductivity and tensile properties with some other hBN types (Sections S9 and S10); and thermal conductivity models vs. experimental data (Sections S11–S14). References [4,5,20,36–40,53,55,65–67] are cited in the Supplementary Materials.

Author Contributions: Conceptualisation and Methodology, N.B.D.D. and E.A.; Formal Analysis and Investigation, N.B.D.D., E.A. and K.E.A.; Writing—Original Draft Preparation, N.B.D.D. and E.A.; Writing—Review and Editing, N.B.D.D., E.A., K.E.A., H.-V.N. and K.I.; Supervision, E.A. and K.I.; Project Administration and Funding Acquisition, K.I. All authors have read and agreed to the published version of the manuscript.

Funding: This work was funded by the Research Council of Norway through the BIA program (grant number: 269618; Mechanical miniaturization in interventional medical instruments project), and by the Norwegian Micro- and Nano-Fabrication Facility (295864 NORFAB III).

Institutional Review Board Statement: Not applicable.

Data Availability Statement: The raw/processed data required to reproduce these findings cannot be shared at this time due to legal restrictions.

Acknowledgments: The authors gratefully acknowledge Paul McMahon and Marius Johansen at SINTEF Industry; Jeyanthinath Mayandi at the University of Oslo; Erik Kalland at Conpart AS; Tri Quang Bui at Østfold University College; and Zekija Ramic, Svein Mindrebøe, Tayyib Muhammad, Chaoqun Cheng at University of South-Eastern Norway for their enthusiastic assistance with laboratory work. We sincerely thank Terje Finstad at the University of Oslo and Helge Kristiansen at Conpart AS for valuable discussions.

Conflicts of Interest: The authors declare no conflict of interest.

References

1. Tummala, R. *Fundamentals of Microsystems Packaging*; McGraw-Hill: New York, NY, USA, 2001.
2. Bhanushali, S.; Ghosh, P.; Simon, G.; Cheng, W. Copper Nanowire-Filled Soft Elastomer Composites for Applications as Thermal Interface Materials. *Adv. Mater. Interfaces* **2017**, *4*, 1700387. [[CrossRef](#)]
3. Bahru, R.; Hamzah, A.; Mohamed, M.A. Thermal management of wearable and implantable electronic healthcare devices: Perspective and measurement approach. *Int. J. Energy Res.* **2020**, *45*, 1517–1534. [[CrossRef](#)]
4. Yuan, C.; Duan, B.; Li, L.; Xie, B.; Huang, M.; Luo, X. Thermal Conductivity of Polymer-Based Composites with Magnetic Aligned Hexagonal Boron Nitride Platelets. *ACS Appl. Mater. Interfaces* **2015**, *7*, 13000–13006. [[CrossRef](#)]
5. Chen, H.; Ginzburg, V.; Yang, J.; Yang, Y.; Liu, W.; Huang, Y.; Du, L.; Chen, B. Thermal conductivity of polymer-based composites: Fundamentals and applications. *Prog. Polym. Sci.* **2016**, *59*, 41–85. [[CrossRef](#)]
6. Li, D.; Zeng, D.; Chen, Q.; Wei, M.; Song, L.; Xiao, C.; Pan, D. Effect of different size complex fillers on thermal conductivity of PA6 thermal composites. *Plast. Rubber Compos.* **2019**, *48*, 347–355. [[CrossRef](#)]
7. Zhu, Z.; Wang, P.; Lv, P.; Xu, T.; Zheng, J.; Ma, C.; Yu, K.; Feng, W.; Wei, W.; Chen, L. Densely packed polymer/boron nitride composite for superior anisotropic thermal conductivity. *Polym. Compos.* **2018**, *39*, E1653–E1658. [[CrossRef](#)]
8. Xu, Y.; Chung, D.D.L. Increasing the thermal conductivity of boron nitride and aluminum nitride particle epoxy-matrix composites by particle surface treatments. *Compos. Interfaces* **2000**, *7*, 243–256. [[CrossRef](#)]

9. Tanimoto, M.; Yamagata, T.; Miyata, K.; Ando, S. Anisotropic thermal diffusivity of hexagonal boron nitride-filled polyimide films: Effects of filler particle size, aggregation, orientation, and polymer chain rigidity. *ACS Appl. Mater. Interfaces* **2013**, *5*, 4374–4382. [[CrossRef](#)]
10. Lee, G.-W.; Park, M.; Kim, J.; Lee, J.; Yoon, H.G. Enhanced thermal conductivity of polymer composites filled with hybrid filler. *Compos. Part A Appl. Sci. Manuf.* **2006**, *37*, 727–734. [[CrossRef](#)]
11. Yang, L.; Wang, L.; Chen, Y. Solid-state shear milling method to prepare PA12/boron nitride thermal conductive composite powders and their selective laser sintering 3D-printing. *J. Appl. Polym. Sci.* **2020**, *137*, 1–13. [[CrossRef](#)]
12. Yuan, Y.; Wu, W.; Hu, H.; Liu, D.; Shen, H.; Wang, Z. The combination of Al₂O₃ and BN for enhancing the thermal conductivity of PA12 composites prepared by selective laser sintering. *RSC Adv.* **2021**, *11*, 1984–1991. [[CrossRef](#)]
13. Zhang, X.; Wu, W.; Zhao, T.; Li, J. The combination of AlN and h-BN for enhancing the thermal conductivity of thermoplastic polyurethane composites prepared by selective laser sintering. *J. Appl. Polym. Sci.* **2022**, *139*, e53051. [[CrossRef](#)]
14. Gao, J.; Hao, M.; Wang, Y.; Kong, X.; Yang, B.; Wang, R.; Lu, Y.; Zhang, L.; Gong, M.; Zhang, L.; et al. 3D printing boron nitride nanosheets filled thermoplastic polyurethane composites with enhanced mechanical and thermal conductive properties. *Addit. Manuf.* **2022**, *56*, 102897. [[CrossRef](#)]
15. Yu, C.; Zhang, J.; Tian, W.; Fan, X.; Yao, Y. Polymer composites based on hexagonal boron nitride and their application in thermally conductive composites. *RSC Adv.* **2018**, *8*, 21948–21967. [[CrossRef](#)] [[PubMed](#)]
16. Zheng, Z.; Cox, M.; Li, B. Surface modification of hexagonal boron nitride nanomaterials: A review. *J. Mater. Sci.* **2018**, *53*, 66–99. [[CrossRef](#)]
17. Zhang, Y.; Gao, W.; Li, Y.; Zhao, D.; Yin, H. Hybrid fillers of hexagonal and cubic boron nitride in epoxy composites for thermal management applications. *RSC Adv.* **2019**, *9*, 7388–7399. [[CrossRef](#)]
18. Merlo, A.; Mokkapati, V.; Pandit, S.; Mijakovic, I. Boron nitride nanomaterials: Biocompatibility and bio-applications. *Biomater. Sci.* **2018**, *6*, 2298–2311. [[CrossRef](#)]
19. Ciofani, G.; Genchi, G.; Liakos, I.; Athanassiou, A.; Dinucci, D.; Chiellini, F.; Mattoli, V. A simple approach to covalent functionalization of boron nitride nanotubes. *J. Colloid Interface Sci.* **2012**, *374*, 308–314. [[CrossRef](#)]
20. Xue, Y.; Li, X.; Wang, H.; Zhao, F.; Zhang, D.; Chen, Y. Improvement in thermal conductivity of through-plane aligned boron nitride/silicone rubber composites. *Mater. Des.* **2019**, *165*, 107580. [[CrossRef](#)]
21. Lin, Z.; Liu, Y.; Raghavan, S.; Moon, K.; Sitaraman, S.; Wong, C.P. Magnetic alignment of hexagonal boron nitride platelets in polymer matrix: Toward high performance anisotropic polymer composites for electronic encapsulation. *ACS Appl. Mater. Interfaces* **2013**, *5*, 7633–7640. [[CrossRef](#)]
22. Tebeta, R.T.; Fattahi, A.; Ahmed, N.A. Experimental and numerical study on HDPE/SWCNT nanocomposite elastic properties considering the processing techniques effect. *Microsyst. Technol.* **2020**, *26*, 2423–2441. [[CrossRef](#)]
23. Crawford, R.J. *Plastics Engineering*, 3rd ed.; Butterworth-Heinemann: Oxford, UK, 1998; p. 530.
24. Ligon, S.C.; Liska, R.; Stampfl, J.; Gurr, M.; Mülhaupt, R. Polymers for 3D Printing and Customized Additive Manufacturing. *Chem. Rev.* **2017**, *117*, 10212–10290. [[CrossRef](#)] [[PubMed](#)]
25. Yuan, S. Development and Optimization of Selective Laser Sintered-Composites and Structures for Functional Applications. Ph.D. Thesis, Nanyang Technological University, Singapore, 2018; pp. 26–27. [[CrossRef](#)]
26. Yuan, S.; Shen, F.; Chua, C.; Zhou, K. Polymeric composites for powder-based additive manufacturing: Materials and applications. *Prog. Polym. Sci.* **2019**, *91*, 141–168. [[CrossRef](#)]
27. Sillani, F.; de Gasparo, F.; Schmid, M.; Wegener, K. Influence of packing density and fillers on thermal conductivity of polymer powders for additive manufacturing. *Int. J. Adv. Manuf. Technol.* **2021**, *117*, 2049–2058. [[CrossRef](#)]
28. Lupone, F.; Padovano, E.; Ostrovskaya, O.; Russo, A.; Badini, C. Innovative approach to the development of conductive hybrid composites for Selective Laser Sintering. *Compos. Part A Appl. Sci. Manuf.* **2021**, *147*, 106429. [[CrossRef](#)]
29. Yuan, S.; Zheng, Y.; Chua, C.; Yan, Q.; Zhou, K. Electrical and thermal conductivities of MWCNT/polymer composites fabricated by selective laser sintering. *Compos. Part A Appl. Sci. Manuf.* **2018**, *105*, 203–213. [[CrossRef](#)]
30. Ronca, A.; Rollo, G.; Cerruti, P.; Fei, G.; Gan, X.; Buonocore, G.; Lavorgna, M.; Xia, H.; Silvestre, C.; Ambrosio, L. Selective Laser Sintering Fabricated Thermoplastic Polyurethane/Graphene Cellular Structures with Tailorable Properties and High Strain Sensitivity. *Appl. Sci.* **2019**, *9*, 864. [[CrossRef](#)]
31. Lanzl, L.; Wudy, K.; Greiner, S.; Drummer, D. Selective laser sintering of copper filled polyamide 12: Characterization of powder properties and process behavior. *Polym. Compos.* **2019**, *40*, 1801–1809. [[CrossRef](#)]
32. Gruber, P.; Ziólkowski, G.; Olejarczyk, M.; Grochowska, E.; Hoppe, V.; Szymczyk-Ziółkowska, P.; Kurzynowski, T. Influence of bioactive metal fillers on microstructural homogeneity of PA12 composites produced by polymer Laser Sintering. *Arch. Civ. Mech. Eng.* **2022**, *22*, 117. [[CrossRef](#)]
33. Hon, K.K.B.; Gill, T.J. Selective Laser Sintering of SiC/Polyamide Composites. *CIRP Annals.* **2003**, *52*, 173–176. [[CrossRef](#)]
34. Do, N.B.D.; Andreassen, E.; Edwardsen, S.; Lifjeld, A.; Aasmundtveit, K.; Nguyen, H.-V.; Imenes, K. Thermal management of an interventional medical device with double layer encapsulation. *Exp. Heat Transf.* **2021**, *25*, 708–725. [[CrossRef](#)]
35. Frick, A.; Rochman, A. Characterization of TPU-elastomers by thermal analysis (DSC). *Polym. Test.* **2004**, *23*, 413–417. [[CrossRef](#)]
36. Nan, C.W.; Birringer, R.; Clarke, D.; Gleiter, H. Effective thermal conductivity of particulate composites with interfacial thermal resistance. *J. Appl. Phys.* **1997**, *81*, 6692–6699. [[CrossRef](#)]

37. Ordóñez-Miranda, J.; Alvarado-Gil, J.; Medina-Ezquivel, R. Generalized Bruggeman Formula for the Effective Thermal Conductivity of Particulate Composites with an Interface Layer. *Int. J. Thermophys.* **2010**, *31*, 975–986. [[CrossRef](#)]
38. Sun, Y.; Zhou, L.; Han, Y.; Cui, L.; Chen, L. A new anisotropic thermal conductivity equation for h-BN/polymer composites using finite element analysis. *Int. J. Heat Mass Transf.* **2020**, *160*, 120157. [[CrossRef](#)]
39. Heinle, C.; Brocka, Z.; Hülnder, G.; Ehrenstein, G.; Osswald, T. Thermal conductivity of polymers filled with non-isometric fillers: A process dependent, anisotropic property. In Proceedings of the 67th Annual Technical Conference of the Society of Plastics Engineers (ANTEC 2009, Chicago), Chicago, IL, USA, 22–24 June 2009; pp. 883–889.
40. Henze Boron Nitride Products AG. HeBoFill ®CL-ADH 020. In *Technical Datasheet*; Henze BNP AG: Lauben, Germany, 2020; pp. 49–50.
41. Zajac, J.; Heiselberg, P. Measurements of thermal diffusivity, specific heat capacity and thermal conductivity with LFA 447 apparatus. *Aalb. Univ.* **2013**, *144*, 5–11.
42. Salmon, D.R.; Brandt, R.; Tye, R.P. Pyroceram 9606, A certified ceramic reference material for high-temperature thermal transport properties: Part 2-certification measurements. *Int. J. Thermophys.* **2010**, *31*, 355–373. [[CrossRef](#)]
43. Polymer Orientation. Available online: <http://www.personal.psu.edu/irh1/PDF/Orientation.pdf> (accessed on 23 October 2021).
44. Girgsdies, F. *Peak Profile Analysis in X-ray Powder Diffraction*; Electron Microscopy Group, Department of Inorganic Chemistry, Fritz-Haber-Institut der MPG: Berlin, Germany, 2015; p. 12.
45. Jørgensen, J.K.; Andreassen, E.; Salaberger, D. The effect of fiber concentration on fiber orientation in injection molded film gated rectangular plates. *Polym. Compos.* **2019**, *40*, 615–629. [[CrossRef](#)]
46. Granlund, H.; Andreassen, E.; Skjønsvell, E.; Høydalsvik, K.; Diaz, A.; Breiby, D.W. Measuring and simulating morphology gradients in injection-molded talc-reinforced isotactic polypropylene. *J. Polym. Sci. B Polym. Phys.* **2014**, *52*, 1157–1167. [[CrossRef](#)]
47. Kugler, S.K.; Kech, A.; Cruz, C.; Osswald, T. Fiber Orientation Predictions—A Review of Existing Models. *J. Compos. Sci.* **2020**, *4*, 69. [[CrossRef](#)]
48. Chen, H.; Zhu, W.; Tang, H.; Yan, W. Oriented structure of short fiber reinforced polymer composites processed by selective laser sintering: The role of powder-spreading process. *Int. J. Mach. Tools Manuf.* **2021**, *163*, 103703. [[CrossRef](#)]
49. Khudiakova, A.; Berer, M.; Niedermair, S.; Plank, B.; Truszkiewicz, E.; Meier, G.; Stepanovsky, H.; Wolfahrt, M.; Pinter, G.; Lackner, J. Systematic analysis of the mechanical anisotropy of fibre-reinforced polymer specimens produced by laser sintering. *Addit. Manuf.* **2020**, *36*, 101671. [[CrossRef](#)]
50. Heckner, T.; Seitz, M.; Raisch, S.; Huelder, G.; Middendorf, P. Selective Laser Sintering of PA6: Effect of Powder Recoating on Fibre Orientation. *J. Compos. Sci.* **2020**, *4*, 108. [[CrossRef](#)]
51. Tan, P.; Shen, F.; Tey, W.; Zhou, K. A numerical study on the packing quality of fibre/polymer composite powder for powder bed fusion additive manufacturing. *Virtual Phys Prototyp.* **2021**, *16*, S1–S18. [[CrossRef](#)]
52. Kargar, F.; Barani, Z.; Salgado, R.; Debnath, B.; Lewis, J.; Aytan, E.; Lake, R.; Balandin, A.A. Thermal Percolation Threshold and Thermal Properties of Composites with High Loading of Graphene and Boron Nitride Fillers. *ACS Appl. Mater. Interfaces* **2018**, *10*, 37555–37565. [[CrossRef](#)]
53. Pan, C.; Zhang, J.; Kou, K.; Zhang, Y.; Wu, G. Investigation of the through-plane thermal conductivity of polymer composites with in-plane oriented hexagonal boron nitride. *Int. J. Heat Mass Transf.* **2018**, *120*, 1–8. [[CrossRef](#)]
54. Ding, D.; Zou, M.; Wang, X.; Qin, G.; Zhang, S.; Chan, S.; Meng, Q.; Liu, Z.; Zhang, Q.; Chen, Y. Thermal conductivity of polydisperse hexagonal BN/polyimide composites: Iterative EMT model and machine learning based on first principles investigation. *Chem. Eng. J.* **2022**, *437*, 135438. [[CrossRef](#)]
55. Liu, J.; Li, W.; Guo, Y.; Zhang, H.; Zhang, Z. Improved thermal conductivity of thermoplastic polyurethane via aligned boron nitride platelets assisted by 3D printing. *Compos. Part A Appl. Sci. Manuf.* **2019**, *120*, 140–146. [[CrossRef](#)]
56. Ordóñez-Miranda, J.; Alvarado-Gil, J.J. Thermal conductivity of nanocomposites with high volume fractions of particles. *Compos. Sci. Technol.* **2012**, *72*, 853–857. [[CrossRef](#)]
57. Jing, X.; Zhao, W.; Lan, L. The effect of particle size on electric conducting percolation threshold in polymer/conducting particle composites. *J. Mater. Sci. Lett.* **2000**, *19*, 377–379. [[CrossRef](#)]
58. Li, T.-L.; Hsu, S.L.-C. Enhanced Thermal Conductivity of Polyimide Films via a Hybrid of Micro- and Nano-Sized Boron Nitride. *J. Phys. Chem. B* **2010**, *114*, 6825–6829. [[CrossRef](#)]
59. Pietrak, K.; Wiśniewski, T. A review of models for effective thermal conductivity of composite materials. *J. Power Technol.* **2014**, *95*, 14–24.
60. Daneshmehr, S.; Román, F.; Hutchinson, J.M. The surface modification of boron nitride particles. *J. Therm. Anal. Calorim.* **2019**, *143*, 151–163. [[CrossRef](#)]
61. Cui, Z.; Oyer, A.; Glover, A.; Schniepp, H.; Adamson, D.H. Large scale thermal exfoliation and functionalization of boron nitride. *Small* **2014**, *10*, 2352–2355. [[CrossRef](#)] [[PubMed](#)]
62. Ryu, S.; Kim, K.; Kim, J. Silane surface treatment of boron nitride to improve the thermal conductivity of polyethylene naphthalate requiring high temperature molding. *Polym. Compos.* **2018**, *39*, E1692–E1700. [[CrossRef](#)]
63. Hill, R.F.; Supancic, P.H. Thermal Conductivity of Platelet-Filled Polymer Composites. *J. Am. Ceram. Soc.* **2004**, *85*, 851–857. [[CrossRef](#)]
64. Prindl, J. Enhancing Thermal Conductivity of Hexagonal Boron Nitride Filled Thermoplastics for Thermal Interface Management. Master’s Thesis, Lehigh University, Bethlehem, PA, USA, 2015.

65. Henze Boron Nitride Products AG. HeBoFill ®LL-SP 120. In *Technical Datasheet*; Henze BNP AG: Lauben, Germany, 2020; p. 8374.
66. Tseng, H.-C.; Chang, R.-Y.; Hsu, C.-H. Comparison of recent fiber orientation models in injection molding simulation of fiber-reinforced composites. *J. Thermoplast. Compos. Mater.* **2020**, *33*, 35–52. [[CrossRef](#)]
67. Mazahir, S.M.; Velez-Garcia, G.M.; Wapperom, P.; Baird, D. Fiber orientation in the frontal region of a center-gated disk: Experiments and simulation. *J. Nonnewton Fluid Mech.* **2015**, *216*, 31–44. [[CrossRef](#)]

Disclaimer/Publisher’s Note: The statements, opinions and data contained in all publications are solely those of the individual author(s) and contributor(s) and not of MDPI and/or the editor(s). MDPI and/or the editor(s) disclaim responsibility for any injury to people or property resulting from any ideas, methods, instructions or products referred to in the content.

Supplementary Materials

S1. Materials

The materials used in this study are summarized in Table S1. The polymer matrix was thermoplastic polyurethane (TPU) for injection moulding and powder bed fusion (3D printing), and epoxy for casting. Three different types of hexagonal BN (hBN) powder were used for preparation of hBN/polymer composites.

Results presented in the article are based on the polymer composites containing BN3. Sections 9 and 10 of this Supplementary Materials provide additional results of the polymer composites containing BN1 and BN2. This supports the discussion and evaluation of the effects of filler (e.g. particle size, as well as single platelets vs. partly agglomerated particles) on the thermal conductivity and tensile properties of the hBN/polymer composites.

Table S1. Materials used for preparation of hBN/polymer composites.

Name	Materials	Product name, Supplier
hBN particles		
BN1	hBN powder with average particle size of ~ 1 μm	Boron nitride powder, 1 μm , 98% (product no. 255475), Sigma Aldrich, Merck
BN2 ^a	hBN powder. Single platelets with median particle size (D_{50}) of 12 μm and size distribution in the range (0.8–40) μm , specific surface area (BET) ~ 6 m^2/g	HeBoFill LL-SP 120, Henze Boron Nitride Products AG, Germany
BN3 ^a	hBN powder. Platelet agglomerates with D_{50} of 20 μm and size distribution in the range (0.5–31) μm , BET ~ 4 m^2/g	HeBoFill CL-ADH 020, Henze Boron Nitride Products AG, Germany
Polymer matrix		
TPU	Ultrasint TPU 88A (in the form of powder)	BASF, Germany
Epoxy ^b	An epoxy system (for casting) containing: - 35 wt% unmodified bisphenol-F epoxy resin (Araldite GY 285-1) - 35 wt% reactive diluent (Araldite DY 026) 30 wt% amine-based curing agent (Jeffamine D-230 Polyetheramine)	Huntsman

^aInformation about BN2 and BN3 as provided by the supplier [1,2]. Size distributions of BN2 and BN3 are shown in Figure S1. The powder BN3 had a partly agglomerated particle structure, claimed to give good lubricating properties and low viscosity increase [2]. Platelets and spherical agglomerates are shown in Figure S2a.^bThe epoxy system was formulated to have a low viscosity, suitable for preparing composites with high filler content.

S2. Specimen Fabrication

All specimens, with codes, are listed in Table S2 and Table S3. Details about the fabrication by casting and powder bed fusion (PBF) are given below.

Table S2. Specimens fabricated by injection moulding and casting.

Specimen ID	Processing technique	Polymer	BN type	hBN content (wt%)
IM_TPU				0
IM_15BN3				15
IM_25BN3				25
IM_35BN3				35
IM_50BN3				50
IM_65BN3			BN3	65
IM_15BN2	Injection moulding	TPU		15
IM_35BN2				35
IM_50BN2			BN2	50

IM 50BN1			BN1	50
C Epoxy				0
C 35BN3				35
C 50BN3	Casting	Epoxy	BN3	50
C 55BN3				55

Casting:

Composite specimens of epoxy and hBN were prepared by vacuum mixing (Thinky Planetary Vacuum Mixer) followed by casting into a PTFE mould and curing at 150 °C for 18 hours. The epoxy system contained 35 wt% bisphenol-F epoxy, 35 wt% diluent and 30 wt% curing agent (details in the article). This formula was selected to achieve a low viscosity, suitable for preparing composites with a high filler concentration. The epoxy system was mixed with hBN powder in vacuum through four steps, in order to avoid air trapped inside the mixture during mixing. The time for each mixing step was 2 minutes; the rotation speed was 2000 rpm for the first two steps and 1500 rpm for the last two steps; and vacuum was decreased from 50 kPa to 30 kPa, 10 kPa and 2.5 kPa from the first step to the fourth step. The maximum practical filler content was about 55 wt%, for which there was no formation of voids or air bubbles during mixing and casting.

Powder Bed Fusion (PBF):

A desktop PBF 3D printer (SnowWhite, Sharebot, Italy) was employed to fabricate specimens from TPU powder and hBN/TPU powder mixtures. The machine has a maximum build volume of 100 mm x 100 mm x 100 mm, a CO₂ laser (wavelength 10.6 μm, max. power 14 W), a blade for recoating powder (i.e. applying a new layer of powder). The printing was performed in air.

In order to identify appropriate processing parameters for the hBN/TPU composites, the starting point was the parameters suggested for the TPU by the material supplier (for other machines than the one used in this study). However, a higher laser energy density was needed, also for the pure TPU. In addition, a higher hBN content required a higher energy, see Table S3. However, composites with satisfactory fusion (i.e. with enough ductility for practical use) could not be obtained by PBF, at least not with the present powder mixing method and recoater.

Table S3. Specimens fabricated by PBF 3D printing. The process parameters E_v , P , v and L are explained in the article. The laser energy (E_v) was applied three times for each powder layer, i.e. three repeated laser scans (the recommendation from the material supplier was to apply two laser scans). The hatching distance (the distance between two adjacent laser scanning lines for the contour lines and the infill lines) is not included in the table. It was kept constant at 0.1 mm.

Specimen ID	BN content (wt%)	E_v (J/mm ³)	P (W)	v (m/s)	L (mm)	Chamber temp. (°C)	Specimen orientation
PBF TPU	0	0.31	8.4	2.7	0.10	88	xy
BN type 2							
PBF 15BN2	15	0.13	3.5				
PBF 25BN2	25	0.21	5.6	2.7	0.10	88	xy
PBF 35BN2	35	0.31	8.4				
BN type 1							
PBF 35BN1	35	0.31	8.4	2.7	0.10	88	xy
BN type 3							
PBF 35BN3	35	0.31	8.4				
PBF 40BN3 a		0.26	7.0				
PBF 40BN3 b		0.31		2.7			xy
PBF 40BN3 b z		0.31				88	z
PBF 40BN3 b 92		0.31				92	
PBF_40BN3_c		0.35	8.4	2.4	0.10		

PBF_40BN3_e	0.50	10.5	2.1	0.10	88	xy
PBF_40BN3_d_08	40	0.39		0.08		
PBF_40BN3_d		0.39	2.7			xy
PBF_40BN3_d_z		0.39				z

S3. hBN Powders and hBN/polymer Composites Characterized by SEM

Two types of hBN powders from Henze (BN2 and BN3) were used. Particle size distributions of BN2 (single platelets) and BN3 (partly agglomerated) are shown in Figure S1. Platelets and spherical agglomerates of BN3 can be seen in Figure S2a. Figure S2a shows a cast specimen with 55 wt% BN3. A PBF composite printed in the xy plane (specimen PBF_40BN3_d) is shown in Figure S2b, revealing voids.

These SEM micrographs were obtained using Secondary Electron (SE) detectors. In cases where low vacuum was used to minimize image distortion from sample charging, SE were recorded by an “Ultra Variable-pressure Detector” (UVD), which indirectly detects SE emission. Cross-sections were cut along the (2 mm) thickness direction of injection moulded and PBF discs. Similar cross-sections of cast discs were prepared by etching, using an Ar ion milling system (Hitachi IM 4000). The ion etching was conducted with 6 kV accelerating voltage, in cross-section mode (a Ta mask was used for defining the cross-section).

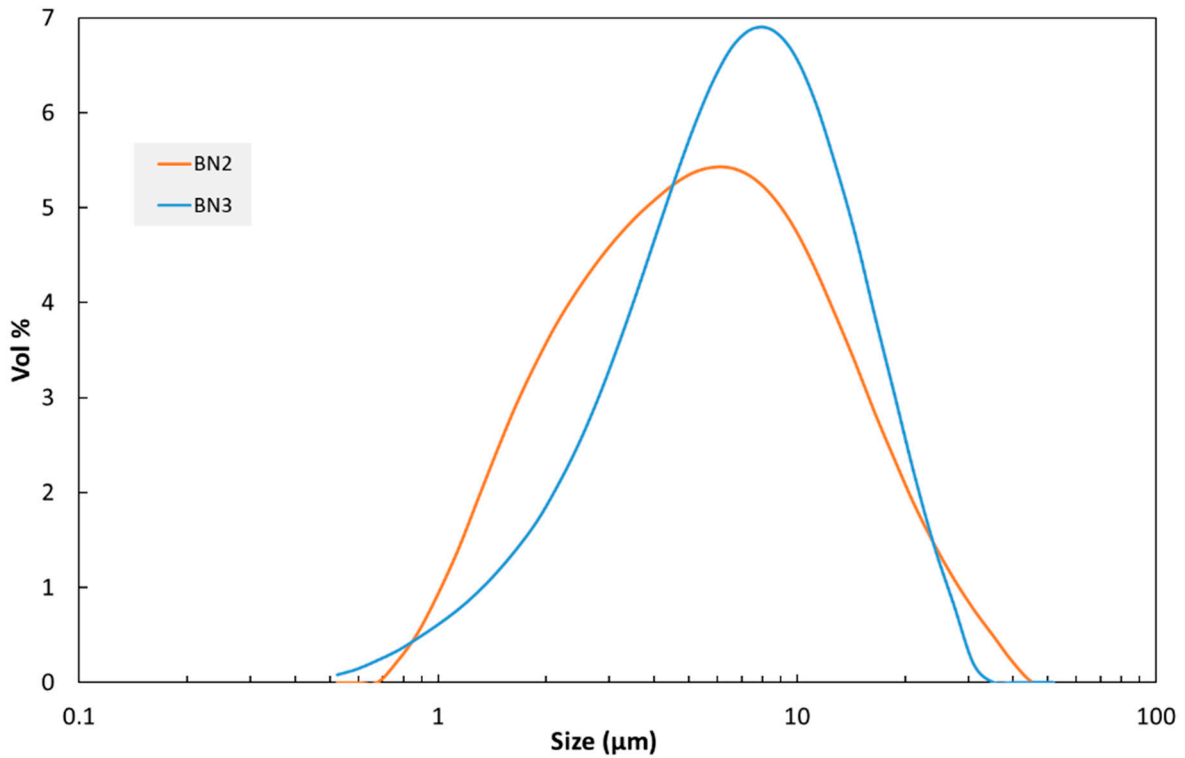


Figure S1. Particle size distribution of BN2 and BN3. Data from powder supplier.

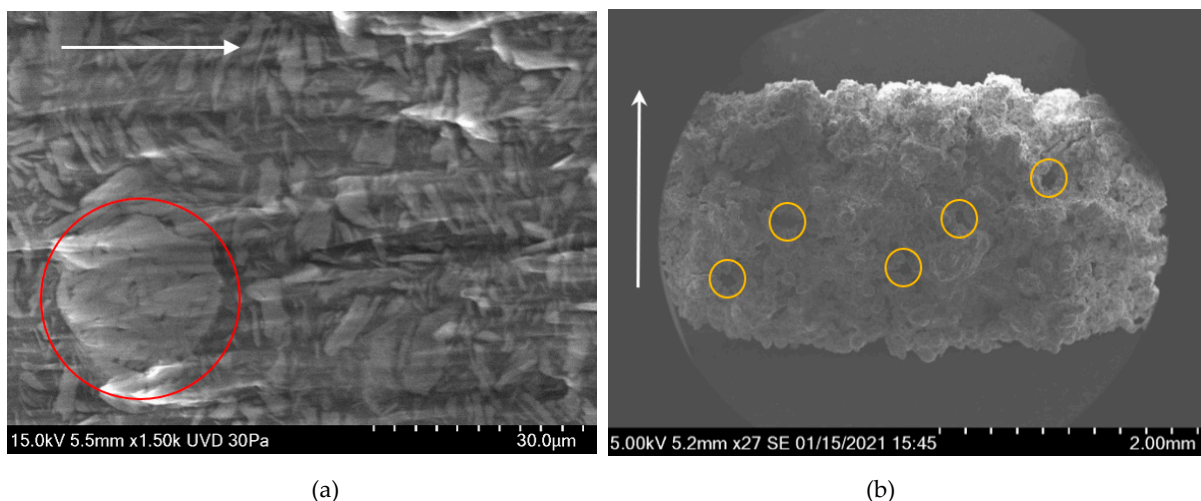


Figure S2. SEM micrographs of cross-sections of disc specimens. The white arrows show the direction of the disc normal. The bright spots are artefacts caused by charging in the SEM. (a) Ion milled cross-section of disc C_55BN3. An agglomerate of hBN platelets is seen inside the red circle. (b) Cross-section of PBF disc printed in the xy plane (specimen PBF_40BN3_d). The yellow circles show the positions of voids.

S4. Determination of Density for the Thermal Conductivity Measurements

The density of some PBF specimens (e.g. PBF_TPU; PBF_15BN2; PBF_25BN2; PBF_35BN2; PBF_35BN3; PBF_40BN3_c; PBF_40BN3_c_z) was measured gravimetrically (Mettler Toledo XS204 with density kit). The measurements were conducted at 20 °C, using water as the immersion liquid. All specimens were measured twice, and they were dried well between each time. The difference between the measured density and the calculated density (based on mass and dimensions) was negligible. Examples: the measured and calculated densities of specimen PBF_40BN3_c were 0.73 g/cm³ and 0.75 g/cm³, respectively. For PBF_TPU, the measured and calculated densities were 0.85 g/cm³ and 0.84 g/cm³. Therefore, calculated densities were used to determine thermal conductivity of all (remaining) samples.

S5. Tensile Testing – Supplementary Experimental Details and Examples of Stress-Strain Curves

Tensile testing of injection moulded specimens was performed with a universal test machine (Zwick Z250), using a 2.5 kN load cell. The specimen was mounted in wedge grips, with grip-to-grip distance of 55 mm. Strains were calculated from displacements measured with an extensometer with initial gauge length of 25 mm. The crosshead speed was 0.5 mm/min up to a strain of 0.25 %, and then changed to 25 mm/min (as suggested described in ISO 527-1:2012). These speeds were chosen in order to have nominal strain rates similar to those typically used in tensile testing of plastics, with the most common (larger) test specimen type 1A of ISO 527-2. PBF specimens were tested with a smaller machine (Lloyd Instruments LR50K) using a 500 N load cell. The crosshead speed was constant (25 mm/min) and an extensometer was not used. Three specimens were tested for each filler concentration, and the reported data are average values.

Figure S3 shows an example of tensile stress-strain curves. These curves illustrate that the two composites with 50% BN2 and BN3, respectively, differ with regard to strength (maximum stress) and strain at break. The differences are small, but statistically significant. See also Figures S9 and S10 below.

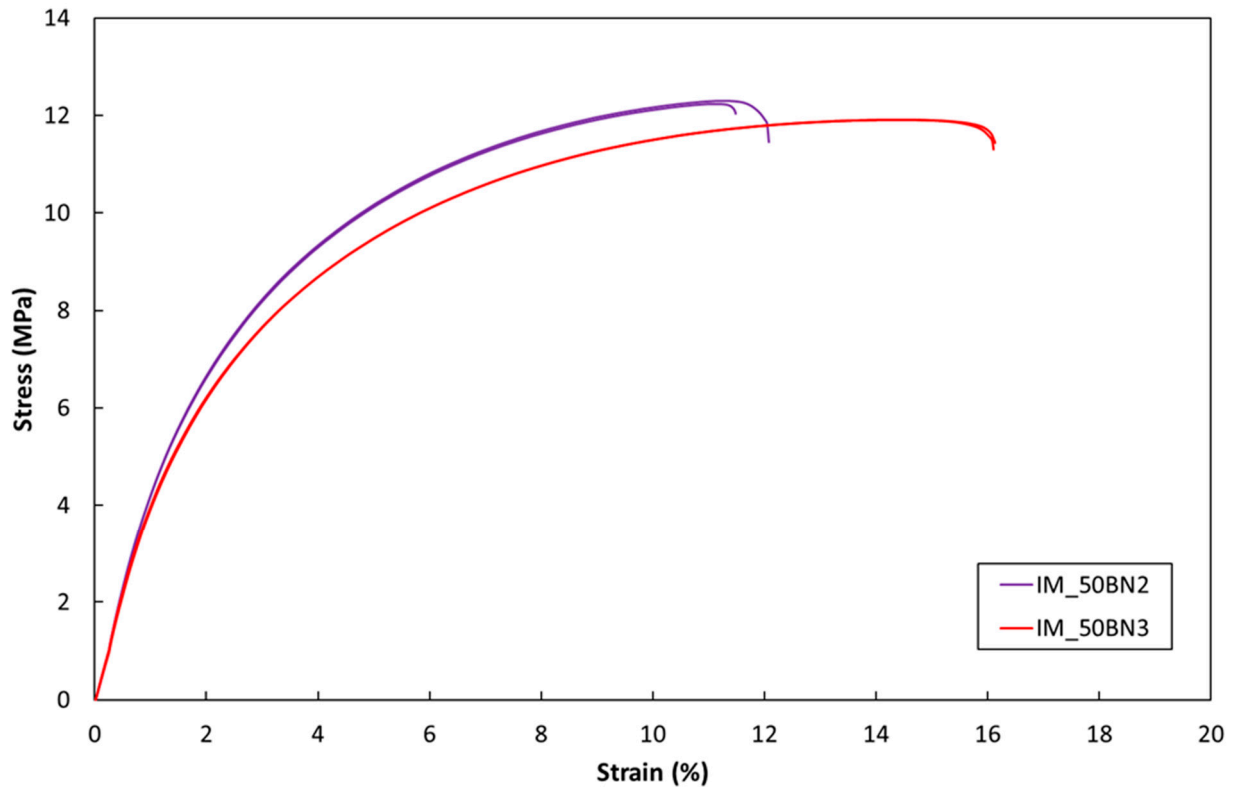


Figure S3. Tensile stress-strain curves for the composites IM_50BN2 and IM_50BN3. Curves for two repeated tests are shown for each composite.

S6. Specimen preparation for XRD of the specimen's mid-plane

Injection-moulded disc specimens were cast in epoxy. To expose the mid-plane for XRD measurement, the specimens were grinded to their half-thickness (1 mm) and polished. XRD data obtained with the half-thickness specimen (referred to as IM_BN3_center), with the X-ray beam towards the mid-plane mentioned above, was compared with data obtained with the original 2 mm thick specimen, in order to evaluate the orientation of hBN platelets in the 'skin' and core regions of injection moulded specimens.

S7. Numerical simulation of platelet orientation in injection moulded discs

The process-induced orientation of plate-like particles in the $\varnothing 25$ mm 2 mm thick disc was simulated with the commercial software Moldex3D (release R2020). The simulation of the injection moulding process involves non-isothermal flow of a non-Newtonian fluid. The platelet orientation was simulated with the improved anisotropic rotary diffusion and retarding principal rate (iARD-RPR) model [3]. This model has four parameters: the effective Jeffery aspect ratio of a cylindrical particle (e.g. plate) (R), a particle-particle interaction parameter (C_i), a particle-matrix interaction parameter (C_M) and a retardation parameter (α). Identifying and verifying model parameters for predicting the orientation of hBN platelets is beyond the scope of this paper, but a small study was performed to assess the sensitivity of the simulated orientation to the four parameters mentioned above, and to the viscosity of the polymer and some moulding parameters.

Numerical simulations were performed to obtain the 3D distributions platelet orientation in the injection moulded disc. As we do not have a verified material model for the orientation of these hBN platelets in a flowing polymer melt (i.e. verified parameters for the iARD-RPR model), the purpose of the simulations is mainly to obtain a qualitative picture of how the orientation varies through the thickness of the disc, in order to compare with the $\langle \cos^2\theta \rangle$ values from XRD, and $\langle \cos^2\theta \rangle$ values used in two of the models for thermal conductivity (section 4.4 in the article).

Figure S4 shows how the orientation varies through the thickness of the disc, at the center point of the disc. The $\langle \cos^2 \theta \rangle$ value (blue curve, A_z) is highest in a "shell" near the surface, and lowest in the midplane/core of the disc. In a skin layer (about 50 μm thick in Figure S4) the orientation decreases towards the surface. This can be attributed to the fountain flow at the flow front and/or thermal effects [4]. The red curve (A_x) in Figure S4 is the orientation of the platelet normal relative to the x axis, i.e. the main flow direction, see Figure S5. Near the surface this value is lower than 0.1, i.e. the platelet normals are essentially perpendicular to the x direction. In the core, the value is 0.4, i.e. the platelet normals have a slightly preferred orientation along the x axis (a random orientation would give $A_x = 1/3$).

Figure S5 shows how the orientation ($\langle \cos^2 \theta \rangle$) varies through the thickness of the disc, in different "slices" through the xy plane. The thickness of the shell and core layers, as well as the maximum and minimum values, varies over the disc area, especially along the main flow path from the gate to the other side of the disc (slice A in Figure S5).

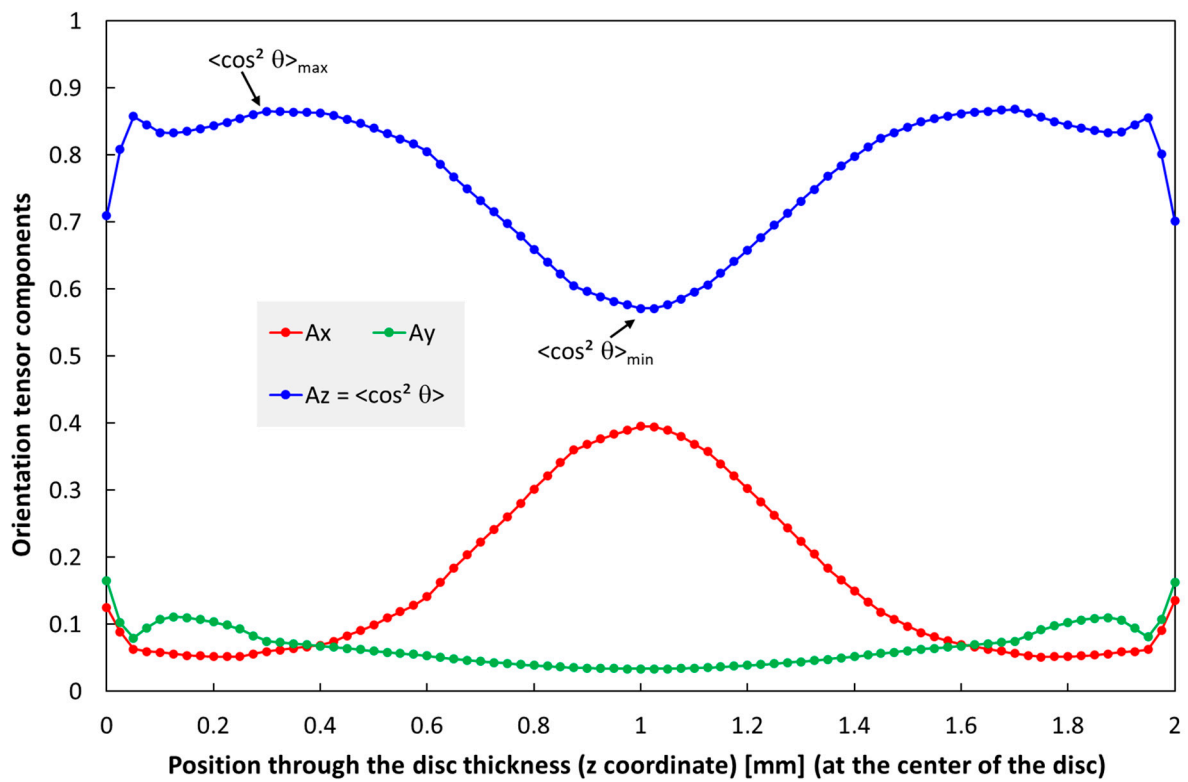


Figure S4. Simulated platelet orientation through the thickness of the 2 mm thick disc; diagonal components of the second order orientation tensor. The three components/curves relate to the coordinate system in Figure S5. The component A_z corresponds to $\langle \cos^2 \theta \rangle$ in other sections of the paper. Parameters for the iARD-RPR orientation model: $R = 0.05$, $C_I = 0.005$, $C_M = 0$, $\alpha = 0.7$. Note that this model does not have a parameter for the platelet fraction as such.

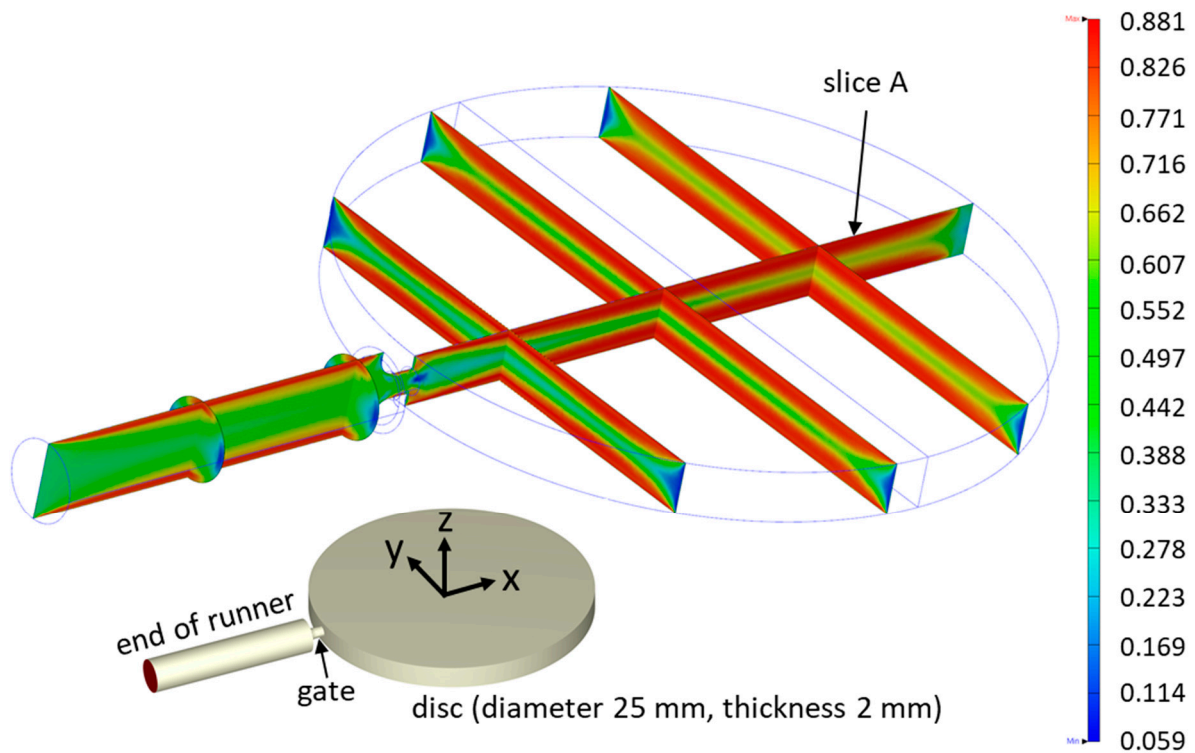


Figure S5. Simulated platelet orientation ($A_z = \langle \cos^2\theta \rangle$) in the 2 mm thick disc. The orientation data are shown in slices through the thickness of the disc, including gate and part of the runner. The model parameters are the same as in Figure S4.

The sensitivity of the simulated orientation to model parameters was also assessed. The main parameter affecting the maximum, minimum and average $\langle \cos^2\theta \rangle$ through the thickness of the disc is the particle–particle interaction parameter (C_i). Typically, the $\langle \cos^2\theta \rangle_{\max}$ values are in the range 0.85-0.97 and the average values are in the range 0.75-0.85.

Here we will only summarize a few trends, based on the orientation through the thickness at the center of the disc, as in Figure S4 .

The main parameter affecting $\langle \cos^2\theta \rangle_{\max}$ is the particle–particle interaction parameter (C_i); $\langle \cos^2\theta \rangle_{\max}$ increases with decreasing C_i . It also increases with decreasing platelet aspect ratio (R) (however, R must differ from the experimental value to have a significant effect) and increasing matrix-particle interaction parameter (C_M). Typically, the $\langle \cos^2\theta \rangle_{\max}$ values are in the range 0.85-0.97.

The $\langle \cos^2\theta \rangle_{\min}$ value is also affected by the parameters, but less than the maximum value. Just as the maximum value, $\langle \cos^2\theta \rangle_{\min}$ also increases with decreasing C_i , but it is insensitive to R . The difference between the maximum and minimum increases with decreasing C_i , and C_i is the dominant parameter.

The average of $\langle \cos^2\theta \rangle$ through the thickness increases with decreasing C_i , and C_i is the dominant parameter. This average is typically in the range 0.75-0.85.

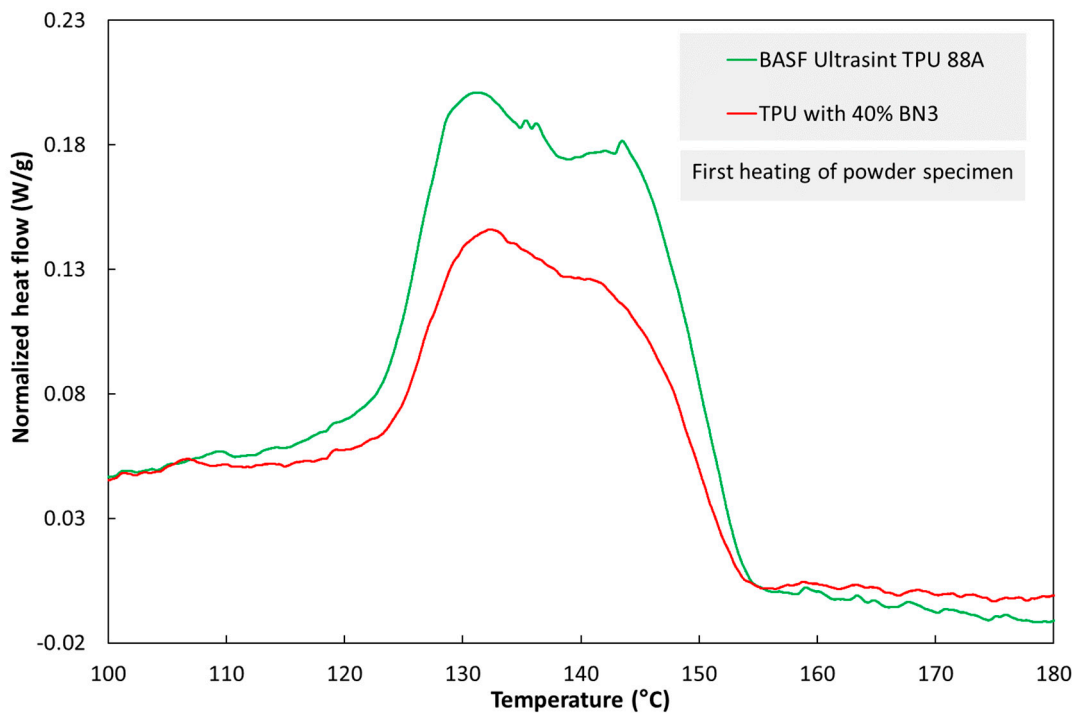
The viscosity of the polymer also influences the orientation. The main effects of increasing the viscosity (via the zero-shear viscosity in the viscosity model) are to reduce the minimum and average $\langle \cos^2\theta \rangle$ through the thickness. However, for a typical viscosity range, the average $\langle \cos^2\theta \rangle$ is only about 0.04 higher or lower than the average values given above.

The injection moulding process parameters also affect the orientation. In the simulations referred to above, the fill time for the disc was set to 0.2 s, which is close to the experimental value. (Other moulding parameters in the simulations were set as in the experiment.) If the fill time is increased to 1.2 s in the simulation, $\langle \cos^2\theta \rangle_{\max}$ decreases, while $\langle \cos^2\theta \rangle_{\min}$ increases. The net effect is that the average $\langle \cos^2\theta \rangle$ through the thickness

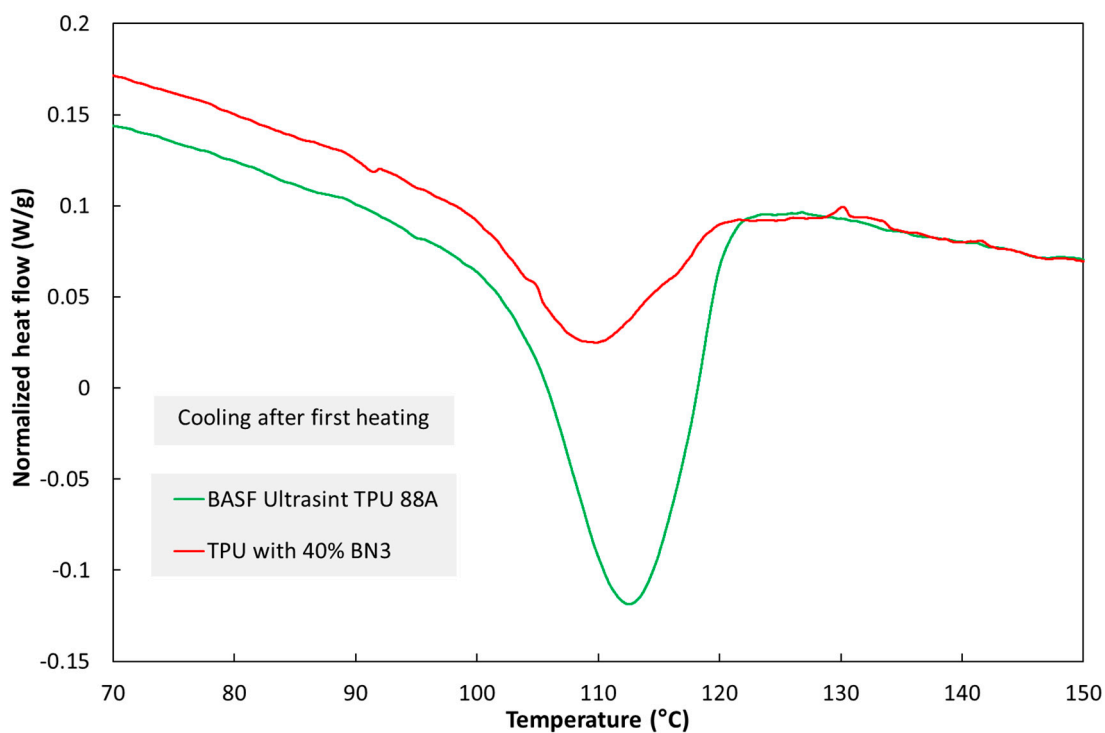
increases slightly – e.g. from 0.77 to 0.81 with the model parameters listed in the caption of Figure S4 .

S8. Differential Scanning Calorimetry (DSC) Results

DSC of the pure TPU and TPU with 40 wt% BN3 was performed using a Perkin Elmer DSC 8500. The heating/cooling rate was 10 K/min, and the samples were heated twice from 25 °C to 255 °C in nitrogen atmosphere. Thermograms of TPU powder and TPU powder with 40 wt% BN3 are shown in Figure S6. The DSC thermograms showed that the TPU with 40 wt% BN3 had a broad melting endotherm, from about 120 °C to 154 °C, with a peak at about 133 °C. The crystallization had a broad exotherm from about 120 °C to 98 °C, with a peak at about 109 °C. The difference between the composite and pure TPU was small (about 2 °C). Therefore, the temperatures in the PBF process can be the same for pure TPU and hBN/TPU composites.



(a)



(b)

Figure S6. DSC thermograms of the pure TPU powder and the TPU powder with 40 wt% BN3 from (a) heating scans and (b) cooling scans.

S9. Additional Results for Thermal Conductivity with Two other hBN Types (BN1 and BN2)

In addition to BN3 (used in the article), two other filler types (BN1 and BN2, see Supplementary section S1) were used to study the thermal conductivity of hBN/TPU composites. The additional results in this section supplements and supports the discussion in the article, regarding the effects of filler (e.g. particle size, as well as single platelets vs. partly agglomerated particles) on the thermal conductivity of the hBN/polymer composites.

Figure S7 shows that for IM composites with 50 wt% hBN, there was a clear effect of hBN type; BN2 and BN1 gave the highest and lowest conductivity, respectively. The same trend was seen for the PBF composites, although the effect was weaker.

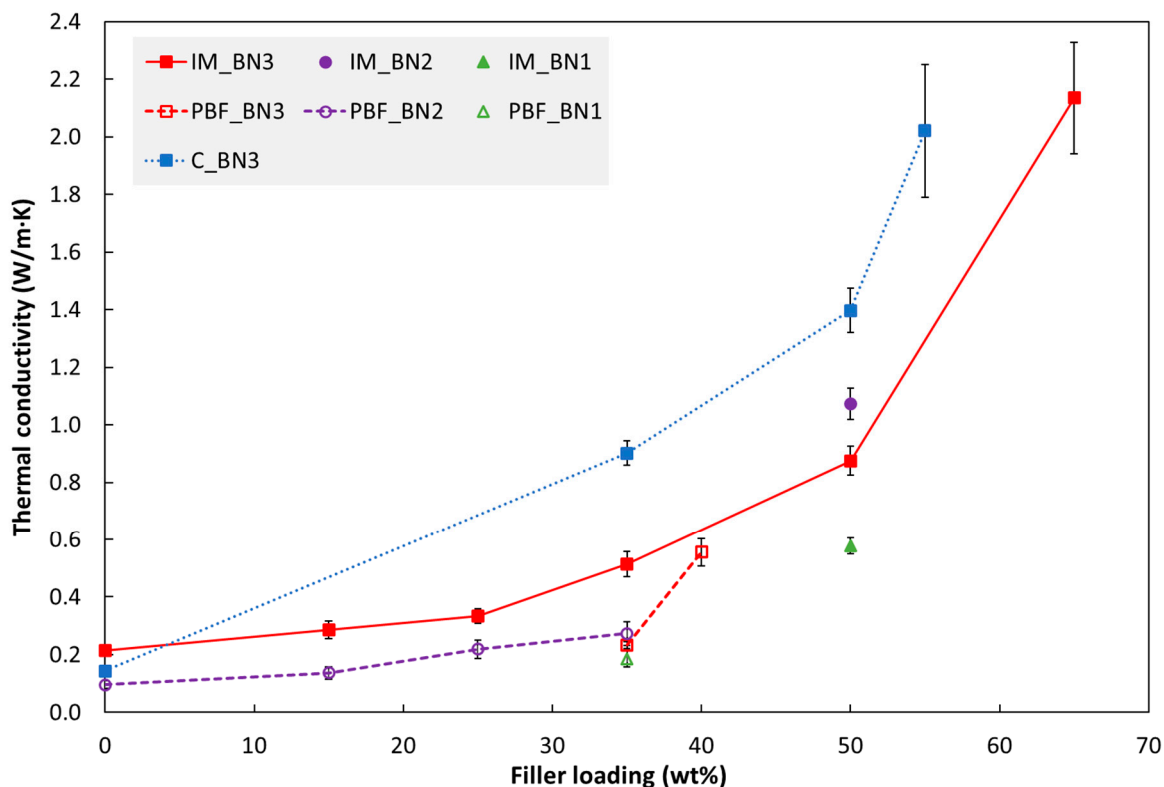


Figure S7. Thermal conductivity (at 30 °C) of composites fabricated by injection moulding ("IM"), powder bed fusion ("PBF") and casting ("C") as a function of hBN loading. The PBF specimen with 40 wt% BN3 was processed with a higher laser energy density than the other PBF specimens in this figure, see Figure 3 in the article and Table S3.

S10. Additional Results for Tensile Properties with Another hBN type (BN2)

In addition to hBN type BN3 (used in the article), another type (BN2, see Supplementary section S1) was also used in tensile tests. The additional results supports and supplements the discussion (in the article) regarding effects of filler (e.g. particle size, as well as single platelets vs. partly agglomerated particles) on the material processing and tensile properties.

The tensile properties of injection moulded specimens containing hBN type BN2 and BN3 are shown in Figure S8 – Figure S10. The tensile modulus increases monotonously with increasing filler loading in this range. The strength and strain at break values are almost unaffected by adding 15 % hBN. With 35 % hBN, both these values are reduced. With 50% hBN, the strength values are higher than that for 100 % TPU, while the strain at break values are similar to those for 35 % hBN. With 65 % hBN (only BN3) the highest strength and the lowest strain at break are observed. There are small, but statistically significant, differences between composites with BN2 and BN3, see also Figure S3.

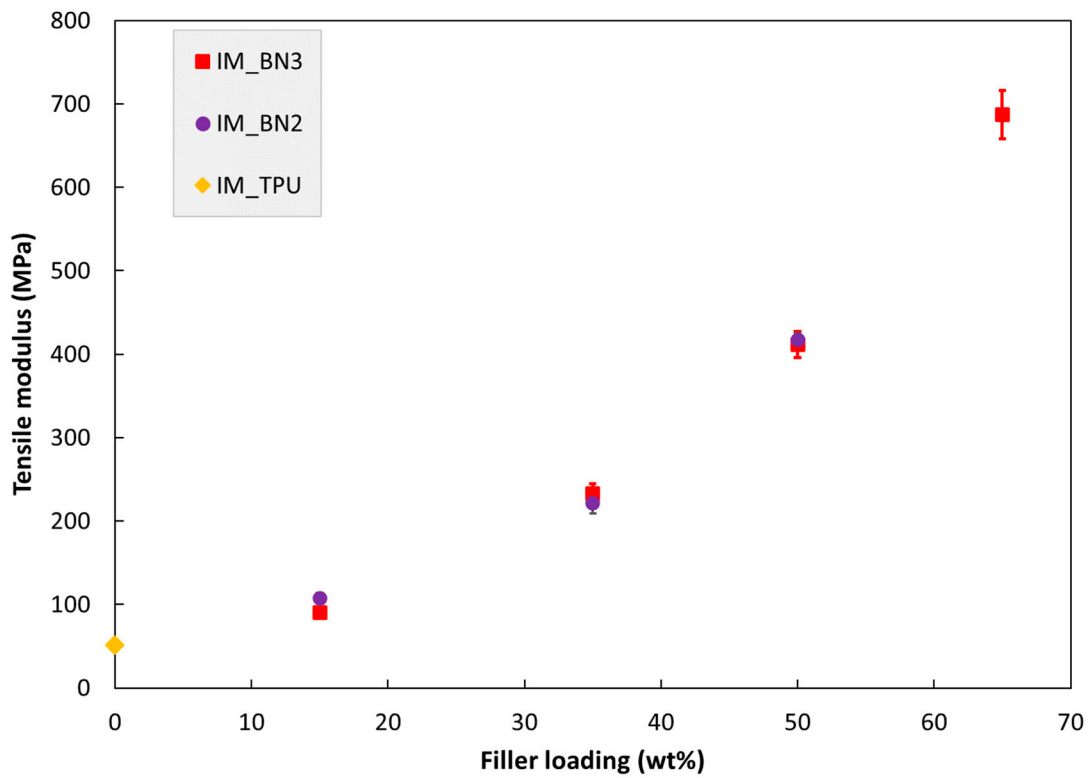


Figure S8. Tensile modulus of injection moulded specimens as a function of hBN loading. The specimen IM_TPU is 100% TPU.

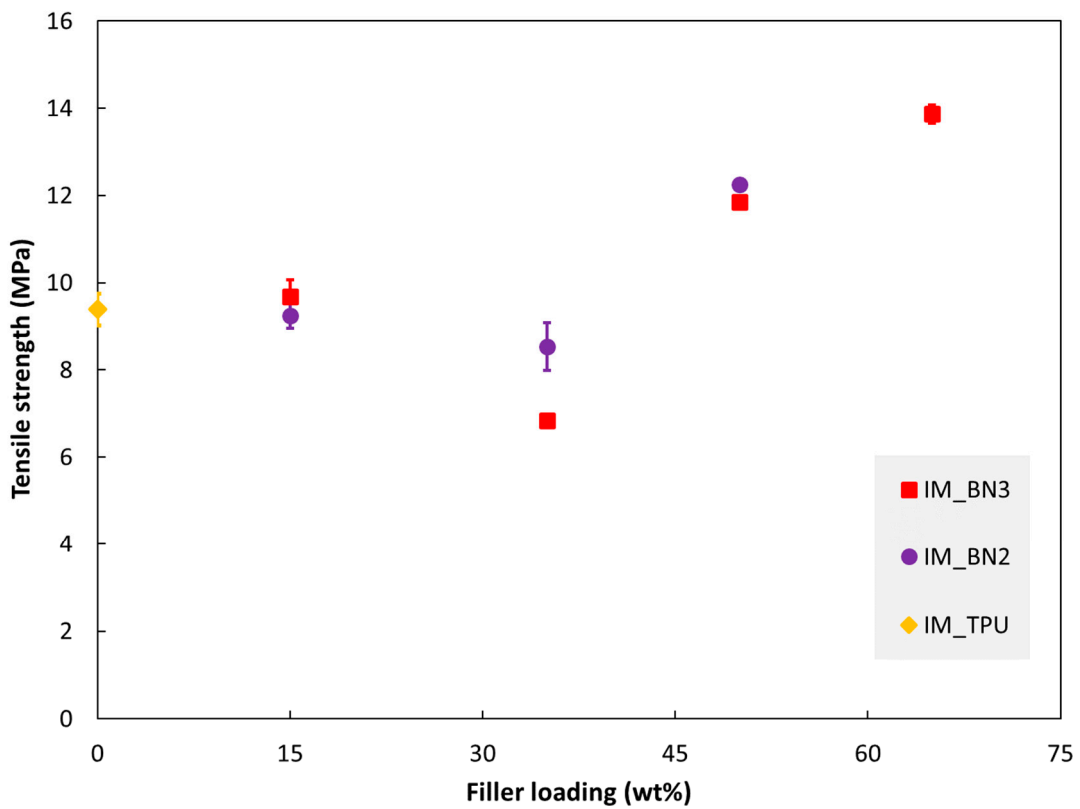


Figure S9. Tensile strength of injection moulded specimens as function of hBN loading.

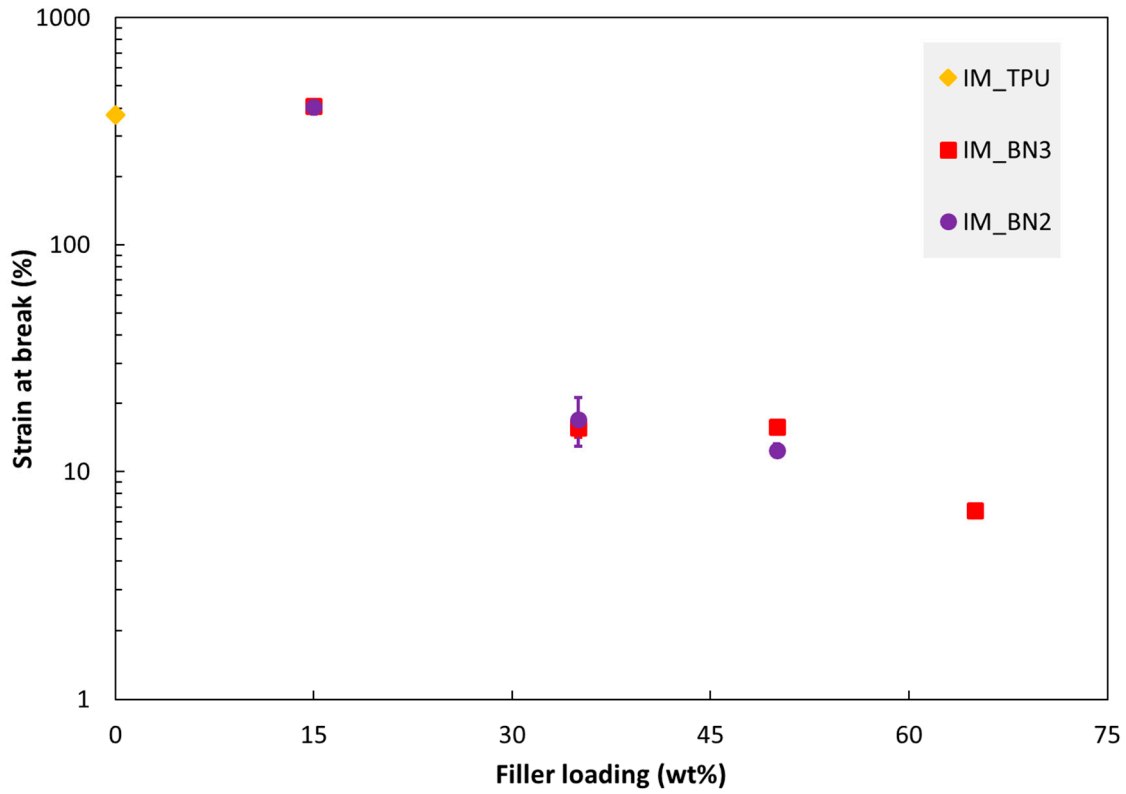


Figure S10. Strain at break of injection moulded specimens as a function of hBN loading.

S11. The Model of Nan et al.

The experimental thermal conductivities in this article were analyzed by comparing with the effective medium approximation (EMA) model introduced by Nan et al. [5]–[8]. This model, for the thermal conductivity of composites, includes effects of particle shape (ellipsoids, which can represent platelets), particle orientation and interfacial thermal resistance. It has been used in some studies of composites with hBN. However, it is limited to particles with isotropic thermal conductivity, while our hBN platelets are anisotropic. Also note that the model does not take into account filler-filler contact or nonuniform particle distributions. Hence, it is restricted to low filler fractions, and it can not predict the percolation threshold.

This supplementary section provides details about this model and background for the parameters used in our study.

In the model of Nan et al. [5], the through-plane thermal conductivity (K_{33}) of a composite with oblate ellipsoidal particles ($p < 1$) (which can represent platelets) is expressed by Eq. S1:

$$K_{33} = K_m \frac{1 + f[\beta_{11}(1 - L_{11})(1 - \langle \cos^2 \theta \rangle) + \beta_{33}(1 - L_{33})\langle \cos^2 \theta \rangle]}{1 - f[\beta_{11}L_{11}(1 - \langle \cos^2 \theta \rangle) + \beta_{33}L_{33}\langle \cos^2 \theta \rangle]} \quad (\text{S1a})$$

with:

$$L_{11} = L_{22} = \frac{p^2}{2(p^2 - 1)} + \frac{p}{2(1 - p^2)^{3/2}} \cos^{-1} p \quad (\text{S1b})$$

$$L_{33} = 1 - 2L_{11} \quad (\text{S1c})$$

$$p = \frac{a_3}{a_1} \quad (\text{S1d})$$

$$\beta_{ii} = \frac{K_{ii}^c - K_m}{K_m + L_{ii}(K_{ii}^c - K_m)} \quad (\text{S1e})$$

$$K_{ii}^c = \frac{K_p}{1 + \frac{\gamma L_{ii} K_p}{K_m}} \quad (\text{S1f})$$

$$\gamma = (1 + 2p) \frac{R_{BD} K_m}{a_3} \quad (\text{S1g})$$

$$\langle \cos^2 \theta \rangle = \frac{\int \rho(\theta) \cos^2 \theta \sin \theta d\theta}{\int \rho(\theta) \sin \theta d\theta} \quad (\text{S1h})$$

where:

K_m and K_p are the **thermal conductivities** of the matrix and particles (hBN platelet in our case), respectively. The K_m value is taken from the measured data; 0.22 W/m·K for the injection moulded TPU and 0.14 W/m·K for the cast epoxy. The K_p value used is the average thermal conductivity of hBN (300 W/m·K), see also sensitivity analyses below. The hBN platelet has anisotropic thermal conductivity due to its layered structure [8]. The in-plane thermal conductivity (along the (002) plane) of hBN is about 600 W/m·K, due to strong covalent bonds between B atoms and N atoms. The through-plane thermal conductivity (along the (100) plane) is around 2–30 W/m·K [9]. The K_p value has a minor effect on the thermal conductivity of the injection moulded composites, which have $\langle \cos^2 \theta \rangle$ in the range 0.75 to 1, as shown in Figure S12.

f is the volume fraction of particles (vol%)

K_{ii}^c is the **equivalent thermal conductivity** along the ii symmetric axis of the composite unit cell (with 11 and 33 representing in-plane and through-plane directions, respectively)

L_{ii} are **geometrical factors**, dependent on the particle shape (on our case: $L_{11} = L_{22} = 0.037$; $L_{33} = 0.926$)

p is the **ellipsoid particle aspect ratio**; in our case a_1 is the platelet diameter and a_3 is the thickness. According to information from the hBN powder supplier, a_1 and a_3 of powder BN3 are about 20 μm and 1 μm , respectively. Hence, the value of p used for the model is 0.05.

R_{BD} is the **interfacial thermal resistance** between particle and matrix (a property concentrated on a surface with zero thickness). The R_{BD} range of ($10^{-8} - 10^{-6}$) $\text{m}^2\text{W/K}$ for the hBN/polymer composites have been found by previous studies on polymer composites with hBN [6]–[8], [10]. Hence, the R_{BD} values from 0 to 10^{-6} $\text{m}^2\text{W/K}$ are used in our paper.

$\langle \cos^2 \theta \rangle$ is a measure of the **orientation of the ellipsoid particles** in the matrix (platelets in our case); θ is the angle between a platelet surface normal and the specimen surface normal; $\rho(\theta)$ is a distribution function describing the platelet orientation. Hence, $\langle \cos^2 \theta \rangle$ is 1, 1/3 or 0 for platelets with in-plane, random or through-plane orientation, respectively (as illustrated in Figure S11) [5]. The $\langle \cos^2 \theta \rangle$ values in our study are based on the data from the XRD measurements of the IM and cast specimens, as presented in Figure 11 in the article. The cast (hBN/epoxy) specimens have $\langle \cos^2 \theta \rangle$ values in the range (0.4 – 0.65) for hBN loadings in the range (21.6 – 38.5) vol%. For the IM (hBN/TPU) specimens, the $\langle \cos^2 \theta \rangle$ values of composites with (8.3 – 14.6) vol% hBN are about 0.85, and composites with (21.6 – 48.7) vol% hBN have average $\langle \cos^2 \theta \rangle$ values in the range of (0.75 – 0.85).

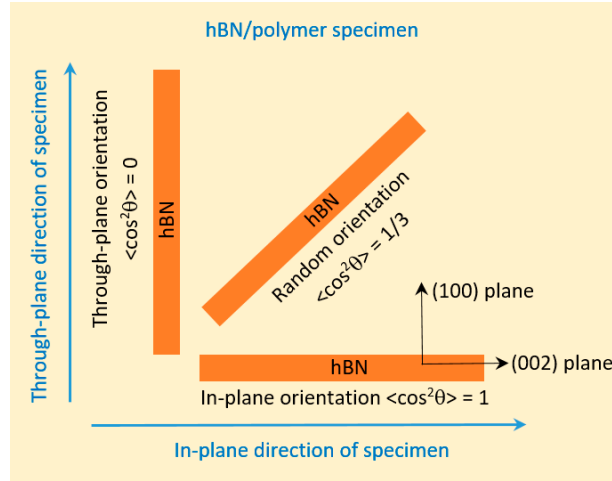


Figure S11. Orientation of hBN platelets; through-plane, random and in-plane.

There are uncertainties in our data with regard to using this model to interpret our experimental results. For instance, the interfacial thermal resistance is unknown, and the average orientation of platelets through the cross section is uncertain, at least for injection moulded specimens. Other parameters are also uncertain, such as the size and aspect ratio of the platelets.

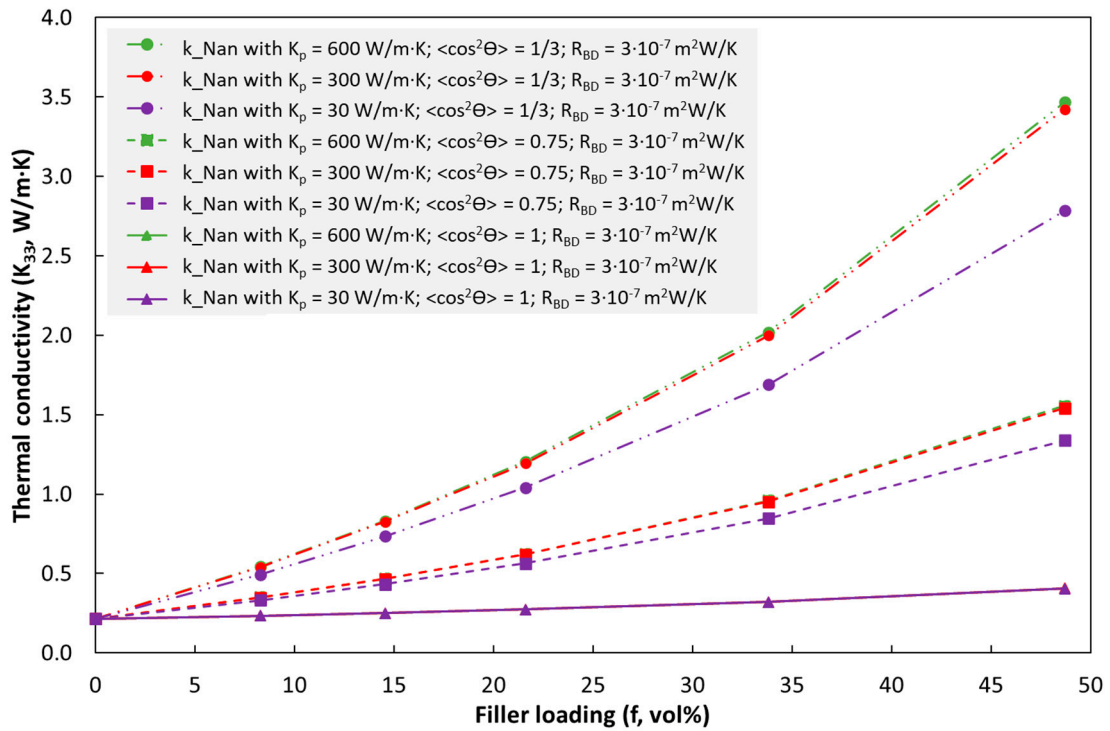
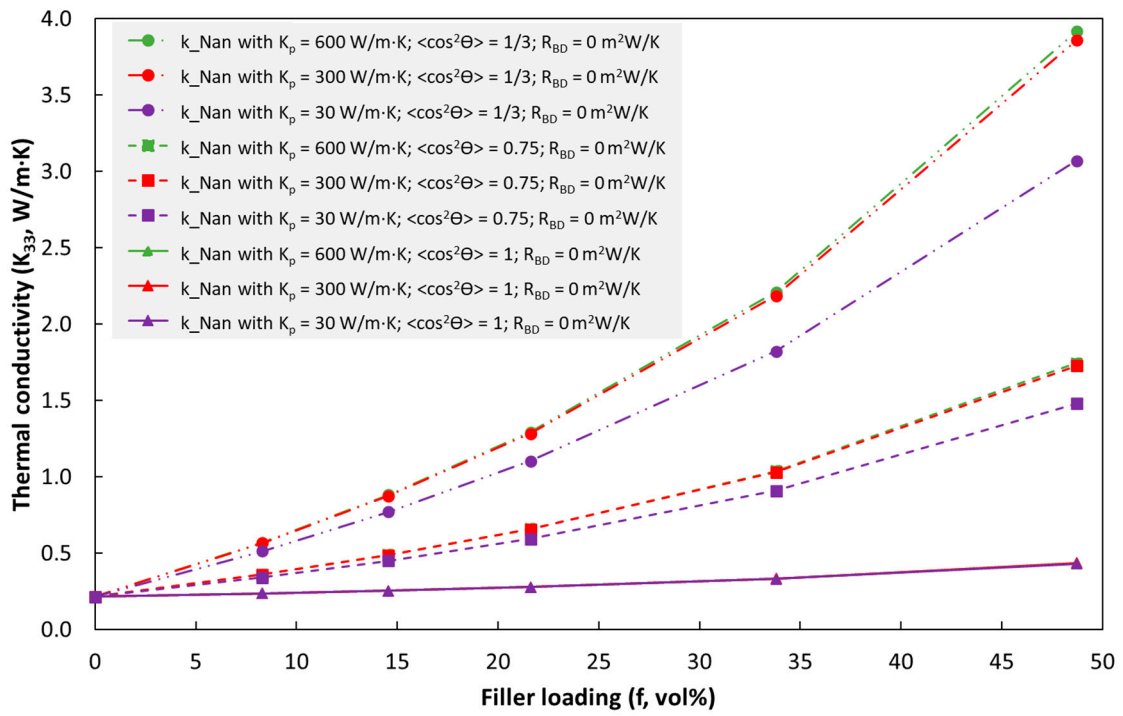
In order to evaluate these limitations and uncertainties, the effect of various parameters on the model through-plane conductivity (K_{33}) are shown in Figure S12a-c. In each diagram (a to c), K_{33} is plotted as function of platelet loading for selected values of platelet conductivity ($K_p = 30, 300$ and 600 W/m·K) and average platelet orientation ($\langle \cos^2\theta \rangle = 1/3, 0.75$ and 1). The interfacial thermal resistance (R_{BD}) is $0, 3 \cdot 10^{-7}$ and 10^{-6} m²W/K, in Figure S12a, Figure S12b and Figure S12c, respectively.

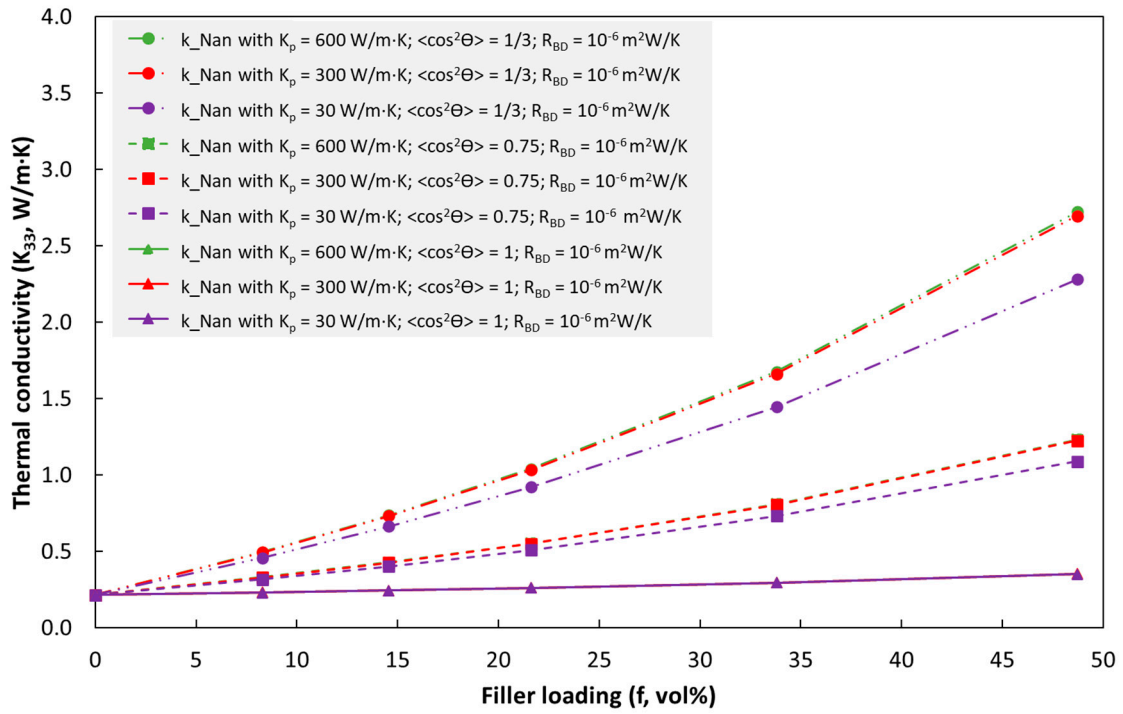
Figure S12 shows that for $\langle \cos^2\theta \rangle = 1$ (in-plane orientation of platelets), the K_{33} value is the same for the three selected K_p values. The effect of R_{BD} is also small.

For $\langle \cos^2\theta \rangle = 0.75$, the K_{33} value is practically the same whether K_p is set to 300 or 600 W/m·K, while K_{33} is reduced when K_p is reduced to 30 W/m·K (although the reduction in K_{33} is small for platelet fractions below about 20 vol%). The effect of R_{BD} is noticeable for this orientation. For K_p set to 300 or 600 W/m·K, K_{33} (at 48.7 vol% hBN) is reduced from about 1.75 to about 1.25 W/m·K when R_{BD} is increased from 0 to 10^{-6} m²W/K.

Also for the lowest orientation in Figure S12, i.e. $\langle \cos^2\theta \rangle = 1/3$, K_{33} is nearly independent of K_p in the range 300 or 600 W/m·K, but reducing K_p to 30 W/m·K has a quite large effect on K_{33} . The sensitivity to R_{BD} is also higher for this orientation.

Hence, for our injection moulded specimens, with $\langle \cos^2\theta \rangle$ in the range 0.75 to 1, a K_p value of 300 W/m·K can be used, although K_{33} is slightly overpredicted with this K_p value. However, it is difficult to estimate the R_{BD} value via model fits, due to uncertain average $\langle \cos^2\theta \rangle$ values through the specimen thickness and uncertain platelet dimensions, as well as potential platelet-platelet contact or nonuniform platelet distributions or voids. Anyhow, comparing experimental data with model predictions with different R_{BD} and $\langle \cos^2\theta \rangle$ values can give some insight.





(c).

Figure S12. Effects of K_p , $\langle \cos^2\theta \rangle$ and R_{BD} on the thermal conductivity K_{33} of the model of Nan et al. (Eq. S1). Other parameters: $K_m = 0.22$ W/m·K; $p = 0.05$; $a_3 = 1$ μm ; Note that, for $\langle \cos^2\theta \rangle = 1$, the curves for $K_p = 30$; 300 and 600 W/m·K overlap. Also, for $\langle \cos^2\theta \rangle = 0.75$ and $1/3$ the curves for $K_p = 300$ and 600 W/m·K overlap.

To complement the comparison between this model and experimental data for injection moulded composites in the article, Figure S13 compares the model with experimental data for cast composites. In this figure, the lower and upper experimental values of $\langle \cos^2\theta \rangle$ (0.4 and 0.65) were used in the model. For the data up to about 34 vol% filler, the agreement between model and experiments is OK, if we assume that the average $\langle \cos^2\theta \rangle$ through the disc thickness is somewhat less than 0.4 (since it may be lower in the core than at the surface, at which the XRD measurements was performed) and the effective R_{BD} value is much lower than 10^{-6} (here "effective" means that there is some filler-filler contact in the specimens which is not accounted for in the model). However, at the highest filler loading (about 38 vol%), the model clearly underpredicts the experiment, if parameters assumedly represent an upper limit conductivity for this case ($\langle \cos^2\theta \rangle = 1/3$ and $R_{BD} = 0$). Hence, at this loading there seems to be a percolation effect in the experimental data, if we believe this model is correct at lower loadings.

S12. The model of Ordóñez-Miranda et al.

Ordóñez-Miranda et al. [11] combined the Nan model above with the Bruggeman integration principle. The resulting model is claimed to be better at high particle volume fractions than the Nan model. However, Ordóñez-Miranda et al. only considered the case with random orientation of particles.

The Ordóñez-Miranda ("O-M") model was implemented by solving Eq. 11 in ref. [11] in combination with Eq. S1b-S1h above (with $\langle \cos^2\theta \rangle = 1/3$).

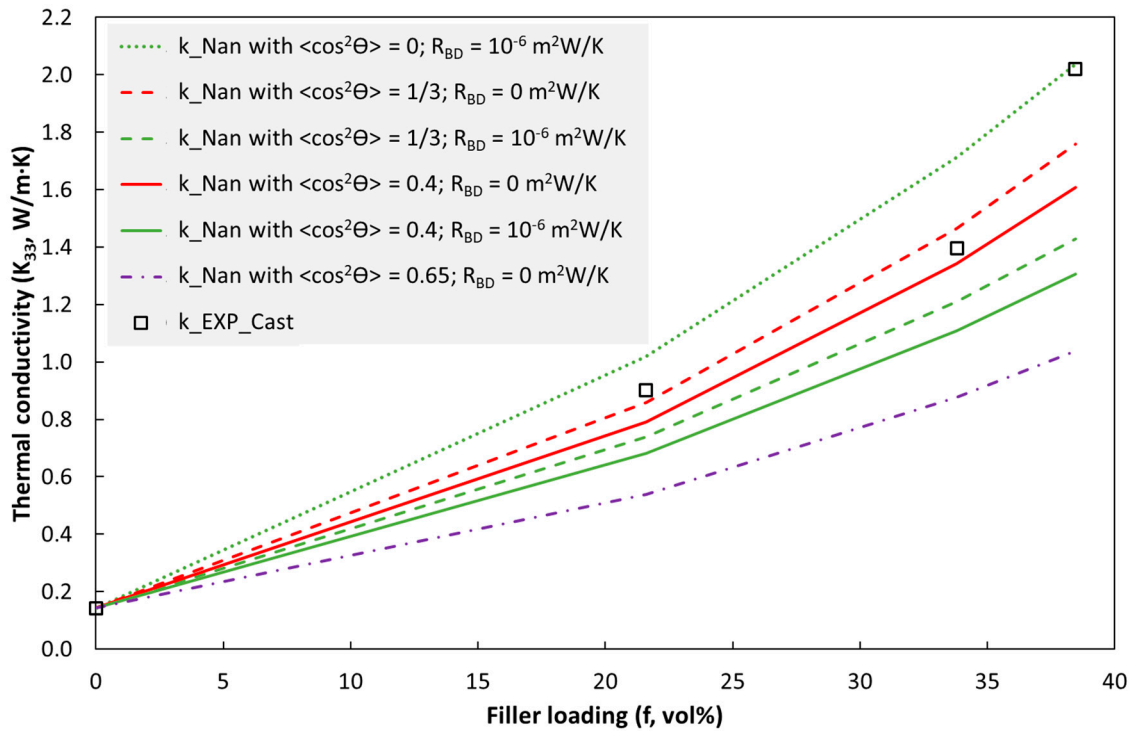


Figure S13. The model of Nan et al. compared to measured thermal conductivities of cast BN3/epoxy composites (k_{EXP_Cast}). In addition to the model parameters given in the legend, the model parameters were $K_m = 0.14$ W/m·K, $K_p = 300$ W/m·K, $p = 0.05$ and $a_3 = 1$ μ m. ($\langle \cos^2\theta \rangle = 0.4$ and 0.65 are the lower and upper limits of the experimental data obtained by XRD).

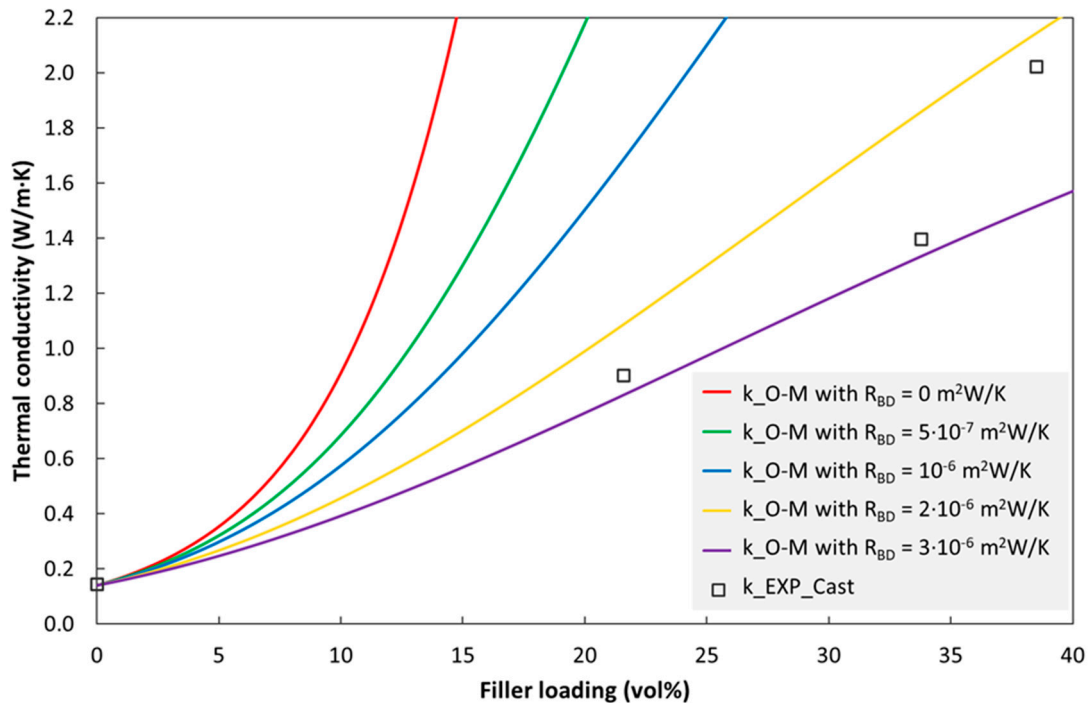


Figure S14. Ordóñez-Miranda model (k_{O-M}) compared to measured values for cast BN3/epoxy composites (k_{EXP_Cast}). In addition to the model parameters given in the legend, the model parameters were $K_m = 0.14$ W/m·K, $K_p = 300$ W/m·K, $p = 0.05$, $a_1 = 20$ μ m, $a_3 = 1$ μ m, and $\langle \cos^2\theta \rangle = 1/3$.

S13. The Model of Sun et al.

Based on a finite element model, Sun et al. [12] derived an analytical model for the thermal conductivity of hBN/polymer composites. In addition to the effects included in the Nan model above, the Sun model also takes into account the anisotropic thermal conductivity of the hBN platelets. Hence, in principle it should be more accurate than the Nan model in section S11 above. However, the Sun model has the same limitations as the models above regarding no filler-filler contact and a homogeneous platelet distribution.

The model of Sun et al. is given by Eqs. S2-S4 below. Note that the expression for K'_y contained an error in ref. [12]. The corrected expression is given below (correction received from Dr. Sun, the first author of ref. [12]).

$$\begin{bmatrix} K_{xx} & K_{xy} & K_{xz} \\ K_{yx} & K_{yy} & K_{yz} \\ K_{zx} & K_{zy} & K_{zz} \end{bmatrix} = C^{-1} \begin{bmatrix} K'_x & 0 & 0 \\ 0 & K'_y & 0 \\ 0 & 0 & K'_z \end{bmatrix} C \quad (S2)$$

$$\frac{K'_x}{\varepsilon_{p,x}\varepsilon_{t,x}K_m} = 1 + \left[\frac{K_{f,in}f^8 + 3(a+9)}{2(3+700K_{f,in}R_{BD})} - 1 \right] f \quad (S3)$$

$$\frac{K'_y}{\varepsilon_{p,y}\varepsilon_{t,y}K_m} = 1 + \left[\frac{9K_{f,in}f^8 + \sqrt{3}(a+9)}{2+700K_{f,in}R_{BD}} - 1 \right] f$$

$$\frac{K'_z}{\varepsilon_{p,z}\varepsilon_{t,z}K_m} = 1 + \frac{3}{2} \left[\frac{5K_{f,o}f^3 + \sqrt{3}(1+1/a)}{1+10^6K_{f,o}R_{BD}} - 1 \right] f$$

with

$$\begin{aligned} \varepsilon_{p,x} &\approx 1.00 \sim 1.05; \quad \varepsilon_{p,y} \approx 0.99 \sim 1.06; \quad \varepsilon_{p,z} \approx 1.00 \\ \varepsilon_{t,x} &\approx 0.93 \sim 1.00; \quad \varepsilon_{t,y} \approx 0.99 \sim 1.05; \quad \varepsilon_{t,z} \approx 1.00 \sim 1.06 \end{aligned}$$

$$C = \begin{bmatrix} \cos\alpha\cos\gamma + \sin\alpha\sin\beta\sin\gamma & -\sin\alpha\cos\beta & -\cos\alpha\sin\gamma + \sin\alpha\sin\beta\cos\gamma \\ \sin\alpha\cos\gamma - \cos\alpha\sin\beta\sin\gamma & \cos\alpha\cos\beta & -\sin\alpha\sin\gamma + \cos\alpha\sin\beta\cos\gamma \\ \cos\beta\sin\gamma & \sin\beta & \cos\beta\cos\gamma \end{bmatrix} \quad (S4)$$

where

K_{xx}, K_{yy}, K_{zz} are thermal conductivities of the hBN/polymer composites along the x, y, z axes.

K'_x, K'_y, K'_z are the thermal conductivities of the homogenized hBN/polymer composite along three directions in the ideal uniform dispersion model.

K_m is the thermal conductivity (W/m·K) of the polymer matrix

$K_{f,in}$ and $K_{f,o}$ are the thermal conductivity of hBN in the in-plane direction (100 – 1000 W/m·K) and through-plane direction (2 – 40 W/m·K), respectively. According to ref. [12], the K_{zz} value of the Sun model is almost independent of the thermal conductivity of the filler hBN, when the in-plane thermal conductivity of hBN is in the range of (100 – 1000) W/m·K, and the through-plane thermal conductivity of hBN is in the range (2 – 40) W/m·K [12]. Therefore, in our study, the values 300 W/m·K and 2 W/m·K were used for the in-plane ($K_{f,in}$) and through-plane ($K_{f,o}$) conductivities of h-BN, respectively.

a is the diameter to thickness ratio of the hBN platelets (the inverse of p in the EMA model).

f is volume fraction of filler (vol%)

R_{BD} is the interfacial thermal resistance between filler and polymer matrix.

$\varepsilon_{p,x}, \varepsilon_{p,y}, \varepsilon_{p,z}$ are position correction factors along the x, y and z axis (all are close to 1)

$\varepsilon_{t,x}, \varepsilon_{t,y}, \varepsilon_{t,z}$ are tilt angle correction factors (all are close to 1)

In our study, all the correction factors ($\varepsilon_{p,x}, \varepsilon_{p,y}, \varepsilon_{p,z}, \varepsilon_{t,x}, \varepsilon_{t,y}, \varepsilon_{t,z}$) were set to 1 for simplifying the calculations.

α , β , γ are the tilt angle deviations of the hBN platelets in three directions; γ in the Sun model corresponds to θ in the Nan model.

K_{zz} in the Sun model [12] corresponds to the through-plane conductivity of the Nan model above. Eqs. S2-S4 were calculated with a Python code in our study. The conductivity K_{zz} in the thickness direction of the disc was calculated by averaging over the angles α and β , for a given γ value. Our calculations were validated by comparing with the data in Figures 7 and 10 in ref. [12]. The values were similar, except small difference at volume fractions above 60% in Figure 10b of ref. [12]. The reason for this is unclear.

The Sun model generally predicts lower conductivities than the Nan model. For the cast specimens, the Sun model underestimates the conductivity for all three data points in the interval 20-40 vol% hBN, see Figure S15, but the model may give fair predictions for loadings up to 10 vol%. As for the Nan model, the experimental data has a larger curvature vs. filler loading (vol% hBN) than the model predictions.

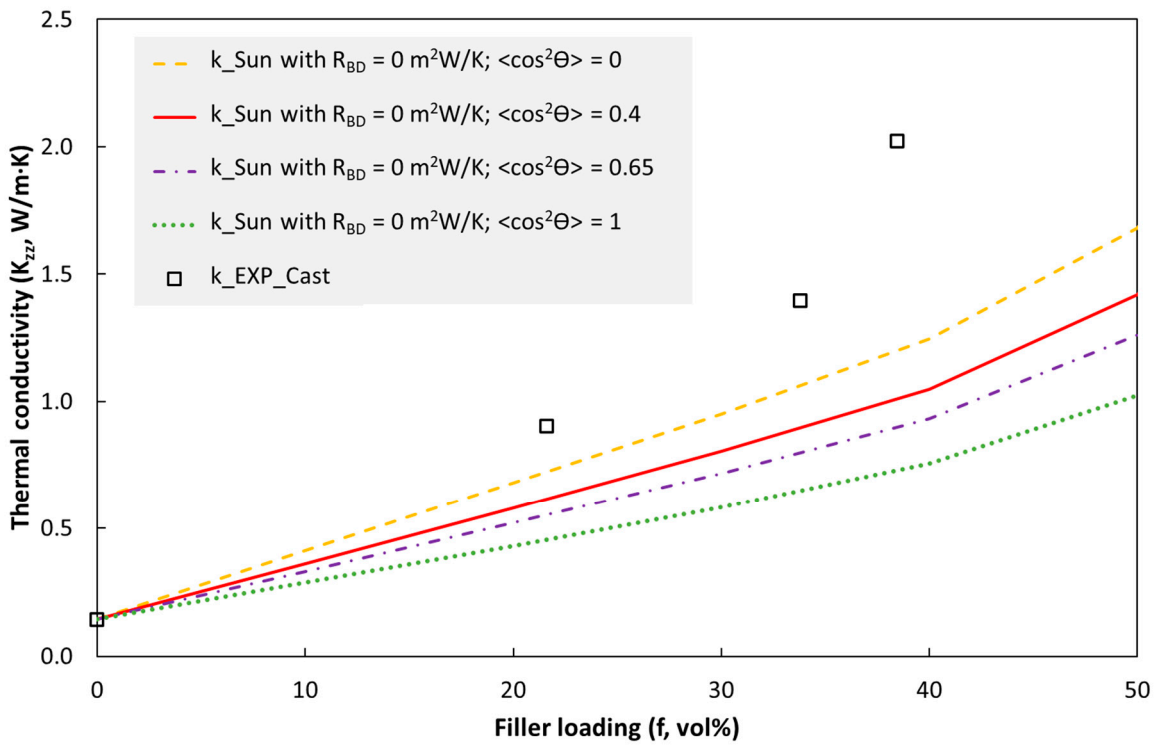


Figure S15. The Sun model (k_{Sun}) compared with the measured values for cast BN3/epoxy composites ($k_{\text{EXP_Cast}}$). Parameters used in the model are $K_m = 0.14$ W/m·K; $K_{f,\text{in}} = 300$ W/m·K and $K_{f,o} = 2$ W/m·K; $a = 20$; $R_{\text{BD}} = 0$ m²W/K; and γ equal to θ given by $\langle \cos^2\theta \rangle = 0, 0.4, 0.65,$ and 1 (0.4 and 0.65 are the lower and upper limits of the experimental data obtained by XRD).

S14. The Lewis-Nielsen Model

The Lewis-Nielsen model for the thermal conductivity is given by Eq. S5 [13]:

$$k = k_m \left[\frac{1 + fA\xi}{1 - f\xi\psi} \right] \quad (\text{S5a})$$

$$\xi = \frac{k_p/k_m - 1}{k_p/k_m + A} \quad (\text{S5b})$$

$$\psi = 1 + f \left[\frac{1 - f_m}{f_m^2} \right] \quad (\text{S5c})$$

Here f is the particle volume fraction, A is a particle geometry factor, f_m is the maximum volume fraction (often 0.8-0.85 for platelets [13]). The geometry factor represents the effective particle shape in the direction in which the conductivity is measured. Hence, the average particle orientation is embedded in this geometry factor. The drawback of this model is that the geometry factor is mainly an empirical fitting parameter.

In Figure S16, the Lewis-Nielsen model is compared to experimental data for injection moulded specimens. One set of model parameters (A and f_m) can not describe the experimental dataset, if f_m is in the interval stated above. An increase in A is with increasing particle volume fraction is in line with the formation of conducting "chains" of particles as discussed in the article. If a lower value of f_m is used, the model gives a better fit to the experimental data, see Figure S17, but this has no physical basis.

In Figure S18, the Lewis-Nielsen model is compared to experimental data for cast specimens. Note that a best fit yields almost the same f_m as for the injection moulded specimens, but this is again unphysical and due to the overfitting to capture the last data point. The Lewis-Nielsen model can fit the overall non-linearity of the experimental data set with relevant f_m values, but there are only four data points, and the three first data points probably follow a roughly linear trend, while the last point is higher than this trend due to the formation of "chains" of platelets.

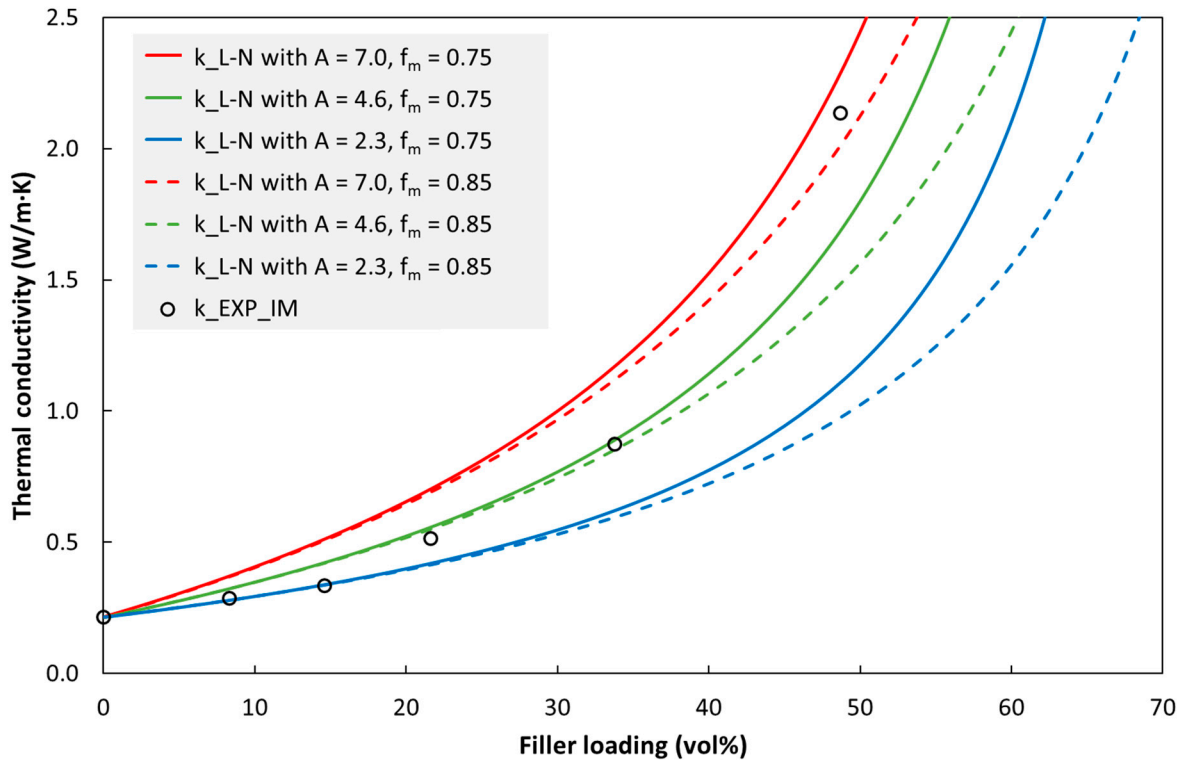


Figure S16. The Lewis-Nielsen model (k_{L-N}) and experimental data for injection moulded specimens of BN3/TPU (k_{EXP_IM}). Other parameters: $k_m = 0.22$ W/m·K and $k_p = 300$ W/m·K.

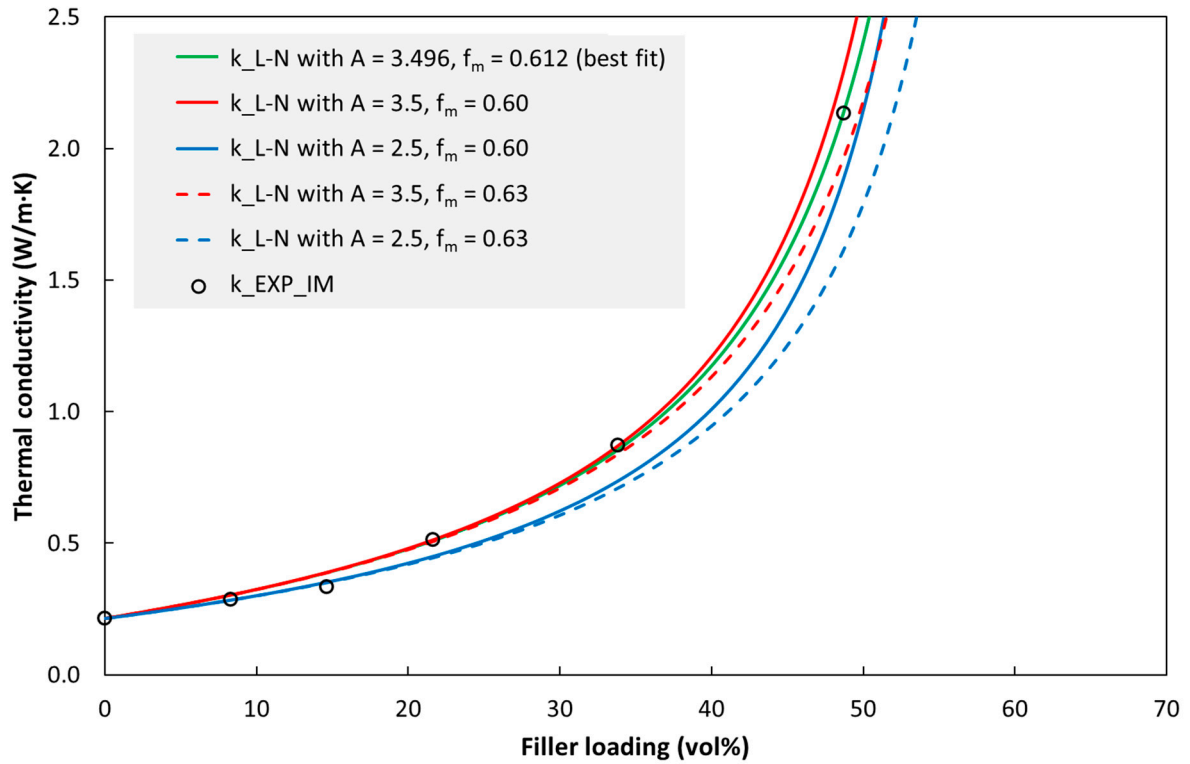


Figure S17. The Lewis-Nielsen model (k_{L-N}) and experimental data for injection moulded specimens of BN3/TPU (k_{EXP_IM}). Other parameters: $k_m = 0.22$ W/m·K and $k_p = 300$ W/m·K.

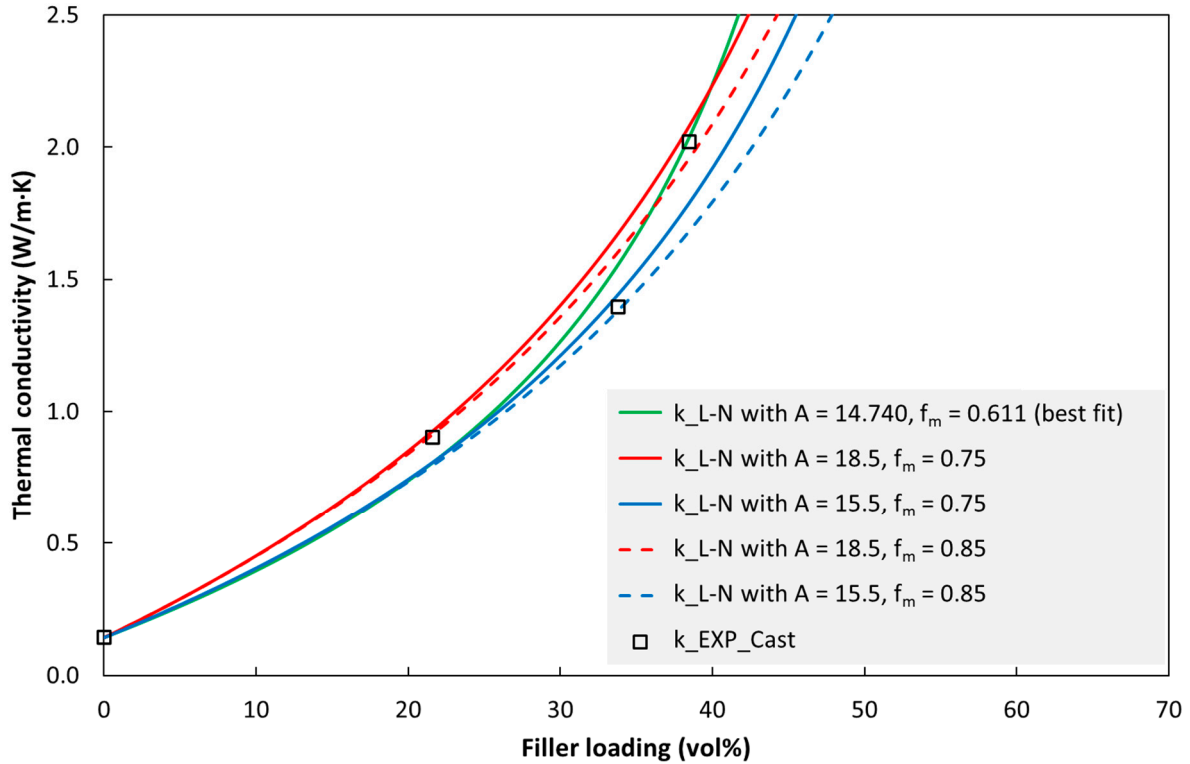


Figure S18. The Lewis-Nielsen model (k_{L-N}) and experimental data for cast specimens of BN3/epoxy (k_{EXP_Cast}). Other parameters: $k_m = 0.14$ W/m·K and $k_p = 300$ W/m·K.

References

1. Henze Boron Nitride Products AG, "HeBoFill ® LL-SP 120," *Technical Datasheet*, p. 8374, 2020.
2. Henze Boron Nitride Products AG, "HeBoFill ® CL-ADH 020," *Technical Datasheet*, pp. 49–50, 2020.
3. H.-C. Tseng, R.-Y. Chang, and C.-H. Hsu, "Comparison of recent fiber orientation models in injection molding simulation of fiber-reinforced composites," *Journal of Thermoplastic Composite Materials*, vol. 33, no. 1, pp. 35–52, Jan. 2020, doi: 10.1177/0892705718804599.
4. S.M. Mazahir, G.M. Velez-Garcia, P. Wapperom, and D. Baird, "Fiber orientation in the frontal region of a center-gated disk: Experiments and simulation," *J Nonnewton Fluid Mech*, vol. 216, pp. 31–44, Feb. 2015.
5. C. W. Nan, R. Birringer, D. R. Clarke, and H. Gleiter, "Effective thermal conductivity of particulate composites with interfacial thermal resistance," *J Appl Phys*, vol. 81, no. 10, pp. 6692–6699, 1997, doi: 10.1063/1.365209.
6. C. Yuan, B. Duan, L. Li, B. Xie, M. Huang, and X. Luo, "Thermal Conductivity of Polymer-Based Composites with Magnetic Aligned Hexagonal Boron Nitride Platelets," *ACS Appl Mater Interfaces*, vol. 7, no. 23, pp. 13000–13006, 2015, doi: 10.1021/acsami.5b03007.
7. Y. Xue, X. Li, H. Wang, F. Zhao, D. Zhang, and Y. Chen, "Improvement in thermal conductivity of through-plane aligned boron nitride/silicone rubber composites," *Mater Des*, vol. 165, p. 107580, 2019, doi: 10.1016/j.matdes.2018.107580.
8. C. Pan, J. Zhang, K. Kou, Y. Zhang, and G. Wu, "Investigation of the through-plane thermal conductivity of polymer composites with in-plane oriented hexagonal boron nitride," *Int J Heat Mass Transf*, vol. 120, no. December, pp. 1–8, 2018, doi: 10.1016/j.ijheatmasstransfer.2017.12.015.
9. H. Chen, V. v. Ginzburg, J. Yang, Y. Yang, W. Liu, Y. Huang, L. Du, and B. Chen, "Thermal conductivity of polymer-based composites: Fundamentals and applications," *Prog Polym Sci*, vol. 59, pp. 41–85, 2016, doi: 10.1016/j.progpolymsci.2016.03.001.
10. J. Liu, W. Li, Y. Guo, H. Zhang, and Z. Zhang, "Improved thermal conductivity of thermoplastic polyurethane via aligned boron nitride platelets assisted by 3D printing," *Compos Part A Appl Sci Manuf*, vol. 120, no. February, pp. 140–146, 2019, doi: 10.1016/j.compositesa.2019.02.026.
11. J. Ordóñez-Miranda, J. J. Alvarado-Gil, and R. Medina-Ezquivel, "Generalized Bruggeman Formula for the Effective Thermal Conductivity of Particulate Composites with an Interface Layer," *Int J Thermophys*, vol. 31, no. 4–5, pp. 975–986, May 2010, doi: 10.1007/s10765-010-0756-2.
12. Y. Sun, L. Zhou, Y. Han, L. Cui, and L. Chen, "A new anisotropic thermal conductivity equation for h-BN/polymer composites using finite element analysis," *Int J Heat Mass Transf*, vol. 160, p. 120157, 2020, doi: 10.1016/j.ijheatmasstransfer.2020.120157.
13. C. Heinle, Z. Brocka, G. Hülner, G. Ehrenstein, and T. Osswald, "Thermal conductivity of polymers filled with non-isometric fillers: A process dependent, anisotropic property," in *Proceedings of the 67th Annual Technical Conference of the Society of Plastics Engineers (ANTEC 2009, Chicago)*, Jun. 2009, pp. 883–889.

**Novel encapsulation of a
medical ultrasound probe**

Nu Bich Duyen Do

**Doctoral dissertations at the
University of South-Eastern
Norway no. 182**

ISBN 978-82-7206-829-4 (print)
ISBN 978-82-7206-828-7 (online)

usn.no